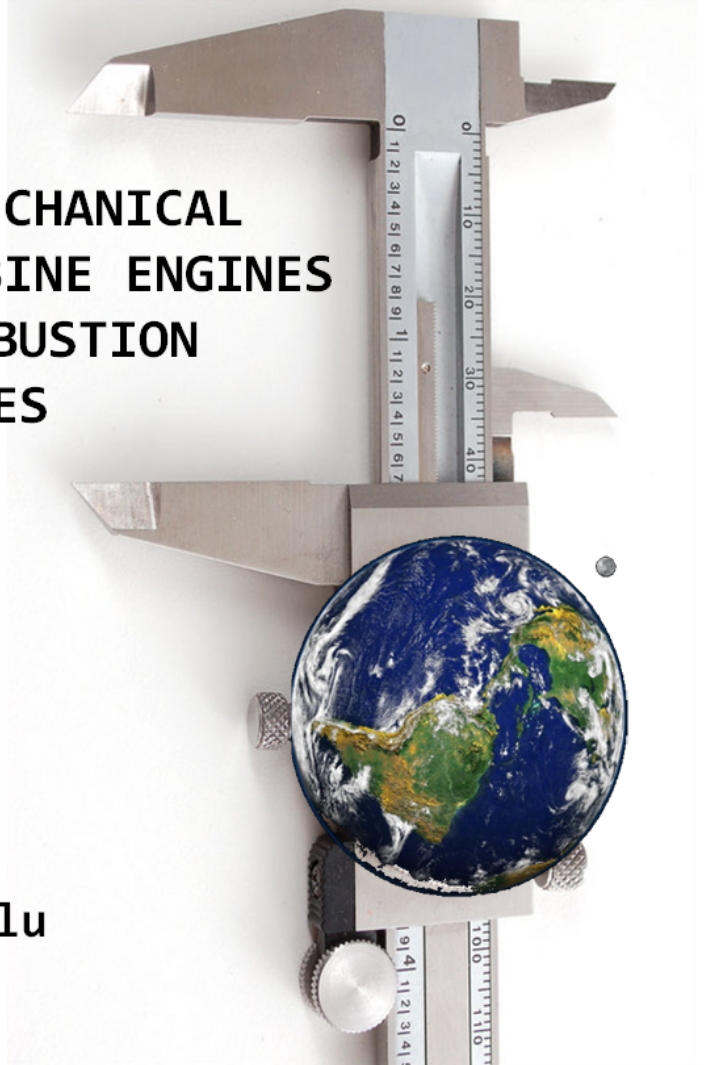


**THE ANALYSIS OF MECHANICAL  
INTEGRITY IN GAS TURBINE ENGINES  
SUBJECTED TO COMBUSTION  
INSTABILITIES**

**A. Can Altunlu**



**THE ANALYSIS OF MECHANICAL INTEGRITY  
IN GAS TURBINE ENGINES SUBJECTED TO  
COMBUSTION INSTABILITIES**

A. Can Altunlu

## **Composition of the graduation committee:**

### *Chairman and secretary:*

Prof.dr. F. Eising                                      University of Twente

### *Promotoren:*

Prof.dr.ir. A. de Boer                                University of Twente

Prof.dr.ir. T. Tinga                                  Netherlands Defence Academy, University of Twente

### *Assistant Promotor:*

Dr.ir. P.J.M. van der Hoogt                        University of Twente

### *Members:*

Prof.dr.ir. R. Akkerman                            University of Twente

Prof.dr.ir. R. Benedictus                         Delft University of Technology

Prof.dr.ir. T.H. van der Meer                    University of Twente

Prof.ir. D. Stapersma                              Netherlands Defence Academy, Delft University of  
Technology

Dr. P.R. Alemela                                    Alstom Power

*This research was financially supported by the European Commission in the Marie Curie Actions - Networks for Initial Training program, under call FP7-PEOPLE-2007-1-1-ITN, Project LIMOUSINE, with project number 214905.*

The analysis of mechanical integrity in gas turbine engines subjected to combustion instabilities

Altunlu, Abdullah Can

PhD thesis, University of Twente, Enschede, The Netherlands

July 2013

ISBN: 978-90-365-0055-5

DOI: 10.3990/1.9789036500555

URL: <http://dx.doi.org/10.3990/1.9789036500555>

© 2013 by A.C. Altunlu, Enschede, The Netherlands

Printed by: Ipskamp Drukkers, Enschede, The Netherlands

*Keywords: Gas turbine, thermo-acoustics, combustion instabilities, mechanical integrity, monitoring, fatigue, creep, fracture mechanics*

*Cover: A calliper dares to measure the world, designed by Can Altunlu.*

**THE ANALYSIS OF MECHANICAL INTEGRITY IN GAS  
TURBINE ENGINES SUBJECTED TO COMBUSTION  
INSTABILITIES**

DISSERTATION

to obtain  
the degree of doctor at the University of Twente,  
on the authority of the rector magnificus,  
Prof.dr. H. Brinksma,  
on account of the decision of the graduation committee,  
to be publicly defended  
on Friday, July 12<sup>th</sup>, 2013 at 14.45 hrs

by

Abdullah Can Altunlu

born on 31 August 1985

in Istanbul, Turkey



This dissertation is approved by:

Prof.dr.ir. A. de Boer      (*Promotor*)

Prof.dr.ir. T. Tinga      (*Promotor*)

Dr.ir. P.J.M. van der Hoogt   (*Assistant Promotor*)

dedicated to

my family

*Bülent, Nesrin and İdil Altunlu*

for their endless support, love and encouragement

and

my motivational and inspirational

supervisor and friend

*Peter van der Hoogt*



## Summary

Stringent regulations have been introduced towards reducing pollutant emissions and preserving our environment. Lowering  $\text{NO}_x$  emissions is one of the main targets of industrial gas turbine engines for power generation. The combustion zone temperature is one of the critical parameters, which is directly proportional to  $\text{NO}_x$  emission levels. Premixing an excessive amount of air with fuel before delivering to the combustor can reduce the temperature, at which combustion takes place, by burning a leaner mixture. Therefore, new generation combustion systems for modern gas turbines have been introduced, which are named lean, premixed (LP) combustion systems. However, LP combustion systems are prone to thermo-acoustically induced combustion instabilities, which are excited by a feedback mechanism between heat release, pressure and flow-mixture oscillations. Consequently, high amplitude oscillations of pressure are generated and heat transfer is generated, which results in mechanical vibrations at elevated temperatures, and hence degradation of mechanical integrity of combustor components due to fatigue and creep damage.

The present work in this thesis is focused on the development of efficient analysis tools to investigate the sensitivity of mechanical integrity and to assess the lifetime of structures at combustion instabilities.

In the design stage, it is desirable to predict the lifetime of the combustor. However, analysis of the engine components is problematic in the entire operating range, which is customised with respect to the demand. The engine can experience various scenarios. In this regard, the structural health of the combustor must be monitored in-service and assessed to prevent the deterioration of the materials resulting in catastrophic failure. The first part of this thesis introduces a methodology for structural health monitoring (SHM) techniques. Prior to the investigation, the acoustic and structural properties are analysed using experimental, analytical and numerical methods, and the fluid-structure interaction driven by combustion instabilities is indicated. In this section the application of vibration, acoustic and thermal based SHM techniques to a laboratory-scaled combustion system (LCS), designed and built in the University of Twente, is described. Finally, the most efficient combination of these techniques based on structural dynamics is presented to accurately assess a damaged structure excited by the instabilities.

The second part presents the analysis and validation of two-way interaction between the limit cycle behaviour of the unstable pressure oscillations and the structural vibrations. Furthermore, the prediction of fatigue and creep lifetime elevated by the combustion instabilities is considered. A two-way coupled fluid-structure interaction (FSI) analysis including Computational Fluid Dynamics (CFD) and Finite Element Method (FEM) is performed. The characteristic frequency, amplitude of pressure oscillations, fluid velocity and heat fluxes are calculated. The supplementary usage of the measured data and FSI analysis is found to be an efficient method to resolve the key instability parameters in the design stage, and to improve the safe-life design performance of the components.

The third part describes the theory of eXtended Finite Element Method (XFEM) based fracture mechanics analysis for Ni-based superalloys, which are typically used for combustors. In this model, the crack growth is quantified by an effective parameter to account for fatigue and creep. First, the model is validated with benchmark cases from the literature. Next, the method is applied to the combustion system (LCS) to predict the remaining lifetime reduction due to oscillating pressures at elevated temperatures and introduced hold times. This tool enables accurate analysis with a relatively high computational speed for damage-tolerant life design.

The last part deals with lifetime assessment of an LP combustion system in an industrial gas turbine engine, including part load and base load operation and combustion instabilities. A sequentially coupled CFD and FEM analysis is performed to calculate the temperature and pressure profile generated by the combustion process and the resulting stresses and strains in the combustion liner. The predicted failure pattern closely agrees with the observations in practice. The low-cycle fatigue (LCF) and creep lifetime of the liner is calculated. Next, the in-service measurement of pressure oscillations at base-load operation is analysed by a developed optimisation algorithm to obtain the minimum (optimum) data record time for a representative of ensemble of pressures. The algorithm is based on probabilistic analysis to compare the approximating model parameters for statistical distributions of various data record times. The pressure oscillations, with sufficiently enough data record time, are observed to reveal statistically deterministic characteristics, even though the physical process of combustion instabilities is characterised stochastic. Following, a rainflow algorithm is applied to the pressure oscillations data of optimum time record to translate the data with complex character into sets of basic cycles. The mean and the peak-to-peak alternating amplitude for each cycle in the histogram is determined. Subsequently, the (very) high-cycle fatigue (HCF/VHCF) lifetime of the liner is calculated due to instabilities. The damage matrix calculation shows that large amplitudes of less frequent pressures cause the highest damage. The approach described in this part enables a robust assessment of the mechanical integrity of the combustion liner in condition monitoring of the engine.

## Samenvatting

Overheden hebben strenge regels ingevoerd om ons milieu te beschermen en de uitstoot van vervuilende stoffen te verminderen. Bij industriële gasturbines voor stroomopwekking is het verlagen van stikstofemissies dan ook een topprioriteit. Een kritische parameter hierbij is de temperatuur in de verbrandingszone, omdat deze recht evenredig is aan de stikstofuitstoot. Deze temperatuur kan verlaagd worden door de brandstof op weg naar de verbrander met veel lucht te mengen en zo een armer mengsel te verbranden. Er wordt daarom in moderne gasturbines nu gewerkt met een nieuwe generatie verbrandingssystemen: de zogenaamde lean, premixed (LP) verbrandingssystemen. De verbranding in LP systemen verloopt echter niet altijd even stabiel. Er ontstaan thermo-akoestische instabiliteiten door de wisselwerking tussen hitteafgifte, druk en variaties in de brandstoftoevoer en mengverhouding. Dit leidt tot grote drukschommelingen en warmteoverdracht die resulteren in mechanische trillingen bij hoge temperaturen. Dit leidt tot degradatie van onderdelen van de verbrandingskamer ten gevolge van vermoeiing en kruip..

Het in dit proefschrift gepresenteerde onderzoek richt zich op de ontwikkeling van efficiënte analysemethoden om de mechanische integriteit van apparatuur en de gevoeligheid ervan voor instabiliteiten tijdens het verbrandingsproces te analyseren en de levensduur ervan bij dergelijke instabiliteiten te voorspellen.

In de ontwerpfase is het van belang om de levensduur van de verbrander te kunnen voorspellen. Analyse van de onderdelen is echter niet afdoende, omdat turbines niet standaard zijn, maar ieder aangepast aan specifieke eisen van gebruikers. Er kunnen zich verschillende scenario's voordoen. De verbrander moet daarom tijdens het gebruik gecontroleerd en beoordeeld worden om degradatie van de materialen en hieruit voortvloeiend uitval (met mogelijk catastrofale gevolgen) te voorkomen.

In het eerste deel van dit proefschrift wordt een methodologie gepresenteerd voor 'structural health monitoring' (SHM). Voorafgaand aan het onderzoek worden de akoestische en structurele eigenschappen onderzocht met gebruik van experimentele, analytische en numerieke methodes, en wordt een indicatie gegeven van de interactie tussen gas en constructie als gevolg van instabiliteiten tijdens het verbrandingsproces. Dit deel beschrijft hoe met SHM-technieken de invloed wordt gemeten van trillingen, geluid en hitte op een door de Universiteit van Twente ontworpen en in het laboratorium nagebouwd verbrandingssysteem (laboratory-scaled combustion system, LCS). Tot slot wordt aangegeven wat op basis van dynamisch gedrag de meest efficiënte combinatie van deze technieken is voor een juiste beoordeling van de toestand van een door genoemde instabiliteiten beschadigde constructie.

Het tweede deel van het proefschrift bestaat uit de analyse en validatie van de wisselwerking tussen de instabiele drukschommelingen, die het karakter hebben van een limi t cycle oscillation (LCO), en de structurele trillingen. Verder wordt onderzocht hoe materiaal vermoeiing en kruipschade door de instabiele verbranding kan worden voorspeld. Er wordt

gekeken hoe gas en constructie elkaar beïnvloeden door middel van een gekoppelde fluid-structure interaction (FSI) analyse inclusief Computational Fluid Dynamics (CFD) en Finite Element Method (FEM). Er worden berekeningen gepresenteerd van de karakteristieke frequentie en amplitude van drukschommelingen, de stroomsnelheid van de vloeistof (gas) en warmtestromen. Het aanvullend gebruik van de gemeten data met de FSI-analyse blijkt een efficiënte manier om al in de ontwerpfase waarden te vinden voor belangrijke instabiliteitsparameters, zodat de prestaties van de componenten kan worden verbeterd.

Het derde deel beschrijft hoe door middel van breukmechanica volgens de eXtended Finite Element Method (XFEM) een analyse kan worden gemaakt van de hoogwaardige nikkellegeringen die doorgaans voor verbrandingskamers worden gebruikt. In dit model wordt de groei van de scheur met een effectieve parameter gekwantificeerd om rekening te houden met de gevolgen van materiaal vermoeiing en kruipschade. Het model wordt eerst gevalideerd met voorbeelden uit de literatuur. Vervolgens wordt de methode toegepast op het verbrandingssysteem (LCS) om te voorspellen hoeveel de rest levensduur wordt verkort door drukschommelingen bij hoge temperaturen die een bepaalde tijd aanhouden. Dit instrument levert voor ontwerpers relatief snel een nauwkeurige voorspelling over hoe lang de gasturbine de schade kan doorstaan.

Het laatste deel gaat in op het schatten van de levensduur van een LP verbrandingssysteem van een industriële gasturbine, waarbij rekening wordt gehouden met gebruik op halve en normale kracht (part/base load) en instabiele verbranding. Er worden achtereenvolgens een CFD en een FEM analyse uitgevoerd om het temperatuurverloop en het drukverloop tijdens het verbrandingsproces in kaart te brengen en de belasting op de binnenwand van de verbrandingskamer te meten. Het voorspelde schade patroon komt nauw overeen met observaties in de praktijk. Er worden levensduurberekeningen van de binnenwand gemaakt, rekening houdend met low-cycle fatigue (LCF) en kruipschade. Hierna worden metingen van drukschommelingen bij een op normale kracht draaiend systeem geanalyseerd door middel van een eigen optimalisatie-algoritme. Hiermee wordt bepaald hoe lang er minimaal (optimaal) metingen verricht moeten worden om een representatieve verzameling drukmetingen te hebben. Het algoritme is gebaseerd op een waarschijnlijkheidsanalyse. Hiermee worden de benaderde modelparameters voor statistische verdelingen van verschillende meetperiodes vergeleken. Als de metingen lang genoeg duren, blijken de drukschommelingen statistisch deterministische karakteristieken te vertonen, ondanks het feit dat het fysieke instabiele verbrandingsproces stochastisch is. Vervolgens wordt een rainflow counting algoritme toegepast op de drukschommelingen gemeten in de optimale meetperiode om de complexe data te vertalen naar verzamelingen basiscycli. Voor iedere cyclus in de histogram worden het gemiddelde en de van piek tot piek variërende amplitude berekend. Hierna wordt de (very) high-cycle fatigue (HCF/VHCF) levensduur van de binnenwand berekend, rekening houdend met de instabiliteiten. Uit de berekening van de schades blijkt dat de grootste schade afkomstig is van minder vaak voorkomende maar uitzonderlijk sterke drukschommelingen. Met de in dit deel beschreven aanpak kan tijdens de continue bewaking van de conditie van de turbine de mechanische integriteit van de binnenwand van de verbrandskamer goed worden beoordeeld.

# Contents

- Summary ..... vii
- Samenvatting ..... ix
- 1 Introduction ..... 1
  - 1.1 Motivation ..... 2
  - 1.2 Research objective..... 6
  - 1.3 Outline..... 7
  - References ..... 9
  - Research publications..... 10
- 2 Sensitivity of combustion driven structural dynamics and damage to thermo-acoustic instability: combustion – acoustics – vibration..... 11
  - 2.1 Introduction ..... 12
  - 2.2 Sample problem: Aero-Box ..... 13
    - 2.2.1 Design of the Aero-Box ..... 14
    - 2.2.2 Analytical model ..... 14
    - 2.2.3 Acousto-elastic interaction ..... 15
    - 2.2.4 Modal characterisation ..... 16
    - 2.2.5 Structural damage detection ..... 17
    - 2.2.6 Damage detection by frequency shift method..... 18
    - 2.2.7 Damage localisation by flexibility method ..... 19
    - 2.2.8 Discussion on the Aero-Box ..... 21
  - 2.3 Laboratory-scaled generic combustor test setup ..... 21
    - 2.3.1 Design of the combustor ..... 22
    - 2.3.2 Material compliance and properties ..... 23
    - 2.3.3 Specimen configuration..... 24
    - 2.3.4 Instrumentation..... 25
    - 2.3.5 Structural condition monitoring ..... 26
    - 2.3.6 Combustion-driven dynamics ..... 27
    - 2.3.7 Acoustic characterisation ..... 30
    - 2.3.8 Structural characterisation..... 31
    - 2.3.9 Acoustical and structural response ..... 34
    - 2.3.10 Structural damage monitoring..... 38



2.4	Concluding remarks and discussions .....	43
	Acknowledgements .....	44
	References .....	44
<b>3</b>	<b>Fluid-structure interaction of combustion instabilities and fatigue/creep lifetime assessment .....</b>	<b>49</b>
3.1	Introduction .....	50
3.2	Experiment and method .....	52
3.2.1	Experimental combustor system design .....	53
3.2.2	Instrumentation.....	54
3.2.3	Materials and compliance.....	54
3.3	Fluid structure interaction (FSI) coupling strategy .....	55
3.3.1	Fluid domain: Computational fluid dynamics model.....	57
3.3.2	Solid domain: Computational structural dynamics model .....	58
3.4	Lifetime assessment .....	59
3.4.1	Temperature-structure analysis .....	59
3.4.2	Phenomenological modelling.....	60
3.4.3	Material behaviour and lifing.....	60
3.5	Results .....	61
3.5.1	Combustion and acoustic characterisation .....	62
3.5.2	Life assessment .....	72
3.6	Conclusions .....	74
3.7	Discussions.....	75
	Appendix A. Experimentation – emissivity & reflectivity.....	75
	Appendix B. Finite element formulation for the FSI .....	76
	Acknowledgements .....	77
	References .....	77
<b>4</b>	<b>XFEM-based fracture mechanics implementation for fatigue and creep crack growth of a nickel-based superalloy .....</b>	<b>81</b>
4.1	Introduction .....	82
4.2	Theory .....	84
4.2.1	Contour integral evaluation and domain integral representation .....	84
4.2.2	Time-dependent creep crack growth .....	89
4.2.3	Crack modelling: XFEM displacement approximation .....	92

4.2.4	Level set method and representation of the implicitly described crack .....	94
4.2.5	Crack growth algorithm: tracking and control (direction and magnitude).....	95
4.3	Benchmark cases for validation .....	97
4.3.1	Creep damage around a crack-tip .....	97
4.3.2	Thermally stressed body case.....	98
4.3.3	Compact tension (3-D) case .....	99
4.4	Conclusions .....	108
	Acknowledgement.....	108
	References .....	108
<b>5</b>	<b>Accelerated remaining life consumption of a crack due to thermo-acoustic oscillations in gas turbines .....</b>	<b>113</b>
5.1	Introduction .....	114
5.2	Methodology of the multiphysical analysis .....	114
5.2.1	Combustor test system .....	115
5.2.2	Materials and compliance.....	116
5.2.3	Finite element model.....	116
5.2.4	Fracture mechanics model.....	117
5.3	Results .....	121
5.3.1	Combustion characterisation .....	121
5.3.2	Temperature-structural analysis .....	122
5.3.3	Residual lifing .....	124
5.4	Concluding remarks and discussions .....	126
	Acknowledgement.....	127
	References .....	127
<b>6</b>	<b>Lifetime analysis using integrated fluid-structure approach for combustion dynamics in gas turbines.....</b>	<b>131</b>
6.1	Introduction .....	132
6.2	Problem description and methodology.....	133
6.3	Multiphysical modelling .....	136
6.3.1	Geometry.....	137
6.3.2	Computational fluid dynamics model .....	137
6.3.3	Material behaviour .....	138
6.3.4	Finite element model: Base material .....	139

6.4	Combustion dynamics analysis .....	140
6.4.1	Statistical distribution and probabilistic analysis .....	141
6.4.2	Rainflow cycle counting algorithm .....	143
6.5	Lifetime prediction .....	144
6.6	Results .....	146
6.6.1	Combustion generated loads .....	146
6.6.2	Structural behaviour at part and base load .....	149
6.6.3	Structural response at base load .....	151
6.6.4	Structural and acoustic modal response .....	154
6.6.5	Statistical and probabilistic analysis of data record .....	157
6.7	Life assessment .....	160
6.8	Conclusions .....	163
	Appendix: Stress analysis and assumptions .....	164
	Acknowledgement.....	165
	References .....	165
<b>7</b>	<b>Conclusions and recommendations</b> .....	<b>168</b>
7.1	Conclusions .....	169
7.2	Recommendations .....	175
	References .....	176
	<b>Acknowledgements</b> .....	<b>177</b>
	<b>About the author</b> .....	<b>182</b>

## 1 Introduction

A. Can Altunlu

*University of Twente, Faculty of Engineering Technology, Section of Applied Mechanics, 7500 AE, Enschede, The Netherlands*

---

### **Abstract**

*In this section an introduction to the work presented in this thesis is given. Firstly, the motivation behind the work is described, starting with an introduction to typical gas turbine engines with an emphasis on their combustor section, both in terms of design and performance properties. Next, the need of using lean premixed combustion systems, driven by low emission targets and gas turbine engine efficiency, is highlighted and a short description of combustion instabilities is provided. Then the main topic of this thesis is introduced: the link between the combustion instabilities and the need for reliable mechanical integrity tools. The research objectives are formulated and, finally, the outline of the research is provided, describing the relation between the chapters presented throughout this thesis.*

## 1.1 Motivation

Reducing pollutant emissions and preserving the environment, as well as maintaining efficiency and performance of gas turbines, are the key directions of engine manufacturers towards a sustainable economic future. The stringent regulations on emissions have led to the development of lean, premixed (LPM) combustion systems in gas turbine engines. The NO<sub>x</sub> emissions are lowered by reducing peak combustion temperatures by thoroughly premixing air and fuel to form a lean-mixture prior to delivery into the combustor. However, LPM combustion systems are susceptible to thermo-acoustically induced combustion instabilities. The instabilities lead to high amplitude oscillations of pressure and enhanced heat transfer, which result in severe mechanical vibrations at high temperatures. In this regard, a combined fatigue and creep damage is elevated, which must be assessed by means of lifetime of the combustor.

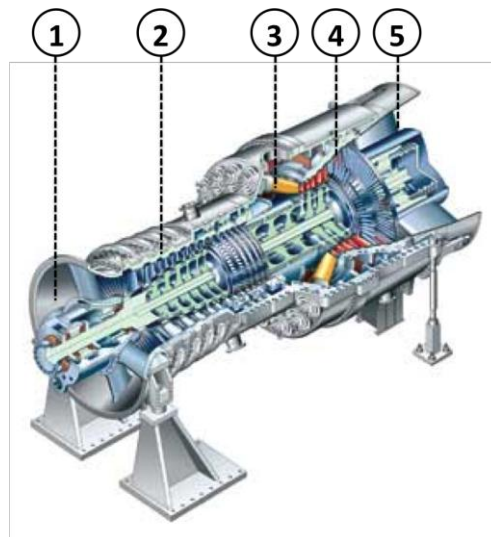


**Figure 1.1. Siemens SGT5-8000H gas turbine engine. Main components: inlet (1), compressor (2), combustion chamber (3), turbine (4), exhaust (5)**

In Figure 1.1, a typical modern industrial gas turbine engine, Siemens SGT5-8000H, is depicted, which is one of the most powerful and efficient stationary gas turbines used for power generation. The turbine power output of 375 MW can be increased to over 570 MW and an efficiency of more than 60% in a combined cycle power plant. The main principle of a combined cycle is to use hot exhaust gases from the gas turbine, and to extract heat from the gases to generate steam for a steam turbine, thus the overall efficiency is increased by recovering more useful energy from the heat. The gas turbine limit emissions are defined as NO<sub>x</sub> 25 ppm and CO 10 ppm.

The working principle of the gas turbine engine (Figure 1.1) can be described as follows. The incoming air at atmospheric conditions enters the inlet (1), and is compressed to high pressure through the compressor stages (2). Next, pressurised air is premixed with fuel (i.e. natural gas) before delivery into the combustor. Subsequently, the combustion process of the lean-mixture takes place at constant pressure in the combustion chamber (3). Furthermore, in the turbine section (4), energy is extracted from the high-pressure hot gases flowing from the

combustion chamber. The resulting motion of the turbine drives the compressor and a generator. After the turbine section, the exhaust gases flow through the exhaust section (5), and can be used to operate a steam turbine.

The energy demand of the developing world is considerably increasing due to rapid economic growth; therefore fossil fuels maintain their dominance to meet these urgent needs in the foreseeable future with their current availability and well-known practice. Reducing fossil fuel use is critical in order to reach emission targets and to curb the rise in global temperature; on the other hand, improving energy efficiency and performance qualifies as a crucial step in that direction. It should be noted that energy efficiency and performance does not only refer to combustion efficiency of gas turbines, but also to environmental friendliness, durability, reliability, and cost-effectiveness.

**Table 1.1. NO<sub>x</sub> emission standards for new turbines [2]**

Combustion turbine type	Combustion turbine heat input at peak load	NO <sub>x</sub> emission standard
New turbine firing natural gas, electric generating	≤ 50 MMBtu/h (≤ 3 MW)	42 ppm at 15% oxygen (O <sub>2</sub> ) or 290 ng/J of useful output (2.3 lb/MWh)
New turbine firing natural gas, mechanical drive	≤ 50 MMBtu/h (≤ 3 MW)	100 ppm at 15% O <sub>2</sub> or 690 ng/J of useful output (5.5 lb/MWh)
New turbine firing natural gas	> 50 MMBtu/h and ≤ 850 MMBtu/h (3 MW – 110 MW)	25 ppm at 15% O <sub>2</sub> or 150 ng/J of useful output (1.2 lb/MWh)
New, modified, or reconstructed turbine firing natural gas	> 850 MMBtu/h (> 110 MW)	15 ppm at 15% O <sub>2</sub> or 54 ng/J of useful output (0.43 lb/MWh).

Among the fossil fuels, natural gas is one of the major combustion fuels used in gas turbines for industrial and utility electric power generation. Because it is the cleanest of the known fossil fuels, this makes it pre-eminently suitable for reducing emissions of pollutants into the atmosphere. Natural gas is a combustible mixture of hydrocarbon gases that consists of a high percentage of methane (70 - 90%) and varying amounts of ethane, propane, butane, and inerts (typically nitrogen, carbon dioxide, hydrogen sulphide, and helium). The main products of the combustion of natural gas in stationary gas turbines are carbon monoxide (CO), carbon dioxide (CO<sub>2</sub>), water vapour (H<sub>2</sub>O), unburned hydrocarbons (UHC), particulate matter (mainly carbon), oxides of sulphur (SO<sub>x</sub>, mainly SO<sub>2</sub> and SO<sub>3</sub>), and oxides of nitrogen (NO<sub>x</sub>, mainly NO and NO<sub>2</sub>). Among the exhaust composition of gas turbines, CO<sub>2</sub> and H<sub>2</sub>O are natural consequences of complete combustion of hydrocarbon fuels, which implies that a reduction of these can be realised only by combusting less fuel. Therefore, they have not been recognised as pollutants in every country's legislation, even though they are considered as

being among the greenhouse gases [1]. Furthermore, the emissions of UHC, particulate matter, and  $\text{SO}_x$  are negligibly small for high power stationary gas turbine engines using natural gas, and more stringent measures have been introduced for  $\text{NO}_x$  [1]. They are known to contribute in causing adverse health and environmental effects, such as the production of chemical smog, acid rain, and depletion of ozone in the stratosphere. The environmental Protection Agency (EPA) established  $\text{NO}_x$  emission standards for new and modified engines depending on their combustion turbine heat input at peak load and application area [2]. Table 1.1 presents the  $\text{NO}_x$  emission standards according to the combustion turbine heat input at peak load (MMBtu/h: Million British thermal units per hour) of engines. Maximum emission limit is defined as 15 ppm for the highest power engines using natural gas. Note that the  $\text{NO}_x$  emission standards in ppm, listed in Table 1.1, are referenced to 15%  $\text{O}_2$  so that a correction formula depending on the  $\text{O}_2$  in-site measurement must be applied [1].

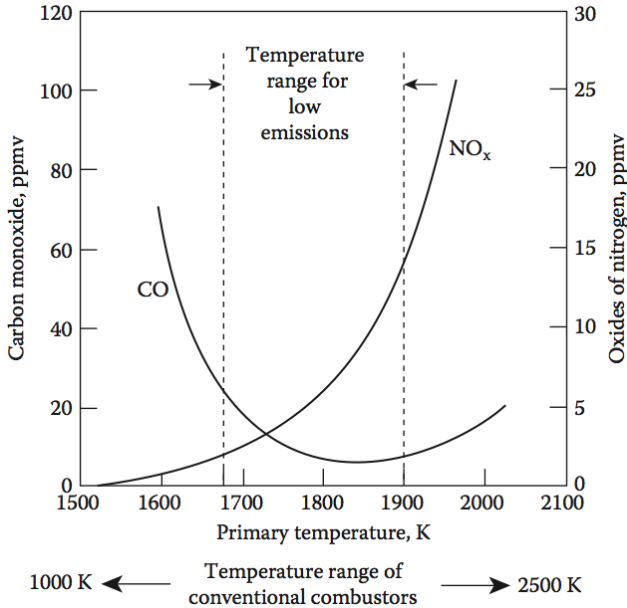


**Figure 1.2. Influence of primary-zone temperature on CO and  $\text{NO}_x$  emissions [1]**

The combustion zone temperature emerges as the most critical parameter, which has a significant impact on pollutant emissions of gas turbine combustors. Figure 1.2 illustrates the temperature dependence of CO and  $\text{NO}_x$  for typical conventional combustors [1]. As seen in the figure, the threshold temperature for CO is 1670 K, and below this temperature CO formation exhibits a rapid increase in amounts. On the other hand,  $\text{NO}_x$  is not produced in significant amounts until around 1900 K. However, a further increase in temperature results in excessive amounts of  $\text{NO}_x$ . The trend of the two curves conflicts; however, there is a relatively narrow temperature range from 1670 K to 1900 K so that CO and  $\text{NO}_x$  are kept below 25 and 15 ppmv, respectively. Moreover, on the one hand maintaining the combustion temperature within a relatively narrow range over engine power settings must be achieved to meet emission standards, and on the other hand material strength of engine components at elevated temperatures is inevitably limited by their maximum allowable operation temperature to conserve the mechanical integrity of engines in the long term. Therefore, in combustor design an optimum target must be defined between the conflict parameters, such as

high combustion efficiency, minimum pollutant emissions, and long lifetime and safe operation expectancy.

Premixing a large amount of air with fuel prior to its injection into the combustion prevents formation of local high temperatures. Hence, burning a leaner mixture can reduce the peak temperature. The concept for combustion technology has been introduced in modern gas turbine engines: lean-premixed (LPM) combustion systems.

LPM combustion systems are prone to combustion instabilities. These combustion systems generally operate near the lean blowout limit, thus a perturbation in the equivalence ratio is likely to produce heat release oscillations. Hence, if these oscillations match with one of the chamber acoustic resonance frequencies, high amplitude oscillations of pressure are generated. These pressure oscillations elevate the mechanical load in the chamber, which results in high amplitude vibrations. Furthermore, the unsteady flow enhances heat transfer, thus higher temperature exposure to the components. High amplitude vibrations together with elevated temperatures can lead to failure of the system. Figure 1.3 illustrates a comparison between an intact burner assembly and a damaged burner assembly due to combustion instabilities.

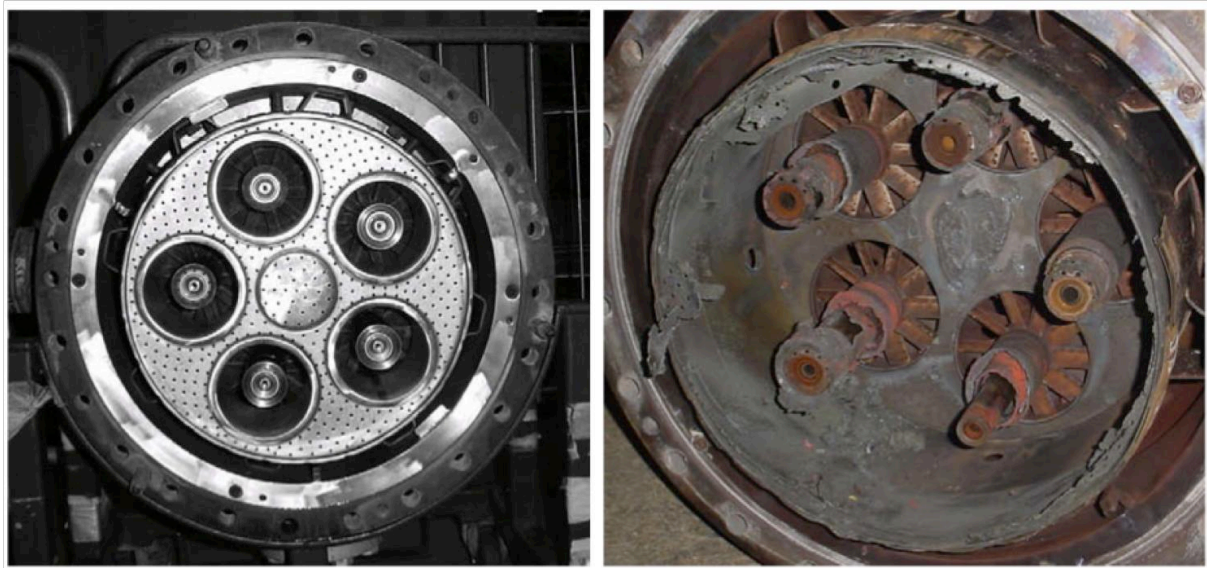


**Figure 1.3. Burner assembly – intact (left) and damaged (right) [3]**

Combustion instabilities in LPM combustion systems reveal substantial challenges to maintain reliability and safety. The instabilities are characterised to be detrimental to the mechanical integrity of the combustor components due to high amplitude oscillations of pressure and enhanced heat transfer. If the possible damage cannot be detected, monitored and accurately assessed, in extreme cases, not only the combustor fails, but also a part, torn away from a component due to the damaging process, can be liberated into the gas path through the turbine section, which results in complete failure of hot gas path components. Therefore, the instabilities must be predicted and recognised in the design stage, and precautions must be taken in advance to prevent unexpected failures of in-service components. However, avoiding or controlling instabilities remains challenging within the entire range of operating settings, depending on power transition (idle to nominal), or climate conditions. Thus, developments of



mechanical integrity tools are essential to ensure and maintain the reliability and safety, as well as the efficiency, of the new and existing engine components.

The LIMOUSINE project, supported by the European Commission under the Marie Curie Initial Training Network (ITN) program, was initiated for more systematic research on combustion instabilities. The target of the project is to investigate the thermo-acoustic instabilities in combustion systems, and the resulting unstable pressure oscillations, which leads to elevated mechanical vibrations at high temperatures. The project team consists of six academic partners (University of Twente, Netherlands – BRNO University of Technology, Czech Republic – Keele University, UK – Imperial College London, UK – University of Zaragoza, Spain – Boston University, USA), two research institutions (CERFACS, France – DLR, Germany) and five industrial partners (Ansys, UK – IfTA, Germany – (GDF Suez) Electrabel, Netherlands & Laborelec, Belgium – Sulzer Turbo Services, Netherlands – Siemens Power Generation, Germany).

The main collaborators within the project have performed multiphysical work. A laboratory-scaled combustion system (LCS) has been experimentally investigated by means of the thermo-acoustic instabilities by Roman Casano [4], and the dynamic interaction of the fluid and structure in this regime has been numerically analysed by Shahi [5], the steady-state and transient behaviour of an industrial combustion system (ICS) is discussed by Matarazzo [6]. The laboratory-scaled combustion system (LCS), which is designed and built at the University of Twente, is representative for gas turbine applications. It enables the investigation of interaction between combustion, acoustics and vibration. The investigation presented in this thesis is associated with these topics. The main focus is on improving the understanding of two-way interaction between combustion instabilities and structure, and the development and application of design and operation tools used for mechanical integrity analysis of the combustor.

In the next section, the research objectives and outline of this thesis are presented. The flow of the following chapters is described in the outline section of this chapter.

## **1.2 Research objective**

The main objective of this thesis is the development and application of experimental and numerical tools to analyse and assess the mechanical integrity of gas turbine engines subject to combustion instabilities. Further, the developed tools are aimed to be applicable to both the laboratory-scaled combustion system and the industrial combustion system.

The main objective is subdivided into a number of lower level objectives. The following topics are considered as sub-objective of this research:

- Development and application of structural health monitoring techniques to analyse the changes in structural dynamics due to the transition from stable to unstable combustion.
- Prediction of the fatigue and creep lifetime (crack-initiation) reduction due to combustion instabilities using a combined fluid-structural approach.

- Development and demonstration of an efficient tool to perform remaining lifetime prediction (crack-growth) by fracture mechanics analysis including fatigue and creep aspects.

- Development of a probabilistic and statistical analysis algorithm to robustly assess in-service pressure oscillations by means of lifetime.

Each of these sub-objectives contributes to achieve the main objective of this work. In the next section, these topics are addressed within the content of the thesis.

### 1.3 Outline

The thermo-acoustic instability in lean premix combustor systems is a multiphysical phenomenon, which is therefore investigated in an interdisciplinary framework. A schematic overview of the relevant topics and the associated chapters in this thesis is depicted in Figure 1.4. The relation between the different chapters will be discussed below.

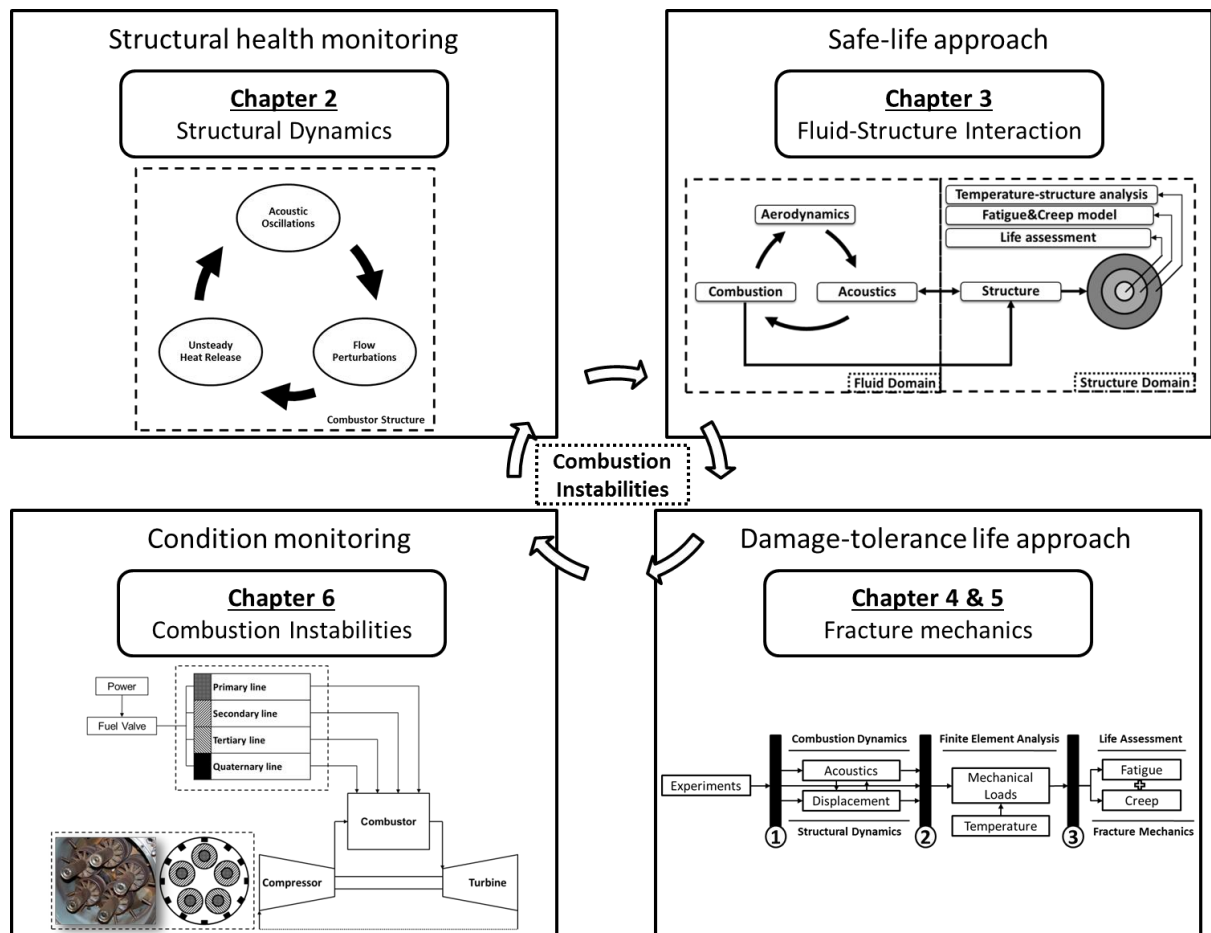


**Figure 1.4. Schematic overview of the chapters presented in this thesis**

It is desired to predict the limit-cycle pressure oscillations and characteristic frequencies over the whole operating range. A significant amount of effort is devoted to either the design measures on the combustion hardware to avoid instability, or passive/active control

techniques to control the instabilities. The current state of the art provides fair accuracy in the predictions, but still needs improvement. Moreover, prevention or control is difficult within the entire operation envelope due to variations of power settings or environmental conditions, such as climate. Therefore, it is crucial to enhance understanding of the instabilities and to monitor and predict the effects on the mechanical integrity of components in order to take measures in the design stage and assess the component lifetime.

In this regard, Chapter 2 presents a methodology for structural health monitoring (SHM) during the unstable combustion process. A comparative analysis based on structural dynamics is carried out for the intact and damaged structure. Also in this chapter, the combustion system (LCS) is described, together with the integrated equipment. Also its acoustic and structural modal properties are obtained by experimental and numerical techniques.

It is important to resolve the two-way interaction between the oscillating pressure load in the fluid and the motion of the structure under the limit cycle conditions. Therefore, Chapter 3 describes the analysis of fluid-structure interaction (FSI) using a combined Computational Fluid Dynamics (CFD) and Finite Element Method (FEM) approach on the combustion system (LCS), which is a modified version of the system presented in Chapter 2. The results of the FSI analysis are applied in two ways here. Firstly, the resulting structural loads are used in a fatigue and creep lifetime prediction, showing a significant reduction of the lifetime when instabilities occur. Secondly, the combination of the FSI analysis and measured data is utilised to obtain the characteristic frequency and acoustic pressure amplitudes. The growth rate of pressure oscillations is estimated by extrapolating the FSI results to the measured peak pressure by proposed growth functions. This method will be shown to be very effective in predicting the instabilities once the peak pressures are known for a certain operating range.

In chapter 3, a safe-life approach is applied for the combustion system, assuming that no initial damage is present in the combustor. However, in practice damage may already exist from the beginning due to manufacturing or handling errors, or damage growth may be promoted at local hot spots due to the loads driven by the combustion process. As discussed before, it is vital to detect and monitor the damage, but in addition a remaining lifetime assessment tool is required to schedule the inspections and preventive replacements that prevent any catastrophic failure from occurring.

In Chapter 4, a method is developed for a damage-tolerance life assessment for Ni-based superalloys, which are typically used for combustors. The methodology includes the eXtended Finite Element Method (XFEM) based fracture mechanics analysis covering fatigue and creep aspects. In this chapter, the method is described and validated with benchmark cases from the literature. The accuracy and speed of the computation makes this method stand out as decisive tool, both in design stage and during service. Chapter 5 deals with the implementation of the method described in Chapter 4 to the combustion system (LCS). The amplitudes of pressure oscillations, temperature levels and introduced hold times are linked to crack propagation life, thus remaining lifetime. When this method is used in combination with the SHM method proposed in Chapter 2, the safety and reliability of the engine can be ensured.

Although the developed methods in the first chapters have been applied to the test-scale combustor (LCS), application to real industrial gas turbines with their inherent complexity

reveals considerable challenges. In Chapter 3, it will be shown that even though the characteristic frequency is predicted reasonably close to the measurements, the prediction of limit cycle pressure oscillations only shows a fair agreement. However, in Chapter 5, the fatigue lifetime will be shown to be very sensitive to the pressure amplitudes.

Therefore, in Chapter 6, in-service measurements of pressure oscillations in a real industrial gas turbine engine are used to calculate the lifetime reduction due to combustion instabilities. CFD and FEM analyses are performed for stable operation to calculate the stresses and strains, and the associated creep and fatigue lifetime is calculated. The predicted failure pattern of the combustion liner is compared to observations in practice. The number of cycles to failure must include the effect of the combustion instabilities. However, processing the long data record time of measurements is computationally expensive and time consuming. Therefore, an optimisation algorithm was developed, based on statistical distribution and probabilistic analysis, to obtain the minimum data record time that is still representative for the entire data set at the same operating setting. Next, a rainflow cycle counting algorithm is applied to the data record to reduce the stochastic pressure oscillations into a set of basic reversals for fatigue analysis. The calculated damage matrix then relates the mean, amplitude and frequency of pressures to the fatigue lifetime. This smart and decisive tool leads to a powerful method to monitor the mechanical integrity of the combustor.

Finally, in Chapter 7, the main results are summarised and conclusions are drawn with respect to the research objectives. Furthermore, recommendations for further research directions are mentioned.

## References

- [1] Lefebvre, A. H., and Ballal, D. R., 2010, Gas turbine combustion: Alternative fuels and emissions, Taylor & Francis, Boca Raton.
- [2] Environmental Protection Agency, 2006, "Standards of Performance for Stationary Combustion Turbines; Final Rule," Federal Register Citation 71 FR 38482, Standard 40 CFR Part 60 Washington, DC, USA.
- [3] Goy, C. J., James, S. R., and Rea, S., 2005, "Monitoring combustion instabilities: E.ON UK's experience," Combustion Instabilities in Gas Turbine Engines: Operational Experience, Fundamental Mechanisms, and Modeling, T. C. Lieuwen, and V. Yang, eds., American Institute of Aeronautics and Astronautics, pp. 163-175.
- [4] Roman Casado, J. C., 2013, Ph.D. Thesis, University of Twente, Enschede, Netherlands (in progress).
- [5] Shahi, M., 2014, Ph.D. Thesis, University of Twente, Enschede, Netherlands (in progress).
- [6] Matarazzo, S., 2013, Ph.D. Thesis, University of Twente, Enschede, Netherlands (in progress).

## Research publications

The chapters from two to six are based on the papers, which are listed below under the *journal publications*. Furthermore, the *conference and symposium publications*, which have been published during this work, are also given below.

### Journal publications:

- 4- Altunlu, A.C., van der Hoogt, P., de Boer, A., “ Sensitivity of combustion driven structural dynamics and damage to thermo-acoustic instability: combustion – acoustics – vibration”, *Journal of Engineering for Gas Turbines and Power* (*accepted*). [**Chapter 2**]
- 3- Altunlu, A.C., van der Hoogt, P., de Boer, A., “Accelerated remaining life consumption of a crack due to thermo-acoustic oscillations in gas turbines” (*submitted*). [**Chapter 4 & 5**]
- 2- Altunlu, A.C., Shahi, M., Pozarlik, A., van der Hoogt, P.J.M., Kok, J.B.W., de Boer, A., “Fluid-structure interaction of combustion instabilities and fatigue/creep lifetime assessment” (*in progress*). [**Chapter 3**]
- 1- Altunlu, A.C., Matarazzo, S., Tufano, S., Tinga, T., Laget, H., Stopford, P., Boer, A., Kok, J.B.W., “Lifetime analysis using integrated fluid-structure approach for combustion dynamics in gas turbines” (*in progress*). [**Chapter 6**]

### Conference and symposium publications:

- 6- Altunlu, A.C., van der Hoogt, P., de Boer, A., “Accelerated life consumption due to thermo-acoustic oscillations in gas turbines: XFEM & Crack”, *International Council of the Aeronautical Sciences 2012 (ICAS2012)*, Brisbane, Australia, September 23-28, 2012.
- 5- Altunlu, A.C., Shahi, M., Pozarlik, A., van der Hoogt, P.J.M., Kok, J.B.W., de Boer, A., “Fluid-structure interaction on combustion instability”, *International Congress on Sound and Vibration 19 (ICSV19)*, Vilnius, Lithuania, July 08-12, 2012.
- 4- Matarazzo, s., Laget, H., Vanderhaegen, E., Altunlu, A.C., Tufano, S., “Thermal boundary effects on a GT liner structure”, *International Congress on Sound and Vibration 19 (ICSV19)*, Vilnius, Lithuania, July 08-12, 2012.
- 3- Altunlu, A.C, van der Hoogt, P., de Boer, A., "Sensitivity analysis on combustion driven damage mechanisms", *International Congress on Sound and Vibration 18 (ICSV18)*, Rio de Janeiro, Brazil, July 10-14, 2011.
- 2- Altunlu, A.C, van der Hoogt, P., de Boer, A., "Life assessment by fracture mechanics analysis and damage monitoring technique on combustion liners", *Proceedings of ASME Turbo Expo 2011*, Vancouver, Canada, June 6-10, 2011.
- 1- Altunlu, A.C, van der Hoogt, P., de Boer, A., "Damage evolution by using the near-tip fields of a crack in gas turbine liners", *17th International Congress on Sound and Vibration (ICSV17)*, Cairo, Egypt, 18-22 July 2010.

## 2 Sensitivity of combustion driven structural dynamics and damage to thermo-acoustic instability: combustion – acoustics – vibration

A. Can Altunlu, Peter J. M. van der Hoogt, André de Boer

University of Twente, Faculty of Engineering Technology, Section of Applied Mechanics, 7500 AE, Enschede, The Netherlands

---

### Abstract

**T**he dynamic combustion process generates high amplitude pressure oscillations due to thermo-acoustic instabilities, which are excited within the gas turbine. The combustion instabilities have a significant destructive impact on the life of the liner material due to the high cyclic vibration amplitudes at elevated temperatures. This work presents a methodology developed for mechanical integrity analysis relevant to gas turbine combustors and the results of an investigation of combustion-acoustics-vibration interaction by means of structural dynamics. In this investigation, the combustion dynamics was found to be very sensitive to the thermal power of the system and the air-fuel ratio of the mixture fed into the combustor. The unstable combustion caused a dominant pressure peak at a characteristic frequency, which is the first acoustic eigenfrequency of the system. Besides, the higher-harmonics of this peak were generated over a wide frequency-band. The frequencies of the higher-harmonics were observed to be close to the structural eigenfrequencies of the system. The structural integrity of both the intact and damaged test specimens mounted on the combustor was monitored by vibration-based and thermal-based techniques during the combustion operation. The flexibility method was found to be accurate to detect, localise and identify the damage. Furthermore, a temperature increase was observed around the damage due to hot gas leakage from the combustor that can induce detrimental thermal stresses enhancing the lifetime consumption.

**Keywords:** structural dynamics, structural health monitoring, damage, combustion, thermo-acoustics, instability.

## 2.1 Introduction

In modern gas turbines used for power generation, lean premixed combustion technology is generally desired to accommodate the balance between the emission targets and the efficiency. However, the gas turbine becomes more susceptible to combustion instabilities leading to thermo-acoustic oscillations [1]. In general, particular combustion operation settings stimulate the acoustic wave propagation to form a coupling between the combustion dynamics and the structural vibrations. The variations of the pressure flow field due to the flame dynamics create pressure oscillations that can lead to thermo-acoustic instability. Basically, when the pressure and heat release are in phase, the flame acts as a strong sound source inside the combustor and amplifies the liner vibration amplitudes. When they are out of phase, the flame-sourced sound field is attenuated, leading to a stable system.

The Rayleigh criterion, which is an energy balance definition providing an explanation of the system stability, can be expressed in an integral formulation [2]

$$\int_0^{\tau} \int_0^V p'(x, t) q'(x, t) dt dV > \int_0^{\tau} \int_0^V \phi(x, t) dt dV \quad (2.1)$$

where  $V$  is the volume of the domain (combustor volume),  $\tau$  is the period of the oscillation,  $p'$  is the pressure oscillation and  $q'$  is the heat release perturbation,  $x$  is the length coordinate,  $t$  is the time,  $\phi$  is the wave energy dissipation. The equation is the balance criterion that states whether the net energy gained by the system (left-hand side) exceeds the sum of losses due to the radiation of the sound at the boundaries (right-hand side): instability occurs.

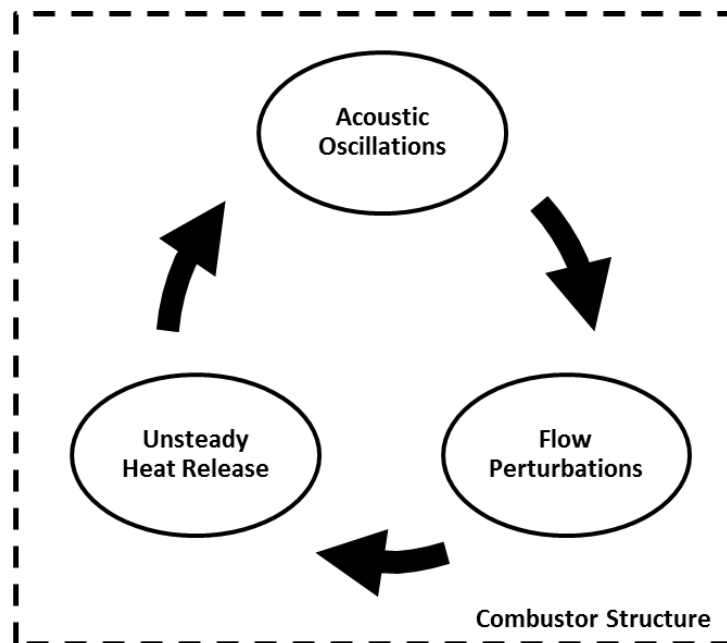


**Figure 2.1. The feedback mechanism of thermo-acoustic instabilities in combustion processes**

The loop of the thermo-acoustic feedback mechanism [1] is composed by the unsteady heat release that generates sound waves leading to acoustic oscillations and velocity fluctuations, which in turn perturbs the heat release. This feedback mechanism is directly linked with the structural domain of the system. The dynamic interaction within the combustor brings about the limit cycle pressure oscillations that cause elevated liner wall

vibration amplitudes. The contribution of fatigue damage can become more profound in the lifetime consumption of the combustor due to the high amplitude of the cyclic wall vibrations. Damage can occur in the form of a crack initiated at possible flaws or at hot spots in the structure. The structural health must be monitored and assessed to ensure the structural integrity, durability and reliability of the gas turbine engines for highly efficient lean combustion technologies and reduced emissions. A considerable amount of work has been published in the combustion research area in terms of fluid dynamics, improvement of efficiency and emissions [3-7]. Furthermore, together with the published research on the thermo-acoustic instabilities in the literature [1, 8-13], the coupled-domains within the thermo-acoustic feedback mechanism have been investigated to include the multi-physics, such as combustion-acoustics [14, 15], and acoustics-vibrations [16, 17]. Recent efforts in investigation of the interaction between combustion-acoustics-vibrations have been included in the literature [18-20], in fact their work focuses on stable combustion. Furthermore, recent efforts have been conducted in combustion instabilities analysis to cover the two-way interaction of the fluid-structure [21-23], however the results are not linked to structural damage conditions.

This work presents an investigation performed in a combustor test system to explore and assess the structural dynamics characteristics, under intact and damaged conditions, altered by the dynamic two-way interaction between the oscillating pressure load in the fluid and the motion of the structure under limit cycle conditions due to thermo-acoustic instabilities. Since the complexity of the combustor system was enhanced by the existence of the multiphysical interactions and the instability phenomenon, the methodology development started with a sample problem with well-defined initial and boundary conditions. Section 2.2 presents the results of the experimental, analytical and coupled/uncoupled numerical approaches used for modal characterisation of the sample problem. Furthermore, the validation of the structural health monitoring techniques is described and the findings are stated in the last sub-section. In section 2.3, the design of a laboratory-scaled generic combustor and the adopted methods and materials are presented. In addition, the application of the methods to the combustor test setup is described with an emphasis on linking the structural dynamics, acoustics and combustion dynamics. Then, the results on the analysis of the combustion-driven structural life consuming phenomena due to the combustion instability are presented. In the final section, the results are summarised and the conclusions are drawn.

## **2.2 Sample problem: Aero-Box**

In this section, the structural and acoustic characterisation of a simplified test setup, the so-called Aero-Box, using analytical, numerical and experimental approaches is presented. Subsequently, the applied structural health monitoring techniques are described. The Aero-Box is a fairly stiff structure with well-defined test and boundary conditions [24]. Therefore, tests under both intact and damaged conditions provide a basic understanding of the relation between eigenfrequencies, mode shapes, flexibility and damage state. Lastly, this section is concluded by discussing the structural response and damage state in the Aero-Box as well as the challenges of applying the methods to the combustor test setup.



### 2.2.1 Design of the Aero-Box

The structural responses of intact and damaged flexible plates are explored in the Aero-Box shown in Figure 2.2. The dimensions (a), front view (b), side view (c) and the damaged flexible plate including an initial centre-crack with length  $a_0$  in the total assembly (d) are illustrated in the figure. The test system consists of a hollow aluminium box with 30 mm thick walls, a 30 mm thick plate to cover the top of the box and an excitation source, loudspeaker. The loudspeaker inside the box generates an interior sound field resulting in vibration of the flexible plate that can be attached to the front side of the box. The Aero-Box has a high stiffness to avoid any interaction between the plate and the Aero-Box, whose first eigenfrequency is 1270 Hz. The aluminium plate material properties are: Young's modulus (E) of 70.5 GPa, Poisson's ratio ( $\nu$ ) of 0.3 and density ( $\rho$ ) of 2700 kg/m<sup>3</sup>. The flexible plate was attached to the box by reinforcement strips bolted to the box, thus satisfying a clamped on all edges condition. The dimensions of the plate are: 160 mm width, 210 mm height and 1.1 mm thickness. A slot-type crack was machined in the plate till the cutting tool-tip reaches the next surface across the thickness. Note that the crack in the damaged plate configuration is not a through-thickness-crack but a deep-surface-crack with a 35 mm initial crack length, 3 mm crack width.

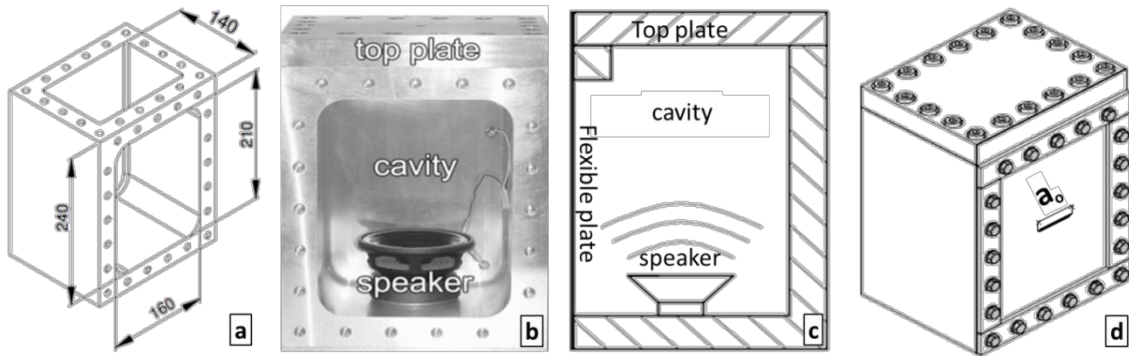


Figure 2.2. The dimensions and the configuration of the Aero-Box

### 2.2.2 Analytical model

Analytical equations were used to obtain the structural and acoustic eigenfrequencies to validate the experimental and numerical results. The eigenfrequencies of the first six modes of the rectangular plate were analytically calculated by [25]

$$f_{ij} = \frac{\lambda_{ij}^2}{2\pi L_p^2} \sqrt{\frac{EB_p^3}{12\gamma(1-\nu^2)}} \quad (2.2)$$

where  $\lambda_{ij}$  is the dimensionless frequency parameter of rectangular plates, which is a function of the boundary conditions applied to the plate and the aspect ratio of the plate (defined as the length to width ratio),  $L_p$  is the length and  $B_p$  is the thickness of the plate and  $\gamma$  is the mass per unit area of the plate ( $\gamma = \mu * B_p$  with density  $\rho$ ). The aspect ratio of the flexible plate is 0.762 and the  $\lambda_{ij}^2$  values were interpolated between aspect ratios of 2/3 and 1.0. The  $\lambda_{ij}^2$  values for a clamped on all edges condition are listed in Table 2.1 [25]. The calculations were performed

under the assumption that the influence of the air to the dynamic behaviour of the flexible plate is negligible.

**Table 2.1. The interpolated values for  $\lambda_{ij}^2$ .**

	Mode Sequence					
	1	2	3	4	5	6
$\lambda_{ij}^2$	29.58	50.8	68.22	78.49	94.64	109.84
(ij)	S(1,1)	S(2,1)	S(1,2)	S(3,1)	S(2,2)	S(3,2)

The acoustic eigenfrequencies of the Aero-Box can be analytically calculated considering a closed rectangular volume (acoustic cavity) with acoustically hard walls by the following equation [25]

$$f_{ijk} = \frac{c}{2} \sqrt{\left(\frac{i}{L_x}\right)^2 + \left(\frac{j}{L_y}\right)^2 + \left(\frac{k}{L_z}\right)^2} \quad (2.3)$$

where  $c$  is the speed of sound,  $i, j, k$  are the number of half waves in the three length directions ( $L_x, L_y, L_z$ ) associated with  $x, y$  and  $z$  coordinates (160, 240 and 140 mm), respectively. The analytical calculation results for both the structural  $S(i,j)$  and acoustic  $A(i,j,k)$  modes are listed in Table 2.2.

### 2.2.3 Acousto-elastic interaction

The interaction between fluid and structure can be apparent as the dynamic behaviour of the structure is evidently influenced by the media in contact. The eigenfrequencies and mode shapes can be altered due to the coupled mechanism. Thus, the coupling between the acoustic volume and the adjacent structure domain was analysed by the finite element method (FEM). The acousto-elastic interaction analysis includes acoustic elements to represent the acoustic pressure waves in the cavity and shell elements to enable the displaced motions of the structure. The acoustic and the structure mesh are coupled at the interface, which ensures the exchange of the fluid and structural loads between acoustic and structure domains. Thus, the acoustic pressure-driven structural displacements and hence the bounce-back generation of an effective fluid load due to these motions are provided. The general governing equations of the system [26] can be written in the following form

$$[M^f]\{\ddot{P}\} + [K^f]\{P\} = \{F_f\} - \rho_o[C]^T\{\ddot{u}\} \quad (2.4)$$

$$[M^s]\{\ddot{u}\} + [K^s]\{u\} = \{F_s\} - [C]\{P\} \quad (2.5)$$

where  $\{P\}$  is the nodal pressure vector,  $\{u\}$  is the nodal displacement vector,  $[M^f]$  is the assembled fluid equivalent “mass” matrix,  $[K^f]$  is the assembled fluid equivalent “stiffness” matrix,  $[M^s]$  is the assembled structural mass matrix,  $[K^s]$  is the assembled structural stiffness matrix,  $\rho_o$  is the density, and  $[C]$  is the so-called coupling matrix, which represents the effective surface area composed by the nodes at the interface. In the interface surface, the vector containing the nodal displacements is associated with the fluid domain and the vector containing nodal pressures is associated with the structural domain through the coupling

matrix. Thus, the exchange of the quantities is included within each domain. The coupled acoustic and structural problem takes the following form [27]

$$\begin{bmatrix} [M^s] & [0] \\ [M^{fs}] & [M^f] \end{bmatrix} \begin{Bmatrix} \{\ddot{u}\} \\ \{\ddot{P}\} \end{Bmatrix} + \begin{bmatrix} [K^s] & [K^{fs}] \\ [0] & [K^f] \end{bmatrix} \begin{Bmatrix} \{u\} \\ \{P\} \end{Bmatrix} = \begin{Bmatrix} \{F^s\} \\ \{F^f\} \end{Bmatrix} \quad (2.6)$$

where  $[M^{fs}] = \rho_o[C]^T$  is the assembled fluid-structure coupling “mass” matrix,  $[K^{fs}] = -[C]$  is the assembled coupling “stiffness” matrix,  $\{F^s\}$  and  $\{F^f\}$  are the structural and fluid load vectors, respectively. In the finite element representation, the shared nodes at the interface are equipped by the displacement and pressure degrees of freedom and the acoustic domain assumes that the fluid is compressible and inviscid and no mean flow velocity is considered. The mean fluid density and the pressure are uniform in the acoustic field. The calculated eigenfrequencies from coupled and uncoupled FEM can be seen in Table 2.2.

#### 2.2.4 Modal characterisation

Experiments were performed on the aluminium flexible intact plate to examine the dynamic modal parameters (eigenfrequencies and mode shapes). The surface vibrations of the plate were scanned by a Laser Doppler Vibrometer (LDV) at 9x9 measurement grid points on the plate, which was found to be the optimum scan grid for an accurate analysis. Hereafter, this technique will be called Vibration-Based (VB) technique.

**Table 2.2. Test setup eigenfrequencies [Hz] with the intact plate**

Mode No.	Measured	Analytic	FEM uncoupled	FEM coupled
S(1,1)	309	310 (0.3%)	306 (1.0%)	311 (0.6%)
S(2,1)	515	532 (3.3%)	519 (0.8%)	514 (0.2%)
S(1,2)	704	714 (1.4%)	715 (1.6%)	710 (0.9%)
A(1,0,0)	744	715 (3.9%)	734 (1.3%)	732 (1.6%)
S(3,1)	858	822 (4.2%)	868 (1.2%)	864 (0.7%)
S(2,2)	901	991 (10.0%)	911 (1.1%)	905 (0.4%)
A(0,0,1)	1087	1072 (1.4%)	1107 (1.8%)	1103 (1.5%)
A(0,1,0)	1232	1225 (0.6%)	1253 (1.7%)	1254 (1.8%)
S(3,2)	1235	1150 (6.9%)	1241 (0.5%)	1236 (0.1%)
S(1,3)	1310	-	1338 (2.1%)	1338 (2.1%)
A(1,0,1)	1333	1288 (3.4%)	1362 (2.2%)	1347 (1.1%)

The experimental, analytical and numerical results for the structural eigenfrequencies are listed in Table 2.2. The (percent) deviation in the results compared to the measured results is written in parentheses. Note that the value in parentheses on the presented tables represents the deviation of the corresponding result throughout this work. The calculated eigenfrequencies show some deviation from the measurements, nonetheless the coupled FEM provides better predictions in general. The deviation in the structural eigenfrequencies of the

plate for the analytical calculation can be caused by the interpolation of the  $\lambda_{ij}$  values obtained from the literature. Note that  $S(1,3)$  is not included in the list, since this mode is out of the given  $\lambda_{ij}$  range. Besides, the interior of the Aero-Box was machined from a single piece aluminium slab that contains fillets on the corners. And the loudspeaker placed inside the Aero-Box occupies a space and reduces the acoustic volume and influences the acoustical behaviour in the cavity [24]. The differences in the acoustic eigenfrequency results can be attributed to the fact that the interior volume is slightly different from the theoretical rectangular box volume in the analytical calculations. In the numerical models, the bolt connection of the plate and the frame, which was modelled as bonded-connection (perfectly clamped), and the presence of the loudspeaker, which was not modelled, can cause deviation.

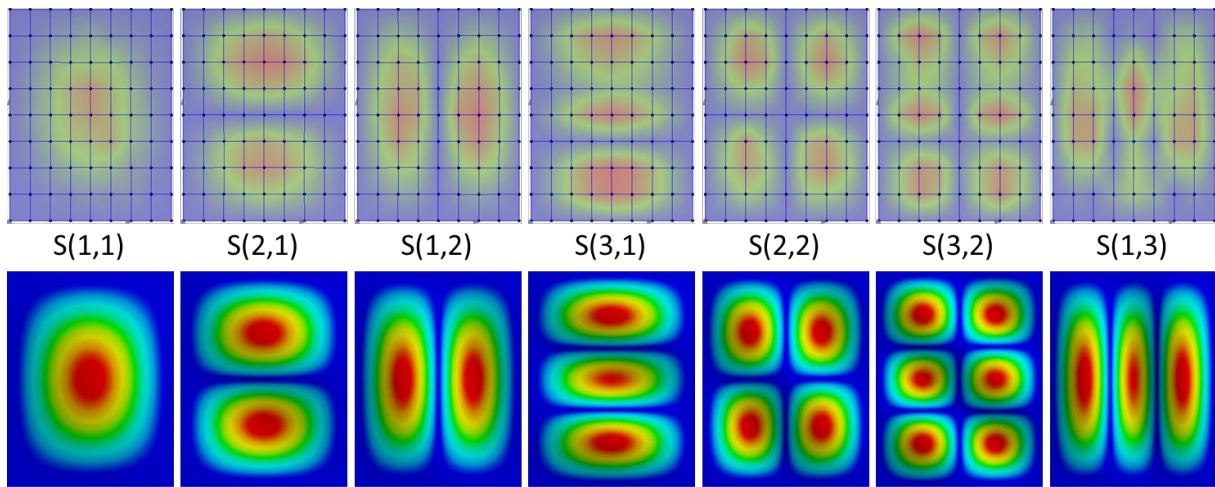


**Figure 2.3. Experimental (above) and numerical (below) results for the mode shapes of the intact plate configuration**

The experimental and numerical results for the mode shapes are depicted in Figure 2.3 for the intact plate configuration. The experimentally predicted mode shapes show an excellent match with the numerical calculations.

### 2.2.5 Structural damage detection

Structural response monitoring and damage/fault detection at the earliest possible stage is crucial to assure the safety of the component, assess the residual lifetime, plan the required maintenance intervals and set the inspection requirements. Vibration-based damage monitoring is one of the non-destructive methods to examine the dynamic properties of the structures. Basically, the vibration-based method tracks the alterations of the modal parameters due to possible damage such as eigenfrequencies, mode shapes, modal damping, modal strain energy and flexibility [28-39]. Much research has been conducted on the frequency shifts for damage prognostics [30, 38]. The statistical variation of the eigenfrequencies is less than the other modal parameters in the case of random error sources [40, 41], nevertheless, the feasibility of this technique can be enhanced by picking up the most sensitive eigenfrequencies to damage. Those selected eigenfrequencies reduce the necessary monitoring locations and indicate damage while other modes can remain insensitive. However, the frequency shift monitoring can be misleading in some cases when damage in

the structure reshapes and rearranges the mode shapes in such a way that the eigenfrequency of interest actually loses its sequence within the mode numbers and swaps with the new eigenfrequency [42]. Therefore, the mode shape information together with the eigenfrequencies can provide better accuracy in health monitoring. The location of the damage in the geometry can be determined by pursuing the changes in the measured flexibility of the structure. The localisation is based on comparison of the flexibility matrixes using the mass-normalised mode shapes and eigenfrequencies of the intact and the damaged structure. The flexibility matrix [36, 37] is inversely proportional to the square of the eigenfrequencies; therefore, the flexibility matrix is very sensitive to the changes in the low frequency modes of the structure.

### 2.2.6 Damage detection by frequency shift method

A centre-crack, as described in section 2.2.1, was introduced in the plate. The eigenfrequencies of the damaged plate were measured using the VB technique. The results were cross checked by the so-called Acoustic Emission (AE) technique, which is elastic radiation generated by the rapid release of energy from sources within the material (plate) under an external excitation source (loudspeaker). Therefore, a microphone was used instead of the LDV for the measurement. The alteration of the first seven eigenfrequencies due to the damage state in the plate is presented in Table 2.3. The VB and AE monitoring techniques applied to the damaged plate show a very good match. The structural stiffness decreases due to the damage, as a result the eigenfrequencies decrease in the damaged case as seen in the table.

**Table 2.3. Eigenfrequencies [Hz] of the intact and damaged plate.**

Mode No.	Intact Plate (VB)	Damaged Plate (VB)	Damaged Plate (AE)
S(1,1)	309	299 (3.2%)	300 (2.9%)
S(2,1)	515	509 (1.2%)	510 (1.0%)
S(1,2)	704	693 (1.6%)	694 (1.4%)
S(3,1)	858	838 (2.3%)	837 (2.4%)
S(2,2)	901	900 (0.1%)	898 (0.3%)
S(3,2)	1235	1227 (0.6%)	1225 (0.8%)
S(1,3)	1310	1282 (2.1%)	1283 (2.1%)

A sensitivity analysis was performed to obtain the most sensitive mode to the current damage configuration by calculating the difference in the structural eigenfrequencies between the intact and damaged plate. The results for the VB and AE techniques are shown in Figure 2.4. The mode 1, S(1,1), was found to give the most distinguishable response to the damage because the introduced damage (centre-crack) is positioned on one of the node points within the mode shape.

A numerical analysis was carried out to predict the mode shapes of the damaged plate configuration, which is described in section 2.2.1. The comparison of the mode shapes

between the intact and damaged cases is presented in Figure 2.5. As seen from the figure, the presence of the centre-crack causes a swap between the modes S(1,3) and S(4,1) and deterioration in mode shapes of some higher modes, in which the crack location coincides with the node points of the particular mode. The actual deviation in the mode S(1,3) with respect to the damage is hindered, since the two adjacent modes exchange their modal sequence. In conclusion, the most sensitive mode is very much dependent on the damage location and the orientation, therefore the selection of the mode to monitor is crucial to be able to capture the small changes in the dynamic structural properties. However, damage detection by the frequency shift method can be misleading as the mode sequence can reshuffle due to the damage configuration.

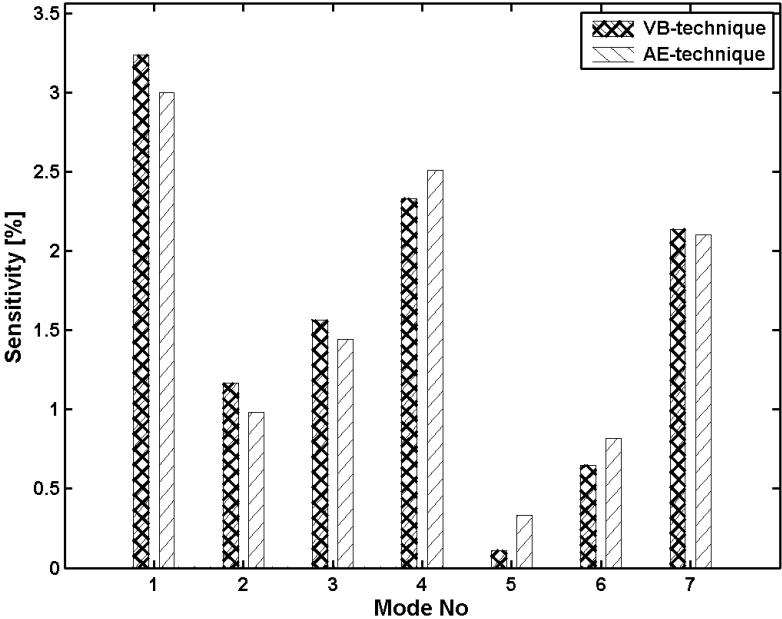


Figure 2.4. Sensitivity analysis on eigenfrequencies

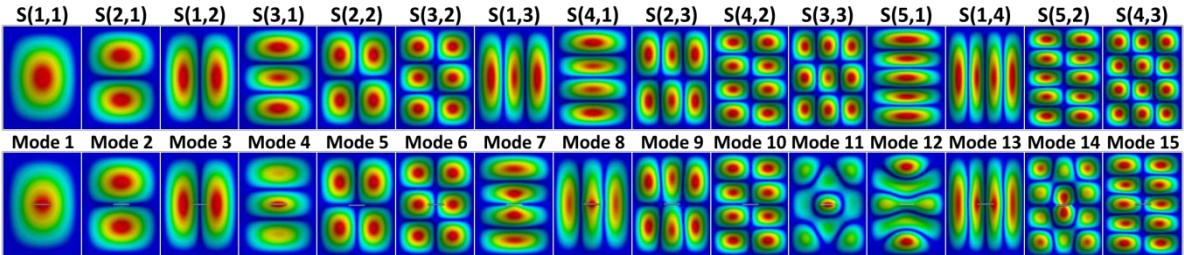


Figure 2.5. Damage sensitivity of mode shapes (top: intact and bottom: damaged)

2.2.7 Damage localisation by flexibility method

The system stiffness matrix is more sensitive to higher modes than lower modes, thus obtaining the accurate dynamic stiffness matrix requires measuring a significant amount of higher modes [43]. However, experimentally extracting higher modes of the system is challenging due to practical limitations. On the contrary, the flexibility matrix, which is defined as the inverse of the stiffness matrix, is inversely related to the square of the natural frequencies, hence higher modes contribute less to the flexibility matrix; instead it is more

sensitive to the changes in lower modes. The flexibility method is based on the change of the flexibility matrix, which is composed of the mode shape and the reciprocal of the natural frequency. In theory, the structural damage reduces the stiffness [44] and increases the flexibility. The responsiveness of the flexibility matrix to a structural deterioration serves as a good indicator in structural health monitoring. The homogeneous dynamic equilibrium equation can be expressed as

$$[K][\Phi] = [M][\Phi][\Omega] \quad (2.7)$$

where  $[K]$  is the stiffness matrix,  $[M]$  is the mass matrix,  $[\Phi] = [\Phi_1, \Phi_2, \dots, \Phi_n]$  is the mode shape matrix where the mode-shape vectors are mass-normalised to unity as  $[\Phi]^T[M][\Phi] = [I]$ ,  $[\Omega] = \text{diag}(\omega_i^2)$  is the modal stiffness matrix,  $i (= 1, \dots, n)$  is the mode shape number indicator,  $n$  is the number of degrees of freedom and  $\omega$  is the modal frequency. The flexibility matrix,  $[G]$ , related to the modal data can be derived as [43]

$$[\Phi]^T[K][\Phi] = [\Phi]^T[M][\Phi][\Omega] \quad (2.8)$$

$$[G] = [K]^{-1} = [\Phi][\Omega]^{-1}[\Phi]^T = \sum_{i=1}^n \frac{1}{\omega_i^2} \{\Phi_i\}\{\Phi_i\}^T \quad (2.9)$$

The change in the flexibility matrix with respect to the initial reference data set for the intact case and the data set for the damaged case is given by

$$[G_\Delta] = \{\delta_{im}\} = [G_h] - [G_d] \quad (2.10)$$

where  $[G_\Delta]$  is the change in the flexibility matrix,  $\delta_{im}$  are the elements of  $[G_\Delta]$ .  $[G_h]$  and  $[G_d]$  are the intact and damaged case flexibility matrices, respectively. The parameter used to detect and locate the damage in the structure is the degree of change in the flexibility for each measurement location. It can be characterised by [36]

$$\bar{\delta}_m = \max_i |\delta_{im}| \quad (2.11)$$

where  $\bar{\delta}_m$  is the maximum absolute value of the elements in each corresponding column in  $\mathbf{G}_\Delta$  and  $m$  is the degree of freedom.

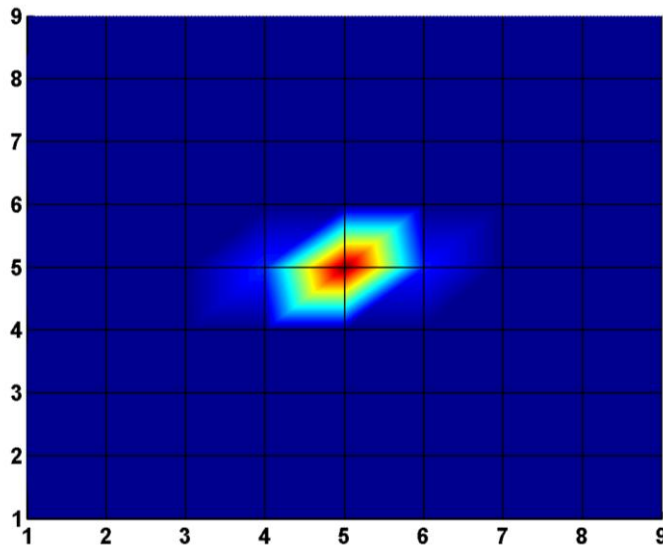


Figure 2.6. Damage localisation by the flexibility method



The presence of the damage reduces the stiffness of the structure and the flexibility is the inverse of the stiffness. Thus the structural response of the plate alters as damage occurs by increasing the local flexibility of the structure. The damage in the flexible aluminium plate was detected and localised by comparing the flexibility matrices of the intact and damaged cases shown in Figure 2.6. Since the slot-type crack machined into the specimen is not through-thickness, yet a deep-surface-crack, in the figure the change in the local flexibility is concentrated at the damage location and the traces to the sides are visible representing the centre-crack configuration aligned transversely.

### **2.2.8 Discussion on the Aero-Box**

The applicability of the methodology was verified and validated in a sample problem, the so-called Aero-Box. Two cases, intact and damaged plates, were investigated to assess the structural health monitoring methods. Both VB and AE techniques provide a non-contact structural health monitoring, however the VB technique is superior in overcoming the challenges of elevated temperature conditions, high amplitude loading and harsh environment conditions due to combustion process. The damage was detected using the frequency shift method and the most sensitive eigenfrequency to the damage configuration was found. Moreover, the location and the severity of the damage were also predicted using the flexibility method. The results of this method show that identification of the modal parameters enables construction of the flexibility matrix. The change in the measured entities of the matrices between the initial reference intact case and damaged case was captured to detect and localise the damage. Both damage monitoring methods can be performed using only test data without requiring any additional models for the structure. However, the field-of-interest in the structure should be determined with hot spot analysis to avoid a full modal analysis. Thus, the flexibility method can be used for damage localisations accompanying the frequency shift method, which can be applied on a single measurement point excluding the node points of the most sensitive mode, to detect the presence of the damage. It should be highlighted that with regard to the measurements, the acousto-elastic fully coupled finite element model was found to be more accurate in general compared to the analytical and uncoupled FEM calculations. This result indicates the existence of an interaction between the enclosed acoustic volume and the flexible structure that is also observed in combustors [45]. The outcome of this study was utilised as a reference to describe the behaviour of the complex combustor system, of which the investigation is presented in the next section.

### **2.3 Laboratory-scaled generic combustor test setup**

In this section, the investigation of the impact of the combustion driven limit cycle oscillations on the structural properties under the intact and damaged conditions is presented. The methodology described in the previous section is utilised for a laboratory-scaled generic combustion test system. For this purpose, a test combustor setup [46] depicted in Figure 2.7, which can be modified to generate stable and unstable combustion conditions, was utilised in



this research. Two geometric configurations of the combustor were investigated, namely a single liner combustor and a double liner combustor. In the latter configuration, the limit cycle oscillations were observed due to the combustion instabilities. In this configuration, the acoustic field was enlarged by doubling the liner length, and consequently, the acoustic eigenfrequencies of the combustor decreased inversely proportional to the length. The first acoustic eigenfrequency was excited by the combustion process and the resulting pressure oscillations were generated. The materials used in the combustor and their compliance are described in the next sections with an emphasis on the similarities to a typical combustor base material. Next, a comparative investigation on the combustion stability, considering the operational input parameters and the liner length, is presented. Finally, the results are linked to the structural dynamics of the intact and damaged cases.

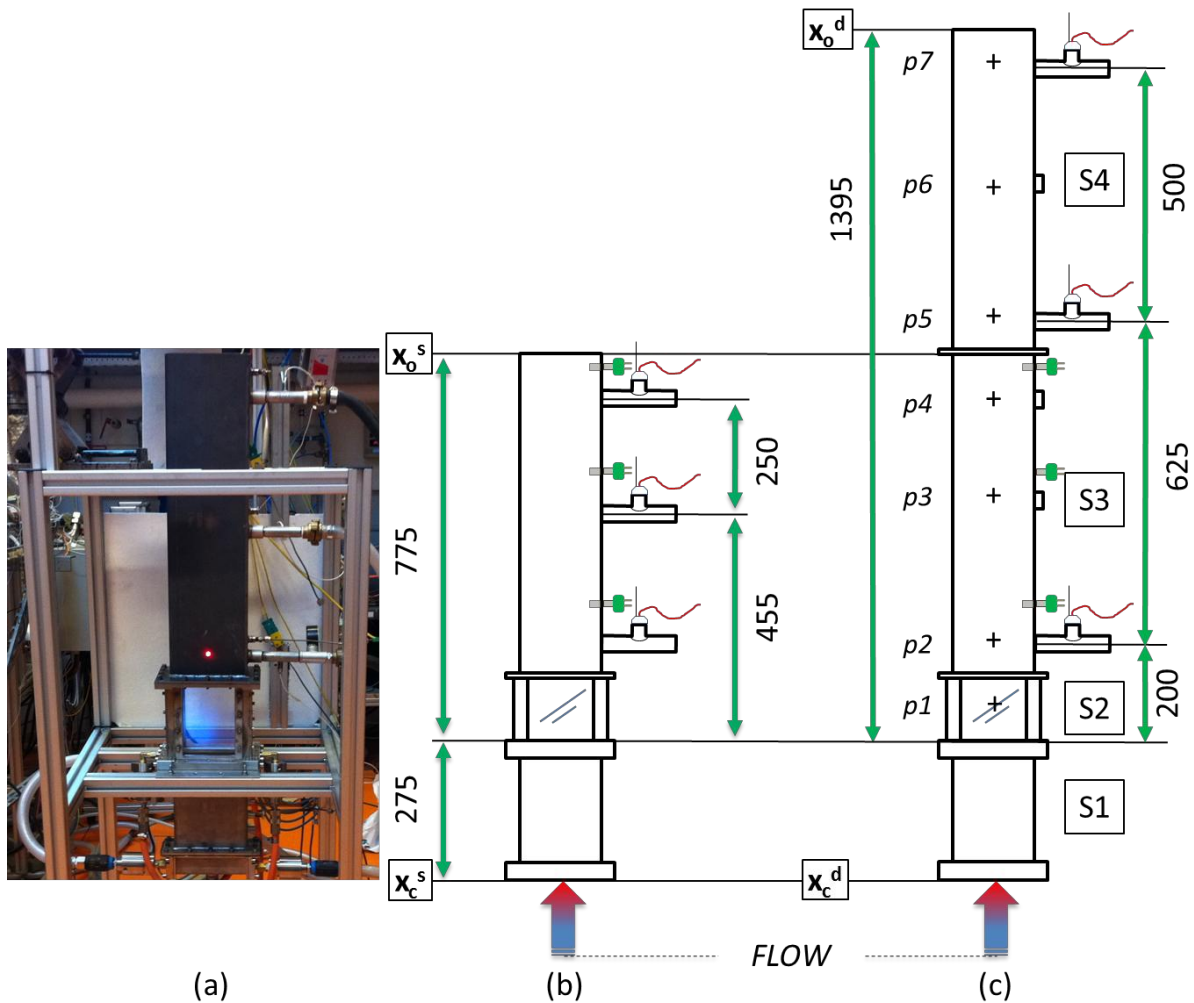


**Figure 2.7. Combustor test system - single (a, b) and double (c) liner configurations [upstream section (S1), flame-box (S2) and a rectangular liner (S3 and S4)]**

### 2.3.1 Design of the combustor

In Figure 2.7, the single (S3) and double liner (S3+S4) configurations of the test combustor are depicted and the dimensions are listed in Table 2.4. The marks indicated as ‘ $p$ ’ designate the gas pressure and temperature and the liner surface vibration measurement

locations. The combustor was designed as a Rijke tube configuration consisting of mainly two sections, the acoustically closed upstream and the downstream (flame-box and the liner). The upstream section (S1) consists of an air-feeding box, a rectangular duct with a 25x150 mm hollow cross-sectional area and 275 mm long, and an equilateral triangular wedge as a flame holder, where methane as the fuel is injected through the holes on both sides (Figure 2.8). The downstream section consists of a flame-box (S2) and a rectangular liner (S3 and S4). The flame-box is surrounded by four quartz glass windows providing an optical access to the flame. The rectangular geometry eases to assemble the glass windows. Additionally, the glass windows can be replaced by an intact or a damaged test specimen to investigate the structural dynamics during the operation while visualising the flame through the side windows. The turbulent flame is technically premixed and flame stabilisation takes place on the wedge wake in the combustor test system. The combustor is supported from the bottom of the flame-box.

**Table 2.4. Combustor test system dimensions**

Section	Dimension [mm]
Combustor outer width	158
Upstream outer depth	33
Downstream outer depth	58
Wall thickness	4
Quartz glass thickness	5
Specimen thickness	1

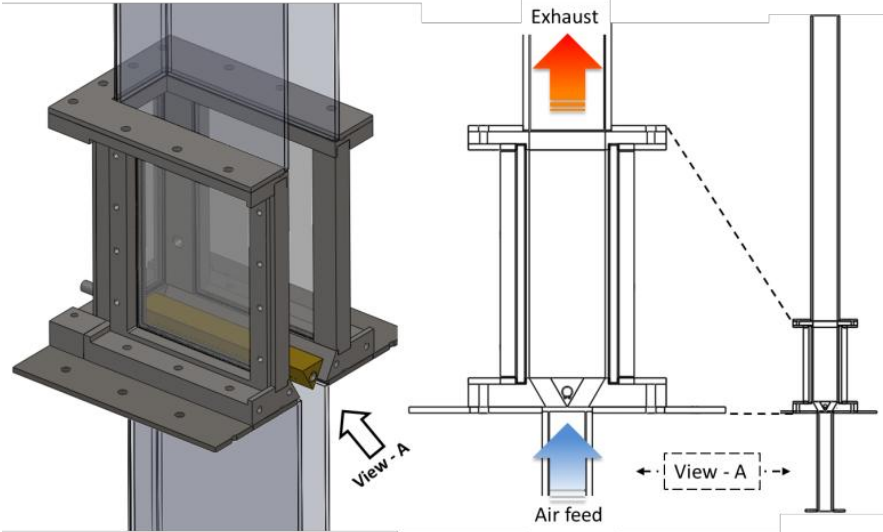


**Figure 2.8. Combustor flame-box and wedge**

**2.3.2 Material compliance and properties**

During the combustion process, the liner is exposed to elevated temperatures; therefore the influence of temperature levels on the structural properties becomes crucial. The combustor liner and the flame-box are made of austenitic stainless steel (AISI) Type310. Type316 was chosen as the specimen material that has sufficiently enough heat and corrosion

resistance at the test temperatures within relatively short exposure time and well established properties. Since the specimen was replaced with a new one in every new experiment, this material serves satisfactorily for the test purposes with its cost-effectiveness. The compliance of the test material can be seen in Figure 2.9 in comparison to a typical combustor base material, nickel-base superalloy Alloy230 (Haynes230) [47, 48]. The materials used in the test setup exhibit analogical trends to the Alloy230 and satisfactory properties within the experimental conditions. In the three materials, the effect of the temperature on the thermal expansion and elastic modulus is fairly proportional, whereas the ultimate tensile strength decreases dramatically beyond 900 K. There is a clear switch due to the transition from normal low temperature mechanisms to creep controlled mechanisms as can be observed from the drastic decline in the stress to rupture time curve.

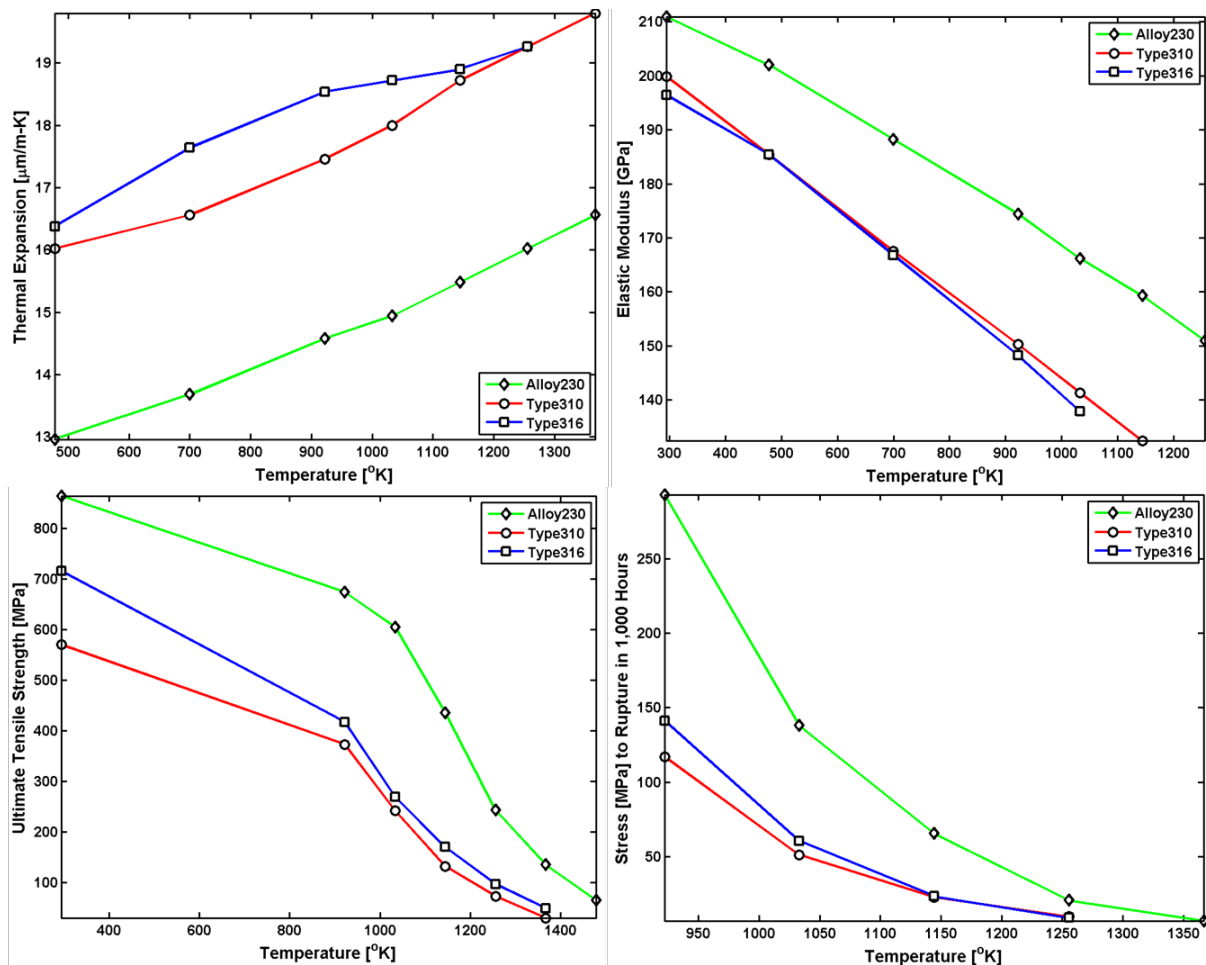
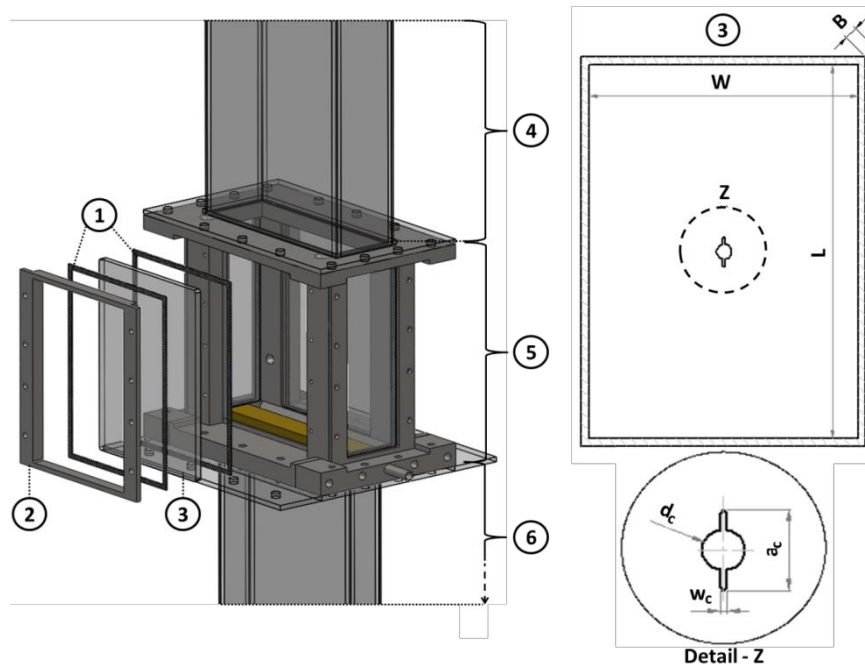


Figure 2.9. Temperature dependence of the material properties

### 2.3.3 Specimen configuration

The dimensions of the test specimen used in the combustor are 150 x 108 x 1 mm, length (L), width (W) and thickness (B), respectively. The damage on the specimen is represented by a centre-hole of 6 mm diameter ( $d_c$ ) and an adjacent crack was machined towards its length direction of 6 mm to each side that creates a crack length of 18 mm ( $a_c$ ) and the crack width is 1 mm ( $w_c$ ). The geometric representation of the specimen, the introduced damage and the assembly of the flame-box can be seen in Figure 2.10. The numbered items in the figure

respectively are; gaskets (1), the supporting frame (2), quartz glass or specimen (3), liner (4), flame-box (5), upstream (6) and damage configuration (detail-Z). The hatch area showed in the specimen geometry (3) is the contact area with the gaskets and hence sandwiched by the supporting frame and the flame-box.



**Figure 2.10. Flame-box assembly and specimen configuration**

### 2.3.4 Instrumentation

The structural modal characterisation tests were performed on the combustor test setup as a bare structure to link the structural dynamics later in the combustion experiments. The two experimentation procedures will be mentioned as cold and hot cases, respectively.

In the cold case, the vibration modes of the combustor test system were analysed by two methods, the roving hammer impact test and the shaker test. In the roving hammer test, an accelerometer was placed at a single degree of freedom (DOF) and an impact hammer was used to excite at the measurement grid (DOFs). The shaker test includes the electro-mechanical shaker to excite the system at a fixed reference point and the LDV was used to travel between the measurement grid points. The shaker was attached to the combustor liner with a stinger that enables the applied force to be aligned along the stinger axis. The generated random noise excitation was characterised by a force transducer. The frequency response functions between the measured wall velocity and the excitation force were recorded by a data acquisition and an analyser system (Siglab). A software package (ME'scopeVES) was used to extract the modal parameters.

The combustion tests hot case covers the combustor inner temperature, pressure and liner wall velocity recordings and the combustor surface temperature measurement by an infrared (IR) camera. The temperature inside the combustor was measured by K-type thermocouples. The dynamic pressure measurement sensors were attached in the side-tubes that are connected to the semi-infinite hoses and external coolers were directed towards the devices. This

technique overcomes the high temperature effects to the piezoelectric pressure transducers and provides non-reflecting acoustic conditions. The liner wall vibration was recorded by a LDV via a data acquisition system, DAQ (National Instruments). The mass flow controllers for fuel and for air were used and the flow was controlled by a PC via LabVIEW program [49]. The vibration analysis of the specimen attached to the flame-box (Figure 2.10) was utilised by the LDV mounted on a traverse system that enables automated measurements (Figure 2.11).

**2.3.5 Structural condition monitoring**

The structural health monitoring system is depicted in Figure 2.11, including the LDV (3) for vibration characterisation and the IR camera (2) for thermal characterisation mounted on a programmable traverse system (1), which can slide in the x-y plane. In the figure, the clamping position of the test setup is denoted as “C”. Since the combustor environment is harsh at high temperature and elevated vibration levels exist due to the unstable combustion process, a non-contact vibration-based damage monitoring method was utilised to analyse the structural dynamics and the health of the combustion liner during operation (Figure 2.12). The technique used here is capable of detecting the presence of damage, localising and quantifying the severity of the damage by examining changes in the measured dynamic response of the structure.

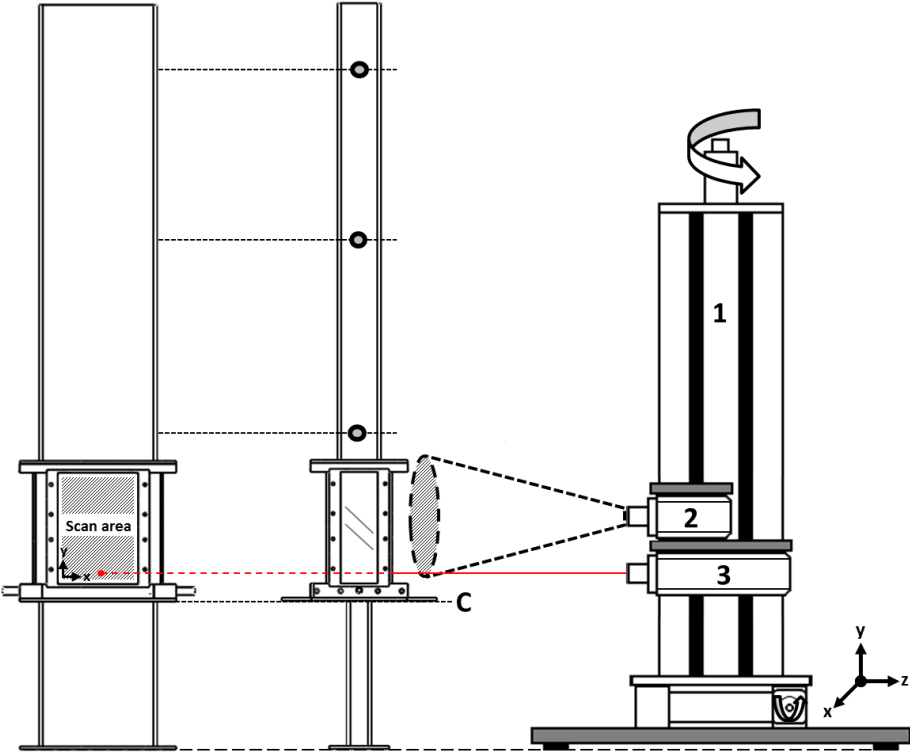


**Figure 2.11. Schematic representation of structural condition monitoring system**

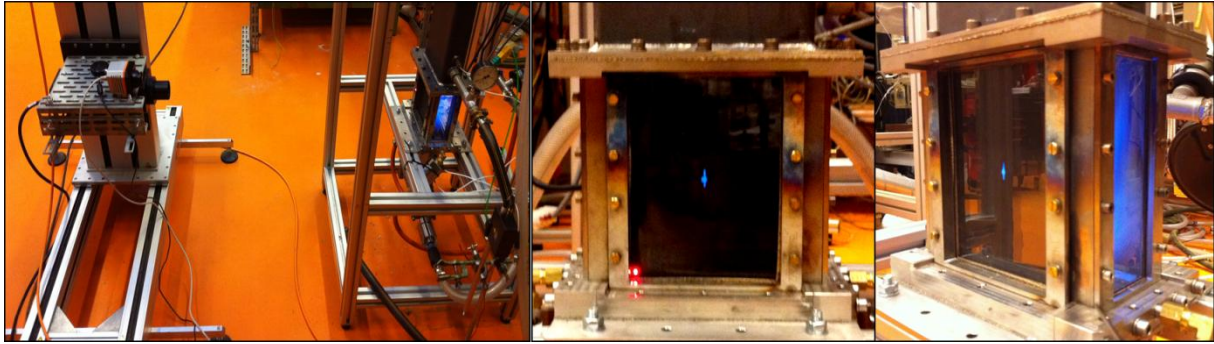


Figure 2.12. Laser surface scan on the damaged specimen mounted in the flame-box.

### 2.3.6 Combustion-driven dynamics

Four test cases were carried out in the test system as listed in Table 2.5. In the investigation, two test system configurations (single and double liners) are included as described in section 2.3.1 and the initial operation setting varies from 40 to 60 kW for the thermal power and from 1.4 to 1.6 for the air-fuel (equivalence) ratio, which is the mass ratio in the mixture normalised by the stoichiometric air-fuel ratio.

Table 2.5. Combustion test cases

Case Code	Thermal power	Air-fuel ratio	Test system configuration	Combustion stability
Case11	40 kW	1.4	Single liner	Stable
Case12	60 kW	1.6	Single liner	Stable
Case21	40 kW	1.4	Double liner	Stable
Case22	60 kW	1.6	Double liner	Unstable

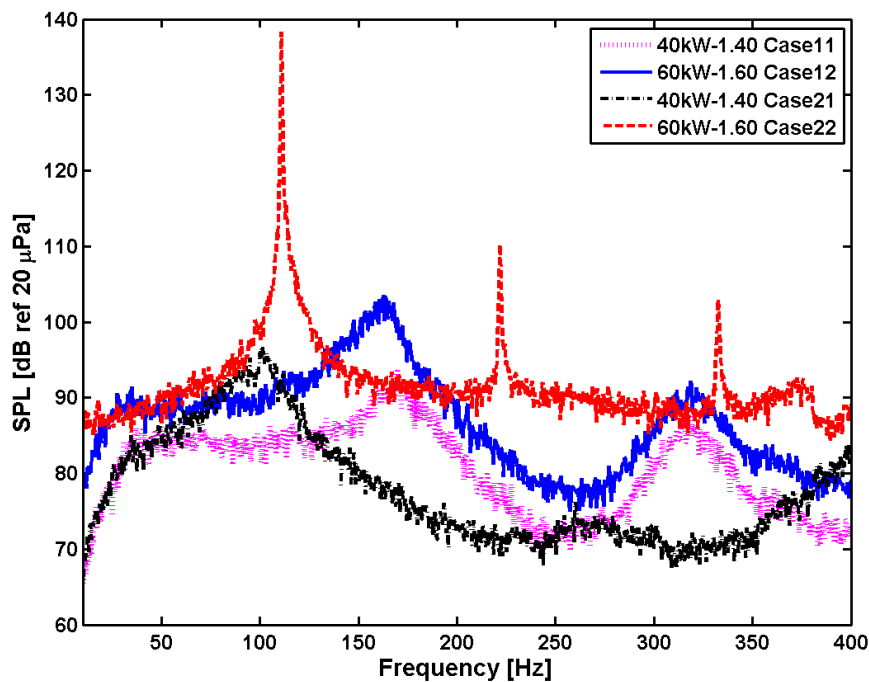


Figure 2.13. Pressure spectrum of the combustor



In Figure 2.13, the pressure spectrum for the test cases is shown. There was no limit cycle regime observed in the cases Case11, Case12 and Case21, in which the flame was stable and generated a low-level combustion noise only. Instability was observed, however, in Case22 at the frequency of 111 Hz while the pressure amplitude inside the combustor was around 160 dB. The frequency of the acoustic pressure at the flame excites the first acoustic mode of the combustor that induces the instability. The acoustic characterisation is presented in the next section (Table 2.6 and Table 2.7). Furthermore, the system generates characteristic frequencies as the higher-harmonics of the limit cycle frequency at 222 Hz and 333 Hz. These visible peaks are considered as the higher-order modes of the system [13, 50]. Note that the pressure signals are obtained from the transducer located at the top measurement location for all cases. Recalling the combustor test system design (Figure 2.7), the three pressure transducers were mounted at the bottom; middle and top location of the liner length. In the single liner configuration, these measurement points correspond to  $p_2$ ,  $p_3$  and  $p_4$ , whereas  $p_2$ ,  $p_5$ ,  $p_7$  locations are used in the double liner configuration.

A stability map containing nine operating points was created in terms of thermal power and air-fuel ratio to characterise the combustor (Figure 2.14). In the figure, the combustion process tends to become unstable with increasing air-fuel ratio for a leaner mixture combustion and with increasing power. A transition line is observed that divides the map into stable and unstable operating zones. The operating points on the transition line implied a dynamic system characteristic including two different combustion regimes: stable and unstable. A bifurcation at these certain operating conditions can occur depending on the initial operation setting, air-fuel ratio and power as in this work, due to the sequential direction of the test points (initial operation settings) that indicates the nonlinear characteristics of combustion instabilities [51].

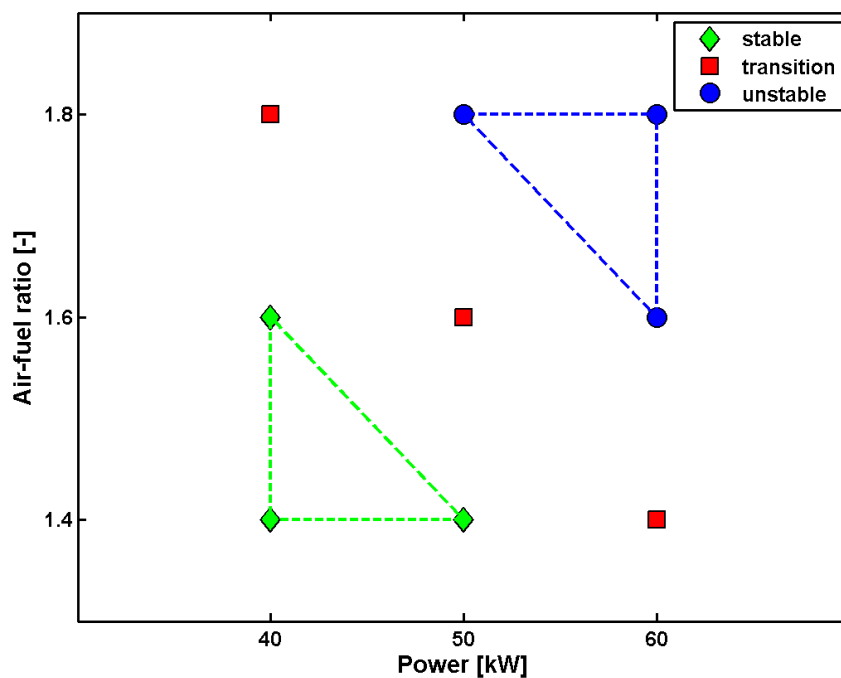
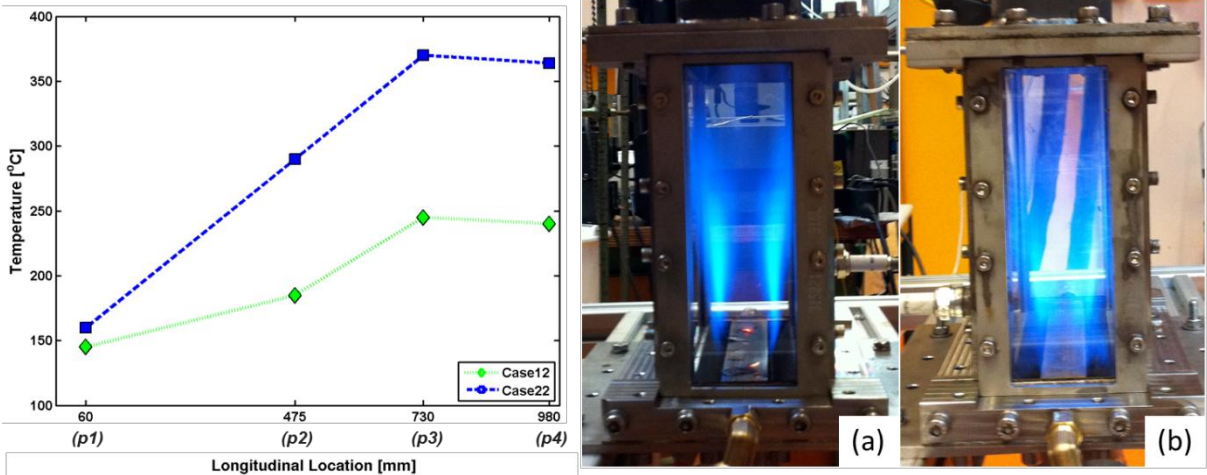


Figure 2.14. Stability map for the double liner configuration

The surface temperatures were measured at the same locations ( $p1$ ,  $p2$ ,  $p3$  and  $p4$ ) for the cases Case22 and Case12 that have the same initial operation settings (Figure 2.7). The liner surface temperature profile and the flame profiles are depicted in Figure 2.15. The maximum surface temperature is measured as 370 °C for the Case22 and 245 °C for Case12. Since the test system is technically uncooled, the main heat transfer processes are the radiation heat flux from the gas, the convection heat flux from the gas, the conduction heat flux across the wall thickness and the convection heat flux to the surrounding air. In the figure, accounting for the energy balance, the trend of the curves can be considered as a comparative indicator for the flame height that exhibits a bend-down at ' $p3$ ' location in both cases. Regardless of the length of the combustor, an analogous liner surface temperature curve was obtained under the same operating conditions and generalised initial test conditions (inlet pressure, inlet temperature and mass flow). Since the distance between the two temperature measurement nodes of ' $p3$ ' and ' $p4$ ' is 250 mm, the exact interpretation on the flame length would not be feasible due to the insufficient data within these two nodes. However, the relative flame occupying cross-section area of the stable and unstable combustion flame differs (Figure 2.15). The turbulence advances the flame speed in gaseous fuel-air mixtures and elevates the burning rates in gas turbine engines [52]. According to Damkohler [53] and Schelkin [54], the burning velocity is related to the turbulence intensity, hence the wrinkled flame front that increases the specific flame surface area yielding an increase in fresh mixture consuming ability. Hence, the temperature levels are proportionally increased. The aforementioned findings imply that the system instability is associated with elevated pressure levels and increased structure temperatures in comparison to the stable system (single liner) under the same initial operating conditions.



**Figure 2.15. Liner surface temperature profile and flame profile for Case12-stable (a) and Case22-unstable (b)**

Note that the start-up of the experiments was held relatively by progressing the input parameters up to the desired test case settings within time-to-start to sustain the initial experimental conditions. The structure was heated up gradually, avoiding thermal shocks in the start-up periods, and it was air-cooled down in shut-off periods.



### 2.3.7 Acoustic characterisation

The acoustic modal properties of the combustor test system with single and double liner configuration at room temperature and at the operation temperature (Case12 and Case22) were characterised experimentally, analytically and numerically. Note that hereafter, the single liner configuration will be denoted as the superscript '(s)' and the double liner is denoted as '(d)'. From the previous experiments [46], the acoustic boundary conditions of the combustor downstream were obtained by means of reflection coefficient ( $R$ ) that are closed ( $R = 1$ ) at one end ( $x_c = 0$ , where the wedge is located) and open ( $R = -1$ ) at the other end ( $x_o =$  the height of the combustor downstream). The end conditions for the single ( $x_o^s - x_c^s$ ) and double ( $x_o^d - x_c^d$ ) liner configurations can be seen in Figure 2.7. Furthermore, the mean temperature was measured as 1200K inside the downstream part for the initial operating conditions of 60kW power and 1.6 air-fuel ratio. The acoustic eigenfrequencies of a rectangular volume (combustor) for the open-closed end condition are calculated by the following equation [25]

$$f_{ijk} = \frac{c}{2} \sqrt{\left(\frac{i}{2L_x}\right)^2 + \left(\frac{j}{L_y}\right)^2 + \left(\frac{k}{L_z}\right)^2} \quad (2.12)$$

where  $c$  is the speed of sound,  $i, j, k$  are the number of half waves in the three length directions ( $L_x, L_y, L_z$ ) associated with  $x, y$  and  $z$  coordinates (height, width and depth of the combustor), respectively. For the first mode, quarter-wave acoustic mode  $A(1,0,0)$ , the equation is simplified as  $f=c/4L_{eff}$ , where  $L_{eff}$  is the effective length. The effective length of a closed-open end tube is given as  $L_{eff} = L_x + (R_r)(a_{tube})$ , where  $R_r$  is the radiation resistance that is taken as '0.6' and  $a_{tube}$  is the radius of the tube opening [55]. Note that the combustor in this work has a rectangular cross section. Therefore, this area is related to a tube opening cross section, which has the same area of the combustor in order to obtain an equivalent radius to calculate the effective length. The numerical results were calculated using a FEM code in the commercial software ANSYS and a finite volume method (FVM) Helmholtz solver AVSP. The reader is referred to the reference for more information on the AVSP [46]. The characteristic acoustic frequency of the combustor without mean flow is presented in Table 2.6 for the single liner configuration at room temperature ( $T_{room}$ ) and at 1200K ( $T_{60-1.6}$ ) and in Table 2.7 for both the single and double liner configurations at  $T_{60-1.6}$ . These frequencies correspond to the first quarter-wave acoustic mode  $A(1,0,0)$  of the combustor. In the presented results, the superscript ' $\prime$ ' denotes that the end correction is applied and the deviation in the results compared to the experimental results are specified in parentheses. As presented in the tables, the experimental results show deviation compared with the predicted results that is attributed to some parameters that are not included in the numerical model, such as the possible acoustic damping presence in the combustor test setup and the additional volume created by the semi-infinite hoses attached to the combustor to avoid high temperature effect in the piezoelectric pressure transducers. Furthermore, in the analytical calculation the entire geometry is assumed to have the same cross section; however, the depth of the upstream part of the combustor is half of the downstream part. However, the analytical results

show a good coherence at both room and high temperatures for the single liner configuration. On the other hand, the acoustic response of the double liner configuration is predicted accurately by numerical calculations. The direct proportionality of the eigenfrequencies to the speed of sound, and considering that the speed of sound is proportional to the square root of the temperature, results in an apparent jump in the characteristic acoustic frequency of the single liner configuration at a mean temperature of  $T_{60-1.6}$  inside the combustor. As seen in Table 2.7, a reduction in the range of 32%-37% of the characteristic acoustic frequency is obtained when the liner is doubled, which is due to the larger acoustic period.

**Table 2.6. Characteristic acoustic frequency [Hz] of the single liner configuration ( $\dagger$ : end correction)**

Test Temperature	Experimental	Analytical	FEM	FVM	Analytical $\dagger$	FEM $\dagger$	FVM $\dagger$
<sup>(s)</sup> $T_{\text{room}}$	84	82 (2.4)	91 (8.3)	92 (9.5)	80 (4.8)	89 (6.0)	90 (7.1)
<sup>(s)</sup> $T_{60-1.6}$	163	165 (1.2)	175 (7.4)	171 (4.9)	161 (1.2)	170 (4.3)	166 (1.8)
<i>Difference</i>	94%	101%	92%	86%	101%	91%	84%

**Table 2.7. Characteristic acoustic frequency [Hz] of the single and double liner configurations ( $\dagger$ : end correction)**

Test Temperature	Experimental	Analytical	FEM	Analytical $\dagger$	FEM $\dagger$
<sup>(s)</sup> $T_{60-1.6}$	163	165 (1.2)	175 (7.4)	161 (1.2)	170 (4.3)
<sup>(d)</sup> $T_{60-1.6}$	111	104 (6.3)	112 (0.9)	102 (8.1)	110 (0.9)
<i>Difference</i>	32%	37%	36%	37%	35%

### 2.3.8 Structural characterisation

The structural modal characterisation of the combustor test system was performed and the results were validated experimentally and numerically. Two experimental techniques were used, the roving hammer impact test and the shaker test as described in section 2.3.4. The auto-spectra of the output signals were averaged over all the measurement grid points. Hence, all the modes can be captured and missing a mode due to a measurement on the node point was avoided. The experimental and numerical results for the mode shapes and the eigenfrequencies of the first seven modes are presented in Figure 2.16 and Table 2.8, respectively. Note that the measurements are performed on the liner only (Figure 2.7). The results show that the mode shapes are captured well. Furthermore, the predicted structural eigenfrequencies show good agreement with the measurements except two modes (first-torsional  $t(1)$  and the second-bending  $b(2)$  modes) in Table 2.8. In these modes, a large deviation was observed. This deviation is attributed to the production technique of the combustor test system. The downstream liner is composed of two L-shaped profiles welded together to form its rectangular geometry. The two opposite corners contain welds that can have an influence on the structural dynamic behaviour [56]. The corner welds

increase the local stiffness, thus increase the rigidity and act as a stiffener. Therewith, particularly, these torsional and bending modes appear to be shifted further within the mode sequence. This finding is attributed to the following reasons.

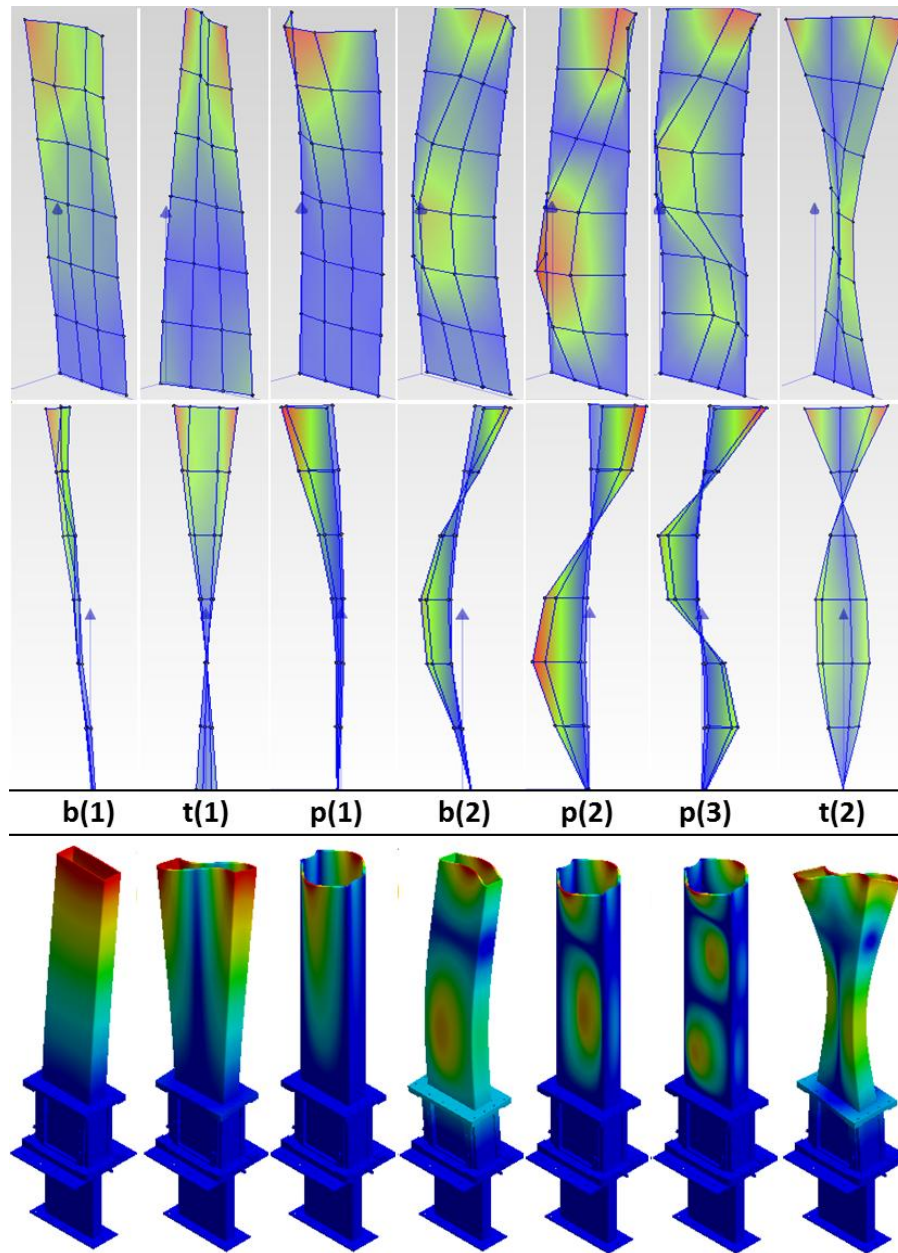


**Figure 2.16. Mode shapes of the single liner configuration (top: Experiment, bottom: FEM)**

As seen from the mode shapes in Figure 2.16, the liner structure deforms with a limited amount of flexure in the first bending mode, thus this mode suffers less from the weld effects. However, in the second bending mode the corner welds experience a significant deflection and thus play a role in the dynamic behaviour. Furthermore, as seen from the experimental results in the second torsional mode, the deformation of the structure is restricted in the liner geometry, whereas the structure deforms together with the flame-box in the numerical results. Hence, the deviation between measurement and simulation caused by the welding is hindered in this mode,  $t(2)$ . The corner weldments require an approximate modelling to accommodate the overall modal analysis. However,

the unknown material properties and the inhomogeneity of the weld turned down the numerical efforts for better prediction of the eigenfrequencies. Considering that the plate modes of the structure are crucial for the acoustic response of the combustor due to change in the acoustic volume (expansion and contraction of the volume) during the combustion process, the numerical results are claimed to be a good prediction, taking note of these remarks. For further analysis, the modal characterisation of the double liner configuration was performed numerically.

It can be remarked that welds are the local discontinuous regions where fatigue cracks can occur. Residual stresses can be generated in weldment due to thermal expansion, plastic deformation and shrinkage during cooling [57]. Even low-level residual stresses can significantly enhance the cracking behaviour in the structures [57, 58] such as in combustion liners [59]. Besides, the welds can alter the structural dynamics due to the local stiff regions and dimensional inhomogeneity of the weld. Therefore, welding should be avoided in the design of the combustors under possible circumstances.

**Table 2.8. Structural eigenfrequencies [Hz] of the single liner configuration at ( $T_{room}$ )**

Mode	Shaker Testing	Impact Testing	Avg-Testing	FEM
Bending - $b(1)$	125	125	125	126 (0.8)
Torsional - $t(1)$	534	534	534	437 (18.2)
Plate - $p(1)$	639	640	639.5	633 (1.0)
Bending - $b(2)$	645	645	645	532 (17.5)
Plate - $p(2)$	673	673	673	671 (0.3)
Plate - $p(3)$	744	742	743	750 (0.9)
Torsional - $t(2)$	764	765	764.5	761 (0.5)

Since the combustion liner material is exposed to elevated temperatures during the combustion operation, the temperature dependence of the material properties must be considered. The surface temperature in the tests for Case22 was observed to vary between 160-370 °C (Figure 2.15). The eigenfrequencies of the specimen scale by the square root of Young's modulus. Hence a temperature increase from room temperature to the maximum temperature of 370 °C ( $T_{Case22}^w$ ) causes a reduction of about 15% of the Young's modulus of the liner material, and thus the eigenfrequencies decrease approximately 8%. The temperature dependency of the material properties is limited within this range (Figure 2.9), therefore the maximum temperature was used as a homogeneous structural temperature in the numerical model. In Table 2.9, the FEM results are presented for single and double liner configurations at  $T_{room}$  and  $T_{Case22}^w$ . In the table, for the double liner configuration 'top' and 'bot' define the location of the mode, which is active either in the top or bottom liner, as depicted in Figure 2.17 for the first two plate modes.

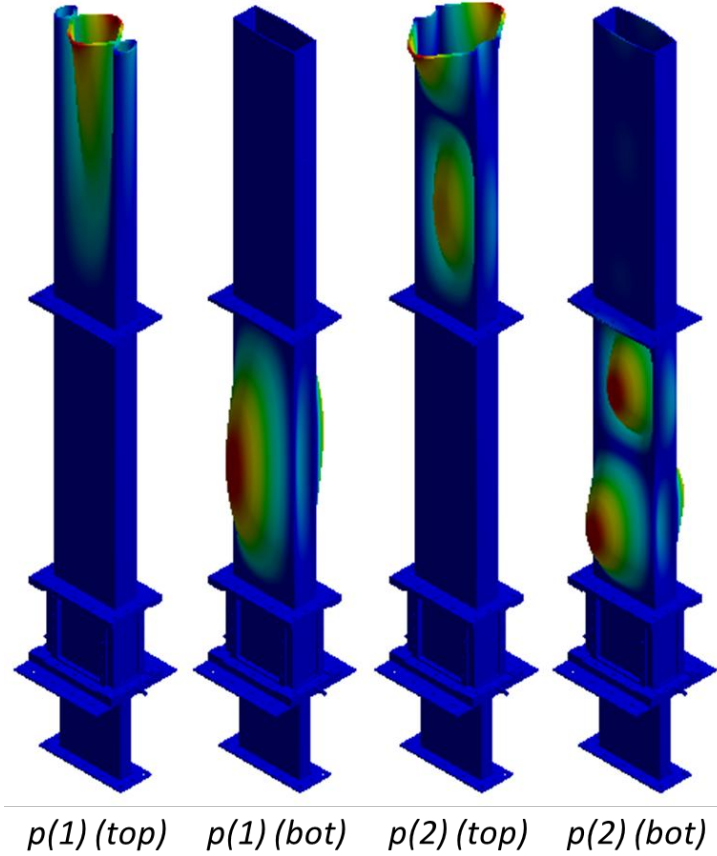


Figure 2.17. First two plate modes in the double liner configurations

Table 2.9. Predicted structural eigenfrequencies [Hz]

Mode No	Single $T_{\text{room}}$	Single $T_{\text{Case22}}^{\text{w}}$	Double $T_{\text{room}}$		Double $T_{\text{Case22}}^{\text{w}}$	
$p(1)$	663	610	(top) 628	(bot) 648	(top) 578	(bot) 596
$p(2)$	671	617	(top) 666	(bot) 714	(top) 613	(bot) 657
$p(3)$	750	690	(top) 743	(bot) 829	(top) 684	(bot) 763
$p(4)$	875	805	(top) 865	(bot) 995	(top) 796	(bot) 915

### 2.3.9 Acoustical and structural response

In this section, the acoustic and the structural responses of the combustor test system, with double liner configuration, during the combustion process are described. The acoustic, combustion and structure domains are interlinked in the experimental results and the observed characteristics of the stable and unstable combustion are discussed. The temperature influence on the acoustic behaviour at  $T_{60-1.6}$  and structural behaviour  $T_{\text{Case22}}^{\text{w}}$  was investigated in the previous sections. The sound pressure level (SPL) and the liner wall velocity ( $v$ ) measurements in time and frequency domain are depicted in Figure 2.18 for the unstable combustion Case22. In the figure, the pressure signal at the three measurement locations,  $p2$ ,  $p5$ ,  $p7$ , and vibration signal at the  $p3$  location are shown. The combustion instability generated a turbulent flame, high amplitude pressure oscillations and a nonlinear system including higher-order harmonics of the characteristic frequency but a deterministic vibration behaviour with a well-shaped cyclic pressure and corresponding vibration of the liner.

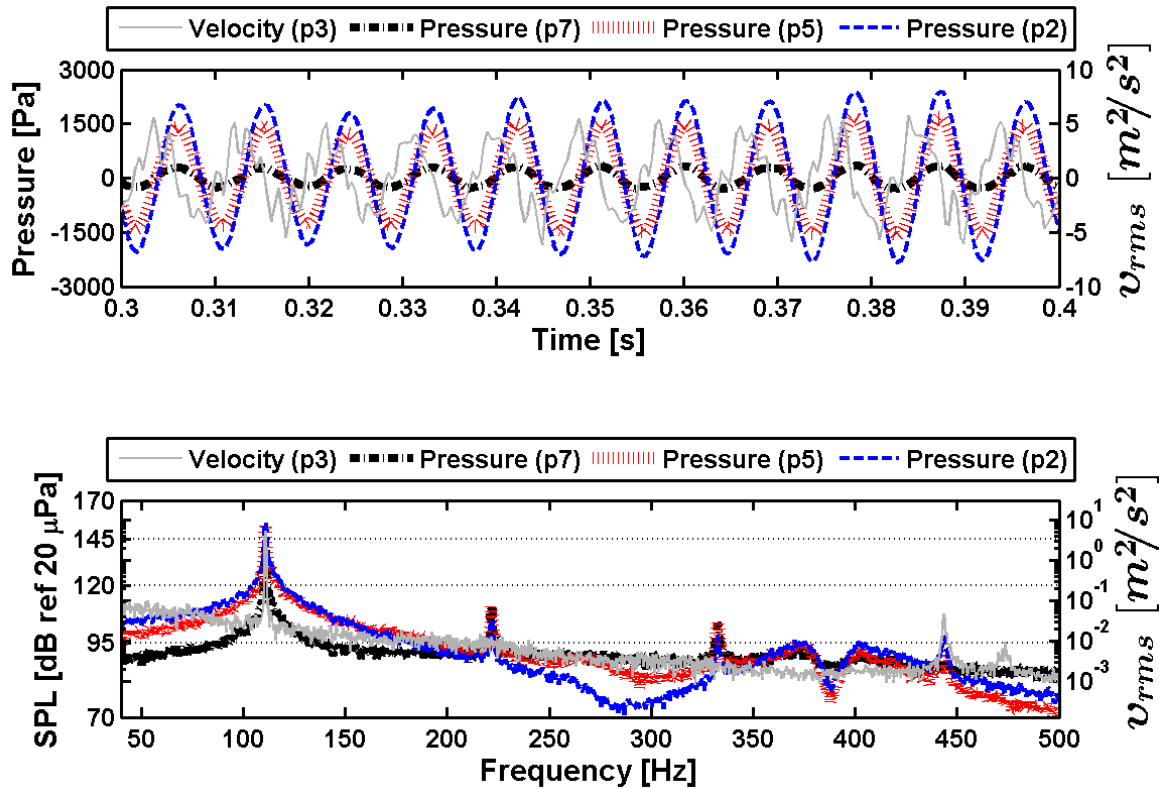


Figure 2.18. Time signal and auto-spectrum of acoustic pressure and velocity of the wall (Case22) – (the measurement locations are showed in parentheses)

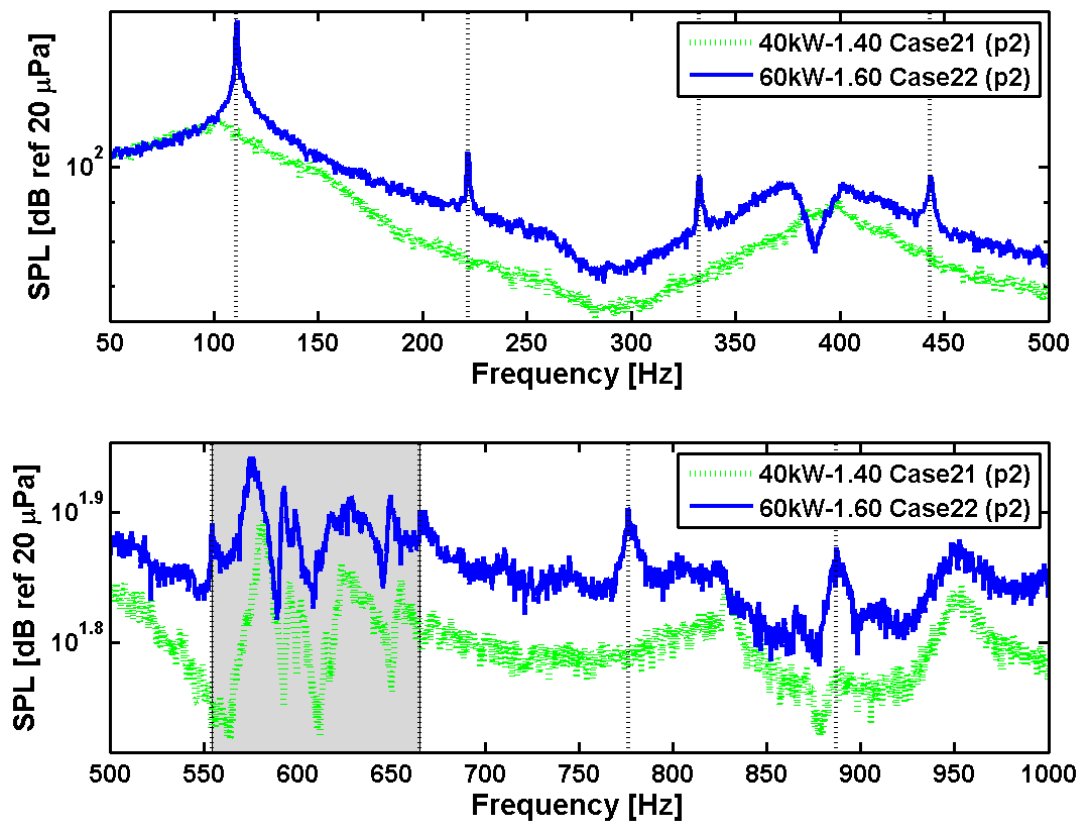
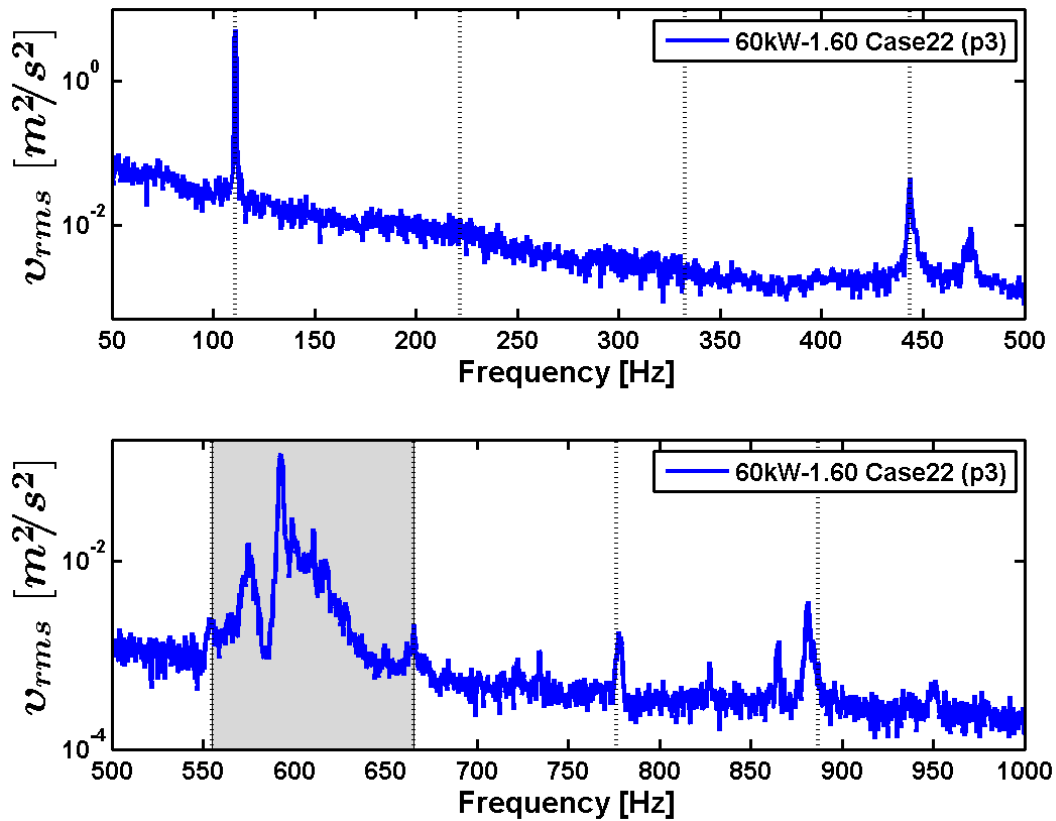


Figure 2.19. SPL inside the combustor



**Figure 2.20. Velocity amplitude of the liner wall**

The SPL and vibration of the liner wall within the range up to 1000 Hz for Case21 and Case22 are shown in Figure 2.19 and Figure 2.20. The y-axis is rescaled in each plot to give a close-up view of the peaks. The higher-order harmonics of the limit cycle frequency are defined by the dashed lines to distinguish the modal frequencies from those harmonics. In Case22, seven more higher-harmonics of the characteristic frequency appeared in the 0 – 1000 Hz range. The generated pressure excites the combustor structure at these higher-harmonic frequencies. The reasons for the deviation in the observed eigenfrequencies in the experiments compared to the numerical results can be due to the use of a mean temperature value instead of the full temperature profile of the fluid and the structure. Besides, unstable combustion is a complex phenomenon and develops varying recirculation zones above the wedge of the combustor; therefore, the acoustic excitation is not completely uniform inside the combustor. The asymmetrical structural dynamics caused by the corner welding and the fact that the measurement devices are mounted on one side of the combustor contribute to the overall deviation. In the numerical analysis, the effect of the surrounding fluid in the structural dynamics was neglected; however, the structural dynamics adjacent to a fluid domain generally couples to the fluid motion. Thus, the fluid affects the structure as damping forces and an added mass. The damping of the plate will be increased accounting, for the fluid and its state. The added mass represents the fluid inertia related to the acceleration of the structure and consequently the back-relation of the surrounding fluid acceleration. Hence, the effective mass and the effective mass moment of inertia of the structure are increased by the added mass components of the fluid inside the combustor with two-way interaction. The following equation [25] can approximately describe the effect of the added mass on the

eigenfrequencies due to the fact that the eigenfrequency of an elastic structure is inversely proportional to the square root of the mass

$$\frac{f_i^{fluid\ medium}}{f_i^{vacuum\ medium}} = \frac{1}{\left(1 + \frac{A_p}{M_p}\right)^{1/2}} \quad (2.13)$$

where  $M_p$  is the mass of the structure and  $A_p$  is the added mass that is generally a function of the structure geometry, boundary conditions and mode number, fluid properties and the fluid state. In this equation, the mode shapes are assumed to be preserved and the effect of the air surrounding the combustor from outside is assumed to be negligible. Thus, it can be concluded that the acousto-elastic coupling, which was described in section 2.2, is expected to contribute to the changes in eigenfrequencies observed in the experiments.

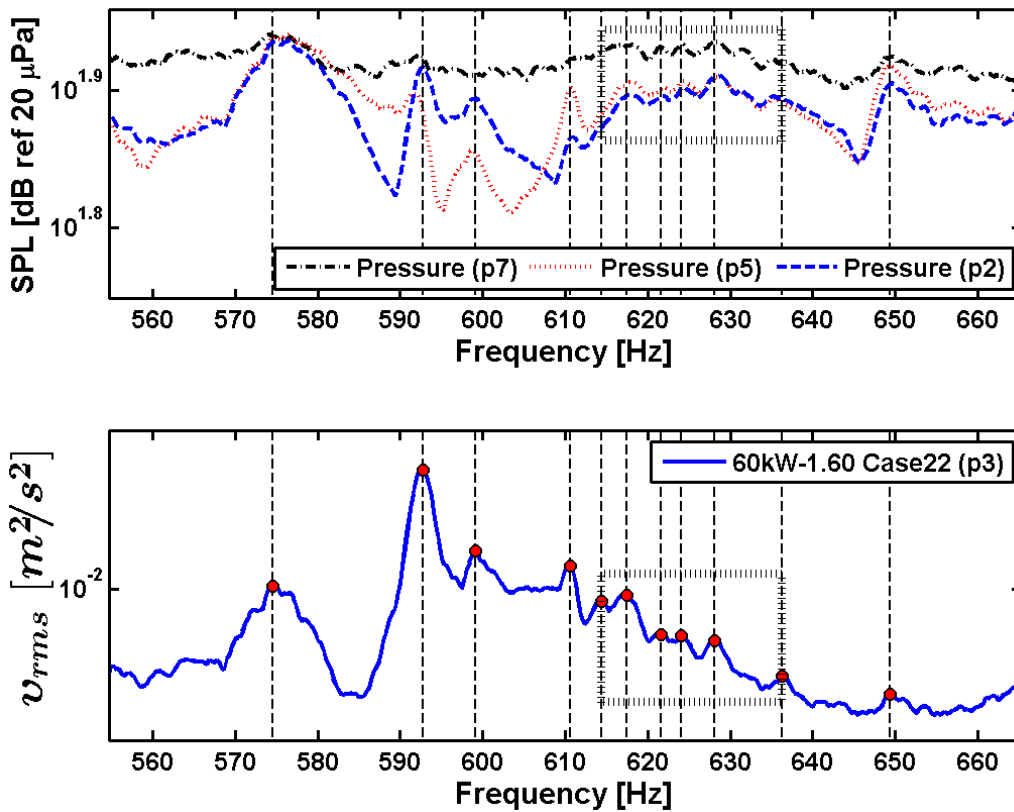


Figure 2.21. SPL and the velocity amplitude of the liner wall

Table 2.10. Experimental and numerical comparison of the frequencies [Hz]

Experiment	FEM	Mode	Deviation
575	578	$p(1)$ (top)	0.5%
593	596	$p(1)$ (bot)	0.5%
599	-	-	-
611	612	$p(2)$ (top)	0.2%
649	657	$p(2)$ (bot)	1.2%

The shaded areas in Figure 2.19 and Figure 2.20 represent the frequency range of 4<sup>th</sup> and 5<sup>th</sup> harmonics of the characteristic frequency. In this range, the structural eigenfrequencies



belonging to the first and the second plate modes take place. The expansion and contraction motion of the walls, due these modes, alters the acoustic volume of the combustor, and thus the pressure inside. Hence, structure to fluid interaction is stimulated and the acoustic pressure is coupled to the wall vibrations. The shaded areas are depicted in Figure 2.21. In the figure, the velocity peaks are marked and the corresponding frequencies (vertical dashed lines) are matched in the pressure spectrum. The frequencies of the peaks in both plots are in agreement. However, the wall vibration peaks enclosed with the rectangular dotted-frame in the figure are found to have limited influence on the pressure. The measured frequencies, where the significant peaks are located, and FEM results are listed in Table 2.10. The results are in good agreement except the frequency of 599 Hz. In this frequency, the pressure amplitudes reach a local-peak at ‘*p2*’ and ‘*p5*’ locations; however, this behaviour is not responsive at ‘*p7*’ location. So, even though the plate modes of the structure interact with the fluid, the main driving mechanism of the thermo-acoustic instability remains independent from these modes, since the characteristic frequency is much lower than the eigenfrequencies belonging to these modes. At the characteristic frequency, a strong fluid-to-structure interaction is generated due to the combustion-driven instability. This results in the highest amplitude of the wall vibrations of the structure at the characteristic frequency.

**2.3.10 Structural damage monitoring**

The presence of damage in the structure leads to a change in the modal parameters. Since the responsiveness of the modal parameters depends on the severity and the location of the damage, the changes in the modal parameters are not identical. Therefore, a dynamic testing was conducted during the combustion operation by means of the frequency shift technique and the flexibility method. The vibration of the plate specimen attached to the flame-box was continuously monitored at the half-diagonal node points to ensure that all modes are covered in the assessment . In the figure, ‘*v<sub>node#</sub>*’ is used to identify the velocity of the measured node number ‘#’ on the scan grid (Figure 2.22).

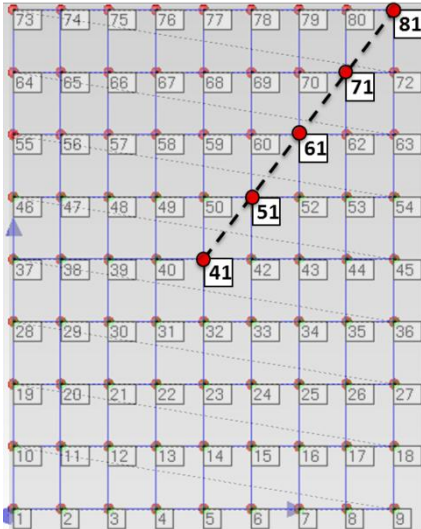


Figure 2.22. Laser zigzag path generation and velocity measurement grid (9x9 nodes: *u<sub>node#</sub>*)

Two experiments were carried out, one on the intact and one on the damaged specimen attached to the flame-box, and the combustor was set to Case22 where the combustion instabilities were observed. Since the abnormal loss of the stiffness due to damage will reflect as a reduction of the measured eigenfrequencies, the damage detection algorithm infers the existence of the damage by the eigenfrequency shift. The stochastic nature of the instability exhibits identical characteristic frequencies but different pressure amplitudes at the higher-harmonics of the characteristic frequencies. Thus, the specimen was excited with different pressure levels that lead to different vibrations. Therefore the velocity amplitudes at each node are normalised with respect to its maximum amplitudes and pressure to avoid differing pressure levels (Figure 2.23 and Figure 2.24). Note that the superscript (accent) ‘ $\hat{\cdot}$ ’ denotes normalisation. In Figure 2.23, the pressure (at ‘ $p7$ ’ location) and velocity measurements are depicted belonging to the intact and the damaged cases for 0-1000 Hz range. The ranges of the y-axes in the figures are set identical. In the damaged specimen, the ‘ $node41$ ’ coincides with the damage location, thus the corresponding velocity data is not available.

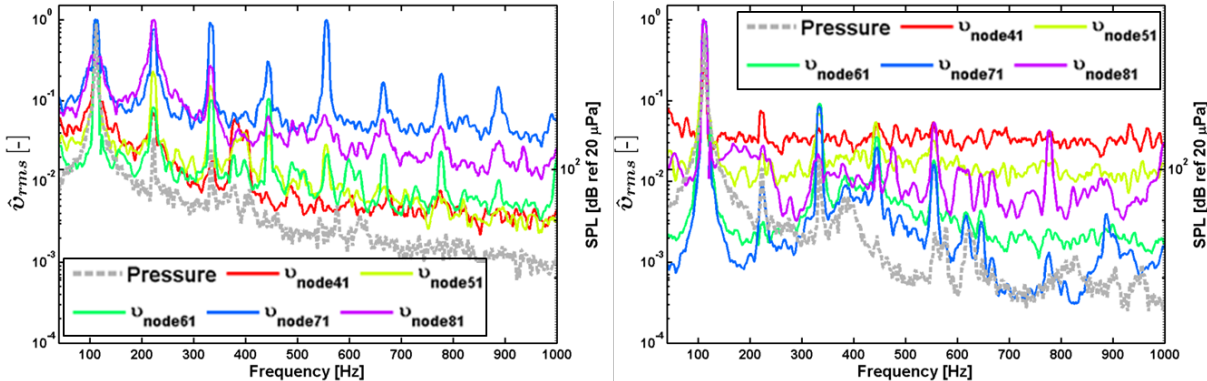


Figure 2.23. Cross-correlations of the pressure (at  $p7$ ) and the velocity of the diagonal-nodes ( $U_{node\#}$ ) of the intact (left) and damaged (right) specimen

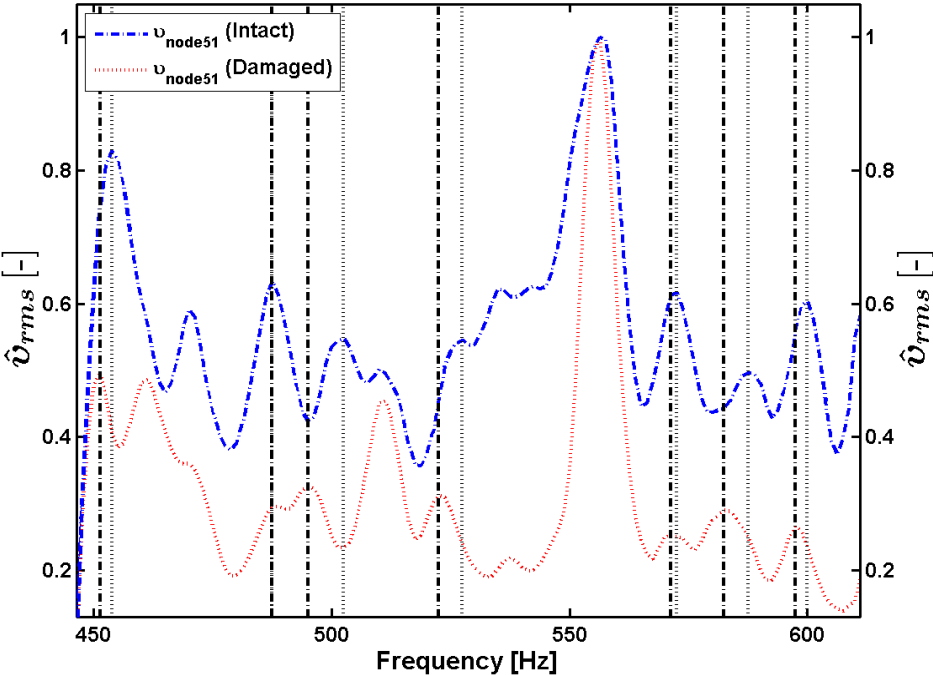


Figure 2.24. Comparison of structural vibrations for the intact and damaged cases

Since, the unstable combustion generated distinct acoustic pressures at four frequencies till 444 Hz, the vibration behaviour was dominated by these pressures in this range. Therefore, the investigation frequency range was scaled down to 445-610 Hz in order to distinguish the structural eigenfrequencies of the system from the frequencies of the dominant acoustic pressures. In Figure 2.24, the vertical lines represent the peak frequency marking for the intact specimen (dotted line) and for the damaged specimen (dash-dot line). Inside each pocket (between two adjacent higher-harmonic frequencies), one distinct peak frequency pair was marked in both intact and damaged plots. The average reduction of representative frequencies in the presented frequency range is less than 1.5 %. The frequency shift method was therefore found to be insensitive to the current damage configuration.

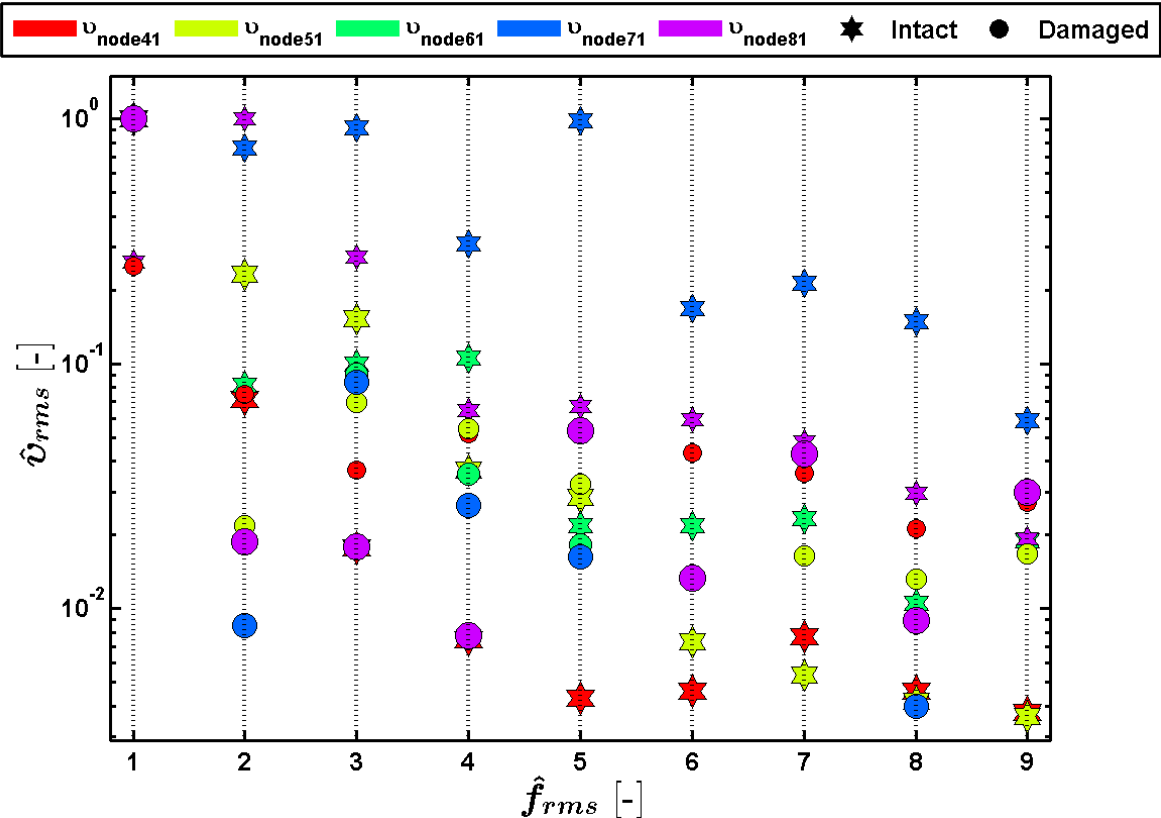


Figure 2.25. Structural response to instability peaks

Table 2.11. Deviation [%] of  $\hat{v}_{rms}$  with respect to the intact and damaged configurations

$\hat{f}$	1	2	3	4	5	6	7	8	9	Avg-v
$v_{node51}$	0,0	90,6	54,7	48,0	13,2	76,0	207,4	214,9	361,5	118,5
$v_{node61}$	0,0	98,0	9,4	66,3	16,4	90,4	89,2	75,5	90,0	59,5
$v_{node71}$	0,0	98,9	90,8	91,5	98,4	99,3	99,4	97,3	97,3	85,9
$v_{node81}$	283,0	98,1	93,4	87,9	20,2	77,5	10,5	69,6	55,6	88,4
Avg-f	70,7	96,4	62,1	73,4	37,1	85,8	101,6	114,3	151,1	

Next, the local response of the structure was investigated under the instability pressure peaks. A new method is proposed, the so-called instability peaks method, which is based on the change of dynamics behaviour of the structure at characteristic and higher-harmonic frequencies. In Figure 2.25, the normalised velocity measurement at each distinct frequency (characteristic frequency and harmonics), which is normalised here by the characteristic frequency ( $\hat{f}$ ), is presented including both intact and damaged cases. As previously discussed,  $v_{node41}$  for the damage case is not available; hence its maximum normalised amplitude does not reach one at any of the distinct frequencies. Furthermore, the maximum amplitude of  $v_{node81}$  is at the second frequency (first harmonic of the characteristic frequency) in the intact case, whereas in the damage case its location shifts to the first frequency, which can be attributed to local mode change due to the damage. Furthermore, in Table 2.11 the absolute deviation of  $\hat{v}_{rms}$  of the damaged configuration from the intact configuration and the average of each row (*Avg-v*, velocity component based) and column (*Avg-f*, frequency component based) are presented.  $v_{node41}$  is excluded from the table due to the aforementioned reasons. As seen from the table, the highest difference between the intact and damage configurations is at 'node51' location and ninth frequency (eight harmonic frequency). This node is the closest measurement location to the damage that leads to the highest change in the velocity amplitude. Furthermore, the sensitivity of the ninth frequency is attributed to local mode alteration due to damage state. However, this method is not reliable to predict the damage location, since the combustion process generates complex behaviour that can lead to a misinterpretation. Moreover, the method requires a prior numerical analysis to obtain the structural modes and define the contribution of the frequency content from the graph.

The frequency shift and instability peaks response methods are not found robustly predictive in structural damage monitoring. Therefore, the vibration measurement is performed on a 9x9 scan grid in the whole specimen area and the flexibility method is applied using two sets of data (intact and damaged cases). The results are depicted in Figure 2.26. The highest flexibility was found on the sides of the centre-crack type damage. The flexibility method captured the damage existence, location and severity.

The influence of damage in the structural dynamics was covered up to this point by means of the modal parameters and the flexibility. The damage can progress during the operation, not only by cyclic pressure amplitudes but also due to the elevated temperature exposure. Furthermore, the thermal gradient presence can enhance the deterioration of the component. The IR camera method was used to obtain the temperature profile evolution on the specimen during the operation. The comparative test results for both the intact and damaged specimens are shown in Figure 2.27. The colour bar is depicted as a representative spectrum to emphasise the distinct temperature field in each frame. In the intact specimen case the temperature increase starts locally and spreads to the upper body as the hot combustion gas flows, whereas in the damaged case the temperature increase concentrates around the introduced damage. This can lead to a reduction of the material strength due to the temperature-dependent properties. The hot gases leaked out through the damage, potentially causing an additional temperature gradient across the structure interacting with the atmospheric environment under this condition. In general, the plastic work fields around the

crack-tip generate thermal energy due to plasticity and hence temperature fields, which leads to a softening of the material [60]. The sustained intense thermal stresses at the damage location can elevate the energy release rate along the crack front and thus the crack driving forces [61]. Therefore, the intensified temperature rise at the damage location would lead to an accelerated crack growth compared to initial design conditions.

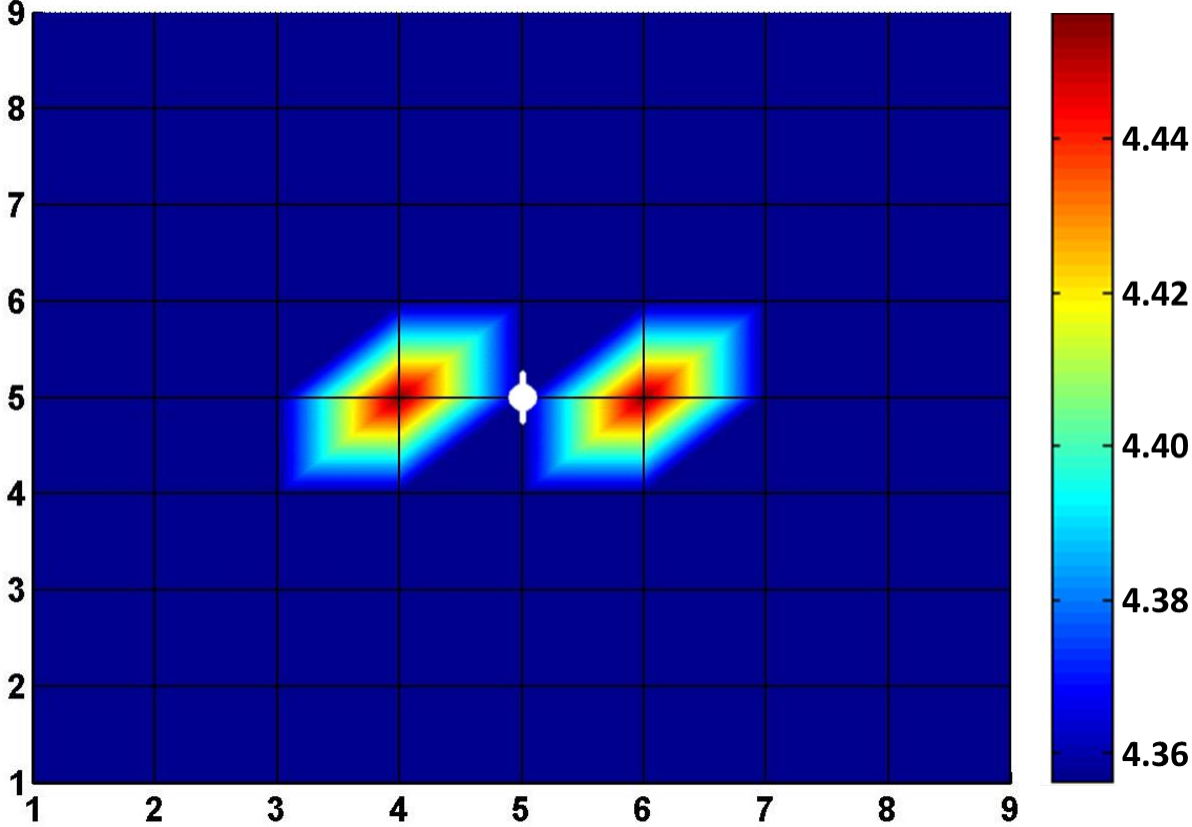


Figure 2.26. Damage localisation due to the change in the flexibility matrix

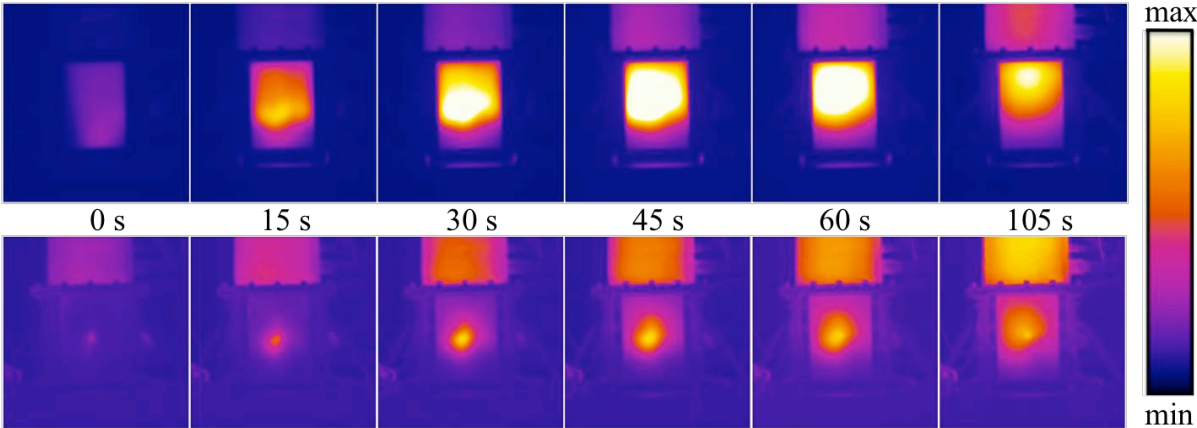


Figure 2.27. Temperature evolution on the intact (above) and damaged (below) specimens

## 2.4 Concluding remarks and discussions

The conclusions of this multiphysical investigation, covering combustion, acoustics and vibration phenomena, can be drawn mainly as follows:

- Limit-cycle pressure oscillations due to combustion instabilities can be generated in the generic combustor test system on demand. The operating points, which induce instabilities, are defined in the instability map.
- The higher-order harmonics of the combustion characteristic frequency due to the nonlinear nature of the combustion instability was generated. Since the harmonics spread over a large frequency band with respect to the order-number, a possible concurrence/interaction of those harmonics with the structural modes of the system is unavoidable. Yet, the full explanation for the number of fairly high amplitudes of the harmonics and the occurrence of the feedback mechanisms that damp some acoustic oscillations is deficient. This effect becomes crucial in designing instability control systems (and its frequency range) for gas turbine engines.
- The generic combustor test system in this work is a basic prototype of an industrial system, which enables an easy operation and validation of numerical calculations with well-defined boundary conditions in a cost-effective manner. Consequently, the test system enables a robust investigation of the combustion-acoustics-structure interrelation under limit cycle conditions. Besides, several variances and analogies between the test system and industrial combustion systems were described throughout the work. The methodology for the structural dynamics assessment nevertheless was proven to be valid and feasible up to a reasonable complexity. Therefore, the core of the modelling procedure can be used to achieve the desired accuracy and complexity by including the circumstances belonging to industrial combustors.
- A real-time combined vibration and thermal based structural assessment method, consisting of a LDV, an infrared camera and a programmable traverse system, was integrated in the combustor test system and enables working continuously during the experiments. The progressive variation in the structural response and the temperature profile were monitored and characterised under combustion driven dynamic loading conditions. The generated pressure was coupled with the structure vibrations in the limit cycle condition. Structural damage detection, localisation and severity quantification was successfully performed by using a combined flexibility and thermography method. For the flexibility method, only a few of the lower modes are sufficient for the measurement to obtain an accurate calculation of the change in the flexibility matrix. The thermography method enables measuring the full-field in image form and fast evaluation. In addition, the thermography method showed that the temperature was localised around the damage in contrast to the intact case during the combustion operation. This incident leads to an accelerated damaging process due to localised softening of the material.
- It should be noted that the variation of the thermal expansion coefficient due to the temperature change can cause a pre-stress effect. The specimen holder in the generic combustion test system enables the specimen to slide inside the fixture due to expansion in longitudinal and transverse directions. This mechanism partially compensates the thermal expansion; however, pre-stress can still remain due to the friction.

## Acknowledgements

The authors would like to acknowledge funding of this research by the EC in the Marie Curie Actions – Networks for Initial Training, under call FP7-PEOPLE-2007-1-1-ITN, Project LIMOUSINE with project number 214905. Additionally, the authors would like to thank J.C. Roman Casado and M. Kapucu from University of Twente Thermal Engineering Department for the experimentation assistance.

## References

- [1] Lieuwen, T., Torres, H., Johnson, C., and Zinn, B. T., 2001, "A Mechanism of Combustion Instability in Lean Premixed Gas Turbine Combustors," *Journal of Engineering for Gas Turbines and Power*, 123(1), pp. 182-189.
- [2] Rayleigh, J. W. S., and Lindsay, R. B., 1945, *The theory of sound*, Dover publications, New York,.
- [3] Crocker, D. S., Nickolaus, D., and Smith, C. E., 1999, "CFD Modeling of a Gas Turbine Combustor From Compressor Exit to Turbine Inlet," *Journal of Engineering for Gas Turbines and Power*, 121(1), pp. 89-95.
- [4] Rao, M. S., and Sivaramakrishna, G., 2009, "Performance Improvement of an Aero Gas Turbine Combustor," *ASME Conference Proceedings*, 2009(48838), pp. 689-694.
- [5] Kim, W.-W., Lienau, J. J., Colket, P. R. V. S. M. B., III, Malecki, R. E., and Syed, S., 2006, "Towards Modeling Lean Blow Out in Gas Turbine Flameholder Applications," *Journal of Engineering for Gas Turbines and Power*, 128(1), pp. 40-48.
- [6] McGuirk, J. J., and Spencer, A., 2001, "Coupled and Uncoupled CFD Prediction of the Characteristics of Jets From Combustor Air Admission Ports," *Journal of Engineering for Gas Turbines and Power*, 123(2), pp. 327-332.
- [7] Bain, D. B., Smith, C. E., Liscinsky, D. S., and Holdeman, J. D., 1999, "Flow coupling effects in jet-in-crossflow flowfields," *Journal of Propulsion and Power*, 15(1), pp. 10-16.
- [8] Bradley, D., Gaskell, P. H., Gu, X. J., Lawes, M., and Scott, M. J., 1998, "Premixed turbulent flame instability and NO formation in a lean-burn swirl burner," *Combustion and Flame*, 115(4), pp. 515-538.
- [9] Cohen, J. C., and Anderson, T., "Experimental Investigation of Near-Blowout Instabilities in a Lean, Premixed Step Combustion," *Proc. 34th Aerospace Sciences Meeting and Exhibit*.
- [10] Dowling, A. P., and Stow, S. R., 2003, "Acoustic analysis of gas turbine combustors," *Journal of Propulsion and Power*, 5(19), pp. 751–763.
- [11] Krebs, W., Flohr, P., Prade, B., and Hoffmann, S., 2002, "Thermoacoustic Stability Chart for High Intense Gas Turbine combustion Systems," *Combustion Science and Technology*(174), pp. 99–128.
- [12] Hubbard, S., and Dowling, A. P., 2001, "Acoustic Resonances of an Industrial Gas Turbine Combustion System," *Journal of Engineering for Gas Turbines and Power*, 123(4), pp. 766-773.
- [13] McManus, K. R., Poinsot, T., and Candel, S. M., 1993, "A review of active control of combustion instabilities," *Progress in Energy and Combustion Science*, 19(1), pp. 1-29.
- [14] Lieuwen, T., 2003, "Modeling premixed combustion-acoustic wave interactions: A review," *Journal of Propulsion and Power*, 19(5), pp. 765-781.
- [15] Tufano, S., Stopford, P., Roman Casado, J. C., and Kok, J. B. W., "Modelling flame-generated noise in a partially premixed, bluff body stabilized model combustor (GT2012-69501)," *Proc. Proceedings of ASME Turbo Expo 2012*.

- [16] Junger, M. C., and Feit, D., 1972, *Sound, Structures, and Their Interaction*, MIT, Cambridge, MA.
- [17] Fahy, F., and Gardonio, P., "Sound and Structural Vibration - Radiation, Transmission and Response (2nd Edition)," Elsevier.
- [18] Huls, R. A., van Kampen, J. F., van der Hoogt, P. J. M., Kok, J. B. W., and de Boer, A., 2008, "Acoustoelastic interaction in combustion chambers: Modeling and experiments," *Journal of Engineering for Gas Turbines and Power*, 130(5).
- [19] Huls, R. A., Sengissen, A. X., van der Hoogt, P. J. M., Kok, J. B. W., Poinsot, T., and de Boer, A., 2007, "Vibration prediction in combustion chambers by coupling finite elements and large eddy simulations," *J Sound Vib*, 304(1-2), pp. 224-229.
- [20] Khatir, Z., Pozarlik, A. K., Cooper, R. K., Watterson, J. W., and Kok, J. B. W., 2008, "Numerical study of coupled fluid-structure interaction for combustion system," *Int J Numer Meth Fl*, 56(8), pp. 1343-1349.
- [21] Alemela, R., Roman Casado, J. C., Kumar, S., and Kok, J., "Simulation of limit cycle pressure oscillation with coupled Fluid-Structure interactions in a model combustor," *Proc. 18th International Congress on Sound & Vibration, ICSV 18*.
- [22] Shahi, M., Kok, J. B. W., and Alemela, P. R., "Simulation of 2-way fluid structure interaction in a 3D model combustor," *Proc. Proceedings ASME Turbo Expo 2012*.
- [23] Altunlu, A. C., Shahi, M., Pozarlik, A., Hoogt van der, P. J. M., Kok, J. B. W., and Boer de, A., 2012, "Fluid-structure interaction on the combustion instability," *19th International Congress on Sound and Vibration, ICSV 2012, International Institute of Acoustics and Vibration (IIAV), Vilnius, Lithuania*.
- [24] Visser, R., 2004, "A boundary element approach to acoustic radiation and source identification," Ph.D. thesis, University of Twente, The Netherlands.
- [25] Blevins, R. D., 2001, *Formulas for natural frequency and mode shape*, Robert E. Krieger publishing company, Malabar, Florida.
- [26] Cook, R. D., Malkus, D. S., Plesha, M. E., 2002, *Concepts and Applications of Finite Element Analysis*, Wiley, New York.
- [27] ANSYS® Academic Research, "Help System: Acoustics," Release 14.0, ANSYS, Inc.
- [28] Cawley, P., and Adams, R. D., 1979, "The location of defects in structures from measurements of natural frequencies," *The Journal of Strain Analysis for Engineering Design*, 14(2), pp. 49-57.
- [29] Stubbs, N., and Osegueda, R., 1990, "Global non-destructive damage evaluation in solids," *The International Journal of Analytical and Experimental Modal Analysis*, 5, pp. 67–79.
- [30] Salawu, O. S., 1997, "Detection of structural damage through changes in frequency: a review," *Engineering Structures*, 19(9), pp. 718-723.
- [31] West, W. M., "Illustration of the use of modal assurance criterion to detect structural changes in an orbiter test specimen," *Proc. Proceedings of the Air Force Conference on Aircraft Structural Integrity*, pp. 1–6.
- [32] Mayes, R. L., "Error localization using mode shapes—an application to a two link robot arm," *Proc. Proceedings of the 10th International Modal Analysis Conference*, pp. 886–891.
- [33] Stubbs, N., Kim, J. T., and Farrar, C. R., "Field verification of a nondestructive damage localization and severity estimation algorithm," *Proc. Proceedings of the 13th international modal analysis conference*, pp. 210–218.
- [34] Ooijevaar, T. H., Loendersloot, R., Warnet, L. L., de Boer, A., and Akkerman, R., 2010, "Vibration based Structural Health Monitoring of a composite T-beam," *Composite Structures*, 92(9), pp. 2007-2015.
- [35] Toksoy, T., and Aktan, A. E., 1994, "Bridge-Condition Assessment by Modal Flexibility," *Exp Mech*, 34(3), pp. 271-278.



- [36] Pandey, A. K., and Biswas, M., 1994, "Damage Detection in Structures Using Changes in Flexibility," *J Sound Vib*, 169(1), pp. 3-17.
- [37] Pandey, A. K., and Biswas, M., 1995, "Damage Diagnosis of Truss Structures by Estimation of Flexibility Change," *Modal Anal*, 10(2), pp. 104-117.
- [38] Doebling, S. W., Farrar, C. R., Prime, M. B., and Shevitz, D. W., 1996, "Damage Identification and Health Monitoring of Structural and Mechanical Systems from Changes in their Vibration Characteristics: A Literature Review."
- [39] Aktan, A. E., Lee, K. L., Chuntavan, C., Aksel, T., "Modal Testing for Structural Identification and Condition Assessment of Constructed Facilities," *Proc. Proceedings of 12th International Modal Analysis Conference*, pp. 462-468.
- [40] Doebling, S. W., Farrar, C. R., and Goodman, R. S., "Effects of Measurement Statistics on the Detection of Damage in the Alamosa Canyon Bridge," *Proc. Proceedings of the 15th International Modal Analysis Conference*, pp. 919-929.
- [41] Farrar, C. R., Doebling, S. W., Cornwell, P. J., and Straser, E. G., "Variability of Modal Parameters Measured on the Alamosa Canyon Bridge," *Proc. Proceedings of the 15th International Modal Analysis Conference*, pp. 257-263.
- [42] Altunlu, A. C., van der Hoogt, P., de Boer, A., "Life assessment by fracture mechanics analysis and damage monitoring technique on combustion liners," *Proc. ASME Turbo Expo 2011*.
- [43] Berman, A., and Flannell, W. G., 1971, "Theory of Incomplete Models of Dynamic Structures," *Aiaa J*, 9(8), pp. 1481-&.
- [44] Adams, R. D., Cawley, P., Pye, C. J., and Stone, B. J., 1978, "A Vibration Technique for Non-Destructively Assessing the Integrity of Structures," *Journal of Mechanical Engineering Science*, 20(2), pp. 93-100.
- [45] Huls, R. A., 2006, "Acousto-Elastic Interaction in Combustion Chambers," Ph.D. thesis, University of Twente, The Netherlands.
- [46] Roman Casado, J. C., Alemela, P. R., and Kok, J. B. W., "Experimental and Numerical Study of the Effect of Acoustic Time Delays on Combustion Stability," *Proc. 18th International Congress on Sound and Vibration 2011 (ICSV 18)*, International Institute of Acoustics & Vibration.
- [47] Haynes International, 2003, "High-temperature Tech Brief: HAYNES® 230® Alloy," <http://www.haynesintl.com/pdf/h3060.pdf>.
- [48] Haynes International, "HAYNES® HR-120TM alloy," <http://www.haynesintl.com/pdf/h3125.pdf>.
- [49] Roman Casado, J. C., and Kok, J. B. W., 2012, "Combustor eigen frequencies of pressure oscillations and their dependence on the burner impedance and a dimensional numbers," *Proc. ASME Turbo Expo 2012* June 11-15.
- [50] Lieuwen, T., and Neumeier, Y., 2002, "Nonlinear pressure-heat release transfer function measurements in a premixed combustor," *Proceedings of the Combustion Institute*, 29(1), pp. 99-105.
- [51] Seo, S., 2003, "Combustion instability mechanism of a lean premixed gas turbine combustor," *Journal of Mechanical Science and Technology*, 17(6), pp. 906-913.
- [52] Lefebvre, A. H., and Ballal, D. R., 2010, *Gas turbine combustion: Alternative fuels and emissions*, Taylor & Francis, Boca Raton.
- [53] Damkohler, G., 1939, "English translation: NACA Tech. Memo. No. 1112, 1947.," *Z. Elektrochem.*, 46(601), p. 113.
- [54] Schelkin, K. I., 1943, "English translation: NACA Tech. Memo. No. 1110, 1947," *Soviet Physics - Journal of Technical Physics*, 13(520).
- [55] Blackstock, D. T., 2000, *Fundamentals of physical acoustics*, Wiley, New York.

- [56] Palmonella, M., Friswell, M. I., Mottershead, J. E., and Lees, A. W., 2005, "Finite element models of spot welds in structural dynamics: review and updating," *Comput Struct*, 83(8-9), pp. 648-661.
- [57] Link, L. R., "Fatigue crack growth of weldments," *Proc. Fatigue and fracture testing of weldments (ASTM STP 1058)*, American Society for Testing and Materials, pp. 16–33.
- [58] Bucci, R. J., "Effect of residual stress on fatigue crack growth rate measurements," *Proc. Fracture Mechanics: Thirteenth Conference (ASTM STP 743)*, American Society for Testing and Materials, pp. 28–47.
- [59] Kim, K. M., Yun, N., Jeon, Y. H., Lee, D. H., and Cho, H. H., 2010, "Failure analysis in after shell section of gas turbine combustion liner under base-load operation," *Engineering Failure Analysis*, 17(4), pp. 848-856.
- [60] Bhalla, K. S., Zehnder, A. T., and Han, X., 2003, "Thermomechanics of slow stable crack growth: closing the loop between experiments and computational modeling," *Engineering Fracture Mechanics*, 70(17), pp. 2439-2458.
- [61] Shih, C. F., Moran, B., and Nakamura, T., 1986, "Energy release rate along a three-dimensional crack front in a thermally stressed body," *International Journal of Fracture*, 30(2), pp. 79-102.



### 3 Fluid-structure interaction of combustion instabilities and fatigue/creep lifetime assessment

A. Can Altunlu <sup>a</sup>, Mina Shahi <sup>b</sup>, Artur Pozarlik <sup>b</sup>, Jim B.W. Kok <sup>b</sup> and André de Boer <sup>a</sup>

<sup>a</sup> University of Twente, Faculty of Engineering Technology, Section of Applied Mechanics, 7500 AE, Enschede, The Netherlands

<sup>b</sup> University of Twente, Faculty of Engineering Technology, Section of Thermal Engineering, 7500 AE, Enschede, The Netherlands

---

#### Abstract

**A** multiphysics problem, the limit-cycle behaviour of unstable oscillations in a laboratory-scaled generic combustor was investigated by a fluid-structural approach. Experimental and numerical analysis were performed to characterise the strong interaction between the aerodynamics, combustion, acoustics and structure due to the instability. The two-way interaction between the oscillating pressure load in the fluid and the motion of the structure under the limit-cycle oscillations (LCO) brought up elevated vibration levels that increase the fatigue damage of the liner material at high temperatures. The time-dependent pressures inside the combustor and corresponding structural velocities were calculated using fluid-structure interaction analysis (FSI), in which pressure and displacement values are exchanged transiently between computational fluid dynamics analysis and computational structural dynamics analysis creating two-way fluid-structure coupling. The steady-state pressure, the characteristic combustion frequency and temperature obtained by experiments were compared to numerical analysis. Subsequently, the numerical results were used to extrapolate the instability evolution for the experimental results. Finally, the full loading history was utilised to assess the lifetime including fatigue and creep aspects. The FSI results for the pressure and temperature oscillations were approximated to predict the full loading-span for the experiments.

**Keywords:** Fluid structure interaction, gas turbine, combustion, thermo-acoustic instability, fatigue, creep, life assessment.

### 3.1 Introduction

In modern gas turbines used for power generation systems, utilising lean premixed combustion technology is motivated by the need to meet low  $\text{NO}_x$  emission targets. However, these systems are prone to thermo-acoustically induced combustion instabilities. The feedback mechanism between the unsteady heat release, acoustic oscillations and flow perturbations in the combustor can lead to instability [1, 2]. The unsteady heat release of a turbulent flame, generated by the perturbations in the flow, builds up high amplitude oscillations with time by adding energy to the acoustic field if the pressure and heat release oscillations are in phase satisfying the Rayleigh criterion [3]. The higher pressure loads at elevated temperatures generated by the unstable combustion process elevate the structural vibration levels of the combustor. Thus the cycle-dependent fatigue and the time-dependent creep damage can threaten the mechanical integrity, and the design targets can drift apart by means of efficiency and emissions. The two-way interaction of the fluid and structure constitute a multiphysics problem.

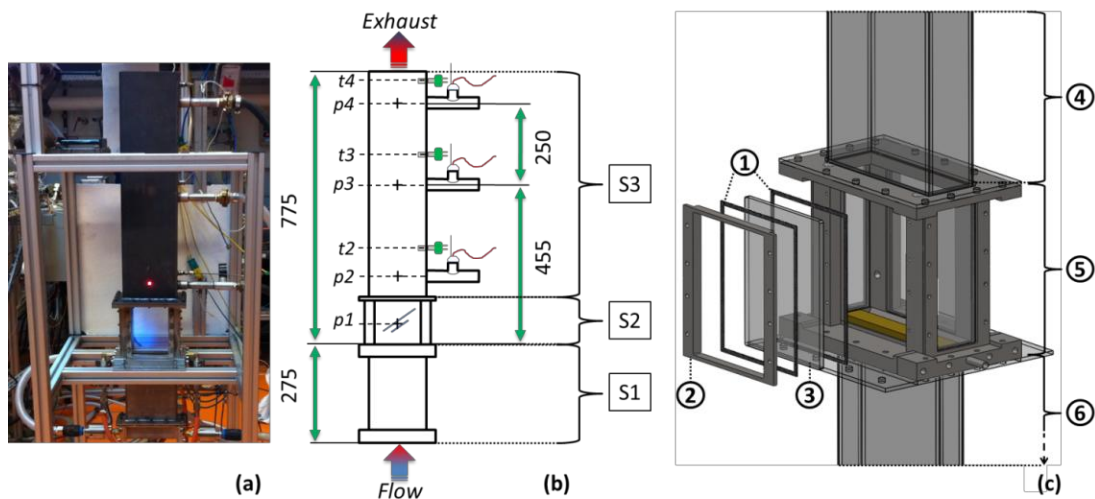


**Figure 3.1. Combustor test system configuration (a) and dimensions (b) and flame-box (c)**

Acoustics and structural vibrations are an inevitable outcome of a combustion process. In the literature, numerous efforts were indicated for combustion research by means of fluid dynamics and process enhancement to improve efficiency and emissions characteristics [4-8]. The multiphysical studies are already present for the interaction between combustion-acoustics [1], and acoustics-vibrations interaction [9, 10]. Recently, Huls *et al.* [11, 12] investigated the combination of these fields for the interaction between combustion-acoustics-vibrations using computational fluid dynamics (CFD) and large eddy simulation (LES) to calculate the loads and then apply them to the structural finite element model (FEM). In this study, the feedback information from the structural domain to the fluid domain was not included. Khatir *et al.* [13] performed a FSI numerical study to investigate the coupling between fluid dynamics and structural dynamics for a combustion system using two commercial software packages. Their work was limited to stable combustion, but the combustion instability phenomenon was not covered. More recently, FSI for combustion instabilities were analysed by Alemela *et al.* [14], considering only a 2D slice of the geometry

for the simulation that neglects the 3D flow patterns. Besides, Shahi *et al.* [15] extended coupled FSI simulations to a 3D model combustor; however, the results were not linked to the lifetime assessment of the structure. Regarding the publications, the amount of attention is very limited on the structural lifetime assessment driven by the coupled fluid and structure effects. Lai [16] performed CFD simulations to predict the liner hot spots induced by the near-wall gas temperature levels and Kiewel [17] assessed the lifetime based on the measured temperature distribution.

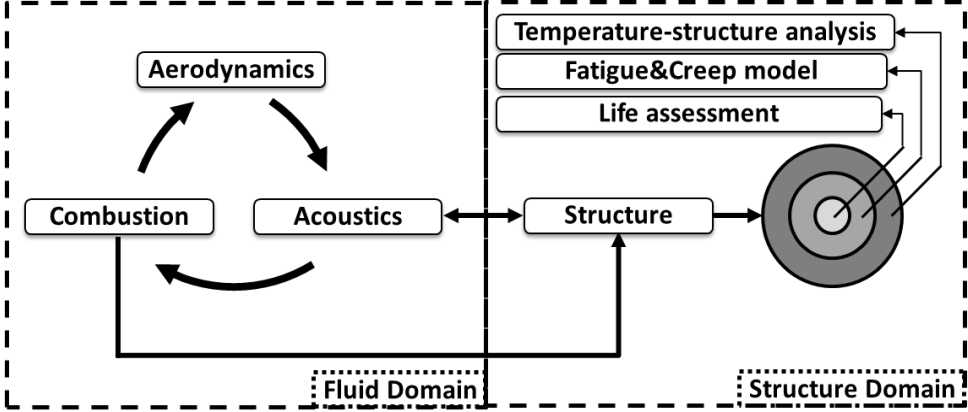


**Figure 3.2. Schematic representation of the methodology**

In this work, the dynamic interaction between the combustion, acoustics and structural vibrations, including the combustion instability, is investigated in a laboratory-scaled partially premixed generic combustor, depicted in Figure 3.1. Experiments and numerical calculations, which are based on two-way coupled FSI simulations, are carried out. The results of the stable and unstable combustion process are highlighted quantitatively in terms of lifetime of the combustor, which is indispensable to the structural integrity assessment, using fatigue and creep lifing methods. The next section presents the experimental approach including the combustor design, instrumentation and measurement techniques, materials and their compliance. In section 3.3, the strategy of the numerical approach for the two-way coupled fluid-structure interaction (FSI) analysis is presented covering the fluid and solid domains. In addition, the growth rates of the pressure and temperature oscillations are extracted from the numerical results, and they are used to describe the growth of the oscillatory amplitudes that are measured experimentally. Section 3.4 describes the material behaviour, temperature-structure analysis and lifing for fatigue and creep. Next, the modal, combustion and acoustic characterisation are presented that depict the comparison between the experimental and numerical results; along with the life assessment of the combustor in section 3.5. In the final section, the conclusions are drawn and the paper closes with a discussion on further numerical improvement and potential instability mechanisms derived from the structure. Accordingly, the schema of this work is depicted in Figure 3.2. Note that, as seen in Figure 3.3, particular geometric models for the structural domain as the field-of-interest were deviated from the combustor test system configuration (a) due to computational benefits while conserving the accuracy adequacy. These are the fluid-structure interaction model (b) and the temperature-structure model for the lifetime assessment (c). The details for the selection of these particular geometric models are described in sections 3.3 and 3.4.

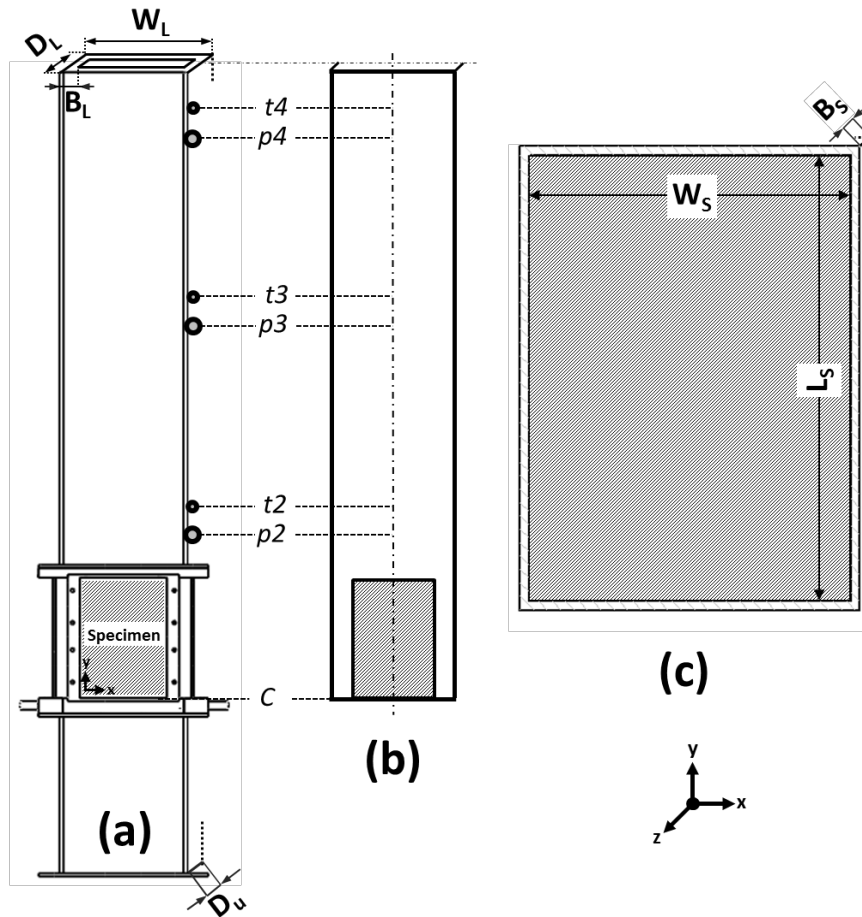


**Figure 3.3. Schematic representation of (a) the combustor, (b) FSI model configuration and (c) temperature-structure model configuration**

### 3.2 Experiment and method

A typical gas turbine combustor is scaled down to a laboratory-size one to investigate the combustion instability phenomenon. The well-defined boundary conditions provide experimental repeatability, and the simplicity of the design eases the computational validation and enables variability of the test configurations such as fuel type, initial test setting (power and air/fuel ratio), combustor materials, liner length, and specimen thickness. However, in this work only initial test settings are varied and the measurements are presented for the test matrix (Table 2.5).

**Table 3.1. Combustion test cases**

Case Code	Thermal power	Air/fuel ratio	Combustion behaviour
Case4012	40 kW	1.2	Unstable
Case4018	40 kW	1.8	Stable
Case6012	60 kW	1.2	Unstable
Case6018	60 kW	1.8	Stable

### 3.2.1 Experimental combustor system design

The generic combustion test system is depicted in Figure 3.1 and the geometric dimensions are given in Table 2.4. In the figure (b), the measurement locations for the pressure are denoted as ' $p\#$ ' and for the fluid temperature as the letter ' $t\#$ '. The test combustor [18] has been designed as a Rijke tube configuration consisting of mainly two sections. The upstream section (S1) consists of an air-feeding box, a rectangular duct with a  $25 \times 150 \text{ mm}^2$  cross-sectional area and 275 mm long and an equilateral triangular wedge as a flame holder, where methane as the fuel is injected through the holes on both sides, fixed at the end. The downstream section consists of a flame-box (S2) and a rectangular liner (S3). The flame-box is surrounded by four windows made of quartz glass that provides an optical access to the flame. Additionally the glass windows can be easily replaced by an intact or a damaged test-specimen to investigate the structural dynamics of the specimen during the operation while visualising the flame through the side windows. The turbulent flame is technically premixed and flame stabilisation takes place on the wedge wake in the combustor test system. The combustor is supported from the bottom of the flame-box on a carrier frame.

**Table 3.2. Combustor test system dimensions**

Section	Dimension [mm]
Combustor outer width ( $W_L$ )	158
Upstream outer depth ( $D_u$ )	33
Downstream outer depth ( $D_L$ )	58
Liner thickness ( $B_L$ )	4
Quartz glass thickness	5
Specimen thickness ( $B_S$ )	1

In practical combustion systems, the heat is taken away from the flame to the structure, herein to the combustor walls or the flame-box specimen, by radiation and convection. The maximum achieved temperature on the structure transferred from the temperature of the gases released by the combustion process is less than the material test system. The test system is uncooled so that the environment is in atmospheric condition, thus the heat is lost from the structure to the environment. Therefore, there is not a sharp temperature gradient across the structure thickness. The structure wall temperature is generated due to the balance between the heat absorption released from the hot gas by convection and radiation and the heat leaves the environment air by convection.

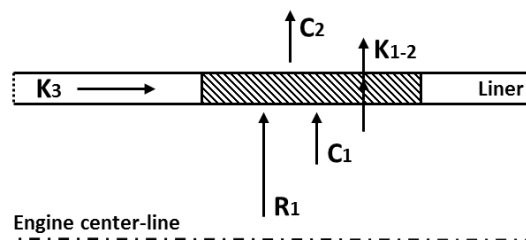


**Figure 3.4. Representation of the heat-transfer in combustor system**



The schema of the heat transfer process in the combustor test system is depicted in Figure 3.4, in which the radiation heat flux from gas is  $R_1$ , the convection heat flux from gas is  $C_1$ , the convection heat flux to the surrounding air is  $C_2$ , the conduction heat flux across the wall thickness is  $K_{1-2}$  and the conduction along the liner wall is  $K_3$ . During the combustion process, the hot section structural group, including the liner and the attached specimen, are heated by convection and the radiation from the combustion hot gases, and inversely air-cooled by convection to the surrounding air. The loss of heat by conduction along the liner wall (and specimen) is comparatively small and therefore is neglected.

### 3.2.2 Instrumentation

The experimental instruments and techniques used on the test system were particularly selected and integrated such that the robustness of the experiments can be maintained at high temperatures. Non-contact type sensors are preferably used in measurements. The sensors, which are in contact with the combustor hardware, are well protected, and an additional cooling is applied to them to ensure stable measurement during the tests. In the combustion experiments, three locations (Figure 3.1) are measured for the combustor inner pressure and the liner wall velocity at  $p_2$ ,  $p_3$ ,  $p_4$ , and combustor inner temperature at  $t_2$ ,  $t_3$ ,  $t_4$ . Infrared thermography has been used to generate thermal images based on liner wall/surface temperatures during the combustion process using an Xenics Gobi 384 infrared camera.

K-type thermocouples are used to measure the fluid temperature. The pressures inside the combustor are monitored by the dynamic pressure measurement sensors attached in the side-tubes that are connected to the semi-infinite hoses. External coolers were directed towards the devices that provide protection for the piezoelectric pressure transducers (Kullite) and a non-reflecting acoustic condition. The structural vibrations are measured by the laser doppler vibrometer, LDV (Polytec OFV 505). The LDV is mounted on an automated measurement traverse system that analyses the vibration response of the specimen plate inserted in the flame-box. Two test techniques, the roving hammer impact test and the shaker test, are utilised for modal analysis, which is performed by ME'scope software. The first technique requires a structural excitation at the measurement grid (DOFs) while the accelerometer (B&K) is placed at a single degree of freedom (DOF). In the latter, the electro-mechanical shaker (B&K) is used to excite the structure at a fixed reference point while the LDV is used to travel over the measurement grid.

### 3.2.3 Materials and compliance

During the combustion process, the liner is exposed to elevated temperatures; therefore the influence of temperature levels on the material properties becomes crucial. The combustor is made of austenitic stainless steel (AISI) Type310, the specimen material is chosen as Type316. These materials have sufficiently enough heat and corrosion resistance at the test temperatures within relatively short exposure time of the tests, well-established properties and cost-effectiveness. The compliance of the test material can be seen in Figure 2.9 in comparison to a typical combustor base material, nickel-base superalloy AlloyX (Hastelloy X) [19, 20]. The materials used in the test setup exhibit analogical trends to the AlloyX and

satisfactory properties within the experimental conditions, such as temperatures and test duration. The usage of Type310 and Type316 pair avoids any pre-stress effects in the specimen, since the thermal expansion properties are coherent. Considering the elastic modulus, the tendency to elastically deform under pressure at high temperatures is nearly identical for these two materials, which implies that the specimen and the liner behaves as a single solid under the loads. Besides, AlloyX maintains its stiffness better than Type310 and Type316 as the temperature increases. The maximum stress that the Type316 can withstand is noticeably close to the AlloyX at 300K; however, around 900K its ultimate tensile strength decays sharper than AlloyX, but reaches Type310 values as the temperature increases. Three alloys exhibit a distinct switch due to the transition from normal low temperature yield to creep controlled mechanisms according to the drastic decline in the stress to rupture time curve; however, the creep properties of AlloyX remain superior. Note that, since nickel-based superalloys are of interest to the gas turbine community, the life assessment is performed for AlloyX, even though the pressure and metal temperature measurements were done in the combustor test system made of austenitic steels. The measured pressure is independent of the material and the temperature distribution becomes independent as well, once the steady-state conditions are reached. Under this consideration, the hot-spot location in the structure remains the same, but the lifetime will be dependent on the material type.

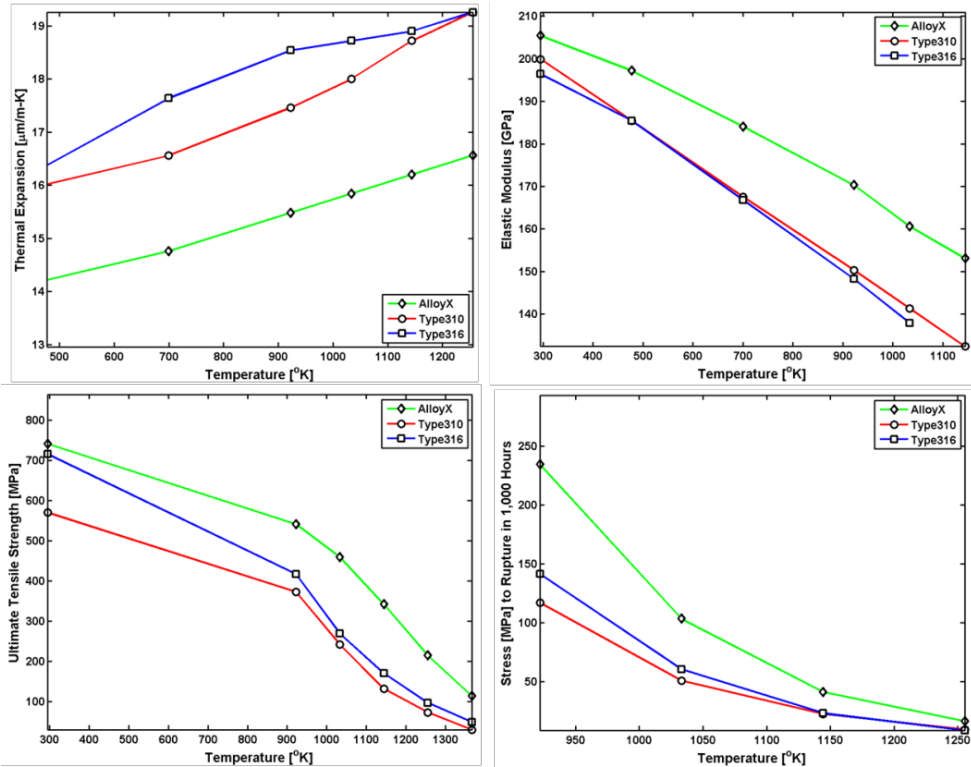


Figure 3.5. Temperature dependence of the material properties

### 3.3 Fluid structure interaction (FSI) coupling strategy

The approaches to the field of coupled problems can be subdivided into two classes: monolithic and partitioned. In a monolithic method the interaction of the fluid and the structure at the interface is treated synchronously. This scheme is more accurate, and a larger

time step can be used compared to partitioned schemes for the same level of accuracy. However, it is still computationally more expensive per time step compared to the partitioned approach [21]. Therefore the latter approach for the fluid-structure interaction was used in this work. In the partitioned approach, separate and independent techniques with the appropriate interface boundary conditions are used for the fluid and solid domains. This approach strives to solve each physical field separately, with communication of interface data in between to connect the components. Thus the matching conditions at the interface (boundary) between fluid and solid regions must satisfy the Euler equation and Cauchy stress, as:

$$\rho_f \cdot \vec{n} \cdot \ddot{\vec{u}} = -\nabla p \cdot \vec{n} \tag{3.1}$$

$$\vec{t} = -p \cdot \vec{n} \tag{3.2}$$

where  $\rho$  is the density,  $\vec{n}$  is the normal vector on the boundary surface,  $u$  is the displacement in this direction,  $p$  is the pressure, and  $\vec{t}$  is the Cauchy stress vector in the solid.

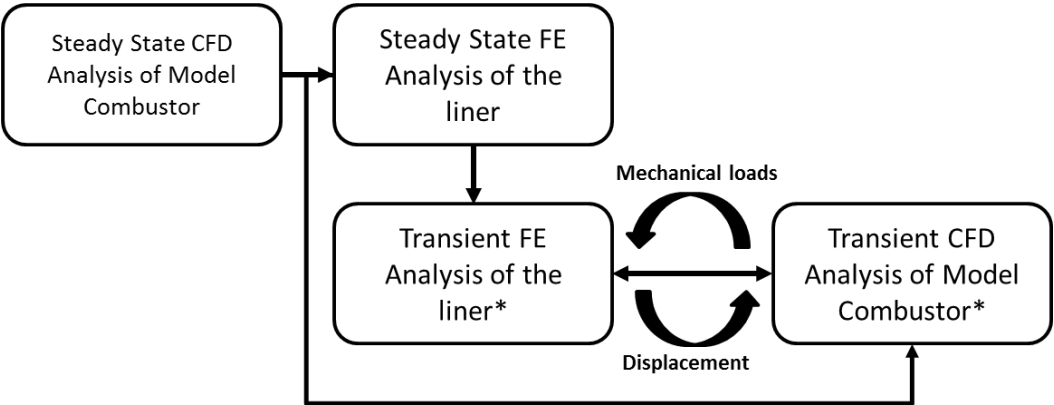


**Figure 3.6. The schematic view of the 2-way FSI numerical setup (\*Steady State results as initial conditions)**

The schematic view of the 2-way fluid structure interaction (FSI) numerical simulation using ANSYS V13.0 Workbench is shown in Figure 3.6. The data from a steady-state solution is fed into the static structural analysis and then to the transient structural and fluid flow. A 2-way coupling between the fluid and structure is obtained by linking the transient modules and then transferring surface loads/displacements across the interface. The total mesh displacement is transferred across the interface by preserving the profile between the two fields, while the total force will be transferred using a conservative formulation. In this way, the quantities from the fluid computations are applied directly on the liner and then the new deformed structure is updated in the fluid simulation; this allows observation of the impact of the wall vibration on the pressure distribution inside the combustion chamber as well as the effect of the modified pressure on the wall vibration. This procedure will be repeated until a converged solution is obtained, then the calculation will continue in the next time step. This procedure has three levels of iterations that are shown in Figure 3.7.

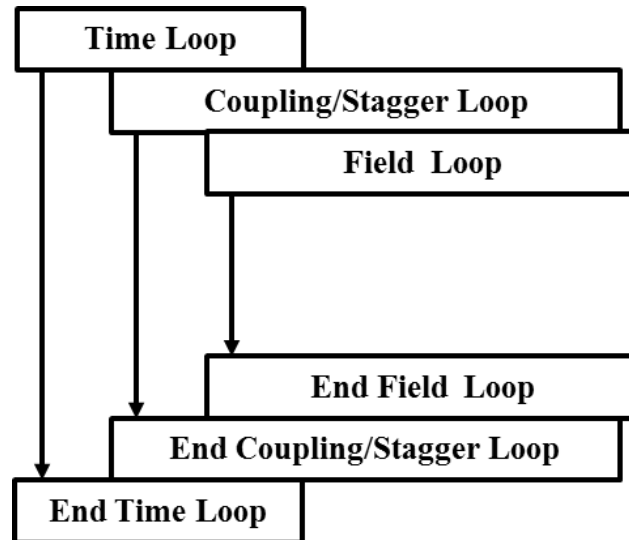


Figure 3.7. The process scheme of the FSI simulation

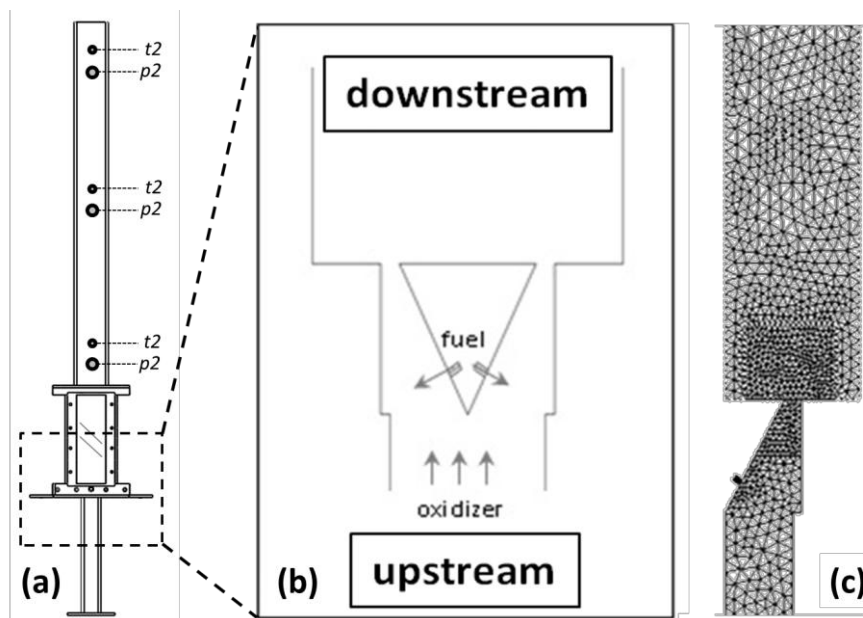


Figure 3.8. (a) Full combustor, (b) close-up section view at the wedge, (c) mesh details

### 3.3.1 Fluid domain: Computational fluid dynamics model

In order to reduce the computational effort, numerical calculations of the reacting flow inside the combustion chamber are done only for the half part of the geometry, which comprises half of the wedge and is 25 mm wide (Figure 3.8). The finite volume mesh consisting of approximately 1.1 M unstructured tetrahedral elements is used. The mesh is refined in the combustion zone and around the fuel inlets. Details about the boundary conditions imposed on the fuel and air inlets are summarised in Table 3.3. The air inlet represents an acoustically closed boundary condition in the model, while the atmospheric outlet acts as an acoustically open boundary condition. These conditions represent the acoustic properties found in the experimental setup. Symmetry boundary conditions are prescribed to the sidewall. Except for the walls downstream of the wedge, the rest are

assumed to be adiabatic. Thermal conductivity of those non-adiabatic walls was considered to be constant; the variation with the temperature was neglected.

The SAS-SST model available in the CFX code is used for the turbulence modelling [22], The Scale-Adaptive Simulation (SAS) is an advanced URANS model which allows better resolution of the turbulent spectrum in unstable flow conditions. This model can change smoothly between LES in regions where the turbulence structure is well resolved and the Shear Stress Transport (SST) model where the unsteady flow is not well resolved. The starting point of the transformation to the SST model is the  $k$ - $\nu_t$  formulation as given by Menter *et al.* [23]. The Burning Velocity Model (BVM) is used for the combustion [24] as a closure term for the combustion source in reacting flow simulations. The reader is referred to the corresponding references for the details of the models [22-26].

The numerical scheme uses a high-resolution advection scheme for spatial and second order backward Euler discretization for time accuracy. Simulations are carried out with a time step of 0.1 ms. At the monitor points the data is stored of the simulations at every time step giving a sampling frequency of 10 kHz, hence the maximum frequency observed is 5 kHz. However, only data up to 1 kHz is presented here. A total calculation time of 0.2 s and residual target value of  $1e-4$  has been achieved.

**Table 3.3. More details about inlet boundary conditions**

	B.c	T (k)	Mixture fraction	Reaction progress	Turbulence (intensity)
Air Inlet	Mass flow rate	293	0	0	5%
Fuel inlet	Normal speed	293	1	0	5%

### 3.3.2 Solid domain: Computational structural dynamics model

Because most of the dynamic coupling between the hot fluid and structure occurs in the region downstream of the wedge, in this simulation only the structure above the wedge is considered, which is shown in Figure 3.3 (b). The wall is simplified to three plates forming half of a duct without quartz glass windows or ports for thermocouples and pressure transducer, however, a rectangular plate with 1 mm thickness is inserted into the flame-box wall on the place of the windows in order to examine the combustion-driven damage mechanisms. The liner of the test rig is modelled as an elastic material (Shell 63 with 4 mm thickness) with the properties representing hot steel at 400°C (Figure 2.9). A total number of 2450 shell elements equally distributed is used for this simulation. Shell63 has both bending and membrane capabilities. Stress stiffening and large deflection capabilities are also included for this type of element. For the basic principles and features of the finite element approximations for structural analysis, the reader is referred to the appendix.

The clamped boundary condition is implemented at one end (at downstream-upstream boundary of the combustor), while symmetry condition is used on side edges. The rest of the geometry is allowed to deform freely depending on the dynamic pressure loads. Mechanical loads, i.e. pressure and shear, are transferred from the CFD domain to structural part at every time step, therefore the same time step as CFD is needed. The direction of loads applied to the geometry can be constant or change and follow the deformed structure. However, surface

loads will follow the structure causing large deformations. By taking this into account the setting for the large deformation in the liner has to be turned on during the simulation. The total calculation real time is 0.2 s.

### **3.4 Lifetime assessment**

Combustion instabilities lead to higher mechanical vibrations of combustion liners at high temperature, and high-cycle fatigue and creep are the two potential failure mechanisms. In this regard, a temperature-structure analysis was performed based on the output of the experiments considering the pressure inside the combustor and temperature profile of the walls as input. The stresses and strains were calculated and used in the lifetime assessment, which includes the fatigue, creep and their interaction using damage summation rule.

#### **3.4.1 Temperature-structure analysis**

The commercial finite element method (FEM) software ANSYS was utilised to perform two 3D FEM analyses; one for the full geometry (a) and one for the specimen geometry (c) only as seen in Figure 3.3. In this manner, a benchmark numerical test was performed to reduce the computation cost. Hereby the full geometry analysis and the specimen geometry-only analysis will be called the full-model and sub-model analysis, respectively. In the full-model, a fully fixed support boundary condition (clamped) at the bottom of the flame-box was applied. This support location represents the scaffolding-like frame that holds the test system as seen in Figure 3.1 (a). And the experimentally measured pressures and surface temperatures were defined as the external data with respect to the dimensions of the geometry. Prior to the computation, the data were mapped and matched on the finite element mesh (point cloud data mapping). The finite element mesh was generated using quadratic volume elements. Two elements were created across the liner wall and the specimen thickness and a finer mesh is used for the welding parts to accommodate the mesh compliance. The temperature-structural analysis was performed to calculate the stress and strain distributions. The applied loads and the boundary conditions are detailed as follows.

In the experiments, the combustion process generates a varying surface temperature and thermal expansion condition at the downstream part that can induce pre-stress effects. Therefore, the assembly of the specimen to the flame-box is designed such that a clearance is present in the housing. This provides some freedom for the attached specimens to slide towards traverse and longitudinal directions. Furthermore, two gaskets (2 mm thick) are accommodated on both sides of the specimen to compensate the third dimension of the volumetric expansion. Hence, the stresses in the specimen are assumed to be mainly covered by the pressure inside the combustor. In the numerical sub-model, the boundary conditions were modelled with an elastic foundation. This elastic support represents the gaskets that sandwich the specimen. Basically, a spring stiffness per unit area was represented by the so-called elastic foundation stiffness (EFS) [24]. EFS was applied on the in-plane and the out-of-plane faces of the support area. This provides resistance to the direction normal to the volumetric expansion of the geometry. In this way, the sub-model can expand due to the

thermal load and can deform out-of-plane direction due to the pressure load. The effects of the temperature and damping were assumed to be negligible for the EFS that is analogical with the gaskets material. As seen in Figure 3.12 and Figure 3.18, the maximum temperature and pressure amplitudes occur at the flame-box region. Since the loads are uniform, constant temperature and pressure load were applied to the specimen model.

### 3.4.2 Phenomenological modelling

Assuming small deformations, the total strain can be described as a cumulative addition of the mechanical strains, which contains the elastic –  $\varepsilon^{el}$  – and inelastic strain –  $\varepsilon^{in}$  – components.

$$\varepsilon^{tot} = \varepsilon^{el} + \varepsilon^{in} = \varepsilon^{el} + \varepsilon^{pl} + \varepsilon^{cr} \quad (3.3)$$

The inelastic strain includes both the plastic (instantaneous) –  $\varepsilon^{pl}$  –, and the creep (time-dependent) –  $\varepsilon^{cr}$  – deformation.

### 3.4.3 Material behaviour and lifing

The elastic behaviour of the material was defined as temperature dependent. The inelastic constitutive theory used in this analysis includes time-independent deformation and time-dependent deformation properties. Prandtl-Reuss stress-strain equations for the time-independent plasticity with a von-Mises yield surface were used. The material is considered to obey the bilinear isotropic hardening model. Norton-type equation was used to model the creep behaviour of the material. The model covers the secondary creep range assuming a long-time equilibrium between the hardening and the recovery mechanics. The equivalent creep strain rate is defined as temperature, stress and time dependent.

$$\dot{\varepsilon}^{cr} = C_1 \bar{\sigma}^{C_2} e^{-C_3/T} \quad (3.4)$$

where  $\dot{\varepsilon}^{cr}$  is the creep rate,  $\bar{\sigma}$  is the applied stress,  $T$  is the temperature [K] and  $C_1$ ,  $C_2$ ,  $C_3$  are the coefficients that include the stress and temperature dependency of the strain rate for the material. Since AlloyX is a creep ductile material, the primary and tertiary stages of creeping are very limited compared to the secondary stage. Thus, the major lifetime consumption due to creep is assumed in the secondary stage. The typical critical creep strain value given is 2%, which is lower than the creep strain at rupture. Hence, creep lifetime is calculated as

$$t_{cr} = \frac{\varepsilon_{critical}^{cr}}{\dot{\varepsilon}_{\Delta t}^{cr}} \quad (3.5)$$

The stress-life relation is potentially applicable to assess high cycle fatigue under the generated stresses well below the elastic limit. However in practice, local plasticity can exist at local discontinuities in the component stress concentration regions [27] in spite of the fact that the stresses obey the elasticity in the net section. Therefore a strain-life relation has been used for the fatigue analysis so that the quantification of the strain defines the dominance of either the elastic or plastic strain component. The material parameters corresponds to fully reversed strain-controlled tests using strain-based approach that satisfies the mean stresses to be near zero. The laboratory-scaled combustor is in atmospheric condition so that there is no

pre-stress or mean pressure exposed to the structure. In such conditions, the cyclic stress-strain behaviour and the strain-life relation is constructed by using the Ramberg-Osgood type to describe the monotonic stress strain behaviour and Coffin-Manson type for the strain life. These equations are given, respectively, by

$$\frac{\Delta\varepsilon}{2} = \frac{\Delta\varepsilon_e}{2} + \frac{\Delta\varepsilon_p}{2} = \frac{\Delta\sigma}{2E} + \left(\frac{\Delta\sigma}{2K'}\right)^{1/n'} \quad (3.6)$$

$$\frac{\Delta\varepsilon}{2} = \frac{\Delta\varepsilon_e}{2} + \frac{\Delta\varepsilon_p}{2} = \frac{\sigma'_f}{E}(2N)^b + \varepsilon'_f(2N)^c \quad (3.7)$$

where  $K'$  is the cyclic strength coefficient [MPa],  $n'$  is the cyclic strain hardening exponent,  $\sigma'_f$  is the fatigue strength coefficient [MPa],  $b$  is the fatigue strength exponent,  $\varepsilon'_f$  is the fatigue ductility coefficient and  $c$  is the fatigue ductility exponent. The elastic and plastic strain terms are included in both equations. In strain-life approach, the total strain amplitude is decomposed into elastic and plastic components of which the curves are formed using the parameters from the literature data [28].

Creep, fatigue and fatigue/creep interaction are potential damage mechanisms for the combustion section components where the components are exposed to cyclic pressure levels at elevated temperatures. Depending on the operation map, a transition from stable to unstable combustion can be activated, in which the combustion dynamics becomes detrimental for the mechanical integrity. As the thermo-acoustic phenomenon appears in the system, the structural vibrations are amplified while the temperature level obeys the initial design scenario. Therefore, the emphasis in this work has been devoted particularly to the fatigue damage leverage in the combustor structure due to the generated pressure oscillations in the unstable combustion. Even though the fatigue damage shows up noticeably, the superimposing creep damage remains throughout the operation. The cycle- and time-dependent two mechanisms were assumed to be interacted linearly in the system, therefore ASME Code Case N 47 [29] is used under fairly conservative prediction for fatigue-creep interaction life assessment. The basis of the assumption is to linearly accumulate, as the life fractions include the cyclic dependent fatigue, so-called Miner's law, and time dependent creep, so-called Robinson's rule (Palmgren-Miner cumulative damage rule),

$$D_{tot} = D_f + D_c = \sum_{i=1}^{n_f} \frac{n_i}{N_{f(i)}} + \sum_{j=1}^{n_c} \frac{t_j}{t_{r(f)}} \quad (3.8)$$

where  $n_i$  is the number of applied cycles and  $N_f$  is the number of cycles to fatigue at  $i$ th stress or strain range level,  $t$  is the service time and  $t_r$  is the creep stress level at  $j$ th stress level and  $n_f$  is the number of stress or strain range levels and  $n_c$  is the number of stress levels. In the linear accumulation method the cyclic and time dependent damage fractions are computed independently and their interaction is only empirically considered in  $D_{tot}$ .

### 3.5 Results

Prior to the investigation, a stability map of the test combustor setup, described in section 3.2, was produced experimentally to decompose the unstable and stable operating points, and in the envelope four extreme points, so-called cases, were chosen for further investigation.



The pressure and temperature inside the combustor and the liner surface temperature measurements for these cases are shown. Next, two cases, which include the highest (unstable) and lowest (stable) loads from the aforementioned cases were chosen. The coupled FSI analysis as explained in section 3.3 was performed and results are compared to the experimental results. Next, the results of the life assessment including fatigue and creep aspects are shown for the worst case. Note that the combustor was heated up gradually and progressed to the desired operating point to prevent possible thermal shocks in the start-up periods.

### **3.5.1 Combustion and acoustic characterisation**

A series of experiments were performed ranging from 40 to 60 kW thermal powers and from 1.2 to 1.8 air/fuel ratios in order to define the stability and instability limit of the combustor system. The stability map is depicted in Figure 3.9. The transition in the air/fuel ratio from 1.6 to 1.4 triggers the instability of the system. Although the acoustic volume of the combustor is unchanged, decreasing the air ratio in the mixture increases the temperature leading to higher acoustic eigenfrequency. Hence, the closed feedback loop for the instability is satisfied in these regimes. Four extreme operating conditions are selected that are the corner points of the stability map. The test cases are listed in Table 2.5. The pressure spectrum of the unstable and the stable combustion is presented in Figure 3.9. Unstable cases, Case6012 and Case4012, show a distinct peak at fundamental quarter wave mode frequency. However, Case6012 has the higher pressure peak compared to Case4012. The higher-harmonics of the first peak with comparably small amplitudes were also generated by the instability due to the presence of non-linearities at limit-cycle oscillations regime. The temperature of the flue gas induced by the combustion depends on the operating points. Thus, as seen from Figure 3.9, the limit-cycle oscillation frequencies, at which the pressure peaks are present, are not fixed but fall within a 5 Hz range at the investigated operating points, which produce combustion instabilities (Case4012 and Case6012). The left bottom and right upper operating points from the stability map (Figure 3.9) are selected for further investigation, which shows the highest and the lowest pressure amplitudes: Case6012 (unstable) and Case4018 (stable).

The experimental results show an apparent temperature gradient along the liner wall, depicted in Figure 3.10, where the non-contact measurements have been performed using a thermographic camera. The temperature levels of the unstable cases, of which the air/fuel ratio is 1.2, are observed to be generally higher compared to the stable test cases with a higher air/fuel ratio. The higher temperature levels are generated due to a greater fuel portion fed into the system. The unstable combustion cases produced a linear-shaped fluid temperature distribution along the liner and gradually decreased towards the exit of the downstream part, so that the trend is also in agreement with the wall temperature measurement between t2 and t4 locations. The temperature is decreased about 15% in Case4012 and 12% in case Case6012 from location t2 to t4 measurement location. Even though the deviation between these two cases at t2 location is about 3.2%, at t4 location this deviation has been increased up to 6.6%. The wall temperature at the flame-box region was found to be the highest for these test cases and nearly uniform temperature distribution was observed. This can indicate a shorter flame

length, having a wrinkled shape and occupying a large space encapsulated in the flame-box region due to the dynamic combustion. On the other hand, in the stable combustion cases there was not neither a temperature evolution trend with respect to the liner length, nor a proportional deviation at the measurement locations.

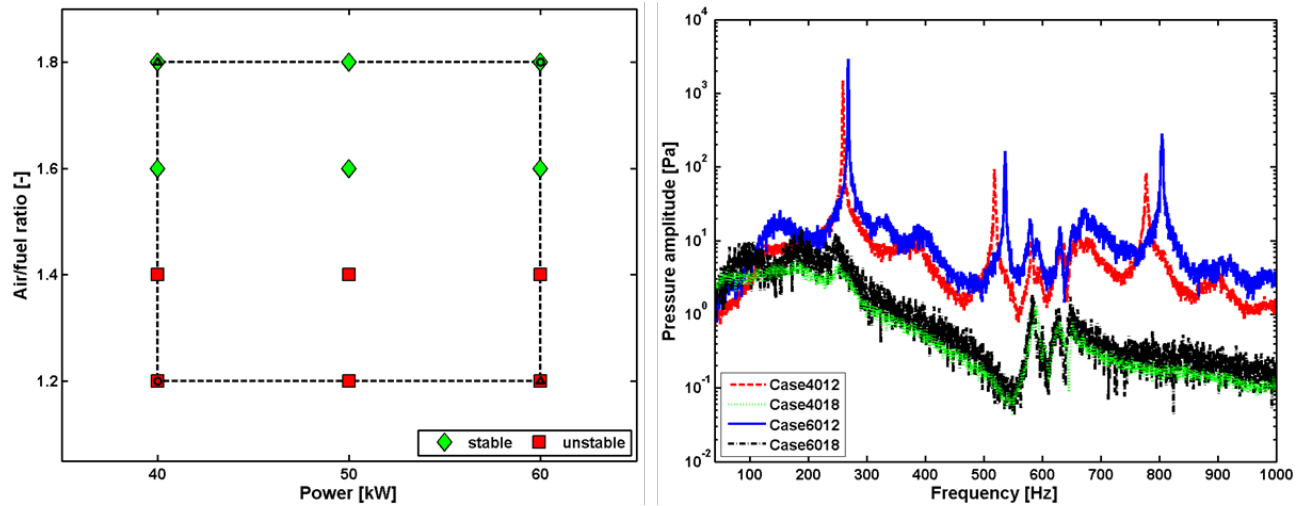


Figure 3.9. Stability map (left) and pressure spectrum at p2 sensor location (right) – (EXP)

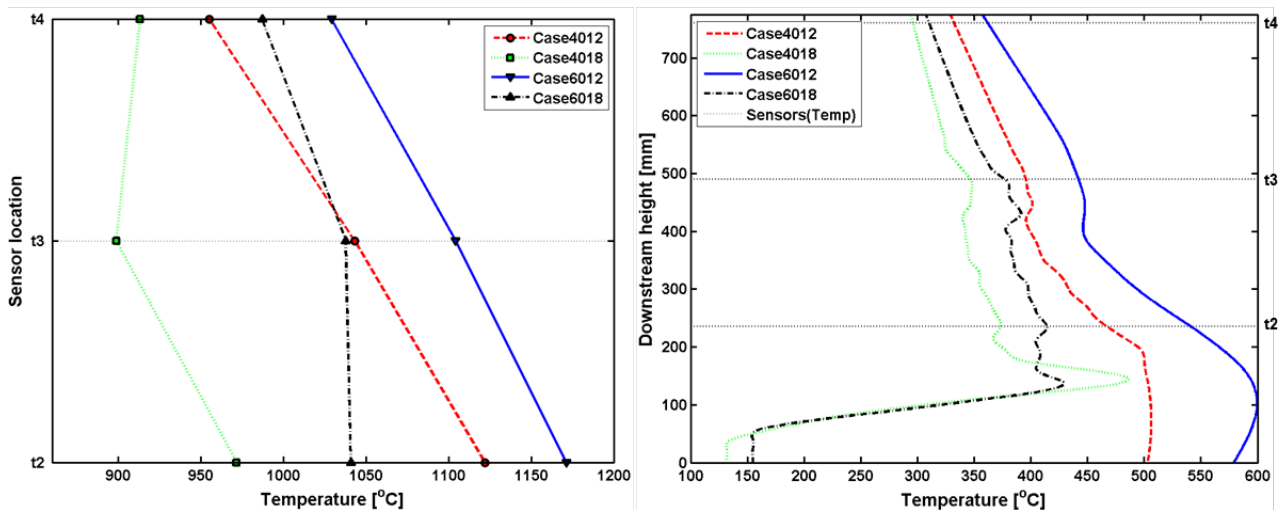


Figure 3.10. The fluid temperatures at sensor locations (left) and the wall temperatures at mid-width (right) – (EXP)

A temperature jump takes place at about the mid-location of the plate after the ignition and progresses upwards and downwards at the flame-box region. The combustion process carries the heat towards the exit of the liner that gradually increases the liner temperature until a balanced state is reached. In Figure 3.11, the contour-lines of the temperature can be seen from the thermal image during the combustion, in which the trace of the burning gases at higher temperature forms a conical shape. During the experiments, it was observed that some of the operating points showed a dynamic system characteristic including stable and unstable combustion regimes. However, after a time delay the operating point revealed one combustion regime, either stable or unstable. This transient behaviour occurrence is attributed to the nonlinear characteristics of combustion instabilities whereby the sequential direction of the investigated test points (initial operation settings, air-fuel (equivalence) ratio and power as in

this work) influences the transient combustion behaviour [30]. To ensure reliable tests, the data acquisition is triggered as the slope of the temperature evolution curve at the representative  $T_{\text{sample}}$  measurement point becomes nearly constant at about zero (Figure 3.11).

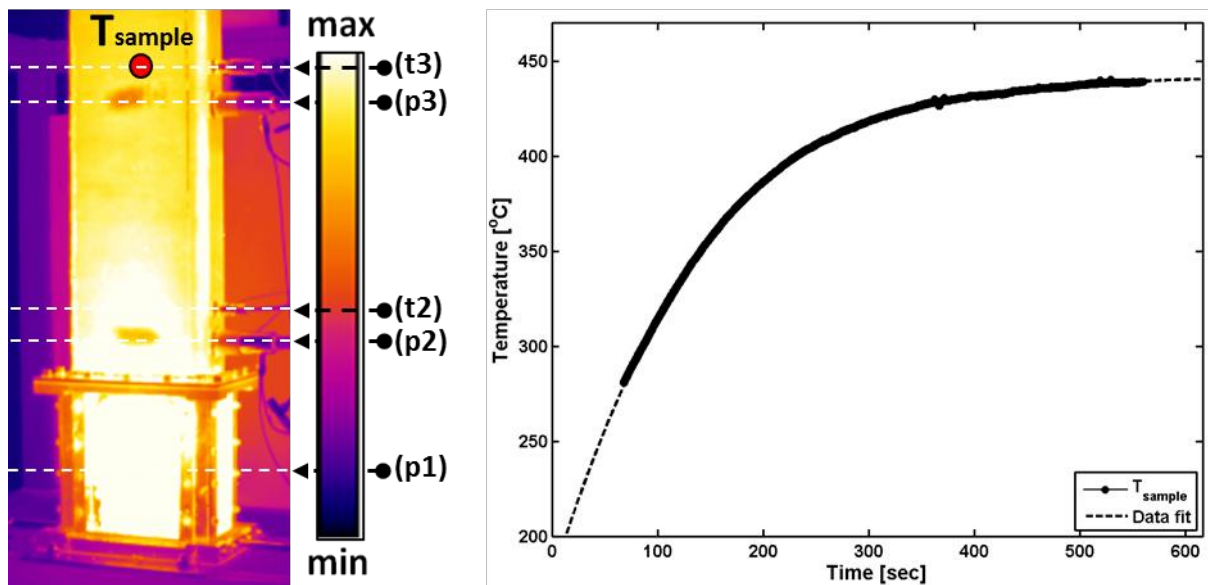


Figure 3.11. The IR camera measurement and the temperature evolution at  $T_{\text{sample}}$  location

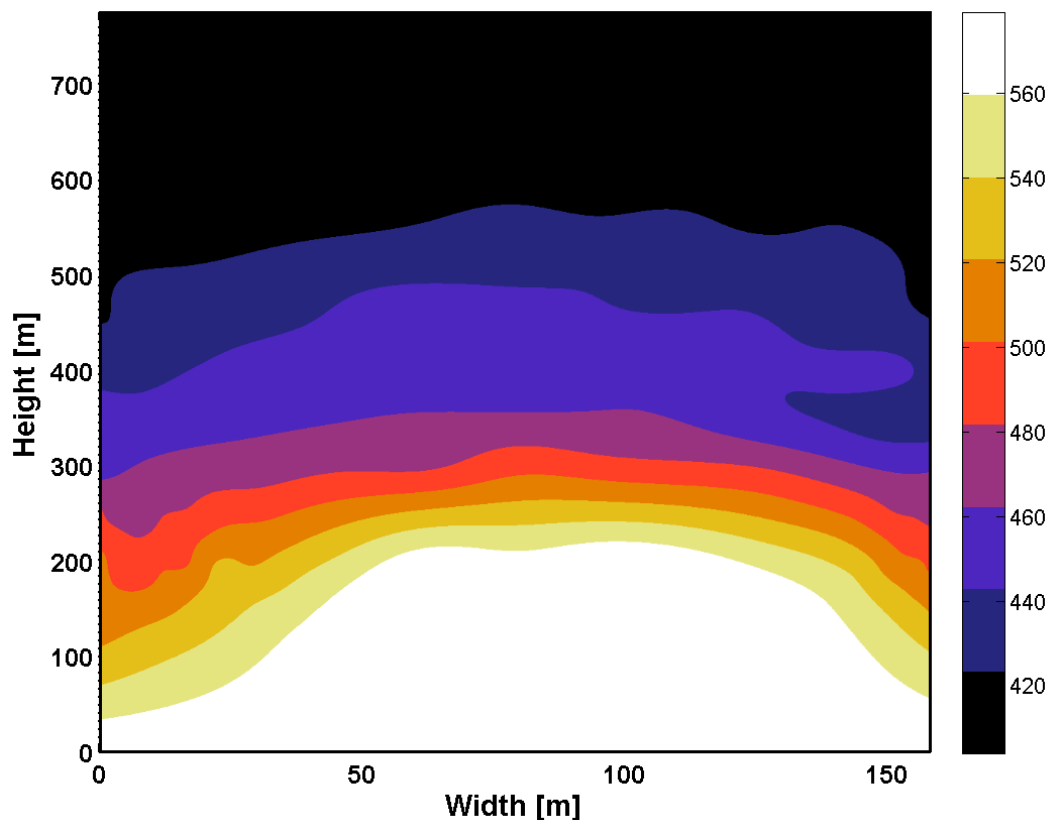
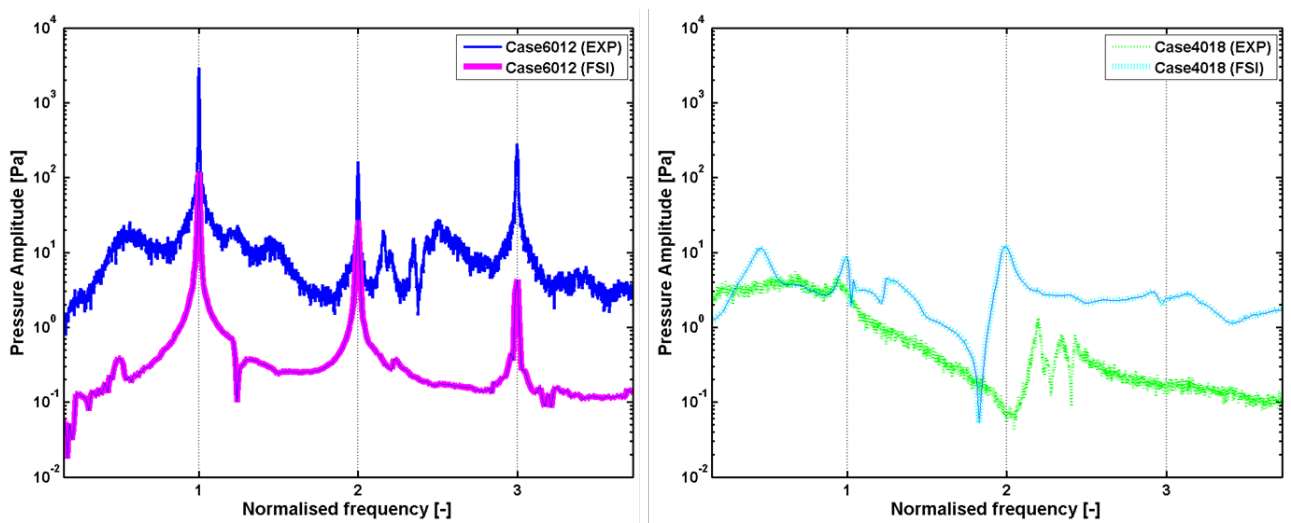


Figure 3.12. The wall temperature [°C] profile OP6012 (EXP)

The wall temperature profile at the downstream (flame-box and liner) of combustor for Case6012 is depicted in Figure 3.12, which is post-processed to avoid the high reflective surfaces zones, which are advantageous for high intensity LDV measurements. The

asymmetry of the temperature distribution in the width direction can be due to the dynamic combustion process. This temperature profile is later used for temperature-structure analysis for lifing.

In Figure 3.13, the pressure spectra from the experiments and FSI simulations are compared for stable and unstable cases and the data obtained from the graph are listed in Figure 3.4. In the figure, the frequency axis is normalised with respect to the measured and simulated first acoustic mode of the combustor ( $f/f_1$ ). Hence, the deviation in the FSI geometry and relative heat losses can be suppressed to enhance the visibility of the comparison. Similar to the experiments, a dominant peak pressure at the first acoustic eigenfrequency was obtained and the higher-harmonics of this peak-value were also predicted.



**Figure 3.13. Pressure spectrum: comparison of (EXP) vs. (FSI)**

However, this comparison shows a distinct difference in the magnitude of instability, which is mainly due to over-prediction of the temperature in the CFD simulation. Furthermore, there are some more limitations for the FSI simulation that potentially restrain the convergence to the experimental results. The experimental measurements have been performed in such a way that the measurement time is sufficiently long to capture the real data, however in the FSI simulations there is a physical time limit to reduce the computational cost and this numerical duration is not always sufficient to reach the peak amplitude as observed in the experiments. The over-prediction of gas temperature can be explained by higher speed of sound and consequently higher acoustic eigenmodes. In the simulation, using a mean temperature that assumes the liner as an isothermal structure with a constant thermal conductivity may be one of the reasons for this deviation from the experiment.

**Table 3.4. Comparison in the pressure spectrum (Cas6012): EXP vs. FSI**

	Characteristic frequency [Hz]	Pressure amplitude [Pa]	SPL [dB]
EXP	268	2894	163
FSI	314	119	136

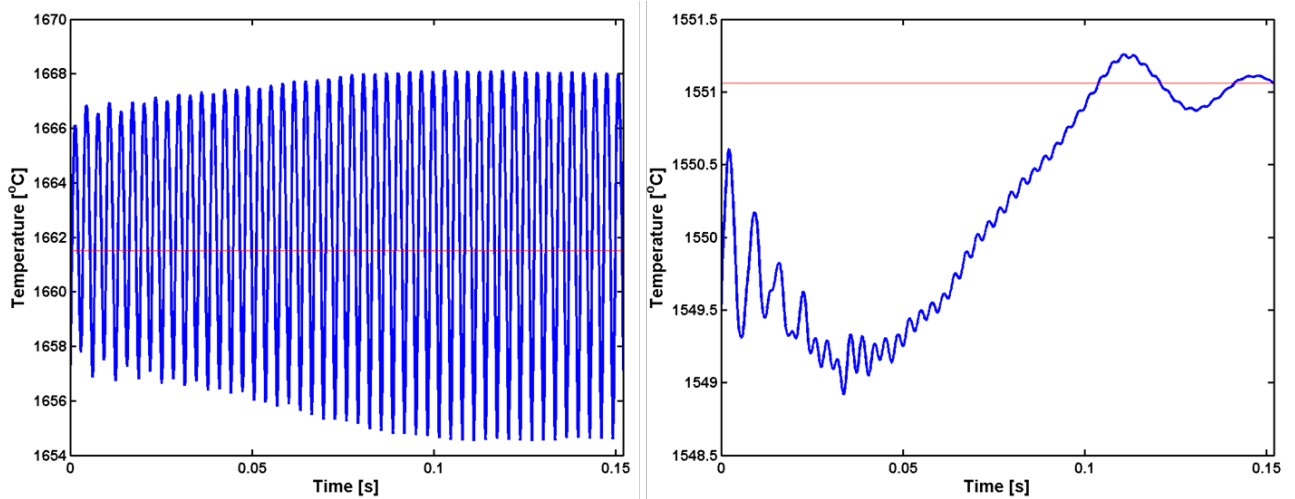


**Figure 3.14. The time evolution of temperature of the self-oscillation combustion for unstable ‘Case6012’ (left) and stable ‘Case4018’ (right) cases at ‘p2’ location – (FSI)**

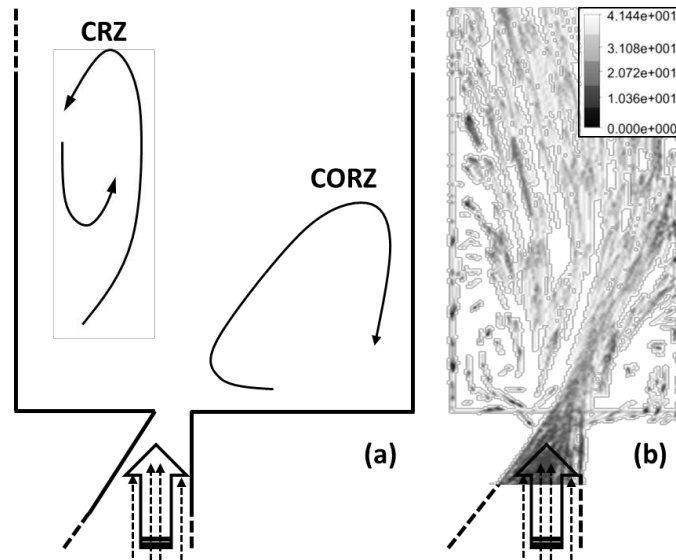


**Figure 3.15. Schematic illustration of the flow patterns (a), and the vector plot of the velocity [m/s] field in a section close to the wedge depth-wise (b) - (FSI)**

Figure 3.14 (left) displays the increase in the temperature during the combustion front propagation, indicating that the combustion is in an unstable oscillatory manner. Temperature is one of the most important variables determining the stability characteristics of the combustor. A slight change in temperature leads to a sudden change in acoustic flow oscillation. As temperature increases, due to the increased flame speed, the flame penetrates into the corner recirculation zone and flashes back (Figure 3.16). As seen in the figure, a central recirculation zone (CRZ) is established in the wake of the centre body that is a form of vortex break down, which is associated with intense swirling-type flow compared to swirling strength [31]. It acts as a flame-holder in the centre of the flow and stabilises the combustion process in a compact region within the downstream. In this zone, the recirculating hot gases mix with the incoming air-fuel mixture. Furthermore, corner recirculation zones (CORZ) are formed as a result of a sudden expansion in the combustion area, which facilitate recirculation of the combustion hot gases near the liner walls of the downstream duct, and contribute to the

ignition of the incoming fresh gases. As a consequence, the flame is stabilised by both the corner recirculation zone (CORZ) and the central recirculation zone (CRZ) that represent a compact enveloped configuration. The temperature oscillates around 1661.5 °C with  $\pm 6.5$  °C. Figure 3.14 (right) shows the simulated temperature behaviour in the stable combustion, where the temperature amplitudes tend to level off at 1551 °C with decaying trend of the reversal amplitudes.

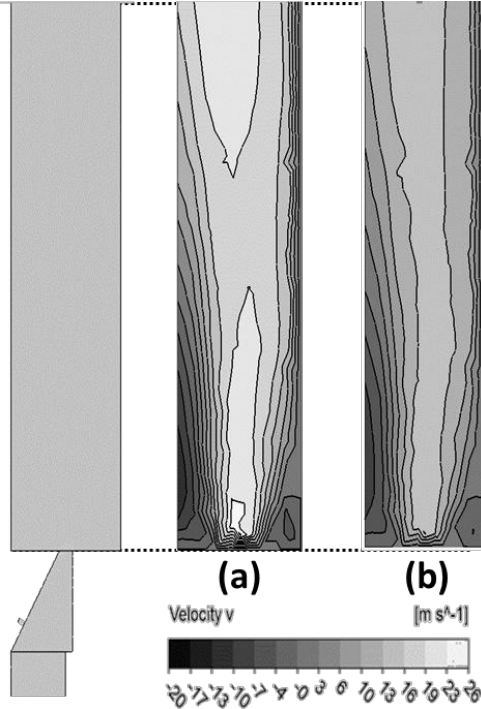


Figure 3.16. The contour plot of the velocity [m/s] field in the middle of the combustor depth-wise: Case6012 (a) and Case4018 (b) - (FSI)

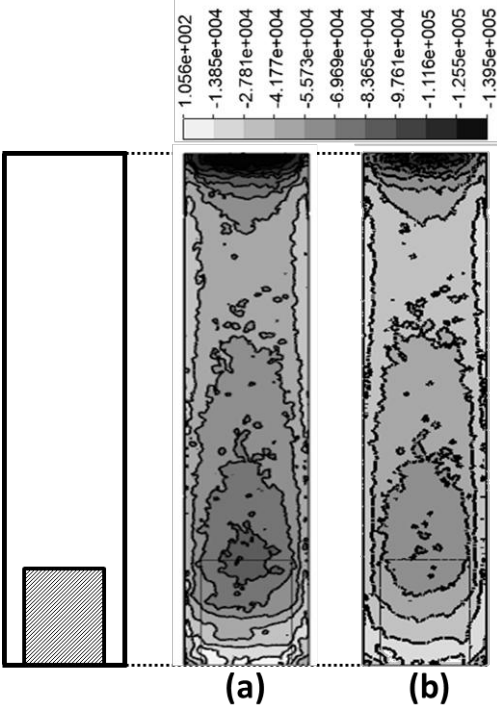


Figure 3.17. The heat flux [W/m<sup>2</sup>] on the hot walls: Case6012 (a) and Case4018 (b) - (FSI)

During the combustion process, heat is transferred from the hot flame by radiation and convection to the liner. However, the radiative heat exchange highly depends on the distance between the flame and the liner and also on the absorption of the colder combustion gases in between. Figure 3.17 depicts the instantaneous heat flux from the liner in both stable and unstable condition. As expected, heat flux is more uniformly distributed on the liner in the stable flame condition due to having a stretched flame.

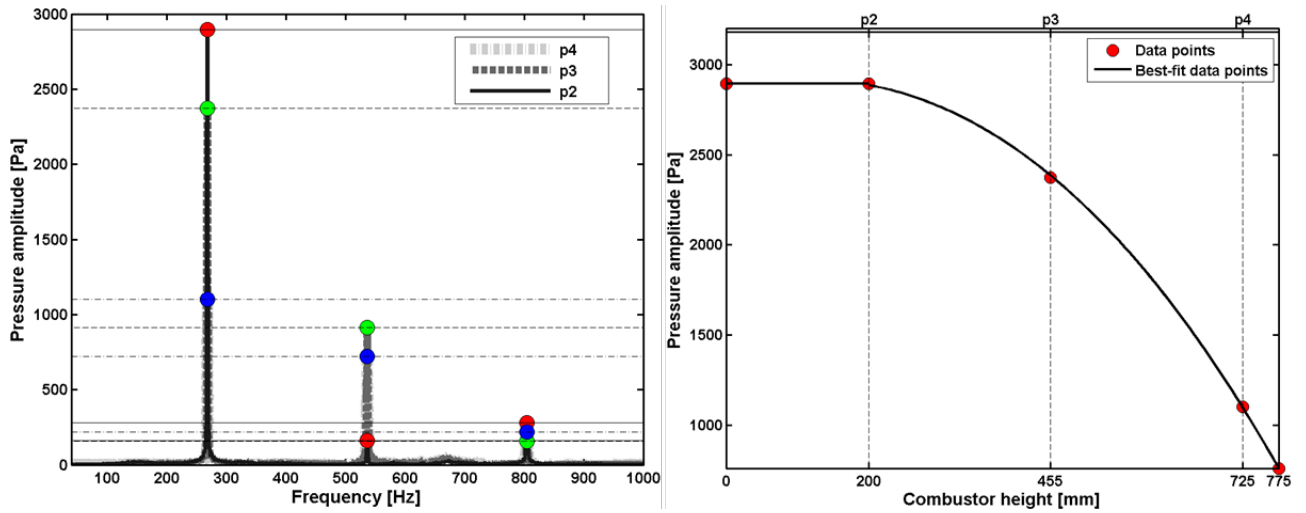


Figure 3.18. Pressure profile for Case60120 - (EXP)

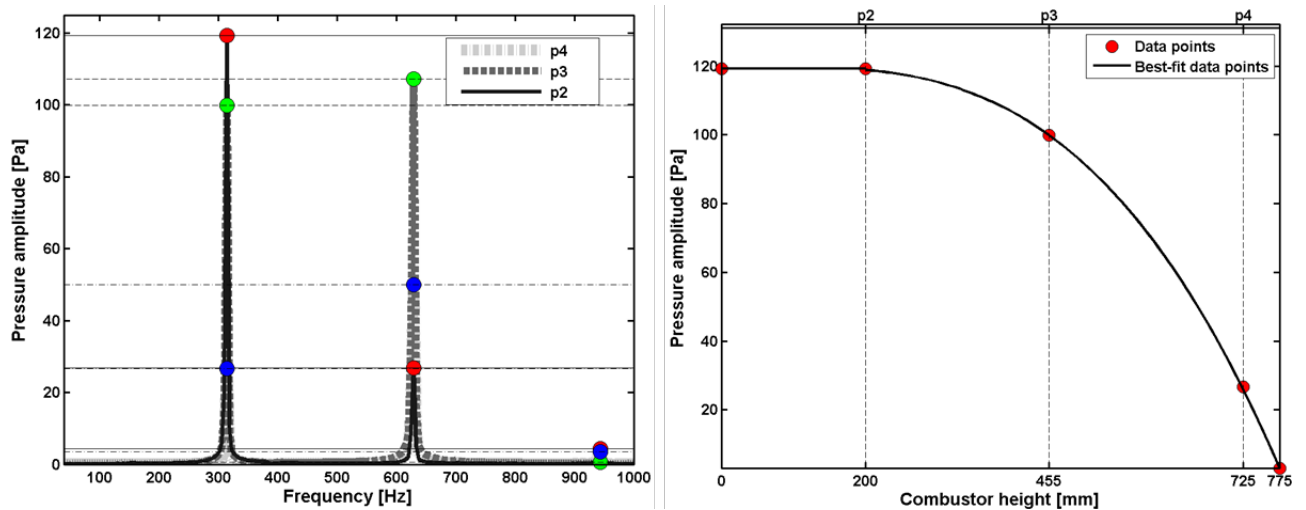


Figure 3.19. Pressure profile for Case60120 - (FSI)

Figure 3.18 and Figure 3.19 shows the instantaneous axial pressure distribution at the LCO frequency along the combustor downstream for the experiments and FSI, respectively. From the previous experiments in the combustion system [32], the pressure at the flame-box region was observed to be constant and equal to the pressure measured at 'p2' sensor location. Thus, the pressure kept constant from 'p2' till the wedge in the figures. Furthermore, since there are three pressure sensors along the downstream, the pressure data between the 'p4' location and the outlet of the downstream was extrapolated till zero pressure amplitude in compliance with the best-fit data points as seen in the figures. The pressure anti-node at the inlet and the node at the outlet of the combustor confirm the open-closed acoustic boundary condition. The pressure amplitude is decreasing along the combustor and the maximum

pressure occurs right above the bluff body, which is matching the theoretical location of maximum pressure for the first quarter wave. Note that it is assumed that acoustic pressure reaches zero at the open end, which is the outlet of the combustor. However, there is some portion of sound radiation into the fluid outside that disintegrates from the sound reflected back down the combustor. So, the pressure drops closer to zero till the wave is kept within the combustor structure bounds but does not reach zero. Therefore, an extra final layer of fluid at the outlet is considered to approximate the effect of radiation. Hence, an end-correction is included to the standard theoretical formula for the calculation of the acoustic eigenfrequencies of an open-closed end volume. This end-correction includes an effective length, in which an extra length is added to the outlet of the volume to consider the actual position of the pressure node [33]. The effective length, which is longer than the physical length of the downstream of the open-ended combustor, leads to lower acoustic eigenfrequencies. For the first mode, quarter-wave acoustic mode (100), the equation reduces to  $f=c/4L_{eff}$ , in which  $L_{eff}$  is the effective length. The effective length of a closed-open end tube is given as [34];  $L_{eff} = L_x + (R_r)(a_{tube})$ , in where  $R_r$  is the radiation resistance that is taken as 0.85 and  $a_{tube}$  is the radius of the tube opening. In fact, in this work a rectangular volume is considered; therefore the area of the combustor cross section corresponds to a tube opening cross section with the same area. Hence, an equivalent radius is obtained to calculate the effective length.

The standard theoretical formula to calculate acoustic eigenfrequencies considering a closed-open end rectangular volume (acoustic cavity) with acoustically hard walls is given by the following equation [35]

$$f_{ijk} = \frac{c}{2} \sqrt{\left(\frac{i}{2L_x}\right)^2 + \left(\frac{j}{L_x}\right)^2 + \left(\frac{k}{L_x}\right)^2} \quad (3.9)$$

where  $c$  is the speed of sound,  $i, j, k$  are the numbers to specify each of the acoustic modes of the volume, which is composed of the three length directions ( $L_x, L_x, L_x$ ) associated with  $x, y$  and  $z$  coordinates, respectively. The acoustic eigenfrequency results for the quarter-wave acoustic mode are listed in Table 2.6 and supported by a separate FEM analysis using shell elements and analytical calculation assuming a mean temperature ( $^gT_{Case6012}$ ) along the downstream. In the table, the superscript ' $\dagger$ ' is used to identify the results that are scaled such that the end correction is considered. The end-corrected results of FEM and analytical results show good agreement, on the other hand, the FSI result is in fair agreement, which can be attributed to the consideration of the physical length of the combustor instead of the effective length. However, if the end-correction is applied to the FSI result, the deviation is reduced reasonably.

**Table 3.5. Characteristic acoustic frequencies [Hz] in the combustor at  $^gT_{Case6012}$**

Case Code	Experiment	FSI	FSI $\dagger$	FEM	FEM $\dagger$	Analytical	Analytical $\dagger$
Case6012	268	314	294	288	270	300	281

In the investigation of thermo-acoustic instabilities, not only combustion dynamics but also the structural dynamics are crucial since the dynamic combustion takes place in a



vibrating structure. A structural modal analysis was carried out to observe if the characteristic frequency or its harmonics coincide with a structural eigenfrequency that can trigger a coupling between the acoustics and the structure. Hence, two experimental modal testing methods at room temperature ( $T_{\text{room}}$ ) and FEM analysis at room temperature and at the operation temperature corresponding to the Case6012 ( ${}^wT_{\text{Case6012}}$ ) were performed. The experimental modal testing methods include the shaker testing and impact testing. In the shaker testing, a shaker is used to excite the structure at one point while the LDV is moved from one point to another in the measurement grid. The data is obtained from the auto-spectrum of the LDV signal that is averaged over the measurement grid points. In impact testing, an accelerometer is placed at one point and the structure is impacted at the points over the measurement grid. The signal is averaged over the impact grid points. The equipment details are described in section 3.2.2. Experimental modal testing is not feasible during the combustion operation due to the hot walls of the structure. Therefore, the results of the two testing methods are averaged (Avg-Testing) and scaled down with respect to the wall temperature,  ${}^wT_{\text{Case6012}}$ . This calculation is performed on the basis of the proportionality of the structural eigenfrequencies to the square-root of the elastic modulus [35], which is temperature dependent, as described in section 3.2.3.

**Table 3.6. Structural eigenfrequencies [Hz] of the combustor**

Mode	Shaker Testing ( $T_{\text{room}}$ )	Impact Testing ( $T_{\text{room}}$ )	Avg-Testing ( ${}^wT_{\text{Case6012}}$ )	FEM ( $T_{\text{room}}$ )	FEM ( ${}^wT_{\text{Case6012}}$ )
Bending ( <i>b1</i> )	125	125	109	126	110
Torsional ( <i>t1</i> )	534	534	466	437*	384*
Plate ( <i>p1</i> )	639	640	558	633	557
Bending ( <i>b2</i> )	645	645	562	532*	468*
Plate ( <i>p2</i> )	673	673	587	671	590
Plate ( <i>p3</i> )	744	742	648	750	660
Torsional ( <i>2nd</i> )	764	765	667	761	669

The experimental and numerical results for the structural eigenfrequencies of the combustor are presented in Table 3.6. The numerical results were obtained by a FEM analysis of the full combustor model using volume elements. The results of the two experimental modal testing methods match very well. Besides, the experimental and numerical results agree fairly well except the modes marked with superscript '\*'. These modes are highly under the influence of the corner-welds used to form a rectangular cross section made by combining two L-shaped profiles. The welds behave like stiffeners and the increased stiffness reduces these eigenfrequencies. The corner welds are not included in the numerical analysis, since the corner-weld volume is not homogeneous over the combustor length that challenges the characterisation of the welds. By comparison to Table 2.6, none of the structural eigenfrequencies are matching with the characteristic frequency observed at the limit-cycle regime, which implies that the source of the peaks at this frequency is structure independent.

Apart from this, the first three plate modes manifest themselves, as observed in Figure 3.9 (pressure spectrum), right after the first higher-harmonic of the characteristic frequency (536 Hz). This indicates that the plate modes interact with the acoustic waves inside the combustor due to the expansion and contraction motion. In addition to the cyclic pressure oscillations due to thermo-acoustic instabilities, the fatigue damage can be enhanced due to the motion of the plate modes.

To obtain pressure fluctuations inside the combustion chamber, several locations along the length of the combustor are monitored, which are shown in Figure 3.1. In this figure, 'p1' to 'p4' are representing the location of the pressure transducers, while 't1' to 't4' are standing for thermocouples. As can be seen in Figure 3.20 (left) the instability growth mechanism is captured by the numerical model. The oscillation grows till about 0.1 s and then it saturates and reaches fixed mean amplitude of oscillation (saturated). The growth rate of the amplitude of pressure fluctuations is calculated and shown in Table 3.7. As can be seen, the growth rate (i.e. 'b') is changing depending on the location of the pressure transducer. It is also representing an alternating increase and decrease in the amplitude of the growth function (i.e. 'a and b') along the combustor pointing to the presence of the pressure nodes. The actual pressure growth at one test case is hard to measure experimentally since the combustor is gradually progressed to reach the corresponding operating point either from another operating point or start-up period. Thus, the actual energy generated to grow the instability will be suppressed due to the existing stored energy inside from the previous operating point. However, characterisation of the pressure growth is important for the life assessment, since the contribution in the lifetime consumption with several occurrences of instability can be high enough. Therefore, the growth function obtained from fitting on the FSI pressure data is used to define the pressure growth of experiments. The curve obtained by the function is extended till the measured pressure amplitude. The area between upper and lower boundaries is the generated energy to create the certain pressure oscillations at the limit-cycle regime. Together with the duration of the pressure oscillations, the growth of the oscillations also contributes to the lifetime consumption of the structure.

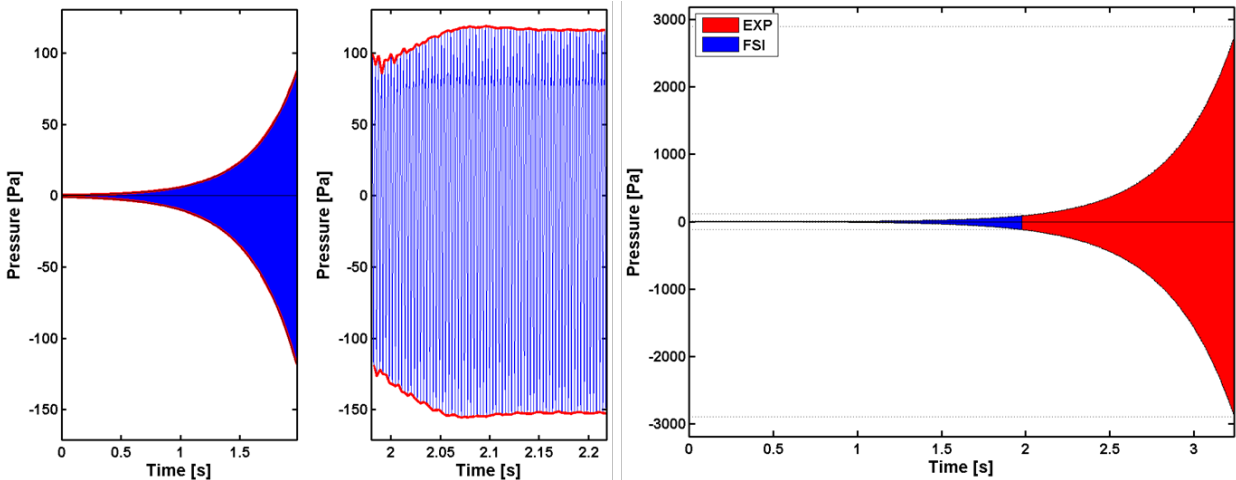


**Figure 3.20. Growth of unsteady pressure predicted by FSI (left) and the extrapolation of the growth from FSI to EXP pressure amplitude**

**Table 3.7: Growth rate of pressure signal during LCO (Growth function =  $ae^{bt}$ )**

Pressure sensors	a	b
p2	91.89	2.66
p3	165.7	3.823
p4	56.88	4.258

### 3.5.2 Life assessment

Initially, a numerical test was carried out to compare the full-model and the sub-model results (described in section 3.4.1). In the analysis, the stress and strain distribution on the specimen geometry was found to be identical for the two numerical tests, which implies the high stiffness of the flame-box structure. Thus, a further investigation was performed in the sub-model in order to reduce the computational cost. The deviation in the temperature and the pressure amplitudes of the corresponding 't2'/p2' locations and the flame-box region are experimentally observed to be practically imperceptible so that a constant temperature and pressure are applied on the specimen in the numerical analysis. The measured temperature and pressure for Case6012 at 't2'/p2' locations are 601.5 °C ( ${}^wT_{\text{Case6012}}$ ) and 2894 Pa ( $P_{\text{Case6012}}$ ), respectively. However, the measured pressure at  ${}^wT_{\text{Case6012}}$  was not sufficient enough to exhibit creeping of the material as observed in the analysis. Therefore, a numerical test pressure was set to  $P_{\text{Case6012}} \times 10^2$ , which leads to the generation of creep strains. The details of the analysis are described in the following paragraph.

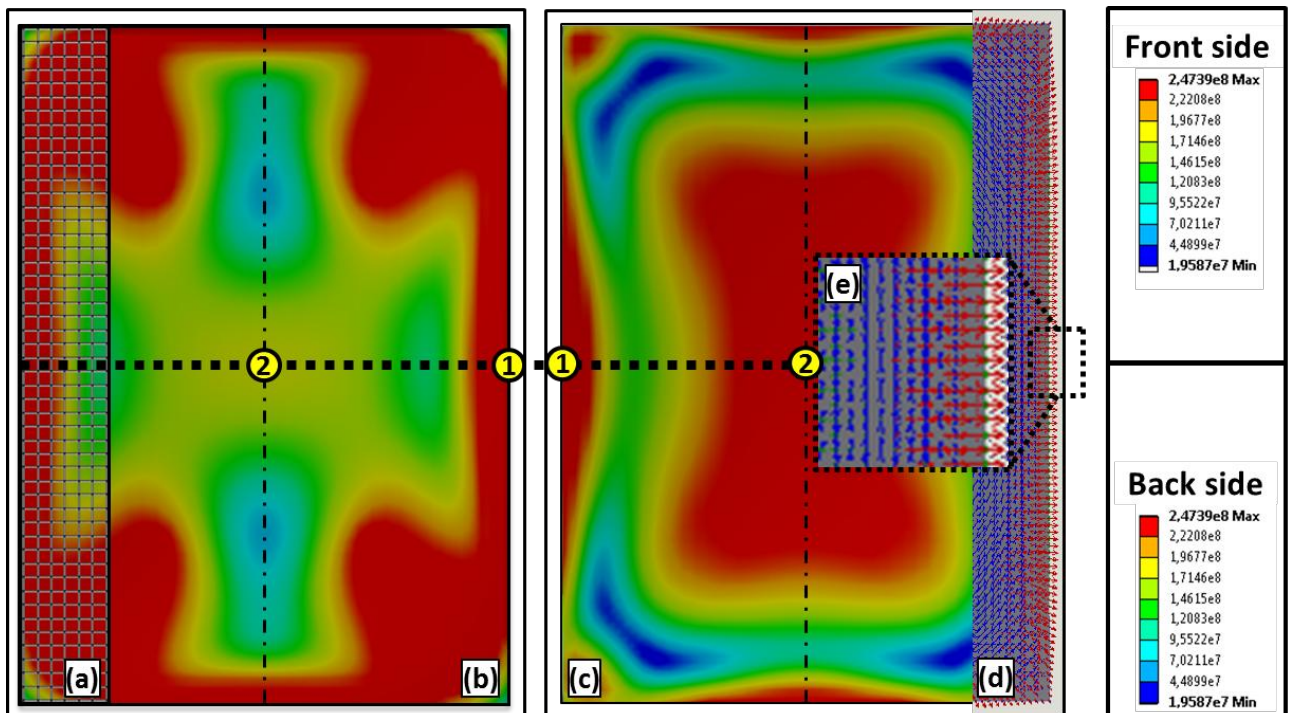


**Figure 3.21. Stress distribution at the front (b) and back sides of the specimen**

The stress-strain distribution of the sub-model was calculated by the temperature-structural analysis presented in Figure 3.21. The behaviour of the structure exposed to temperature and pressure was analysed for 50000 hours by using 15 time steps (1e-5, 0.1, 1,

10, 100, 1000, 2000, 5000, 10000, 15000, 20000, 25000, 30000, 40000, 50000 hours). In the figure, the FEM mesh (a), the stress distribution at the front (b) and back side (c) of the specimen, the principal stress directions (d), the zoomed view (e) are depicted. The results show that the out-of-plane stresses are concentrated near the long edge sections and the maximum principal stress directions in that region, which are indicated with red arrows, are aligned outward in the transverse direction. Assuming that the damage occurs at the stress concentration location and subsequently cracking takes place perpendicular to the maximum principal stress direction, the results imply that this region, the so-called hot spot, is the lifetime limiter, therefore the lifing calculations are based on this consideration. Note that the specimen motion is cyclic due to the pressure oscillations so that the front and the back side exchanges the stress distribution within each cycle.

In Figure 21, the strain distributions on the half-width of the specimen at the front and the back sides are presented. The numbered points are indicated in Figure 20 as (1) the edge and (2) the centre of the specimen. The creep strain amplitudes are the highest at the edge locations of the specimen at both sides since the stress concentration is present. The creep strains sharply decay towards the centre of the specimen from the edge due to the stress profile. However, the creep strains at the back side are developed again due to the tensile-type stresses, while the strains at the front side vanish. On the contrary, the elastic strains spread through the body more smoothly, mainly concentrating at the centre and the edge. Starting from the centre location, the competition between the front and back sides is won by the back side tensile-type stresses reaching its maximum strain amplitude again at the edge. The plastic strains are localised at the edge location and die down sharply with respect to the width of the specimen. Comparably low amplitude plasticity is induced at the back side at the centre; however, the growth in the strain profile was kept limited.

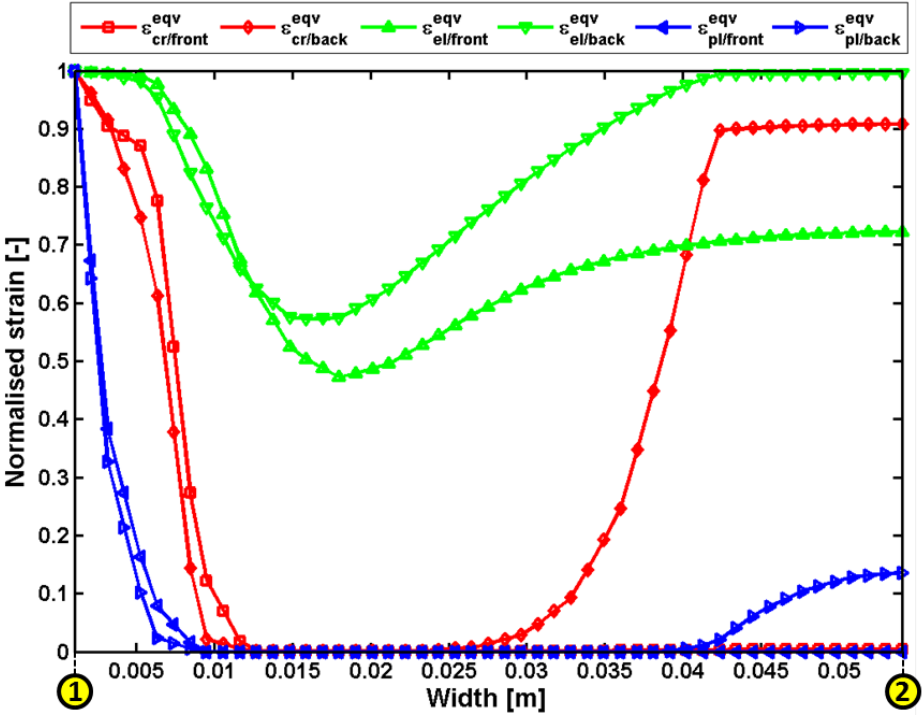


Figure 3.22. Strain distribution on the half-width of the specimen

The creep and fatigue lifetime of the critical location are calculated using the approaches described in section 3.4.3 and results are presented in Table 3.8.

**Table 3.8. Predicted creep and fatigue lifetime**

Pressure Level	$P_{\text{Case6012}} \times 10^2$	$P_{\text{Case6012}} \times 10^1$	$P_{\text{Case6012}}$
Creep lifetime [hours]	74.03	$3.30 \times 10^4$	$1.05 \times 10^6$
Fatigue lifetime [cycles]	$5.09 \times 10^7$	$1.29 \times 10^{10}$	$3.87 \times 10^{12}$

The main life-threatening mechanism is driven by the creeping process. Another important point is that the creep and fatigue lifetime is essentially dependent on the pressure and temperature levels. Transition from stable combustion to unstable regime brings about more than ten times higher pressures, whereas the temperature change remains relatively limited. Thus, as seen from Table 3.8, a ten times increase in the pressure levels consumes around 100% more lifetime.

### 3.6 Conclusions

The thermo-acoustic instability in the combustion process, where the acoustic oscillations, flow perturbations and unsteady heat release form a feedback mechanism, induces a significant relative motion of the liner walls due to fluid-structure interaction. The unstable combustion leads to the severe vibrations of the structure, which in turn lead to accelerated fatigue lifetime consumption. This work explored the mechanism of fluid-structure interaction on the LIMOUSINE setup for the stable and unstable regime both experimentally and numerically. The milestones in the outcome of this research are listed below:

- The acoustic eigenfrequency was found to be very close to the characteristic frequency measured in the unstable Case6012. In addition, the pressure profile at the characteristic frequency matches the first quarter acoustic mode of the combustor. Thus, the source of the instability is highlighted as the intersection of the first acoustic eigenfrequency and the flame frequency in the combustor.
- Distinct characteristic frequencies with peak pressure levels were observed in pressure spectra due to the combustion instabilities. However, the characteristic frequency predicted by the FSI simulation shows a deviation from the measurement that is attributed to the over-prediction of the fluid temperature.
- In the numerical calculations the pressures at these frequencies are sorted by high to low amplitude. Whereas, in the experiments the pressure amplitude at the second higher-harmonic frequency of the characteristic frequency is higher than the one at the first higher-harmonic frequency. This occurrence is attributed to the coupling with the  $\frac{3}{4}$  acoustic mode (300) of the combustor.
- Since the FSI simulations for the unstable cases are computationally very expensive, half of the geometry of the combustor, imposing symmetry boundary condition in the middle plane, was used to reduce the computational cost. The under-prediction of the pressures calculated by the FSI simulations compared to the experiments is attributed to the forced

damping of the pressure oscillations by restricting the three-dimensional turbulent motion of the flow due to the combustion instabilities into a half domain.

The simplifications in the numerical approach, which aimed to reduce the extensive computational time of the FSI simulations for combustion instabilities, brought out deviation between the experimental and numerical results. However, the ways to incorporate the measurements and numerical findings towards combustion system in the prototype development (design) were highlighted. These are stated as follows.

- Using the pressure growth rate functions, obtained by the FSI simulation, the pressures can be resolved by extrapolating the numerically calculated pressures to the measured pressures. The tests for the measurements can be as short as 1 second (see Chapter 7) so that the test duration is not sufficient enough to cause damage in the structure.
- The temperature fluctuations of the wall due to instabilities, which is challenging to measure, can be obtained by incorporating FSI simulations. These fluctuations lead to thermal fatigue, which contributes to lifetime reduction.
- Considering the safe-life approach, the location of crack initiation and the direction of the crack growth are numerically predicted and the corresponding fatigue and creep lifetimes were calculated.

### **3.7 Discussions**

In this work, the LCO is sourced from the first acoustic eigenfrequency of the combustor. Depending on the frequency of the acoustic pressure oscillations generated on the structure's inner surface, the frequency of the limit-cycle and/or the nonlinear harmonics can be coupled to the structural eigenfrequencies and can lead to elevated vibrations in resonance. Those strong vibrations may act as another acoustic source emitting the acoustic waves to the surrounding fluid and thus additional pressure waves can be formed, which can alter the acoustic field in the volume due to this interaction.

Based on the FSI analysis results in Figure 3.14, the combustor is not only exposed to cyclic pressure loading at high temperature but also to temperature fluctuations in time. Thus, the generation of the thermal strains contributes to the overall damage in terms of thermal fatigue. In this regard, three potential phenomena have a direct influence on the damage mechanism and these are; the temperature dependence of the fatigue process due to interaction, thermal fatigue activation due to the thermal stresses caused by the temperature fluctuations, and creep relaxation due to the thermal gradients [36]. However, only the mechanical fatigue and the steady-state creep are included in the lifing procedure in the context of this work.

### **Appendix A. Experimentation – emissivity & reflectivity**

Non-contact measurement techniques were used to minimise any interference with the accuracy of the experiments. The structural surface temperature was measured by an infrared camera and surface velocity by LDV. However, the optimum requirements for both of the techniques somehow contradict. Basically, the object of interest emits infrared radiation as a

function of its temperature level, which is in relation to the infrared energy measured by the infrared (IR) camera. The net energy leaving the surface is the difference between radiosity (J) and irradiation (G) under a heat balance over the surface [37]. The radiosity for a grey, diffuse surface is determined by two components that are the emissive power of the surface and the reflections by the surface.

$$J = \varepsilon E_b + \rho G = \varepsilon E_b + (1 - \varepsilon)G \quad (3.10)$$

where  $\varepsilon$  is the emissivity,  $\rho$  is the reflection ( $\rho=1-\varepsilon$ ),  $E_b$  is the radiation intensity. The assumption for a black body basis on all the incident radiant energy is absorbed for, however even an application of a black paint on the field of interest technically would lead to a grey body with an enhanced absorption, in where some reflection can be present. On the other hand, the liner wall velocity measurements have been performed using an LDV. The technique is based on sending the laser beam towards the target surface and collecting the reflected radiation, which is a function of the relative velocity of the point of interest according to the Doppler effect. The two non-contact measurements for temperature and velocity are superior compared to contact-type techniques. However, a compromise rose by the techniques' characteristics is the different requirement of emissivity and reflectivity for accurate measurements.

## Appendix B. Finite element formulation for the FSI

The FEM formulation is derived from an assumption made on element displacement  $\mathbf{u}$ . A point inside an element is selected where  $\mathbf{u}$  describes the displacement at the point,  $\mathbf{N}$  contains the position of the point and  $\mathbf{d}$  is a vector containing displacement on the nodal points. In a general form, with  $n$  number of nodes in an element  $e$ , it reads as follows:

$$\mathbf{u} = \sum_{k=1}^n N_k^\beta d_k^\beta = \left[ N_1^\beta, N_2^\beta, \dots \right] \begin{Bmatrix} d_1^\beta \\ d_2^\beta \\ \vdots \\ \vdots \end{Bmatrix} = \mathbf{N}\mathbf{d} \quad (3.11)$$

where  $k=1,2,\dots,n$  and  $\beta=1,2,3$  due to 3 dimensions. So the velocity  $\mathbf{v}$  at any chosen point can easily be described as:

$$\mathbf{V} = \sum_{k=1}^n N_k^\beta w_k^\beta = \left[ N_1^\beta, N_2^\beta, \dots \right] \begin{Bmatrix} w_1^\beta \\ w_2^\beta \\ \vdots \\ \vdots \end{Bmatrix} = \mathbf{N}\mathbf{w} \quad (3.12)$$

where  $\mathbf{w}$  is nodal velocity.

Due to large displacements it is necessary to describe equilibrium and geometrical changes in detail. In a deformed body, the internal forces are mainly characterised by Cauchy stresses. Differential equation for equilibrium expressed in Cauchy stresses  $\sigma$  is described as:

$$\text{div}(\sigma) + b = \rho_t \dot{v} \quad (3.13)$$

where  $b$  is the body force acting on the solid,  $\rho_t$  is the mass density in deformed geometry, and  $\dot{v}$  is the acceleration.

The principle of virtual work for this problem is:

$$\int_{V_0} \sigma : \text{grad}(\tilde{V}) J dV_0 + \int_{V_0} b \cdot \tilde{V} J dV_0 + \int_{A_0} t \cdot \tilde{V} J^* dA_0 = \int_{V_0} \rho \dot{v} \cdot \tilde{V} J dV_0 \quad (3.14)$$

The change of the reference volume ( $V_0$ ) to the deformed volume ( $V$ ) is described by

$$J = dV/dV_0 \quad (3.15)$$

where  $J$  is the Jacobian determinant. The change in area element is described by:

$$J^* = dA/dA_0 \quad (3.16)$$

## Acknowledgements

The authors would like to acknowledge funding of this research by the EC in the Marie Curie Actions – Networks for Initial Training, under call FP7-PEOPLE-2007-1-1-ITN, Project LIMOUSINE with project number 214905. The authors would like to thank J.C. Roman Casado from University of Twente Thermal Engineering Department for the experimentation assistance.

## References

- [1] Lieuwen, T., 2003, "Modeling premixed combustion-acoustic wave interactions: A review," *Journal of Propulsion and Power*, 19(5), pp. 765-781.
- [2] McManus, K. R., Poinso, T., and Candel, S. M., 1993, "A review of active control of combustion instabilities," *Progress in Energy and Combustion Science*, 19(1), pp. 1-29.
- [3] Rayleigh, J. W. S., and Lindsay, R. B., 1945, *The theory of sound*, Dover publications, New York,.
- [4] Crocker, D. S., Nikolaus, D., and Smith, C. E., 1999, "CFD Modeling of a Gas Turbine Combustor From Compressor Exit to Turbine Inlet," *Journal of Engineering for Gas Turbines and Power*, 121(1), pp. 89-95.
- [5] Rao, M. S., and Sivaramakrishna, G., 2009, "Performance Improvement of an Aero Gas Turbine Combustor," *ASME Conference Proceedings*, 2009(48838), pp. 689-694.
- [6] Kim, W.-W., Lienau, J. J., Colket, P. R. V. S. M. B., III, Malecki, R. E., and Syed, S., 2006, "Towards Modeling Lean Blow Out in Gas Turbine Flameholder Applications," *Journal of Engineering for Gas Turbines and Power*, 128(1), pp. 40-48.
- [7] McGuirk, J. J., and Spencer, A., 2001, "Coupled and Uncoupled CFD Prediction of the Characteristics of Jets From Combustor Air Admission Ports," *Journal of Engineering for Gas Turbines and Power*, 123(2), pp. 327-332.
- [8] Bain, D. B., Smith, C. E., Liscinsky, D. S., and Holdeman, J. D., 1999, "Flow coupling effects in jet-in-crossflow flowfields," *Journal of Propulsion and Power*, 15(1), pp. 10-16.
- [9] Junger, M. C., and Feit, D., 1972, *Sound, Structures, and Their Interaction*, MIT, Cambridge, MA.
- [10] Fahy, F., and Gardonio, P., "Sound and Structural Vibration - Radiation, Transmission and Response (2nd Edition)," Elsevier.
- [11] Huls, R. A., van Kampen, J. F., van der Hoogt, P. J. M., Kok, J. B. W., and de Boer, A., 2008, "Acoustoelastic interaction in combustion chambers: Modeling and experiments," *Journal of Engineering for Gas Turbines and Power*, 130(5).



- [12] Huls, R. A., Sengissen, A. X., van der Hoogt, P. J. M., Kok, J. B. W., Poinso, T., and de Boer, A., 2007, "Vibration prediction in combustion chambers by coupling finite elements and large eddy simulations," *J Sound Vib*, 304(1-2), pp. 224-229.
- [13] Khatir, Z., Pozarlik, A. K., Cooper, R. K., Watterson, J. W., and Kok, J. B. W., 2008, "Numerical study of coupled fluid-structure interaction for combustion system," *Int J Numer Meth Fl*, 56(8), pp. 1343-1349.
- [14] Alemela, R., Roman Casado, J. C., Kumar, S., and Kok, J., "Simulation of limit cycle pressure oscillation with coupled Fluid-Structure interactions in a model combustor," *Proc. 18th International Congress on Sound & Vibration, ICSV 18*.
- [15] Shahi, M., Kok, J. B. W., and Alemela, P. R., "Simulation of 2-way fluid structure interaction in a 3D model combustor," *Proc. Proceedings ASME Turbo Expo 2012*.
- [16] Lai, M. K., "CFD Analysis of Liquid Spray Combustion in a Gas Turbine Combustor," *ASME Paper 97-GT-309*.
- [17] Kiewel, H., Aktaa, J., and Munz, D., 2005, "Advances in the Inelastic Failure Analysis of Combustor Structures," *High Intensity Combustors – Steady Isobaric Combustion*, Wiley-VCH Verlag GmbH & Co. KGaA, pp. 375-390.
- [18] Roman Casado, J. C., and Kok, J. B. W., 2012, "Combustor eigen frequencies of pressure oscillations and their dependence on the burner impedance and a dimensional numbers," *Proc. ASME Turbo Expo 2012* June 11-15.
- [19] Haynes International, 2003, "High-temperature Tech Brief: HAYNES® 230® Alloy," <http://www.haynesintl.com/pdf/h3060.pdf>.
- [20] Haynes International, "HAYNES® HR-120TM alloy," <http://www.haynesintl.com/pdf/h3125.pdf>.
- [21] Michler, C., Hulshoff, S. J., van Brummelen, E. H., and de Borst, R., 2004, "A monolithic approach to fluid-structure interaction," *Comput Fluids*, 33(5-6), pp. 839-848.
- [22] Menter, F., Kuntz, M., and Bender, R., "A scale-adaptive simulation model for turbulent flow predictions," *Proc. 41st Aerospace Sciences Meeting and Exhibit, The American Institute of Aeronautics and Astronautics (AIAA)*.
- [23] Menter, F. R., and Egorov, Y., 2010, "The Scale-Adaptive Simulation Method for Unsteady Turbulent Flow Predictions. Part 1: Theory and Model Description," *Flow Turbul Combust*, 85(1), pp. 113-138.
- [24] ANSYS, 2010, "Release 11.0 Documentation for ANSYS."
- [25] Egorov, Y., Menter, F. R., Lechner, R., and Cokljat, D., 2010, "The Scale-Adaptive Simulation Method for Unsteady Turbulent Flow Predictions. Part 2: Application to Complex Flows," *Flow Turbul Combust*, 85(1), pp. 139-165.
- [26] Altunlu, A. C., Shahi, M., Pozarlik, A., van der Hoogt, P. J. M., Kok, J. B. W., and de Boer, A., "Fluid-structure interaction of combustion instabilities and fatigue/creep lifing (in progress)."
- [27] Fuchs, H. O., and Stephens, R. I., 1980, *Metal Fatigue in Engineering*, John Wiley & Sons, Inc.
- [28] Brinkman, C. R., Rittenhouse, P. L., Corwin, W. R., Strizak, J. P., Lystrup, A., and DiStefano, J. R., 1976, "Application of Hastelloy X in gas-cooled reactor systems."
- [29] ASME Boiler and Pressure Vessel Code, 1977, "Code Case N-47."
- [30] Seo, S., 2003, "Combustion instability mechanism of a lean premixed gas turbine combustor," *Journal of Mechanical Science and Technology*, 17(6), pp. 906-913.
- [31] Paschereit, C. O., Gutmark, E., and Weisenstein, W., 2000, "Excitation of Thermoacoustic Instabilities by Interaction of Acoustics and Unstable Swirling Flow," *Aiaa J*, 38(6), pp. 1025-1034.

- [32] Müller, R., and Hermann, J., 2012, "Stability limits and non-linear characteristics of a self-excited combustion instability," 19th International Congress on Sound and Vibration, ICSV19, International Institute of Acoustics and Vibration (IIAV), Vilnius, Lithuania.
- [33] Rossing, T. D., 2007, Springer handbook of acoustics, Springer, New York, N.Y.
- [34] Blackstock, D. T., 2000, Fundamentals of physical acoustics, Wiley, New York.
- [35] Blevins, R. D., 2001, Formulas for natural frequency and mode shape, Robert E. Krieger publishing company, Malabar, Florida.
- [36] Kennedy, A. J., 1962, Processes of Creep and Fatigue in Metals, Oliver and Boyd, Edinburgh.
- [37] Kothandaraman, C. P., 2006, Fundamentals of heat and mass transfer, New Age International Publishers.



## 4 XFEM-based fracture mechanics implementation for fatigue and creep crack growth of a nickel-based superalloy

A. Can Altunlu and André de Boer

University of Twente, Faculty of Engineering Technology, Section of Applied Mechanics, 7500 AE, Enschede, The Netherlands

---

### Abstract

The use of the finite element method (FEM) for explicit modelling has been shown to provide the basis for detailed modelling of cracks. Extending the analyses to simulate crack growth behaviour typically leads to a significant increase in effort, particularly from the point of view of updating the finite element geometry. A relatively recent development, which is now becoming more accessible, is the eXtended Finite Element Method (XFEM). The XFEM concept extends the standard finite element approximation by adding a discontinuity function and crack-tip asymptotic functions using the framework of partition of unity. The limitations of real-time model updating are avoided by creating an enriched domain in the cracked body. This work presents an implementation of XFEM-based fracture mechanics analysis in a general purpose finite element software, Abaqus FEA for fatigue and creep crack growth of a combustor material, Ni-based superalloy. A user-defined algorithm is integrated to incorporate the existing XFEM module in Abaqus FEA to enable progressive crack growth for arbitrary shaped 3D cracks due to fatigue and creep conditions. Benefiting from the capabilities of Abaqus FEA, by means of complex geometry modelling and the embedded XFEM feature, as well as extending the simulations to fatigue/creep crack growth within the XFEM framework, provides an efficient tool applicable to industrial gas turbines. In this way the computational costs can be significantly reduced by the fact that arbitrarily shaped, and growing cracks in complex geometries can be characterised without conforming mesh, and remeshing is avoided. Furthermore, the cycle-dependent fatigue and time-dependent creep crack growth theories can be adapted without violating linear elastic fracture mechanics concepts, on which XFEM is based.

**Keywords:** XFEM, fracture mechanics, fatigue, creep, crack, superalloy.

## 4.1 Introduction

Industrial gas turbine engines are widely used in the power generation industry. In gas turbines, power is generated by burning an air-fuel mixture at high pressure and temperature. Therefore, the mechanical integrity of the engines is generally governed by the hot gas path components. Safe-life design approach is generally applied in these components to ensure reliable, durable and safe operation with long lifetime expectancy. However, the robustness and performance of the engines are essentially dependent on the design and operating conditions.

Stringent regulations on pollutant emissions motivated the introduction and development of lean, premixed combustion systems particularly to reduce  $\text{NO}_x$  emissions. The downside of these systems is that they are susceptible to thermo-acoustically induced combustion instabilities. Instabilities generate high pressure oscillating at elevated temperatures, which causes severe damage to the combustion section components. Therefore, damage-tolerance evaluation of in-service components under combined fatigue and creep conditions is critical to maintain the mechanical integrity of the combustion systems in gas turbines. Fracture mechanics is widely used to predict the residual strength and remaining lifetime. Nonetheless, industrial gas turbines remain a challenge due to complex geometry, boundary condition and load-state, for which there is no generic analytical solution. Therefore, numerical analysis is required to provide a rational prediction of fracture characteristics. However, computing the state of stress in a cracked body requires dealing with the discontinuities. Standard finite element methods (FEM) deal with such situations by conforming the mesh to the discontinuity, and repeating this procedure as the crack advances. However, mesh generation and remeshing of a three-dimensional (3D) complex geometry, as in the industrial cases, is computationally expensive. Moreover, the singularity of the asymptotic crack fields requires treating the domain surrounding the crack front with very fine mesh and applying of special schemes such as spider meshing for accurately representing the crack geometry. Capturing the displacement discontinuity across the crack, and the singular nature of the crack-tip stress field at every crack propagation step by remeshing, is computationally demanding where complex structures are concerned.

The eXtended Finite Element Method (XFEM) has been developed, which adapts standard FEM to fracture mechanics computations [1, 2]. In XFEM, a priori knowledge about the local behaviour of the solution is included in the approximation field using partition of unity method (PUM) [3]. Thereby, the finite element space is enriched with a discontinuous function and the near-tip asymptotic solutions, which are added to the standard FEM approximation. Hence, arbitrarily shaped and growing cracks can be characterised without conforming mesh, and remeshing is avoided. In 3D geometries, the discontinuities, which are revealed due to the crack surface and front, can be implicitly described by the level set method (LSM) [4, 5]. A considerable amount of research has been presented in the literature related to XFEM-based fracture mechanics in the areas of crack modelling in a 3D geometry [6-8]. This includes arbitrary branched and intersecting cracks [9], cohesive crack growth [10], mixed-mode crack propagation [11], dynamic crack propagation [12, 13], elastic-plastic

fatigue crack growth [14] and fatigue crack growth implemented into a general purpose finite element software [15]. In particular, implementation of the XFEM into general-purpose finite element software, such as Abaqus FEA, offers unique capabilities in industrial applications, which involve complex geometries to be modelled. The cracks can be modelled independently of the mesh, and the stress state around the crack can be predicted by contour integral evaluation. However, simulating progressive crack growth for arbitrary shaped 3D cracks requires a user-defined algorithm incorporating Abaqus. Moreover, the current usage of the XFEM in Abaqus FEA allows analysis of only stationary cracks in 3D geometries, and evaluation of crack-tip parameters used for time-dependent creep behaviour is not supported, whereas standard FEM applications are available.

When the hot gas path components in the combustion section subjected to creep-fatigue loading conditions during service lifetime are concerned, their mechanical performance at high temperature is of great importance to maintain their mechanical integrity. Solid-solution-strengthened Ni-based superalloys are widely used for the combustion section components in gas turbine engines, where high-temperature strength, oxidation resistance and long-term metallurgical stability is desired [16]. Mainly experimental studies have been conducted to investigate high temperature fatigue crack behaviour and creep crack behaviour, which are listed in Table 4.1. Note that in the table zero hold time indicates fatigue crack growth, whereas infinite hold time refers to creep crack growth. Nonetheless, a generic numerical work to provide a systematic investigation to characterise the variables relevant to crack growth under fatigue and creep conditions is unavailable.

**Table 4.1. Literature summary on experiments of Alloy230 ( $T_{\text{room}}$ : Room Temperature)**

Reference	Temperature [ $^{\circ}\text{C}$ ]	Hold time	Outcome
Lu et al. (2005) [17]	$T_{\text{room}}$ , 816 and 927	zero, 2 min and infinite	The fracture mode transition during creep-fatigue crack growth
Lu et al. (2006) [18]	649, 816 and 927	zero, 3 s to 5 h and infinite	The dependency of creep-fatigue crack growth
Lu et al. (2007) [19]	816 and 927	zero, 2 min, 1 h and infinite	The fracture mechanics parameter compliance with fatigue-creep crack growth rate
Roy et al. (2010) [20]	600, 700 and 800	60 s to 1000 s	The correlation creep-fatigue crack growth rate to testing frequency
Bache et al. (2012) [21]	816 and 927	2 min	The creep-fatigue crack growth at plain-stress conditions
Pataky et al. (2013) [22]	$T_{\text{room}}$ and 900	-	The slip irreversibility in fatigue crack growth

The aim of this work is the development and implementation of a user-defined algorithm for the XFEM-based fracture mechanics analysis of a typical solid-solution-strengthened Ni-based superalloy under fatigue and creep conditions. Implementation of the proposed method

in a general-purpose finite element program, *Abaqus*, enables modelling cracks in 3D complex geometries, relevant to industrial application, without the necessity of conforming mesh and remeshing at every crack increment. Furthermore, the interaction of time-dependent creep and cycle-dependent fatigue can be modelled for this typical gas turbine material within the framework of XFEM using only one fracture parameter.

This paper is organised as follows. The theory of the method, including the J-integral computation with the equivalent domain integral method, stress intensity factors extraction with the interaction integral method, XFEM displacement approximation, and crack front traction and control covering cycle-dependent fatigue crack growth (FCG), time-dependent creep crack growth (CCG) aspects, is presented in section 4.2. Prior to the investigation, in section 4.3 numerical benchmark tests are presented that were systematically performed with the cases, selected from literature, to ensure the validity of the theory and the accuracy of the calculations. First, the relation between CCG parameters,  $C^*$ ,  $C_I$  and  $K$  is analysed [23-25] by FEM and XFEM analysis. Next, the validity of the stress intensity factor (SIF), calculated by FEM and XFEM, under thermo-elasticity conditions is presented [26]. After that, the combined effect of creep and fatigue is analysed in a compact tension (CT) specimen, made of Ni-based superalloy. Then, the results of mixed-mode crack propagation in a modified CT-specimen are presented. Finally, the concluding remarks are provided. Note that the parameters, such as mesh type and size, step size, and boundary conditions, are described in each validation sub-section.

## 4.2 Theory

In this section, the theory of the method presented in this work is described. First, the crack-tip characterisation parameters and their contour integral evaluation are described. These fracture-characterising parameters are widely used in cycle-dependent fatigue crack growth. Second, the time-dependent creep crack growth parameters and their content are described. Next, XFEM displacement approximation for crack modelling is detailed. Finally, the crack growth algorithm to characterise the crack growth including fatigue and creep damage mechanisms is presented within the framework of the overall method.

### 4.2.1 Contour integral evaluation and domain integral representation

Many engineering materials exhibit nonlinear deformation in a crack body. However, as long as nonlinear material deformation is confined to a relatively small region around the crack-tip, linear elastic fracture mechanics (LEFM) can be considered as characterising the fracture behaviour. Under equilibrium conditions, the Griffith energy balance for an increase in the fracture area can be expressed as

$$\frac{dE}{dA} = \frac{d\Pi}{dA} + \frac{dW_s}{dA} = 0 \quad (4.1)$$

where  $E$  is the total energy,  $\Pi$  is the potential energy provided by the internal strain energy and external forces,  $W_s$  is the work required to form new surfaces of crack, and  $A$  is the crack area. Considering the state of equilibrium, zero net change in total energy condition is

conserved during crack growth, as the potential energy of the elastic body is sufficient to overcome the surface energy of the material. The equilibrium condition reads

$$-\frac{d\Pi}{dA} = \frac{dW_s}{dA} \quad (4.2)$$

Basically equivalent to the Griffith model, the potential energy can be represented by the Irwin's energy release rate parameter. The energy release rate, or crack driving force, is defined as the stored energy dissipated during crack growth per unit of formation new fracture surface area.

$$G = -\frac{d\Pi}{dA} \quad (4.3)$$

The potential energy ( $\Pi$ ) can be written as the differential of the strain energy stored in the body ( $U$ ) and the work done by external forces ( $F$ ) as  $\Pi = U - F$ .

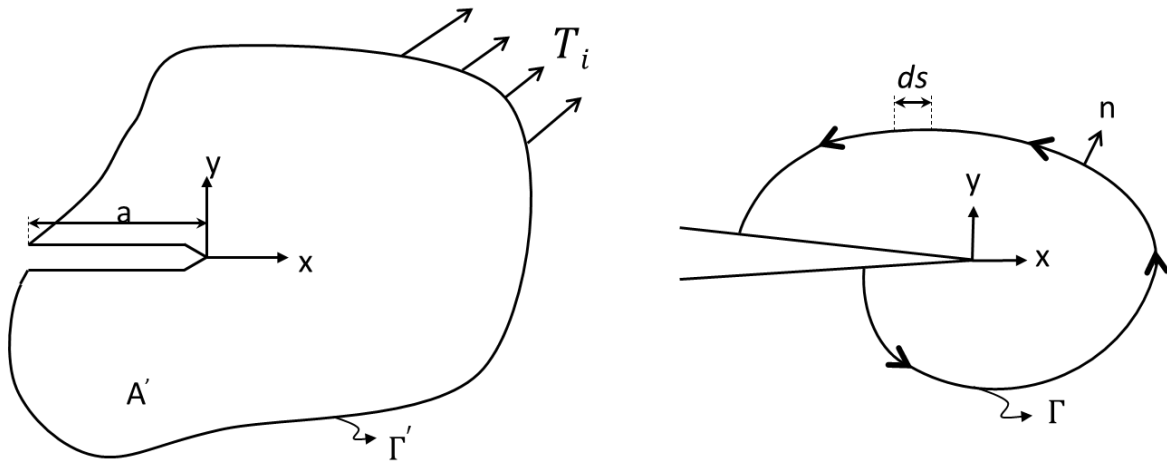


**Figure 4.1. A two-dimensional body containing a crack with a bounding curve by  $\Gamma'$  (left) and arbitrary contour surrounding the tip of a crack (right)**

Consider a two-dimensional body containing a crack with a bounding curve by  $\Gamma'$ , and the corresponding area is  $A'$  (Figure 4.1). The potential energy of an elastic body in the absence of body forces and under quasi-static conditions is given by

$$\Pi = \int_{A'} w dA - \int_{\Gamma} T_i u_i ds \quad (4.4)$$

where  $w$  is the strain energy density,  $\Gamma$  is the portion of the bounding contour  $\Gamma'$ , on which tractions are defined,  $T_i$  is for the traction vector components defined according to the outward normal as  $T_i = \sigma_{ij} n_j$ ,  $n_j$  is the vector of the outward unit normal  $n$  to the contour  $\Gamma$ ,  $u_i$  is for the components of the displacement vector, and  $ds$  is an element along the contour  $\Gamma$ . The tractions are assumed to be independent of the crack length  $a$ , and the crack surfaces are considered to be traction free. The strain energy density is defined as

$$w = w(\varepsilon) = \int_0^\varepsilon \sigma_{ij} d\varepsilon_{ij} \quad (4.5)$$

where the strain energy density varies with the stress  $\sigma_{ij}$  and the strain  $\varepsilon_{ij}$ .

The change in potential energy due to a virtual crack extension is written as



$$\frac{d\Pi}{da} = \int_{A'} \frac{dw}{da} dA - \int_{\Gamma'} T_i \frac{du_i}{da} ds \quad (4.6)$$

The region, where the displacements are defined, satisfies  $du_i/da = 0$ , and also where the tractions are defined, satisfies  $dT/da = 0$ . Therefore the line integration in the equation 4.6 can be performed over the entire contour  $\Gamma$ . The coordinate axis is attached to the crack-tip, hence it moves as the crack grows. Thus a derivative with respect to crack length can be given as

$$\frac{d}{da} = \frac{\partial}{\partial a} + \frac{\partial x}{\partial a} \frac{\partial}{\partial x} = \frac{\partial}{\partial a} - \frac{\partial}{\partial x} \quad (4.7)$$

where  $\partial x/\partial a = -1$ . Rewriting the potential energy change equation gives

$$\frac{d\Pi}{da} = \int_{A'} \left( \frac{\partial w}{\partial a} - \frac{\partial w}{\partial x} \right) dA - \int_{\Gamma'} T_i \left( \frac{\partial u_i}{\partial a} - \frac{\partial u_i}{\partial x} \right) ds \quad (4.8)$$

The first term within the brackets in the area integral above can be evaluated by invoking the definition of strain energy density (when it exhibits the properties of an elastic potential) as follows

$$\frac{\partial w}{\partial x} = \frac{\partial w}{\partial \varepsilon_{ij}} \frac{\partial \varepsilon_{ij}}{\partial x} = \sigma_{ij} \frac{\partial \varepsilon_{ij}}{\partial x} \quad (4.9)$$

Applying the strain-displacement relationship for small strain (constitutive relation  $\varepsilon_{ij} = \partial u_i/\partial x_j$ ), on the fact that  $\sigma_{ij} = \sigma_{ji}$ , gives

$$\frac{\partial w}{\partial x} = \frac{1}{2} \sigma_{ij} \left[ \frac{\partial}{\partial x} \left( \frac{\partial u_i}{\partial x_j} \right) + \frac{\partial}{\partial x_j} \left( \frac{\partial u_j}{\partial x_i} \right) \right] = \sigma_{ij} \frac{\partial}{\partial x_j} \left( \frac{\partial u_i}{\partial x} \right) \quad (4.10)$$

Invoking the equilibrium condition ( $\partial \sigma_{ij}/\partial x_j = 0$ ) leads to

$$\sigma_{ij} \frac{\partial}{\partial x_j} \left( \frac{\partial u_i}{\partial x} \right) = \frac{\partial}{\partial x_j} \left( \sigma_{ij} \frac{\partial u_i}{\partial x} \right) \quad (4.11)$$

If the same assumptions as used to obtain the second term are applied in the area integral above, the first term becomes

$$\frac{\partial w}{\partial a} = \frac{\partial w}{\partial \varepsilon_{ij}} \frac{\partial \varepsilon_{ij}}{\partial a} = \sigma_{ij} \frac{\partial}{\partial x_j} \left( \frac{\partial u_i}{\partial a} \right) \quad (4.12)$$

Invoking the principle of virtual work reads

$$\int_{A'} \sigma_{ij} \frac{\partial}{\partial x_j} \left( \frac{\partial u_i}{\partial a} \right) dA - \int_{\Gamma'} T_i \frac{\partial u_i}{\partial a} ds \quad (4.13)$$

In this way, one of the terms in the line integral is cancelled that leads to

$$\frac{d\Pi}{da} = \int_{\Gamma'} T_i \frac{\partial u_i}{\partial x} ds - \int_{A'} \frac{\partial w}{\partial x} dA \quad (4.14)$$

Applying the divergence theorem and multiplying both sides by -1 and considering  $n_x ds = dy$  gives

$$-\frac{d\Pi}{da} = \int_{\Gamma'} \left( w n_x - T_i \frac{\partial u_i}{\partial x} \right) ds = \int_{\Gamma'} \left( w dy - T_i \frac{\partial u_i}{\partial x} ds \right) \quad (4.15)$$

If the plastic zone is small compared to the crack size, in other words the material experiences small-scale yielding at the crack-tip, the crack driving force or the energy release rate ( $G$ ), is in fact the  $J$ -integral [27, 28] is defined as

$$-\frac{d\Pi}{da} = G = J = \int_{\Gamma} \left( w dy - T_i \frac{\partial u_i}{\partial x} ds \right) \quad (4.16)$$

In the LEFM approach, the stress solutions for elastic stresses and plastic deformation are assumed to be restricted to a small region around the crack-tip that confirms small-scale yielding condition. Additionally, the crack is assumed to be a perfectly sharp root with a fundamentally notch tip radius of zero. These assumptions will cover the capabilities and limitations of the approach.

Considering linear-elastic materials for general loading (straight ahead crack growth), the  $J$ -integral, or strain energy release rate, is related to the stress intensity factor for a general mixed-mode homogeneous crack in two-dimensions as

$$G = J = \eta \frac{1}{E} (K_I^2 + K_{II}^2) \quad (4.17)$$

where  $K_I$  and  $K_{II}$  are the stress intensity factors for mode I and mode II crack loading, respectively,  $E$  is the Young's modulus, and  $\eta$  is defined by the stress state as

$$\eta = \begin{cases} 1 & \text{for plane stress} \\ 1 - \nu^2 & \text{for plane strain} \end{cases} \quad (4.18)$$

where  $\nu$  is the Poisson's ratio.

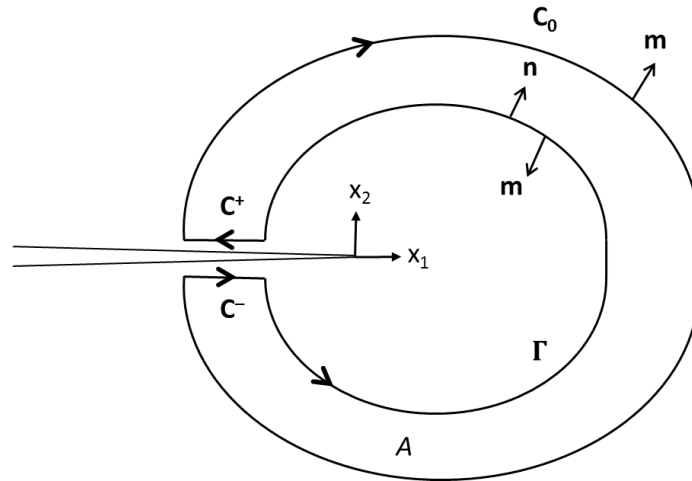


**Figure 4.2. Representative domain in two-dimensions used for computation of mixed-mode stress intensity factors**

In general, the domain form of interaction integrals [29-31] is used to extract the mixed-mode stress intensity factors. In the computation of the energy release rate, the  $J$ -integral can be calculated by converting the line integral into a domain integral using the known finite element shape functions [26, 32, 33].

Consider a crack in two-dimensions as seen in Figure 4.2. The crack-tip coordinate is constructed in the Cartesian coordinate system  $(x_1, x_2)$ . The closed contour  $C$  with outward unit normal vector  $\mathbf{m}$  is defined by  $C = C_0 + C^+ + C^- - \Gamma$ . The area  $A$  is enclosed by the

closed contour  $C$ . Consider the contour encompassing the crack-tip with outward unit normal vector  $\mathbf{n}$ . The contour integral  $J$  is defined for a crack-tip as ( $x \rightarrow x_1$  and  $y \rightarrow x_2$ )

$$J = \int_{\Gamma} \left( w dx_2 - T_i \frac{\partial u_i}{\partial x_1} d\Gamma \right) \quad (4.19)$$

Using the Dirac delta, which eases the implementation in finite element analysis, the equivalent form can be given as

$$J = \int_{\Gamma} \left( w \delta_{1j} - \sigma_{ij} \frac{\partial u_i}{\partial x_1} \right) n_j d\Gamma \quad (4.20)$$

Two states of a crack body are superimposed onto the stress and displacement solution. The state 1 corresponds to the present state, and the state 2 is an auxiliary stress that are given as  $\sigma_{ij}^{(1)}, \varepsilon_{ij}^{(1)}, u_i^{(1)}$  and  $\sigma_{ij}^{(2)}, \varepsilon_{ij}^{(2)}, u_i^{(2)}$ , respectively. The  $J$ -integral for the superposition of the two states is given as

$$J = \int_{\Gamma} \left[ \frac{1}{2} (\sigma_{ij}^{(1)} + \sigma_{ij}^{(2)}) (\varepsilon_{ij}^{(1)} + \varepsilon_{ij}^{(2)}) \delta_{1j} - (\sigma_{ij}^{(1)} + \sigma_{ij}^{(2)}) \frac{\partial (u_i^{(1)} + u_i^{(2)})}{\partial x_1} \right] n_j d\Gamma \quad (4.21)$$

Expanding and rearranging the terms allows for the  $J$ -integral to be separated into the state 1, state 2 and  $I^{(1,2)}$ , which is the interaction integral for states 1 and 2, such that

$$J^{(1+2)} = J^{(1)} + J^{(2)} + I^{(1,2)} \quad (4.22)$$

The interaction integral is given as

$$I^{(1,2)} = \int_{\Gamma} \left( w^{(1,2)} \delta_{1j} - \sigma_{ij}^{(1)} \frac{\partial u_i^{(2)}}{\partial x_1} - \sigma_{ij}^{(2)} \frac{\partial u_i^{(1)}}{\partial x_1} \right) n_j d\Gamma \quad (4.23)$$

where  $w^{(1,2)}$  is the interaction strain energy density given as

$$w^{(1,2)} = \sigma_{ij}^{(1)} \varepsilon_{ij}^{(2)}, = \sigma_{ij}^{(2)} \varepsilon_{ij}^{(1)} \quad (4.24)$$

The superimposed stress states can be expressed in the general form for mixed-mode problems as

$$J^{(1+2)} = J^{(1)} + J^{(2)} + \eta \frac{2}{E} \left( K_I^{(1)} K_I^{(2)} + K_{II}^{(2)} K_{II}^{(1)} \right) \quad (4.25)$$

The following relationship for the interaction integral is obtained

$$I^{(1,2)} = \eta \frac{2}{E} \left( K_I^{(1)} K_I^{(2)} + K_{II}^{(2)} K_{II}^{(1)} \right) \quad (4.26)$$

The mode I SIF in terms of the interaction integral can be obtained by imposing the state 2 as the pure mode I asymptotic fields with  $K_I^{(2)} = 1, K_{II}^{(2)} = 0$

$$K_I^{(1)} = \frac{E}{2\eta} I^{1, Mode I} \quad (4.27)$$

Similarly, choosing the state 2 as the pure mode II asymptotic fields with  $K_{II}^{(2)} = 1, K_I^{(2)} = 0$ , gives the mode II SIF

$$K_{II}^{(1)} = \frac{E}{2\eta} I^{1, Mode II} \quad (4.28)$$

Defining a smoothing function  $q(x_1, x_2)$  such that  $q = 1$  (equals to unity on an open set containing the crack-tip) on  $\Gamma$  and  $q = 0$  (vanishes on an outer prescribed contour) on  $C_0$ .

The interaction integral for the state 1 and state 2 can be expressed as

$$I^{(1,2)} = \lim_{\Gamma \rightarrow 0} \left\{ \int_{\Gamma} [w^{(1,2)} \delta_{1j} - \sigma_{ij}^{(1)} \frac{\partial u_i^{(2)}}{\partial x_1} - \sigma_{ij}^{(2)} \frac{\partial u_i^{(1)}}{\partial x_1}] q m_j ds \right\} \quad (4.29)$$

where  $\Gamma$  is a contour that starts and ends on the crack line, and  $m_j$  is the outward normal component to the domain  $A$ , which is given by

$$\mathbf{m} = \begin{cases} -\mathbf{n} & \text{on } \Gamma \\ +\mathbf{n} & \text{on } C_0 UC^+ UC^- \end{cases} \quad (4.30)$$

Using the divergence theorem, the equivalent area integral can be written as

$$I^{(1,2)} = \int_A \left( \sigma_{ij}^{(1)} \frac{\partial u_i^{(2)}}{\partial x_1} + \sigma_{ij}^{(2)} \frac{\partial u_i^{(1)}}{\partial x_1} - w^{(1,2)} \delta_{1j} \right) \frac{\partial q}{\partial x_j} dA \quad (4.31)$$

Note that the equation above is derived assuming the crack faces are straight and traction-free.

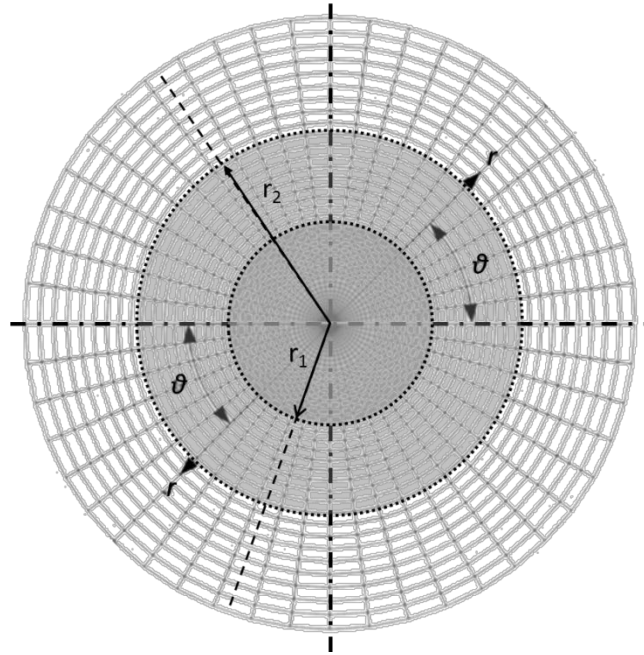


**Figure 4.3. Radius ( $r$ ) from the crack-tip for path-independence and containing elements**

The definition of the radius from the crack-tip specifies the elements for the integration. To this end a sufficiently large radius, i.e. larger than the path-independent radius, has to be selected such that it leads to a path-independent integral so any path (contour)  $\Gamma$  that starts and ends on the crack faces gives the same value of the integral. A representation of the radius from the crack-tip containing the elements is depicted in Figure 4.3.

#### 4.2.2 Time-dependent creep crack growth

Metallic structures, subjected to static load at high temperatures close to the melting point of the material, exhibit time-dependent creep deformation. Nickel-based superalloys are a typical material for combustor cans of gas turbine engines. Its superior creep strength,

thermal-stability and environment resistance make the alloy suitable for high temperature applications. However, these materials can lose their mechanical integrity performance in the presence of a progressing crack. In this regard, the lifetime of the materials is no longer defined by the creep strength and ductility, but by the creep crack growth rate.

Considering a stationary crack in the creep-temperature regime, the stress field relaxes at the crack wake; however, it intensifies locally around the crack-tip. If the crack advances slower relative to the rate of the crack wake relaxing process, the stress intensity is larger. If the crack advancement rate is greater than the time to relax at the crack wake, the stress intensity is relatively smaller. In this regard, the crack velocity depends on the creep rate of the material. In the analysis of the fracture behaviour under creep cracking conditions, the crack-tip parameter, which is dependent on the material and the amount of creep deformation, must take into account time-dependent deformation.

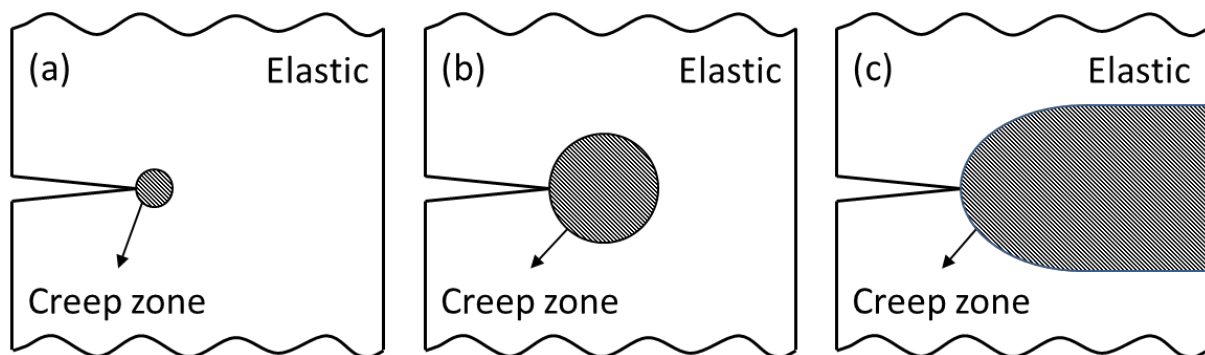


**Figure 4.4. Schematic representation of regimes in creep deformation: (a) Small-scale creep (SSC)  $t/t_c < 1$ , (b) Transition creep (TC) condition  $t/t_c \sim 1$ , and (c) Steady-state creep (SS) condition  $t/t_c > 1$  [34]**

In creep crack growth, three regimes are defined that are small-scale, transient and steady-state, which are classified for materials exhibiting elastic, power-law creep behaviour, depending on the size of the crack-tip zone relative to the specimen dimensions, as depicted in Figure 4.4 [34].

At the onset of crack growth, if the creep zone size is very small relative to the dimensions of the geometry, and is confined locally near the crack-tip, this regime is defined as the small-scale creep (SSC) regime, as shown in Figure 4.4 (a). On the contrary, if the creep zone occupies a relatively large area of the geometry, the entire un-cracked ligament ahead of the crack-tip at the extreme, the regime is defined as steady-state creep (SS) or large-scale creep regime, as seen in Figure 4.4 (c). In the SS regime, generally the creep-crack growth begins under SSC conditions, and the creep deformation progresses by the time that is required to develop SS conditions. Between the SSC and SS conditions, a transition time ( $t_c$ ) is spent by the material during the transition creep (TC) regime, as shown in Figure 4.4 (b). During the SSC and TC regime, the crack-tip stresses and the creep zone size evolve with time [23]. Under SS regime, the crack-tip stress-state and the size of the creep zone reaches a steady-state condition, and no longer changes with time. The fracture parameters for CCG can be determined depending on the size of the creep zone, or the crack-tip creep deformation zone, relative to the dimensions of the geometry.

The path-independent integral  $C^*$  is used to characterise crack growth in a material undergoing SS [35-37]. The  $C^*$  integral is the time-dependent form of the  $J$ -integral. Since the creep rate is a function only of the applied stress in a material exhibiting power-law behaviour, the Hoff's analogy [38] can be applied to SS in order to define the  $C^*$  integral by translating the strains and displacements in the  $J$ -integral formulation into strain rates and displacement rates. In addition, the  $C^*$  integral is path-independent, since  $J$ -integral is path-independent. Note that Hoff's analogy states that if a nonlinear elastic body, which obeys the relationship  $\varepsilon_{ij} = f(\sigma_{ij})$ , and a viscous body, which is characterised by  $\dot{\varepsilon}_{ij} = f(\sigma_{ij})$ , have the same function of stress, then both bodies develop identical stress distributions when identical loads are applied. The  $C^*$  integral is given as

$$C^* = \int_r (\dot{w} dy - T_i \frac{\partial \dot{u}_i}{\partial x} ds) \quad (4.32)$$

where  $\dot{w}$  is the stress work rate density, which is defined as

$$\dot{w} = \int_0^{\dot{\varepsilon}} \sigma_{ij} d\dot{\varepsilon}_{ij} \quad (4.33)$$

The  $C^*$  parameter is valid for crack growth in state of widespread SS. This is associated with the long-time behaviour of the body. Considering a cracked body under remote load, in which the stationary crack in the material is susceptible to creep deformation, the initial response of the material generates elastic strain distribution. In the case of pure Mode I loading, the stresses and strains exhibit a  $1/\sqrt{r}$  singularity near the crack-tip, which can be defined by  $K_I$ . In this case the crack-tip conditions due to the small creep zone (analogous to a plastic zone) can be characterised by  $K_I$  until the evolving creep zone with time is no longer confined within the singularity dominated zone. The creep zone develops over a large portion of the body over long times, eventually reaching the SS regime.

For a growing crack with time, the structural response is governed by the relation between the crack growth rate and the creeping rate. In creep-ductile materials, the crack growth is sufficiently slow so the creep zone has enough time to develop over the entire body, and  $C^*$  is used to characterise the crack-tip behaviour. In creep-brittle materials, the crack growth rate is much higher than the creep zone development, therefore the creep zone localised at the crack-tip remains small, and the crack-tip parameter can be characterised by  $K_I$ . Former works in the literature showed that the austenitic steels behave creep-ductile at relatively lower temperatures (538°C) [35, 39], whereas the nickel-based superalloys show creep-brittle behaviour at higher temperatures (927°C) [19, 40, 41].

The transition characteristics during the change from short-time elastic behaviour under small-scale yielding condition to long-time viscous behaviour under excessive creeping were analysed by Riedel and Rice [25] for a material under uniaxial tension. The material behaviour includes linear elasticity and secondary creep response, which can be given as

$$\dot{\varepsilon} = \frac{\dot{\sigma}}{E} + A\sigma^n \quad (4.34)$$

where  $\dot{\varepsilon}$  is the strain rate,  $\dot{\sigma}$  is the stress rate,  $\sigma$  is the applied stress,  $A$  and  $n$  are the constant and exponent dependent on the creep mechanism, respectively. If the load is applied suddenly

and held constant thereafter, the time-dependent creep zone gradually progresses within the singularity-dominated zone. The stresses can be described by

$$\sigma_{ij} = \left( \frac{C(t)}{AI_n r} \right)^{\frac{1}{n+1}} \tilde{\sigma}_{ij}(n, \theta) \quad (4.35)$$

where  $I_n$  is the integral defined by the corresponding reference [27],  $C(t)$  is the fracture characterising parameter, varying with time, of the local stress singularity enclosed in the creep zone. For stationary cracks, the  $C(t)$  characterises the rate of the crack-tip creep zone. Under small-scale yielding conditions the  $C(t)$  equals the  $C_r$ -integral, and also is related to SIF, and under long-time SS conditions the  $C(t)$  equals the  $C^*$ -integral, which is path-independent within the extensive creep region. Under a constant remote load, the creep strains accumulate in the crack-tip region; simultaneously the stresses in the creep zone exhibit relaxation with time. Under secondary power-law creep, the  $C_r$ -integral parameter can be described in terms of the  $K_I$  for small-scale creep condition as

$$C_t = \frac{1}{(n+1)t} \eta \frac{K_I^2}{E} \quad (4.36)$$

where  $n$  is the power law constant,  $t$  is the time. The  $C_t$  value is related to  $1/t$ , which means it decays with increasing time. The reader is referred to the references for detailed information on the formula derivation [23, 25, 42-44].

The approximation for the creep zone size can be given as

$$r_c(\theta, t) = \frac{1}{2\pi} \left( \frac{K_I}{E} \right)^2 \left[ \frac{(n+1)AI_n E^n t}{2\pi\eta} \right]^{\frac{2}{n-1}} \tilde{r}_c(\theta, n) \quad (4.37)$$

where  $\tilde{r}_c(\theta, n)$  is the angular function. As the creep zone size enlarges,  $C(t)$  leads to the SS regime fracture parameter  $C^*$ . The characteristic (transition) time for transition from SSC to SS is described as

$$t_t = \frac{1}{(n+1)} \frac{1}{C^*} \eta \frac{K_I^2}{E} = \frac{1}{(n+1)} \frac{J}{C^*} \quad (4.38)$$

The transition time,  $t_t$ , is used to quantify the condition for the fracture parameters validity, such that the crack growth behaviour can be characterised by LFM parameters  $C_r$ -integral, thus  $K_I$  if the required time scale is less than the  $t_t$ , while for crack growth requiring times larger than  $t_t$   $C^*$  is the appropriate fracture parameter. The interpolation between short-time (small-scale creep) and long-time (extensive creep) behaviour can be given as [24]

$$C_t = C^* \left( \frac{t_t}{t} + 1 \right) \quad (4.39)$$

### 4.2.3 Crack modelling: XFEM displacement approximation

The element cluster including a crack does not necessarily conform to the crack geometry in XFEM that relatively eases the treatment of crack modelling. In XFEM, the discrete displacement field is approximated by a sum of three parts

$$\mathbf{u} = \mathbf{u}^{\text{fem}} + \mathbf{u}^{\text{dis}} + \mathbf{u}^{\text{tip}} \quad (4.40)$$

where  $\mathbf{u}^{\text{fem}}$  is the continuous part of the displacement field,  $\mathbf{u}^{\text{dis}}$  is the enrichment that accounts for the discontinuity across the crack and  $\mathbf{u}^{\text{tip}}$  is the crack-tip enrichment for the singularities in the stresses and strains. In the continuous domain, the displacement field is approximated by the standard finite element defined as

$$\mathbf{u}^{\text{fem}}(\mathbf{x}) = \sum_{i \in \mathbf{I}} N_i(\mathbf{x}) U_i \quad (4.41)$$

where  $i$  is node number,  $\mathbf{I}$  is the set of all nodes of the element (Figure 4.5),  $N_i(\mathbf{x})$  are the finite element shape functions and  $U_i$  are the nodal displacements that are associated with node  $i$ . The discontinuous field accounts for the discontinuity across the crack surface and is of the form

$$\mathbf{u}^{\text{dis}}(\mathbf{x}) = \sum_{i \in \mathbf{I}^{\text{dis}}} N_i(\mathbf{x}) H(\mathbf{x}) a_i \quad (4.42)$$

where  $\mathbf{I}^{\text{dis}}$  is the set of all nodes belonging to the elements, which are bisected by the crack,  $a_i$  is the unknown parameter of the enrichment at node  $i$ ,  $H(\mathbf{x})$ , the Heaviside function for enriching the elements, whose nodes includes  $\mathbf{I}^{\text{dis}}$ . Let  $\Omega$  be a boundary of a two-dimensional domain including a crack and  $\Gamma_c$  is the displacement discontinuity representing the crack. The spatial position is denoted by  $\mathbf{x}(x, y) \in \Omega$ . The position of a point can be determined relative to the crack location by the discontinuous jump function across the crack described as (Figure 4.5)

$$H(\mathbf{x}) = \begin{cases} 1 & \text{for } (\mathbf{x} - \bar{\mathbf{x}}) \cdot \mathbf{n} > 0 \\ -1 & \text{for } (\mathbf{x} - \bar{\mathbf{x}}) \cdot \mathbf{n} < 0 \end{cases} \quad (4.43)$$

where  $\bar{\mathbf{x}}(\bar{x}, \bar{y})$  is the closest point to the Gauss point  $\mathbf{x}(x, y)$  belonging to crack  $\Gamma_c$  and  $\mathbf{n}$  is the unit outward normal to crack  $\Gamma_c$  at  $\bar{\mathbf{x}}$ . The last term of the discrete displacement field equation is the crack-tip enrichment given by

$$\mathbf{u}^{\text{tip}}(\mathbf{x}) = \sum_{i \in \mathbf{I}^{\text{tip}}} [N_i(\mathbf{x}) \sum_{\alpha=1}^4 F_{\alpha}(\mathbf{x}) b_{i\alpha}] \quad (4.44)$$

where  $\mathbf{I}^{\text{tip}}$  is the set of all nodes of the crack-tip elements,  $b_{i\alpha}$  is the unknown parameters belonging to the crack-tip enrichment,  $F_{\alpha=1-4}$  are the four crack-tip enrichment functions spanning the asymptotic near-tip displacement field of the Westergaard solution to reproduce the asymptotic mode I and mode II displacement fields in LEFM (Belytschko and Black 1999).

Consider a two-dimensional body subjected to a general mixed-mode loading. The crack-tip enrichment functions are derived from the exact asymptotic displacements near the crack-tip, which are expressed as

$$\begin{aligned} \begin{Bmatrix} u_x \\ u_y \end{Bmatrix} &= \frac{K_I}{2\mu} \sqrt{\frac{r}{2\pi}} \left\{ \begin{aligned} &\cos(\theta/2) [\kappa - 1 + 2\sin^2(\theta/2)] \\ &\sin(\theta/2) [\kappa + 1 - 2\cos^2(\theta/2)] \end{aligned} \right\} \\ &+ \frac{K_{II}}{2\mu} \sqrt{\frac{r}{2\pi}} \left\{ \begin{aligned} &\sin(\theta/2) [\kappa + 1 + 2\cos^2(\theta/2)] \\ &-\cos(\theta/2) [\kappa - 1 - 2\sin^2(\theta/2)] \end{aligned} \right\} \end{aligned} \quad (4.45)$$

where  $(r, \theta)$  belongs to the polar coordinate system having the origin at the crack-tip and tangent to the crack at its tip where  $\theta$  is zero,  $K_I$  and  $K_{II}$  are the stress intensity factors, and  $\mu$  and  $\kappa$  are material parameters, which are given as



$$\mu = \frac{E}{2(1+\nu)}, \kappa = \begin{cases} 3 - 4\nu & \text{for plane strain} \\ (3 - \nu)/(1 + \nu) & \text{for plane stress} \end{cases} \quad (4.46)$$

The nodes of the element containing the crack-tip are enriched in the two Cartesian directions with four crack-tip enrichment functions (Fleming 1997), given as

$$[F_\alpha(r, \theta), \alpha = 1 - 4] = \left[ \sqrt{r} \sin \frac{\theta}{2}, \sqrt{r} \cos \frac{\theta}{2}, \sqrt{r} \sin \theta \sin \frac{\theta}{2}, \sqrt{r} \sin \theta \cos \frac{\theta}{2} \right] \quad (4.47)$$

The displacement approximation in XFEM takes the form

$$\mathbf{u} = \sum_{i \in I} N_i(\mathbf{x}) U_i + \sum_{i \in I^{dis}} N_i(\mathbf{x}) H(\mathbf{x}) a_i + \sum_{i \in I^{tip}} [N_i(\mathbf{x}) \sum_{\alpha=1}^4 F_\alpha(\mathbf{x}) b_{i\alpha}] \quad (4.48)$$

in which, from Figure 4.5,  $I^{dis}$  are the nodes circled (the set of nodes associated with the crack interior), and  $I^{tip}$  are the nodes squared (the set of nodes associated with the crack-tip).

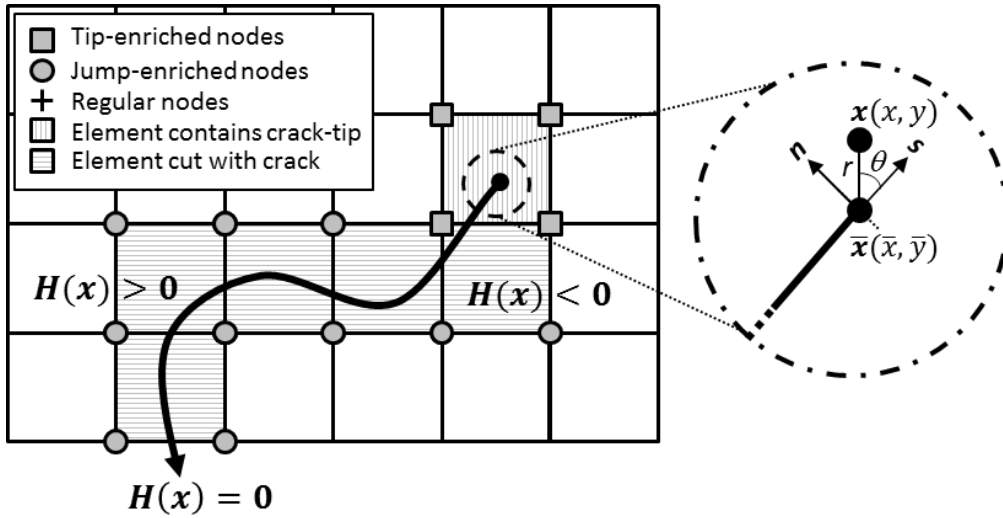


**Figure 4.5. Representation of an arbitrary crack, not aligned with a mesh, with additional degrees of freedom for enriched elements: Jump-enriched by the Heaviside function and tip-enriched by the singular functions (left), and crack-tip with local polar coordinates  $(r, \theta)$ , and normal and tangential coordinates of crack (right)**

#### 4.2.4 Level set method and representation of the implicitly described crack

The level set method is a numerical technique for tracking the evolution of interfaces. It facilitates the construction of enrichment when used with XFEM. The non-planar crack geometry is defined by two orthogonal level set fields that describe the crack surface  $\{\mathbf{x}: \varphi(\mathbf{x}) = 0 \text{ and } \psi(\mathbf{x}) \leq 0\}$ , and crack front  $\{\mathbf{x}: \varphi(\mathbf{x}) = 0 \text{ and } \psi(\mathbf{x}) = 0\}$  [15]. The illustration of the implicit crack representation by level sets is depicted in Figure 4.6. The values of the two functions are used to obtain the location of the crack from the geometric information. Furthermore, the enrichment functions used in the XFEM approximation use a local coordinate system provided by these values. The signed distance to the extended crack surface is represented by  $\varphi$ , and the signed distance to the surface that intersects the crack surface at the crack front (orthogonal to the crack surface) is provided by  $\psi$ . As seen from Figure 4.6, the crack surface is represented by  $\varphi(\mathbf{x}) = 0$  plane (grey surface), and the crack front is represented by the intersection of the planes  $\varphi(\mathbf{x}) = 0$  and  $\psi(\mathbf{x}) = 0$ .

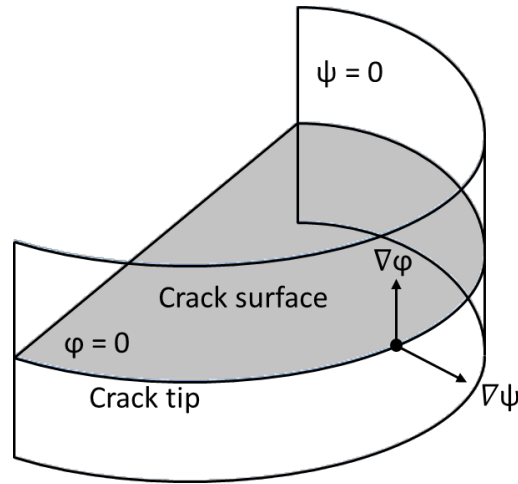


**Figure 4.6. 3D Level set representation by crack surface function  $\varphi$  and crack front function  $\psi$**

The level set representation requires updating in order to construct the new crack surface and crack front as the crack grows. The new start-point of the representation is defined by the crack length increment, which is determined by the crack growth rate. In this regard, a point  $\mathbf{y}$  on the crack front is considered to be located nearest to given  $\mathbf{x}$ . The crack front velocity (crack growth rate) at the point  $\mathbf{y}$  is set to  $\mathbf{F}(\mathbf{y})$ , the value of  $\varphi$  is described as [15]

$$\varphi(\mathbf{x}) = \frac{\mathbf{F}}{\|\mathbf{F}\|} \cdot (\mathbf{x} - \mathbf{y}) \quad (4.49)$$

After obtaining  $\varphi$ ,  $\psi$  can be computed by [15]

$$\psi(\mathbf{x}) = \frac{(\mathbf{F} \times \nabla\varphi) \times \mathbf{F}}{\|(\mathbf{F} \times \nabla\varphi) \times \mathbf{F}\|} \cdot (\mathbf{x} - \mathbf{y}) - \|\mathbf{F}\|\Delta t \quad (4.50)$$

#### 4.2.5 Crack growth algorithm: tracking and control (direction and magnitude)

The onset of cracking can be predicted by contour integral evaluation in a quasi-static situation, however, the crack propagation can be realised by utilising the calculations of the crack advancement direction and magnitude. A crack growth algorithm is developed and implemented in Abaqus incorporating XFEM. The algorithm tracks the crack front and predicts the crack front velocity based on the strain energy release rate by using a crack growth law.

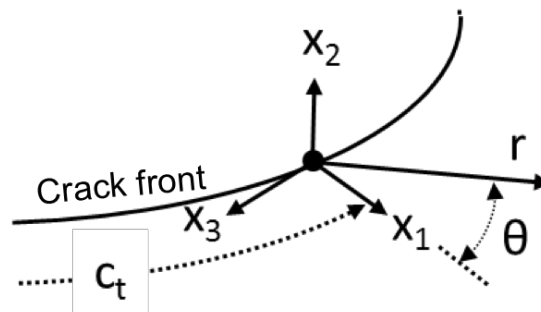


**Figure 4.7. Local coordinate system at a tip point ( $x_1, x_2, x_3$ ) -  $x_1$ : normal to crack front,  $x_2$ : perpendicular to plane of crack,  $x_3$ : tangent to crack front**

Prior to the analysis, level set variables are defined to describe the initial crack geometry, and enriched nodes are determined. In the XFEM analysis, the stresses and displacements of the body under a load are calculated. At the end of the load increment, a post-processing module is executed to obtain the stress intensity factors at the identified crack front with respect to the local coordinate system at tip points (Figure 4.7). The crack growth rates are calculated using the estimated stress intensity factors with respect to a Paris law type crack growth equation. The crack is considered to grow on the  $(x_1, x_3)$  plane, and the angle between the crack growth direction vector and  $x_1$  is determined such that  $K_I$  is maximal. This consideration is consistent with the maximum circumferential (hoop) stress or the maximum principal stress criterion [45], which states that the crack growth is realised in a direction  $\theta = \theta_c$  such that the circumferential (hoop) stress is maximal. As the crack grows with respect to the calculated direction and magnitude, the level set functions are updated. The crack geometry is updated, and the new crack coordinates of crack-tip points are determined for the subsequent analysis.

Under general mixed-mode loadings, the asymptotic near-tip circumferential stress and shear stress are described as

$$\begin{Bmatrix} \sigma_{\theta\theta} \\ \sigma_{r\theta} \end{Bmatrix} = \frac{1}{4\sqrt{2\pi r}} \begin{Bmatrix} 3 \cos(\theta/2) + \cos(3\theta/2) \\ \sin(\theta/2) + \sin(3\theta/2) \end{Bmatrix} + \frac{1}{4\sqrt{2\pi r}} \begin{Bmatrix} -3 \sin(\theta/2) - 3 \sin(3\theta/2) \\ \cos(\theta/2) + 3 \cos(3\theta/2) \end{Bmatrix} \quad (4.51)$$

The circumferential stress in the crack growth direction is a principal stress. In this regard, the angle defining the radial direction of crack growth can be obtained by setting the shear component of the stress ( $\sigma_{r\theta}$ ) to zero. This leads to the following equation

$$\frac{1}{\sqrt{2\pi r}} \cos(\theta/2) \left[ \frac{1}{2} K_I \sin(\theta) + \frac{1}{2} K_{II} (3\cos(\theta) - 1) \right] = 0 \quad (4.52)$$

The angle of crack growth in the crack-tip coordinate system can be expressed as

$$\theta_c = 2 \arctan \frac{1}{4} \left( \frac{K_I}{K_{II}} \pm \sqrt{\left( \frac{K_I}{K_{II}} \right)^2 + 8} \right) \quad (4.53)$$

Using the linear summation rule [46], the interaction of cycle-dependent fatigue crack growth and the time-dependent creep crack growth can be expressed as [47]

$$\left( \frac{da}{dN} \right)^t = \left( \frac{da}{dN} \right)^f + \int \left( \frac{da}{dt} \right)^c dt \quad (4.54)$$

where  $a$  is the crack length,  $N$  is the number of load cycles,  $t$  is the time, and the superscripts  $t, f, c$  are for total, fatigue and creep, respectively. The first part of the equation governs the fatigue contribution per cycle, and the second part is the creep contribution accumulated over a period of time.

Lu et al. [19] showed that the fatigue-creep crack growth of a solid solution strengthened superalloy [16], which is a typical combustor material, can be described by the Paris-Erdogan law type formulation including only one fracture characterising parameter, the  $C_t$ -integral. The crack growth rate including hold-time effects and temperatures in the range of 816 and 927 °C is implicitly in the  $C_t$  value and is defined as

$$\left( \frac{da}{dt} \right) = 0.0447 (C_t)^{0.864} \quad (4.55)$$

### 4.3 Benchmark cases for validation

Starting off with simple two-dimensional geometries and loadings, and then progressing to three dimensions, stress concentrations and nonlinear material behaviour, crack analysis results from the XFEM technique are presented and various benchmark tests have been carried out for validation.

#### 4.3.1 Creep damage around a crack-tip

A creep crack growth analysis has been performed and validated by a plain strain solution for power-law creep relaxation of stresses around a crack-tip [23]. The intention of this benchmarking example is to review the fracture mechanics parameters of creep crack growth by means of transition creep and steady-state creep with an emphasis of creep-brittle and creep-ductile material behaviour. The problem is composed of a plain-strain edge cracked configuration subjected to two-steps loading. First, instantaneous nominal tensile stress Mode I is applied on the circular boundary and the second step holds the loading constantly. In the first step, since the amount of time is insufficient in satisfying any creep deformation, the response is purely elastic and the crack-tip field can be characterised by LFM due to suddenly applied loading. The second step imposes a constant load over time that activates the subsequent creep deformation causing a relaxation of the crack-tip stresses until a steady-state distribution is reached satisfying  $\{t \rightarrow \infty\}$ .

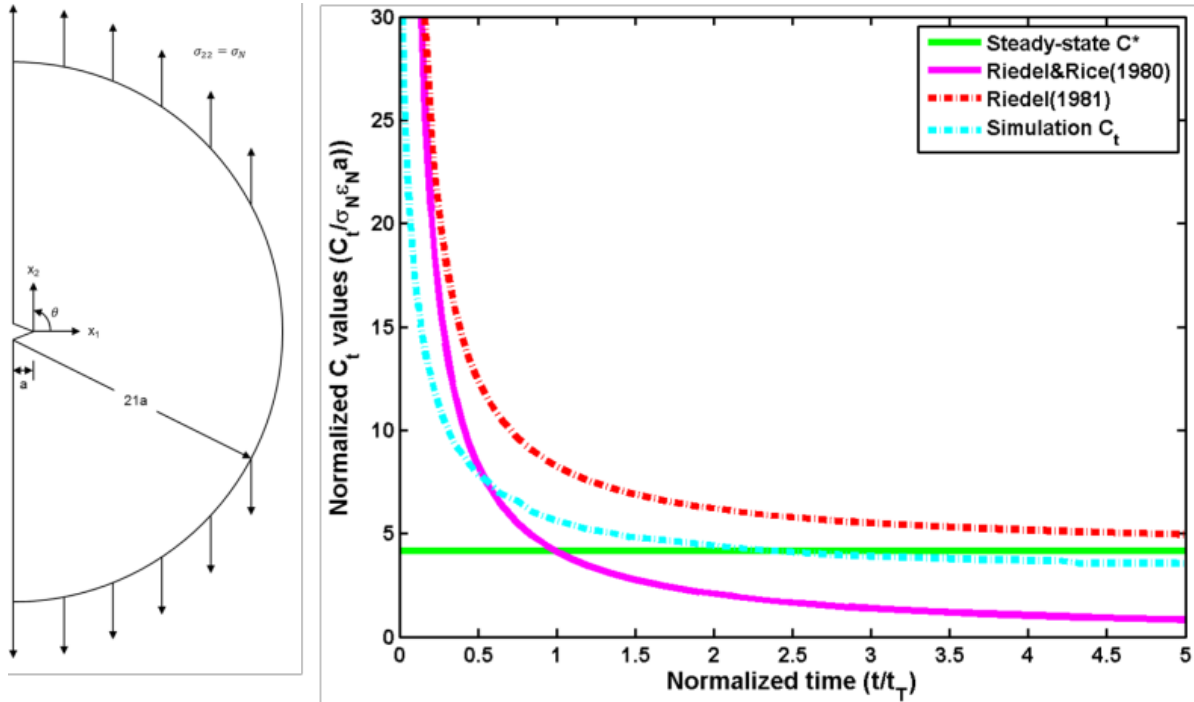


Figure 4.8. Geometry of shallow edge-crack specimen under plain strain under nominal stress conditions.

The material is assumed to be isotropic elastic with  $E=200$  GPa and  $\nu=0.3$ . The material properties for the power law  $A$  and  $n$  are  $5.0 \times 10^{-12}$  per hour and 3 respectively. A far-field constant tensile load of  $\sigma_N=E/2000$  is applied as a concentrated load to the circular boundary edge of the geometry. Four different solutions for normalised  $C_t$  values have been compared

in Figure 4.8 that are obtained by steady state  $C^*$ , Riedel&Rice (1981 approximation, Riedel (1981) interpolation and the numerically calculated  $C_t$ . The transition time ( $t_T$ ) from small-scale creep to extensive creep has been calculated as 22.5 hours. It is apparent that there is a certain period of time where the elastic strains are dominant in the geometry, except a small creep zone around the crack-tip. Therefore, the  $C_t$  parameter can be used to characterize the growth rate of the creep zone around the crack-tip under the assumption of small-scale yielding and can be represented by SIF,  $K_I$ .

However, a steady-state distribution of stresses and creep damage possibly cannot have sufficient time to be developed around the crack-tip in creep-brittle material. Therefore, the creep crack growth assessment of nickel-based super alloys can be correlated with  $C_t$ -Integral evaluation with the assumption of small-scale creep conditions. In fact, the propagation rate of the crack-tip is assumed to be comparable to the creep zone expansion rate.

### 4.3.2 Thermally stressed body case

The structural integrity evaluation of the components, where high temperature environment and severe thermal loadings exist, is essential. In the vicinity of a crack in the structure, the stresses and deformation during transients can vary. The crack field quantities formed under thermo-mechanical loading must be determined and correlated to the intensity parameters. The conformance of the fracture mechanics parameters must be assessed.

A thermo-elasticity problem was examined and the accuracy of the calculations for a single-edged notched specimen under a thermal load was benchmarked with plain strain thermo-mechanical crack analysis [26, 48]. The geometry is depicted in Figure 4.9. The length ( $2L$ ) of the specimen is 2.032 m (80 in), the width ( $W$ ) is 0.508 m (20 in), and the initial crack length ( $a$ ) is the half width. The energy release rate was calculated by the finite domain integral method in a thermo-mechanical field [49, 50] generated by a thermally stressed body including a mathematically sharp crack. The through-thickness edge cracked strip, with crack length,  $a$ , is axially constrained as a boundary condition (at zero and  $2L$  in the length direction) subjected to linear temperature variation through the width with a zero temperature at mid-width. The material is isotropic and linear elastic, with a Young's modulus of 207 GPa ( $30 \times 10^6$  lb/in<sup>2</sup>), a Poisson's ratio of 0.3, and a thermal expansion coefficient of  $1.35 \times 10^{-5}$  per °C ( $7.5 \times 10^{-6}$  per °F). The problem has been solved by a sequentially coupled analysis. The temperature distribution was obtained by a heat transfer analysis that was set on the right and left edges of the geometry and was followed by a stress analysis under the thermal load. As seen from the Figure 4.9, the normalised SIF values conform well to the benchmark solutions over the contours. Furthermore, the calculation revealed a stable solution starting from the third contour leading to very little variation in the results. Using a 3D mesh, even at coarse meshes, provided more accurate results closer to the average SIF over contours, starting from the first contour. This is attributed to capturing different aspect ratios of the element layers across the thickness, which result in variation of SIF values, since the intersection of the crack front with external surfaces has large aspect ratios, whereas the internal layers have relatively lower aspect ratios.

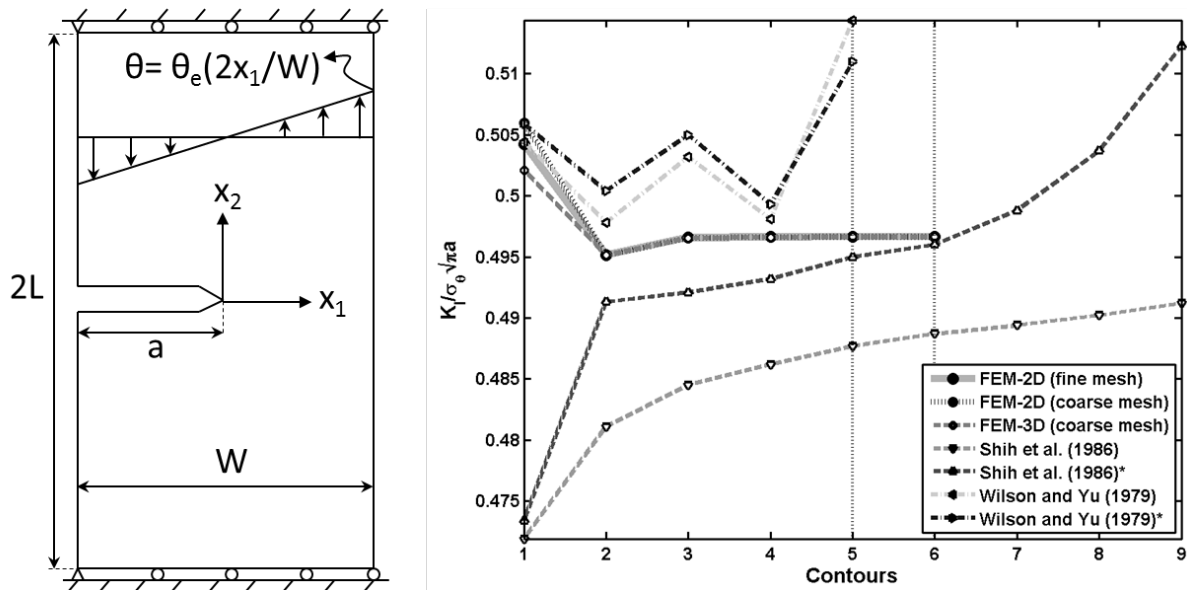


Figure 4.9. Single-edge notch specimen geometry subjected to thermal field

In general, increasing the number of computational contours provides more stable results; however, in Figure 4.9 the solutions obtained from the literature reveal either fluctuation around an average value or non-converging values. In this regard, the crack-tip solution with both fine and coarse mesh provided very stable results compared to the benchmark cases.

Table 4.2. Comparison of normalised SIF results

	FEM-2D (fine mesh)	FEM-2D (coarse mesh)	FEM-3D (coarse mesh)	Shih et al. (1986)	Shih et al. (1986)*	Wilson and Yu (1979)	Wilson and Yu (1979)*
Average	0.4977	0.4979	0.4973	0.4857	0.4951	0.5036	0.5043

### 4.3.3 Compact tension (3-D) case

In the previous sections, the validity of the stress intensity factor was presented for the time-dependent behaviour under a constant remote load and the crack-tip response with respect to the temperature. The time-dependent creep mechanisms under constant pressure at high temperatures are the main damage drivers in combustors during the combustion process. However, the cycle-dependent fatigue mechanisms are activated by the combustion instabilities as high amplitude pressure oscillations are induced. In this section, first the various configurations are analysed for the XFEM method including the mesh size and mesh type in order to find the optimum configuration. A comparison between numerical results of XFEM and FEM, and analytical results is presented. Second, crack propagation rates including hold-time and temperature effects are presented.

The fracture mechanics analyses were performed for two cases: stationary and growing cracks. The first one is for stationary cracks, in which the stress intensity factors were calculated with respect to the computation contours around the crack-tip. In this approach, the *Abaqus* implementation of XFEM was directly utilised including node enrichment by jump and crack-tip functions. However, for crack growth analysis *Abaqus* provides limited

capability, only the crack path can be obtained, but fracture parameters cannot be calculated. Therefore, in the second approach a user-defined algorithm was developed that incorporates *Abaqus* to perform a quasi-static fracture mechanics analysis. As described in section 4.2, the contour evaluation was performed by the domain integral method to calculate the  $J$ -integral, and the interaction integral was used to extract the stress intensity factors. The stress intensity factors were used to calculate the  $C_I$ -integral values. The direction of the crack growth is calculated by the maximum circumferential stress criterion, and the magnitude of the growth by Paris-type law.

The fatigue/creep crack growth simulations were performed on the CT specimen, which is shown in Figure 4.10. The dimensions and material properties are adopted from Lu et al. [19]. The thickness of the specimen is 3.2 mm. The height and the width are 61.0 mm and 50.8 mm, respectively. The material is a typical nickel-based superalloy, Alloy230 [16]. The specimen configuration is in compliance with the American Society for Testing and Materials (ASTM) standard [51]. The theoretical Mode I stress intensity factor  $K_I$  of a CT specimen was calculated using the following equation [52]:

$$K_I = \frac{f\left(\frac{a}{W}\right)P}{B\sqrt{W}} \quad (4.56)$$

where the geometry factor is given by

$$f\left(\frac{a}{W}\right) = \frac{2+\frac{a}{W}}{\left(1-\frac{a}{W}\right)^{3/2}} \left[ 0.886 + 4.64\left(\frac{a}{W}\right) - 13.32\left(\frac{a}{W}\right)^2 + 14.72\left(\frac{a}{W}\right)^3 - 5.60\left(\frac{a}{W}\right)^4 \right] \quad (4.57)$$

where  $P$  is the applied load,  $B$  is the thickness of the specimen,  $a$  is the crack length and  $W$  is the width of the specimen.

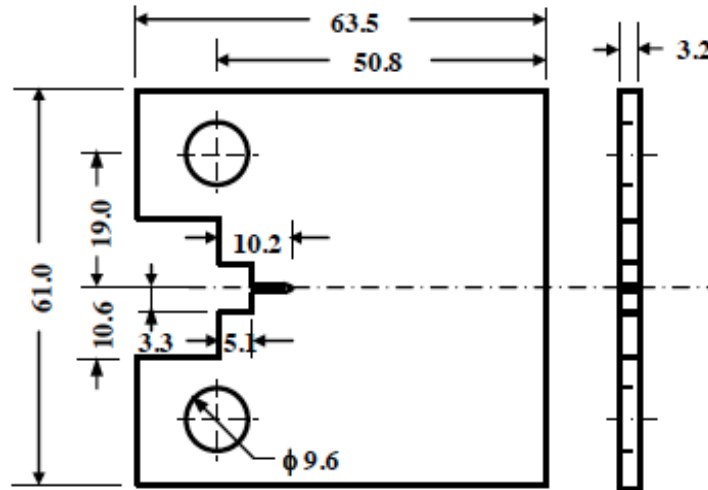


**Figure 4.10. Geometry and dimensions of a compact tension (CT) specimen (units: [mm]) [19]**

As discussed before, the XFEM enables modelling of the crack geometry independently of the structure geometry. This feature obviates the stress singularities without an explicitly defined mesh at the crack-tip, and remeshing for crack growth analysis is avoided. However, the solution using the XFEM method is not completely mesh independent. Even though the XFEM overcomes the crack-tip singularity by introducing tip enrichment function at nodes

associated with the crack-tip, a refined (optimum) mesh is necessary. The tip enrichment is applied to the nodes associated with the crack-front in the three-dimensional geometry. Setting the nodes close to the crack-front by sufficiently refining the mesh can accurately capture the stress gradients, due to the singular nature of the asymptotic fields. Since the crack geometry does not need to conform to the global mesh of the geometry, thus remeshing is not necessary as the crack grows, an enriched partition was created, and a high mesh density is introduced in this region. A global element size is set to constant in the analyses as 0.001 m. And a refined mesh is generated in the region of crack growth prior to the analysis. The usage of the XFEM method in *Abaqus* only provides solutions with the linear brick or tetrahedron elements. A numerical test matrix, presented in Table 4.3, was followed to find the best finite element mesh configuration. The stress intensity factor calculations over the computation contours and crack lengths were compared according to the element type (brick and tetrahedron) and mesh size (0.001, 0.0005 and 0.0002). The element type and size combinations are named as  $m_{11}$ ,  $m_{21}$ ,  $m_{31}$ ,  $m_{12}$  and  $m_{22}$ .

**Table 4.3. Numerical test matrix**

Element size [m]	Brick elements	Tetrahedron elements
0.001	$m_{11}$	$m_{12}$
0.0005	$m_{21}$	$m_{22}$
0.0002	$m_{31}$	

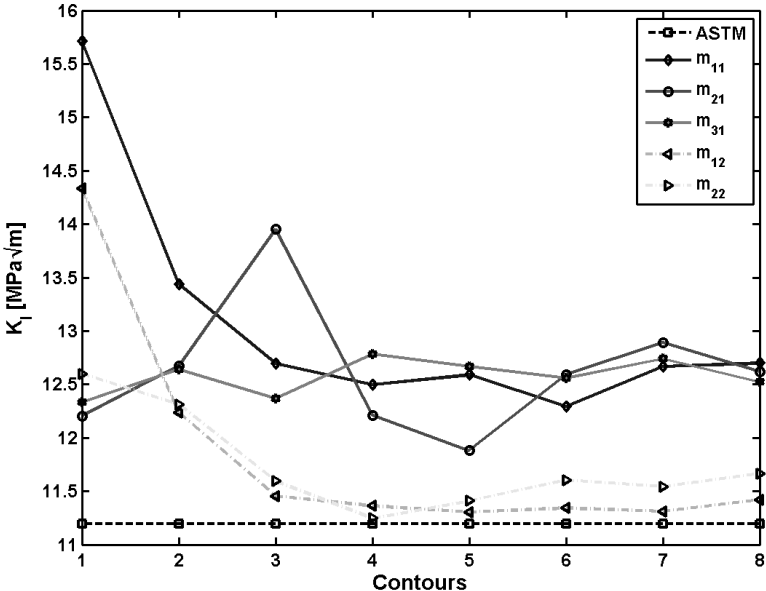


**Figure 4.11. The mesh configuration dependence of SIF calculated at a crack length of 0.015 m**  
**Table 4.4. The average of the SIF values over the contours and the relative errors at Ref: ASTM**

	$m_{11}$	$m_{21}$	$m_{31}$	$m_{12}$	$m_{22}$
Averaged	13.07	12.62	12.57	11.84	11.74
Error [%]	16.7	12.7	12.3	5.7	4.9



In Figure 4.11, the computed SIF values are shown with respect to the contours around the crack-tip. Note that the variation of the SIF values in the thickness direction due to plane stress conditions at the free surface and the plane strain conditions inside the bulk material result in different crack growth magnitudes at thickness layers [15]. However, in this analysis straight crack front is assumed. Therefore, the SIF values were averaged across the thickness. As seen in Figure 4.11, reducing the element size in the analysis for both element types provides more accurate SIF predictions close to the crack-tip, the first two contours. This implies that a higher degree of path independence for the SIF values, which are extracted from the path-independent  $J$ -Integral, was achieved by reducing the mesh size. A certain fluctuation around an average SIF value calculated over the contours is present for brick elements. According to the largest and smallest element sizes for this element type, increasing the mesh density, in other words reducing the element size, revealed an improvement in this regard. However, this fluctuation for the  $m_{21}$  case is larger between the contours 2 and 5, and following all the cases converges to a very short range of a SIF value. This is attributed to local mesh topology generated by the FE software. Moreover, using a higher mesh density reduced the magnitude of the fluctuation; however, a certain fluctuation of SIF values about an average value remained, which is attributed to the discretization errors. Analysis over eight contours is found to be the optimum number for computation regarding accuracy. Thus, further analyses were performed using eight contours. On the other hand, the results of the tetrahedron elements lead to more accurate results in the analytical calculation (ASTM) in comparison to the results of the brick elements. However, there is neither an average value of the SIF, nor convergence over the contours. Moreover, increasing the number of contours generates more deviation from the analytical results. In Table 4.4, the average of the SIF values over the eight contours, and across the thickness, and the relative errors with respect to the analytical solution are listed. From the test cases listed in Table 4.3, increasing the mesh density leads to a higher convergence to the analytical result, and using the tetrahedron elements results in a higher accuracy with respect to the analytical result. However, as a general practice, if the first contour of the calculation is ignored due to the numerical inaccuracies in the stresses and strains at the crack-tip, reducing the tetrahedron element size reveals more deviation from the analytical result as the calculation contours are increased. This is not in line with the general finite element analysis concepts.

In Figure 4.12, the mesh configuration dependence of the SIF during crack growth and the relative errors with respect to the analytical solutions are presented. Note that the SIF values are averaged across the thickness and the computation contours at each crack growth step. The analyses with brick elements produced a very stable error plot during the crack growth, whereas the usage of tetrahedron elements results in a very large range of fluctuation of the relative error during the crack growth. Even though the tetrahedron elements provided more accurate results to the analytical solutions, the analysis generated a very unstable solution. The snapshots of the CT specimen Von Mises stress of crack growth are depicted in Figure 4.13. At the initial stages of the crack growth, stresses are produced in a confined region. When the crack growth progresses, the other features such as loading holes in the CT

specimen affect the stress distribution in the body; however, the main crack driving process zone is very local around the crack-tip. In the third snapshot, the crack already passes the mid-specimen, and produces two high stress regions in the body, one is ahead of the crack-tip, and the other is at the end section of the specimen because high compressive stresses are generated due to crack opening. While the crack approaches the end of the specimen, these two regions meet each other. In conjunction with Figure 4.12, the rate of the SIF values decreases until a crack length of 0.0023 m, and then levels off afterwards. Until this crack length, the capacity of the body to resist fracture is high, since a significant portion of the body is un-cracked, thus has a higher integrity. However, after this crack length, the resistive forces against the crack, emanating from the body, weaken because there is less material remaining ahead of the crack-tip to resist fracture. In this case, the SIF values plot reaches a constant slope, since the crack growth experiences extra-resistive forces.

Using tetrahedron elements a free mesh is generated, which means that the elements in the thickness direction and the elements bisected by the crack at each advancement step are different. When a stationary crack is analysed, the stress intensity factors were averaged across the thickness, therefore the effects of the number of elements in the thickness direction are avoided (Figure 4.11). However, in the crack growth analysis non-even mesh topology, created using the tetrahedron elements, provides a highly non-stable solution (Figure 4.12). On the other hand, using brick elements creates a structured mesh in the enriched region ahead of the crack-tip and also in the thickness direction. Therefore, as seen in Figure 4.12 the errors fall into an error-band, and a stable solution is obtained. As a conclusion, using brick elements provides a very stable solution and accuracy within a certain limit. Furthermore, mesh refinement improves the accuracy of the solution till a certain mesh size, which is sufficiently fine to capture the crack-tip stresses.

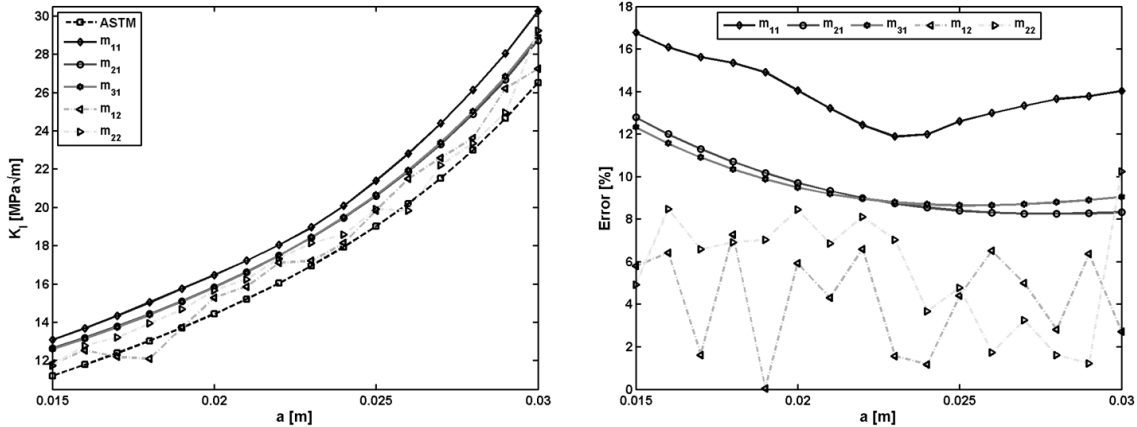


**Figure 4.12. The mesh configuration dependence of SIF during crack growth and the relative errors Ref: ASTM**

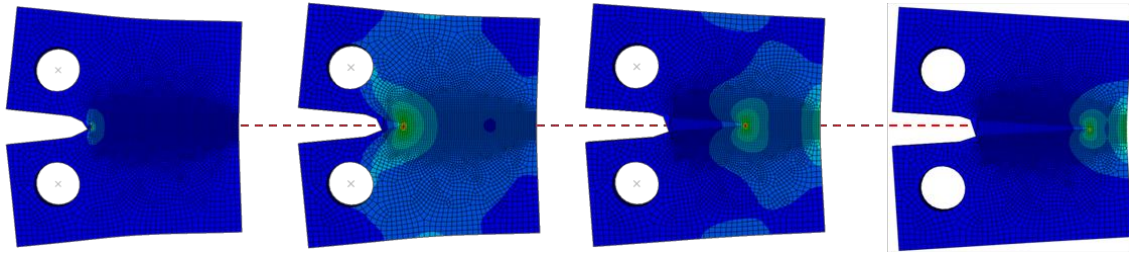


**Figure 4.13. Snapshots of CT specimen Von Mises stress of crack advancement**

The optimum mesh configuration for the XFEM analysis is obtained from the numerical tests. It includes a mesh size of 0.0005 m, which provided good accuracy with less computational cost compared to the mesh size of 0.0001 m. And according to the aforementioned conclusions, linear brick elements are used for the mesh type in the XFEM solutions, in which a structured mesh topology ahead of the crack-tip and across the thickness is created. A comparative analysis was performed to assess the accuracy of the predicted stress intensity factors using the standard FEM, XFEM and analytical solution with respect to the crack lengths and is presented in Figure 4.14. In the figure, the superscript ‘1’ refers to the analysis of the geometry depicted in Figure 4.10 (plane stress condition), and the superscript ‘2’ is for a geometry with a thickness equal to one fourth of the width (the thickness is about 4 times higher compared to the geometry in Figure 4.10), which supports the plane strain conditions. In the standard FEM solution, a focused mesh (Figure 4.3) was generated, and mid-side nodes were positioned to facilitate the modelling of the crack-tip singularity, which is due to the singular strain field around the sharp crack. The focused mesh generation was repeated in every crack propagation step. In this analysis 20-node quadratic brick elements are used, and the crack-tip mesh was created by using 15-node quadratic triangular prism elements with 16 elements at the crack-tip. As seen in Figure 4.14, the results from the standard FEM and XFEM methods are in very close agreement for both the plane stress and plane strain problems, and the deviation of the results from the analytical results is maintained for the different crack lengths. However, as seen from the figure the relative errors are higher in the plane stress problem compared to the plane strain problem. The main reason is that the analytical equation (ASTM), which is obtained from the standard test methods for crack growth [51], is favourable for plane strain problems. The thickness term in this equation is not dependent on either plane stress or strain condition; however, validity of the equation is defined with an aspect (width-thickness) ratio. Therefore, close to the lower limit of the aspect ratio, the geometry obeys the plane stress conditions. In this regard, if the relative errors are calculated with respect to the standard FEM solution rather than the analytical results, in which the calculated SIF values are lower, in Figure 4.11 and Figure 4.12, the analysis with linear brick elements reveals a higher accuracy over the one with tetrahedron elements.

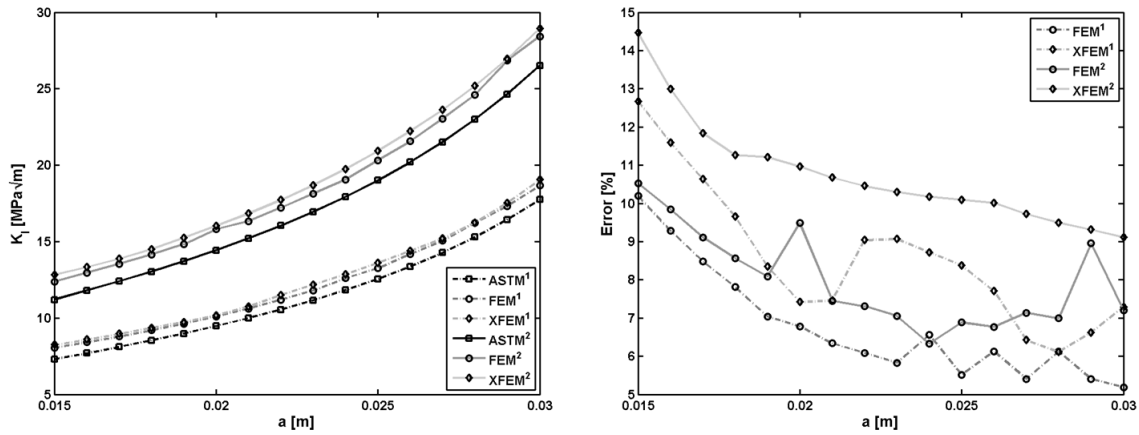


**Figure 4.14. Comparison of the SIF values calculated by the analytical solution, standard FEM and XFEM, and the relative errors Ref: ASTM (superscript '1': plane-stress condition - superscript '2': plane-strain condition)**

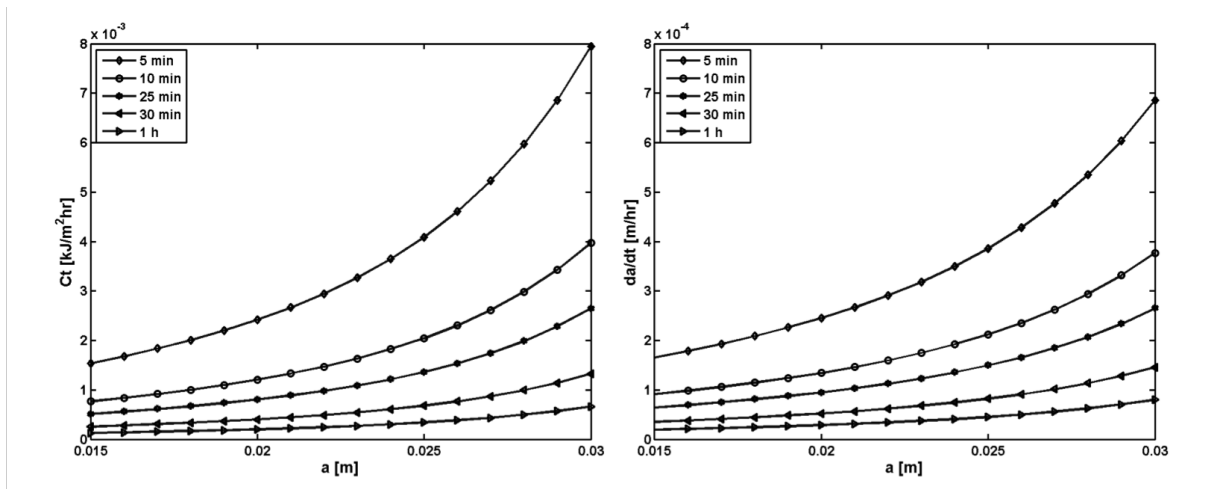


**Figure 4.15.  $C_I$  integral and the unit time crack growth rates ( $da/dt$ ) as a function of crack length for Alloy230 at 816 °C with hold times**

The fatigue-creep crack growth is characterised by superimposing hold times on the triangular waveform used in FCG at maximum load [19]. In Figure 4.15, the evolution of the  $C_I$ -integral and the unit crack growth rates at 816 °C as a function of crack length is depicted for Alloy230. There is a substantial decrease in the  $C_I$  values when the hold times are increased due to the time-dependent creep dominance on the damage mechanism. For lower hold times, the crack grows faster, which consumes more lifetime.

The crack growth rate under constrained conditions decreases due to the stress relaxation, which exhibits significant sensitivity to temperature, mean pressure and hold-time. This is in line with experiments from the literature [21].

The investigation in the CT specimen only includes straight growing cracks. However, in complex geometries relevant to industrial applications, the presence of different geometrical features perturbs the crack path, which results in curvilinear crack growth. The curvature of the crack paths can occur due to geometric asymmetry, multi-axial loading or evolution of material properties under operation. Crack growth behaviour in a modified CT specimen [53], which includes an additional hole in the geometry, was investigated. The additional hole,

which causes an asymmetry in the geometry, is located in such a way that the growing crack leans towards the hole and sinks (approaches) in the hole.

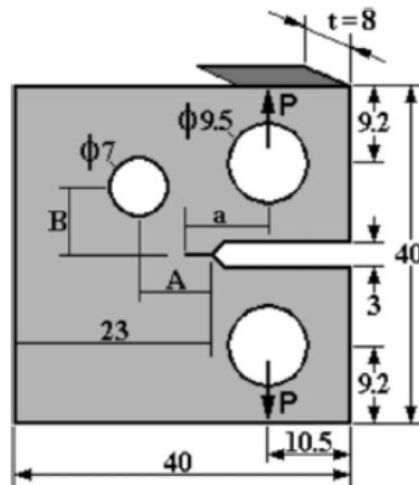


**Figure 4.16. Modified CT specimen geometry (sink-hole configuration:  $A=8.4$  mm and  $B=6.9$  mm) [53]**

In the curved crack path analysis the crack propagation direction, which is a function of  $K_I$  and  $K_{II}$ , is calculated. The new crack front coordinates are updated by utilising the user-defined algorithm that uses the crack length and the crack propagation direction governed by the calculated stress intensity factors. Next, the crack geometry is updated by extending line segments with a kink angle between them, which approximates the curved crack path. The penalty function in the analysis is set such that either the crack reaches the hole or passes the minimum (or maximum) x-coordinate of the hole. When one of these conditions is satisfied, the analysis is terminated. Besides, the crack path is not prescribed prior to the analysis; therefore a sufficiently large region of the mesh is refined, where the crack path will likely coincide.

In Figure 4.17 (a) the digital image of the actual specimen and FEM prediction [53], and (b) XFEM crack path predictions are shown. Different crack increments were used in the XFEM predictions. When smaller crack length increments were used, the computational time was significantly increased due to the higher number of calculation steps. The crack length increments of 1.0 mm and 2.0 mm, used in the XFEM analysis, showed that the crack does not approach the hole, instead it misses the hole. The deviation from the actual crack path is caused by the insufficient calculation steps and crack angles to lean the crack towards the hole. As the crack length increment in the simulation is decreased, crack turning towards the hole is brought forward. The crack length increment of 0.3 mm results in a very early turn of the crack towards the hole, which is not in line with the experiment. This is attributed to the test conditions in practice that cause higher crack increments in the material. The measured crack path is in very good agreement with the XFEM prediction with 0.5 mm crack length increment.

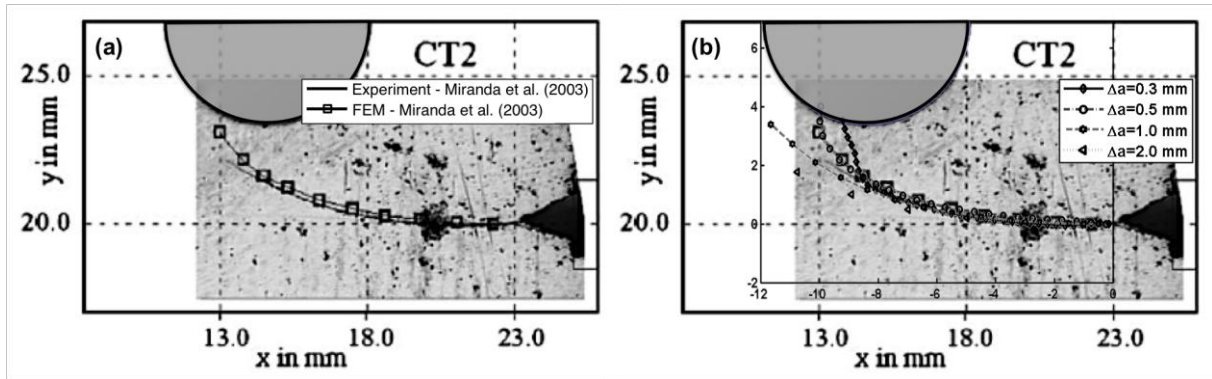


Figure 4.17. Crack path: (a) experiment and FEM [53] and (b) XFEM with different crack length increments ( $\Delta a$ )

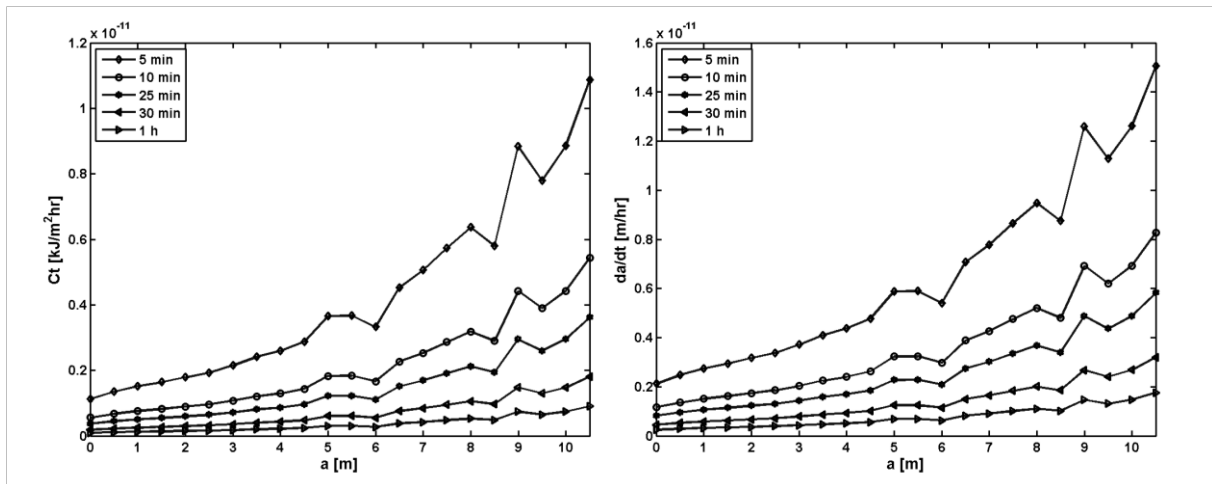


Figure 4.18.  $C_I$ -integral and the unit time crack growth rates ( $da/dt$ ) as a function of crack length for Alloy230 at 816 °C with hold times

In Figure 4.18, the calculation of  $C_I$ -integral and unit time crack growth rate of the modified CT specimen is presented. The  $C_I$  values over the crack length have the same incremental trend as seen in the standard CT-specimen results. However, as seen from the figure the values are perturbed due to curved crack path. The stress-state around the crack-tip is under the influence of other geometric features, the additional hole as in this example. Therefore, the crack growth rate is highly perturbed as the crack front approaches the additional hole.

It should be noted that a number of interacting variables involved in crack growth behaviour in the modified CT-specimen test under fatigue/creep conditions, such as crack path, microstructure, local strain fields, strain rate, creep, temperature and corrosion. Therefore, the crack path is not only governed by the stress-state but also by these interacting variables. In this regard, a multi-scale analysis will address the microstructural effects in the crack path.

## 4.4 Conclusions

A three-dimensional finite element method for crack growth analyses of a typical gas turbine material, a nickel-based superalloy, including the cycle-dependent fatigue and time-dependent creep, was developed based on the eXtended finite element method (XFEM).

The crack conformation is performed by level set methods, associating with the XFEM method. This implementation enables modelling the crack without explicitly meshing the crack faces, and setting the crack geometry independently of the mesh of the main geometry. Thus, the remeshing procedure is avoided in crack growth analysis. The jump in the displacement field across the crack is captured by using special enrichment functions with additional degrees of freedom.

A user-defined algorithm was developed to take creep effects into account besides the already available linear elastic fatigue effect in the general-purpose finite element software, *Abaqus*. In this way, the meshing capabilities of the finite element software and the contour evaluation method for the fracture parameters can be used. On the other hand, the algorithm controls the analysis flow by means of tracking the crack-front, and quantifying the crack growth by the predicted crack growth direction and magnitude. The crack growth magnitude of Alloy230 was calculated with only one fracture parameter, the  $C_I$ -integral, which includes the fatigue and creep effects obeying small-scale yielding assumption. The calculated  $C_I$  values include the load amplitude, stress relaxation with hold-time and temperature effects.

The combined usage of the user-defined algorithm and the finite element software within the framework of XFEM eliminates the difficulties of crack modelling and improved the crack-tip evaluation and advancement in the arbitrary geometries. Furthermore, resolving the time-dependent creep crack behaviour in Alloy230 under the LFM concepts reduces the computational time.

XFEM-based fracture mechanics analysis provides an advantage in computation cost over FEM. However, it is difficult to draw a fair conclusion on the accuracy of calculated stress intensity factors in complex structures relevant to industrial applications without correlations to observations in practice, even though XFEM proved to be accurate in benchmark cases as presented in this work.

## Acknowledgement

The authors would like to acknowledge funding of this research by the EC in the Marie Curie Actions – Networks for Initial Training, under call FP7-PEOPLE-2007-1-1-ITN, Project LIMOUSINE with project number 214905.

## References

[1] Belytschko, T., and Black, T., 1999, "Elastic crack growth in finite elements with minimal remeshing," *International Journal for Numerical Methods in Engineering*, 45(5), pp. 601-620.

- [2] Moës, N., Dolbow, J., and Belytschko, T., 1999, "A finite element method for crack growth without remeshing," *International Journal for Numerical Methods in Engineering*, 46(1), pp. 131-150.
- [3] Melenk, J. M., and Babuška, I., 1996, "The partition of unity finite element method: Basic theory and applications," *Computer Methods in Applied Mechanics and Engineering*, 139(1–4), pp. 289-314.
- [4] Belytschko, T., Moes, N., Usui, S., and Parimi, C., 2001, "Arbitrary discontinuities in finite elements," *International Journal for Numerical Methods in Engineering*, 50(4), pp. 993-1013.
- [5] Stolarska, M., Chopp, D. L., Moës, N., and Belytschko, T., 2001, "Modelling crack growth by level sets in the extended finite element method," *International Journal for Numerical Methods in Engineering*, 51(8), pp. 943-960.
- [6] Moes, N., Gravouil, A., and Belytschko, T., 2002, "Non-planar 3D crack growth by the extended finite element and level sets - Part I: Mechanical model," *International Journal for Numerical Methods in Engineering*, 53(11), pp. 2549-2568.
- [7] Gravouil, A., Moes, N., and Belytschko, T., 2002, "Non-planar 3D crack growth by the extended finite element and level sets - Part II: Level set update," *International Journal for Numerical Methods in Engineering*, 53(11), pp. 2569-2586.
- [8] Sukumar, N., Chopp, D. L., and Moran, B., 2003, "Extended finite element method and fast marching method for three-dimensional fatigue crack propagation," *Engineering Fracture Mechanics*, 70(1), pp. 29-48.
- [9] Daux, C., Moes, N., Dolbow, J., Sukumar, N., and Belytschko, T., 2000, "Arbitrary branched and intersecting cracks with the extended finite element method," *International Journal for Numerical Methods in Engineering*, 48(12), pp. 1741-1760.
- [10] Moes, N., and Belytschko, T., 2002, "Extended finite element method for cohesive crack growth," *Engineering Fracture Mechanics*, 69(7), pp. 813-833.
- [11] Dumstorff, P., and Meschke, G., 2007, "Crack propagation criteria in the framework of X-FEM-based structural analyses," *Int J Numer Anal Met*, 31(2), pp. 239-259.
- [12] Belytschko, T., Chen, H., Xu, J. X., and Zi, G., 2003, "Dynamic crack propagation based on loss of hyperbolicity and a new discontinuous enrichment," *International Journal for Numerical Methods in Engineering*, 58(12), pp. 1873-1905.
- [13] Song, J. H., and Belytschko, T., 2009, "Cracking node method for dynamic fracture with finite elements," *International Journal for Numerical Methods in Engineering*, 77(3), pp. 360-385.
- [14] Elguedj, T., Gravouil, A., and Combescure, A., 2007, "Mixed augmented lagrangian-extended finite element method for modelling elastic-plastic fatigue crack growth with unilateral contact," *International Journal for Numerical Methods in Engineering*, 71(13), pp. 1569-1597.
- [15] Shi, J. X., Chopp, D., Lua, J., Sukumar, N., and Belytschko, T., 2010, "Abaqus implementation of extended finite element method using a level set representation for three-dimensional fatigue crack growth and life predictions," *Engineering Fracture Mechanics*, 77(14), pp. 2840-2863.



- [16] Haynes International Inc., 2009, "HAYNES 230 Alloy, High Temperature Alloys Brochure, Publication No.: H-3024E."
- [17] Lu, Y. L., Liaw, P. K., Wang, G. Y., Benson, M. L., Thompson, S. A., Blust, J. W., Browning, P. F., Bhattacharya, A. K., Aurrecoechea, J. M., and Klarstrom, D. L., 2005, "Fracture modes of HAYNES® 230® alloy during fatigue-crack-growth at room and elevated temperatures," *Materials Science and Engineering: A*, 397(1–2), pp. 122-131.
- [18] Lu, Y. L., Chen, L. J., Liaw, P. K., Wang, G. Y., Brooks, C. R., Thompson, S. A., Blust, J. W., Browning, P. F., Bhattacharya, A. K., Aurrecoechea, J. M., and Klarstrom, D. L., 2006, "Effects of temperature and hold time on creep-fatigue crack-growth behavior of HAYNES® 230® alloy," *Materials Science and Engineering: A*, 429(1–2), pp. 1-10.
- [19] Lu, Y. L., Liaw, P. K., Sun, Y., Wang, G. Y., Thompson, S. A., Blust, J. W., Browning, P. F., Bhattacharya, A. K., Aurrecoechea, J. M., and Klarstrom, D. L., 2007, "Hold-time effect on the elevated-temperature crack growth behavior of solid-solution-strengthened superalloys," *Acta Materialia*, 55(3), pp. 767-775.
- [20] Roy, A. K., Chatterjee, S., Hasan, M. H., Pal, J., and Ma, L., 2010, "Crack-growth behavior of alloy 230 under creep–fatigue conditions," *Materials Science and Engineering: A*, 527(18–19), pp. 4830-4836.
- [21] Bache, M. R., Johnston, R. E., Cook, T. S., Robinson, B. J., and Matlik, J. F., 2012, "Crack growth in the creep-fatigue regime under constrained loading of thin sheet combustor alloys," *Int J Fatigue*, 42(0), pp. 82-87.
- [22] Pataky, G. J., Sehitoglu, H., and Maier, H. J., 2013, "High temperature fatigue crack growth of Haynes 230," *Materials Characterization*, 75(0), pp. 69-78.
- [23] Bassani, J. L., and McClintock, F. A., 1981, "Creep relaxation of stress around a crack tip," *International Journal of Solids and Structures*, 17(5), pp. 479-492.
- [24] Riedel, H., 1981, "Creep Deformation at Crack Tips in Elastic-Viscoplastic Solids," *Journal of the Mechanics and Physics of Solids*, 29(1), pp. 35-49.
- [25] Riedel, H., and Rice, J. R., 1980, "Tensile cracks in creeping solids," *Fracture Mechanics: 12th Conference*, pp. 112-130.
- [26] Shih, C. F., Moran, B., and Nakamura, T., 1986, "Energy release rate along a three-dimensional crack front in a thermally stressed body," *International Journal of Fracture*, 30(2), pp. 79-102.
- [27] Hutchinson, J. W., 1968, "Singular behaviour at the end of a tensile crack in a hardening material," *Journal of the Mechanics and Physics of Solids*, 16(1), pp. 13-31.
- [28] Rice, J. R., and Rosengren, G. F., 1968, "Plane strain deformation near a crack tip in a power-law hardening material," *Journal of the Mechanics and Physics of Solids*, 16(1), pp. 1-12.
- [29] Nikishkov, G. P., and Atluri, S. N., 1987, "Calculation of Fracture-Mechanics Parameters for an Arbitrary 3-Dimensional Crack, by the Equivalent Domain Integral Method," *International Journal for Numerical Methods in Engineering*, 24(9), pp. 1801-1821.
- [30] Yau, J. F., Wang, S. S., and Corten, H. T., 1980, "A Mixed-Mode Crack Analysis of Isotropic Solids Using Conservation-Laws of Elasticity," *J Appl Mech-T Asme*, 47(2), pp. 335-341.

- [31] Shih, C. F., and Asaro, R. J., 1988, "Elastic-Plastic Analysis of Cracks on Bimaterial Interfaces .1. Small-Scale Yielding," *J Appl Mech-T Asme*, 55(2), pp. 299-316.
- [32] Li, F. Z., Shih, C. F., and Needleman, A., 1985, "A Comparison of Methods for Calculating Energy-Release Rates," *Engineering Fracture Mechanics*, 21(2), pp. 405-421.
- [33] Moran, B., and Shih, C. F., 1987, "A General Treatment of Crack Tip Contour Integrals," *International Journal of Fracture*, 35(4), pp. 295-310.
- [34] Liaw, P. K., and Saxena, A., 1986, "Remaining Life Estimation of Boiler Pressure Parts-Crack Growth Studies," Electric Power Research Institute, Palo Alto, CA.
- [35] Saxena, A., "For the characterization of creep-crack-growth behavior in 304 stainless steel," *Proc. Fracture Mechanics: Proceedings of the 12th National Symposium on Fracture Mechanics.*, ASTM, pp. 131-151.
- [36] Landes, J. D., and Begley, J. A., 1976, "Fracture mechanics approach to creep crack growth," *Mechanics of crack growth*, ASTM, pp. 128-148.
- [37] Nikbin, K. M., Webster, G. A., and Turner, C. E., 1976, "Relevance of nonlinear fracture mechanics to creep cracking  
" ASTM STP 601, pp. 47-62.
- [38] Hoff, N. J., 1954, "Approximate Analysis of Structures in the Presence of Moderately Large Creep Deformations," *Q Appl Math*, 12(1), pp. 49-55.
- [39] Curbishley, I., Pilkington, R., and Lloyd, G. J., 1986, "Macroscopic creep crack growth in type 316 stainless steel.: III. Application of linear and nonlinear elastic fracture mechanics," *Engineering Fracture Mechanics*, 23(2), pp. 401-422.
- [40] Fu, L. S., 1980, "Creep crack growth in technical alloys at elevated temperature—A review," *Engineering Fracture Mechanics*, 13(2), pp. 307-330.
- [41] Lu, Y. L., Liaw, P. K., Chen, L. J., Wang, G. Y., Benson, M. L., Thompson, S. A., Blust, J. W., Browning, P. F., Bhattacharya, A. K., Aurrecoechea, J. M., and Klarstrom, D. L., 2006, "Tensile-hold effects on high-temperature fatigue-crack growth in nickel-based HASTELLOY® X alloy," *Materials Science and Engineering: A*, 433(1–2), pp. 114-120.
- [42] Bassani, J. L., Hawk, D. E., and Saxena, A., 1989, "Evaluation of the Ct parameter for characterizing creep crack growth rate in the transient regime," *Nonlinear Fracture Mechanics: Time-dependent fracture*, Volume I, (ASTM STP 995), A. Saxena, J. D. Landes, and J. L. Bassani, eds., American Society for Testing and Materials, Philadelphia, PA, pp. 7–26.
- [43] Saxena, A., 1991, "Creep crack growth in high temperature ductile materials," *Engineering Fracture Mechanics*, 40(4–5), pp. 721-736.
- [44] Kuo, A.-Y., Chen, K.-L., Saxena, A., and Nagar, A., 1992, "An integral formulation of Ct for use in creep crack growth evaluation," *International Journal of Fracture*, 57(3), pp. 269-280.
- [45] Erdogan, F., and Sih, G. C., 1963, "On crack extension in plates under plane loading and transverse shear," *Journal of Basic Engineering*, 85, pp. 519-527.
- [46] Saxena, A., 1980, "A model for predicting the effect of frequency on fatigue crack growth behavior at elevated temperature," *Fatigue & Fracture of Engineering Materials & Structures*, 3(3), pp. 247-255.

- [47] Gayda, J., Gabb, T. P., and Miner, R. V., 1988, "Low Cycle Fatigue (ASTM STP 942)," Fatigue Crack Propagation of Nickel-Base Superalloys at 650°C, H. D. Solomon, G. R. Halford, L. R. Kaisand, and B. N. Leis, eds., American Society for Testing and Materials, Philadelphia, pp. 293-309.
- [48] Wilson, W. K., and Yu, I. W., 1979, "The use of the J-integral in thermal stress crack problems," International Journal of Fracture, 15(4), pp. 377-387.
- [49] Rice, J. R., Mcmeeking, R. M., Parks, D. M., and Sorensen, E. P., 1978, "Recent Finite-Element Studies in Plasticity and Fracture-Mechanics," Computer Methods in Applied Mechanics and Engineering, 17-8(Feb), pp. 411-442.
- [50] Hutchinson, J. W., 1983, "Fundamentals of the Phenomenological Theory of Non-Linear Fracture-Mechanics," J Appl Mech-T Asme, 50(4B), pp. 1042-1051.
- [51] ASTM E647-00, 2000, "Standard test method for measurement of fatigue crack growth rates," ASTM, West Conshocken, USA.
- [52] Tada, H., Paris, P. C., and Irwin, G. R., 2000, The Stress Analysis of Cracks Handbook, American Society of Mechanical Engineers.
- [53] Miranda, A. C. O., Meggiolaro, M. A., Castro, J. T. P., Martha, L. F., and Bittencourt, T. N., 2003, "Fatigue life and crack path predictions in generic 2D structural components," Engineering Fracture Mechanics, 70(10), pp. 1259-1279.

## 5 Accelerated remaining life consumption of a crack due to thermo-acoustic oscillations in gas turbines

A. Can Altunlu, Peter J. M. van der Hoogt, André de Boer

University of Twente, Faculty of Engineering Technology, Section of Applied Mechanics, 7500 AE, Enschede, The Netherlands

---

### Abstract

The combustion instability phenomenon in gas turbine engines causes elevated mechanical vibrations at high temperature levels. Therefore, a combination of fatigue and creep damage is induced during the service of an engine. Cracks initiated from possible hot spots in the engine must be accurately analysed and assessed in order to ensure the reliability and safety as a supplementary to the safe-life approach in the design stage, and to maintain in-service performance incorporating the health and condition monitoring system of the engine. The present work addresses the projection of a remaining lifetime assessment methodology, which is applied in a laboratory-scaled generic combustor, onto the typical gas turbine engine combustor section in terms of estimating the cracking location and its growth. A temperature-structural analysis based on the measured data during the combustion process was utilised to obtain the crack initiation region. Sequentially coupled extended finite element method (XFEM) based fracture mechanics analysis was performed to characterise the crack-tip near fields in a typical combustor nickel-based superalloy. The crack growth rate was described with only one parameter including fatigue and creep conditions, and implemented into the fracture mechanics algorithm. A high amplitude of limit-cycle pressure oscillations due to instabilities, compared to the stable combustion process, increases the crack growth rates significantly, thereby reducing the remaining lifetime. However, introducing hold times at constant loads decreases the crack growth rate due to the stress relaxation around the crack-tip.

**Keywords:** Gas turbine, combustion dynamics, life assessment, crack, XFEM.

### 5.1 Introduction

The technological advancements in industrial gas turbine engines are devoted to efficiency and emission targets. The engines are intended to be working at the designed performance levels during their service life. During their lifetime, the engines can experience various operation scenarios due to the need of flexible energy output. Particularly, the combustor section components experience severe loading conditions and history to meet these output requirements. Complex damage phenomena such as high cycle fatigue, low cycle fatigue and creep can be induced and interact during the service. Hence, reliable analysis of not only the initiation of cracks/flaws but also the growth process plays a significant role in the total life assessment of gas turbine critical components operating under complex loading histories and, which can lead to achieving safety and integrity targets [1-3]. The remaining lifetime of the damaged critical components is strongly dependent on the loading history such as the stress levels, temperature profiles or loading frequency, which can lead to an accelerated crack growth rate or retardation.

In this work, the dynamic two-way interaction between the oscillating pressure load in the fluid and the motion of the structure under limit-cycle conditions due to the thermo-acoustic instabilities in a generic combustor is experimentally investigated. Subsequently, the experimental measurements on the combustion instabilities were extended to numerical integrated remaining life assessment by fracture mechanics analysis. The stress-field ahead of the crack-tip was characterised and correlated to the crack propagation rate including fatigue and creep aspects.

The following sections describe the methodology, the procedure and the theory of the multiphysical approach. In the subsections, the combustor test system and the test materials are detailed and the thermal-structural coupled analysis is described. Next, the fatigue crack growth (FCG) and the creep crack growth (CCG) theory and the proposed method for residual lifing using XFEM is described. In section 5.3, the results are presented and the conclusions and discussions are included in the last section.

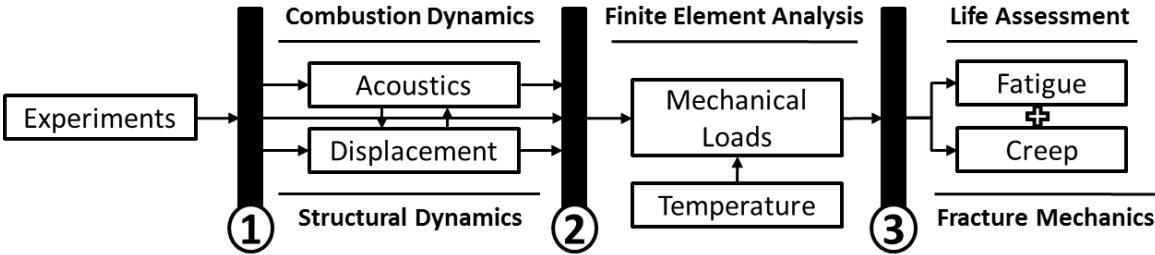


Figure 5.1. The schema of the investigation

### 5.2 Methodology of the multiphysical analysis

Multiphysical domains are interlinked throughout this work including combustion, acoustics, structural dynamics, fracture mechanics and life assessment. The schema of the investigation presented in this work is depicted in Figure 5.1. The physical based two-way interaction during the unstable combustion inside the test combustor is utilised experimentally

in a generic laboratory-scaled combustor. The loading history generated by the combustion process is measured including the cyclic pressure, temperature profile and the combustion characteristic frequency. The measurements are post-processed and imported as the loading condition in the thermal-structure coupled finite element analysis to predict the stress concentration zones. The fracture mechanics analysis is performed to calculate the crack driving parameters, assuming that the crack initiated from the pre-existing defects located in the stress concentration zones. Identical to the service conditions in the industrial gas turbine engines, the crack growth is governed by the fatigue and creep mechanisms in the numerical analysis.

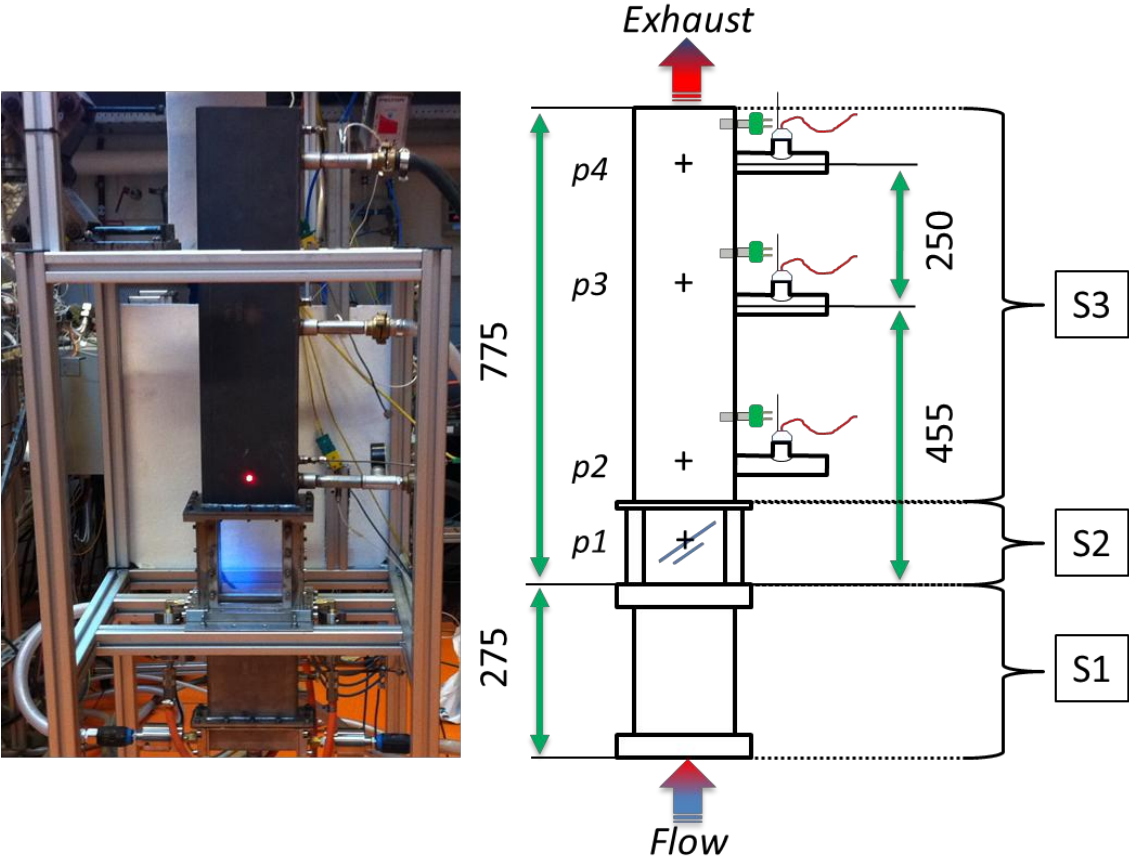


Figure 5.2. Combustor test system configuration

5.2.1 Combustor test system

The laboratory-scaled generic combustor test system is depicted in Figure 5.2. The measurement locations designated as “p#” are the pressure, fluid temperature and the liner wall vibration. The Rijke tube-type combustor mainly consists of two sections; the upstream (S1) and downstream (S2&S3). In Figure 5.3, the full geometry (a), the flame-box configuration (b) and the wedge (c) are visualised. The upstream section includes an air-feeding box, a rectangular duct and an equilateral triangular wedge that is detailed in the figure (c). The wedge acting as the flame holder takes in the fuel (methane) from the side holes (black-arrows) and sprays out the fuel from the small holes (red-arrows). Thus, the fuel and the air flowing upwards along the duct (blue-arrow) constitute a homogeneous mixture

and the initiation takes place to form the flame. The downstream consists of a rectangular liner (S3) and a flame-box (S2). The flame-box detailed in Figure 5.3 (b) is enclosed by quartz glasses (3), sandwiched by two gaskets (1) and mounted on the flame-box by the frames (2). The quartz glasses (4 mm thick) can be replaced with identically sized rectangular metal plates (1 mm thick) that represent the parent liner structure. In this work, the front quartz glass is replaced with a rectangular plate. Hereafter the metal plate will be called the specimen. During the experiments, the side windows are used to visualise the flame shape. Note that the flame stabilisation takes place on the wedge wake and the generated turbulent flame is technically premixed.

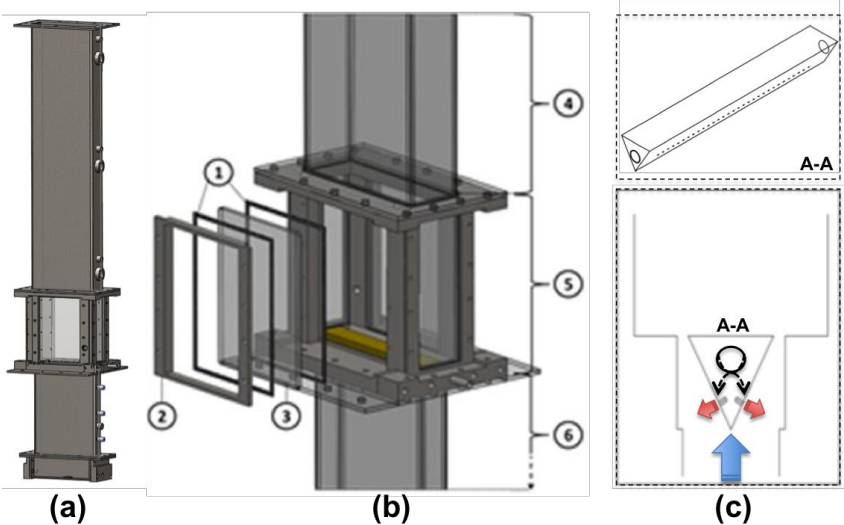


Figure 5.3. Flame-box configuration

**5.2.2 Materials and compliance**

The combustor test system is composed of austenitic stainless steel (AISI) Type310 and Type316 (specimen). The materials were selected because of their cost-effectiveness and sufficiently enough heat and corrosion resistance relative to the test temperatures and durations. The test combustor materials have analogous temperature-dependent thermal and mechanical properties to the typical gas turbine combustion liner material, Alloy230 (Haynes<sup>®</sup> 230) nickel-based superalloy. However, Alloy230 is superior due to its high temperature strength, high resistance to oxidizing environments (up to 1150 °C), long-term thermal stability and low thermal expansion characteristics [4]. Since the measured pressures generated by the combustion process are independent from the material type, and the temperature measurements become independent as well when the steady-state conditions are reached, Alloy230 is considered in this work as though it is of interest to the gas turbine community. Therefore, the experimental output is numerically applied to Alloy230 material to direct a projection towards realistic lifing within an industrial perspective.

**5.2.3 Finite element model**

In the combustor finite element model as seen in Figure 5.6, five sections were included, (1) the downstream, (2) the upstream, (3) the specimen and quartz glasses, (4) the gaskets and

(5) the welds. The material properties for each section are correspondingly: (1) Type310, (2) Type316, (3) Type316 and fused quartz, (4) muscovite mica and (5) Type310 with higher Young's modulus to satisfy the welding stiffness. The finite element mesh was generated using quadratic volume elements. Two elements were created across the liner wall and the specimen thickness and a finer mesh is used for the welding parts to accommodate mesh compliance. A temperature-structural analysis was performed to calculate the stress and strain distributions. The applied loads and the boundary conditions are detailed as follows.

Two FEM analyses were performed, one for the full geometry and one for the specimen geometry only. In this manner, a benchmark numerical test was performed to reduce the computation cost. Hereby the full geometry analysis and the specimen geometry-only analysis will be called the full-model and sub-model analysis, respectively. In the full-model, a fully fixed support boundary condition (clamped) at the bottom of the flame-box was applied. This support location represents the scaffolding-like frame that holds the test system, as seen in Figure 5.2 (left). The experimentally measured pressures and surface temperatures were imported in FEM, and defined as the external data with respect to the dimensions of the geometry. Prior to the computation, the data were mapped and matched on the finite element mesh (point cloud data mapping).

In the experiments, the combustion process generates a varying surface temperature and thermal expansion condition at the downstream part that can induce pre-stress effects. Therefore, the assembly of the specimen to the flame-box is designed such that a clearance is present in the housing. This provides some freedom for the attached specimens to slide towards traverse and longitudinal directions. Furthermore, two gaskets (2 mm thick) are accommodated on both sides of the specimen to compensate the third dimension of the volumetric expansion. Hence, the stresses in the specimen are assumed to be mainly covered by the pressure inside the combustor. In the numerical sub-model, the boundary conditions were modelled with an elastic foundation. This elastic support represents the gaskets that sandwich the specimen. Basically, a spring stiffness per unit area was represented by the so-called elastic foundation stiffness (EFS) [5]. EFS was applied on the in-plane and the out-of-plane faces of the support area. This provides a resistance to the direction normal to the volumetric expansion of the geometry. In this way, the sub-model can expand due to the thermal load and can deform out-of-plane due to the pressure load. The effects of the temperature and damping were assumed to be negligible for the EFS, which is analogical with the gaskets material. Since the peak load amplitudes do not change on the specimen, attached to the flame-box, as seen in Figure 5.6 (a) and (b), a constant temperature and pressure were applied to the model.

#### **5.2.4 Fracture mechanics model**

The lifetime of combustion liners is potentially consumed by fatigue and creep mechanisms; however, their interaction also must be resolved for the crack growth assessment. In the next subsections, the crack growth characterising parameters for fatigue and creep are described. Furthermore, their interaction is formulated to govern the lifing, and the usage of the proposed method in the XFEM framework is described.



#### 5.2.4.1 Cycle-dependent fatigue crack growth

Typically, the crack growth is associated with the strain energy release that is analogous to the dissipated energy to create new fracture surfaces. The components, subjected to cyclic loads in the creep-temperature regime, can experience the stages of the continuous evolving deformation ahead of the crack-tip according to its stress-strain-time response [6]. If the plastic zone is small compared with the crack size, in other words the material experiences small-scale yielding at the crack-tip, the energy release is, in fact, the  $J$ -integral [7, 8]. The  $J$ -integral is defined in the general form as:

$$J = \int_{\Gamma} \left( W dy - \mathbf{T} \cdot \frac{\partial \mathbf{u}}{\partial x} ds \right) \quad (5.1)$$

$$W = \int_0^{\varepsilon^m} \sigma_{ij} : d\varepsilon_{ij}^m \quad (5.2)$$

where  $\Gamma$  is an arbitrary curve enclosing the crack-tip,  $W$  is the mechanical strain energy density varying with the stress,  $\sigma_{ij}$  and the mechanical strain,  $\varepsilon_{ij}^m$ ,  $\mathbf{T}$  is the traction vector on  $\Gamma$  defined according to the outward normal as  $T_i = \sigma_{ij} n_j$ ,  $n_j$  is the vector of the outward unit normal  $\mathbf{n}$  to the curve  $\Gamma$ ,  $\mathbf{u}$  is the displacement vector,  $ds$  is an element of  $\Gamma$ , and  $x$  and  $y$  are the cartesian coordinates with origin at the crack-tip and with  $y$ -direction normal to the crack-line. The  $J$ -integral, or strain energy release rate, is related to the stress intensity factor (SIF) for linear-elastic materials, in the general form as:

$$J = \eta \frac{1}{E} (K_I^2 + K_{II}^2) + \frac{1}{2G} K_{III}^2 \quad (5.3)$$

where  $\eta=1$  for plane stress and  $\eta=(1-\nu^2)$  for plane strain,  $E$ ,  $\nu$ ,  $G$  are the Young's Modulus, the Poisson's ratio and the Shear Modulus, respectively and  $K_{I,II,III}$  are the stress intensity factors for the fracture modes  $I$ ,  $II$  and  $III$ , respectively.

#### 5.2.4.2 Time-dependent creep crack growth

Materials used in gas turbine engine combustors at elevated temperatures show superior creep strength and creep ductility. However, in the presence of a growing crack these materials can fail to exhibit even very small bulk creep deformation. In general, the materials, which experience CCG, can be categorised as creep-ductile or creep-brittle. Previous studies showed that the austenitic steels behave creep-ductile at relatively lower temperatures (538°C) [9, 10], whereas the nickel-based superalloys show creep-brittle behaviour at higher temperatures (927°C) [11-13].

The state of stress at the crack-tip can be characterised by a crack-tip parameter, which drives the approach from idealised laboratory specimens to the actual components acting as a transfer function [14, 15]. However, there is no one unique parameter that can be used in all circumstances [16]. Therefore, the asymptotic solutions for the stresses in the creep zone, obeying the power-law creep of deformation, need to be analysed implying whether or not the  $SIF$  value is valid in the creep zone calculation [17]. In creeping materials, three stages are defined for crack propagation by means of the size of the crack-tip creep zone relative to the specimen dimensions that are small-scale, transient and steady-state [18-20]. Lu et al. [12] showed that a typical combustor material, Alloy230, behaves as a creep-brittle material

(small-scale), of which the accumulated creep strains and the near-tip elastic strains around the crack are at comparable levels. Hence, the  $C_r$ -integral, which is the small-scale creep analogue of the  $J$ -integral, can be utilised as a crack-tip parameter and the time-dependency of the fracture mechanics can be included assuming small-scale yielding [21-23]. The  $C_r$ -integral can be defined by replacing the strains with strain rates and the displacements with the velocities, thus the mechanical strain energy density with the mechanical strain energy rate density, in the  $J$ -integral description. In the general form, the strain energy rate density is described as:

$$\dot{W} = \int_0^{\dot{\epsilon}^m} \sigma_{ij} : d\dot{\epsilon}_{ij}^m \quad (5.4)$$

Under secondary power-law creep, the  $C_r$ -integral parameter can be described in terms of the stress intensity factor ( $K_C$ ) for small-scale creep condition as:

$$C_t = \frac{1}{(n+1)t} \eta \frac{K_C^2}{E} \quad (5.5)$$

where  $n$  is the power-law constant,  $t$  is the time. The reader is referred to the references for detailed information on the formula derivation [17, 24-27].

### 5.2.4.3 Life assessment

The interaction of the cycle-dependent fatigue crack growth and the time-dependent creep crack growth is utilised using a linear summation model [28]. The model in general form is described as [29]:

$$\left(\frac{da}{dN}\right)^t = \left(\frac{da}{dN}\right)^f + \int \left(\frac{da}{dt}\right)^c dt \quad (5.6)$$

where  $a$  is the crack length,  $N$  is the number of load cycles,  $t$  is the time, and the superscripts  $t, f, c$  are total, fatigue and creep, respectively.

When complex loading conditions are present, such as varying loading ratios and frequencies, the behaviour of the crack growth can exhibit dependencies on these parameters [30]. In Eq. (6), the total crack growth rate is composed of the FCG rate relevant to a hold-time test and CCG rate during one cycle that is  $\Delta t = 1/w + t_{hold}$ , where  $w$  is the frequency of the waveform and  $t_{hold}$  is any hold time (dwell period). In the previous sub-section, the FCG and the CCG were expressed relevant to the SIF and thus  $J$ -integral. The total crack growth rate can be expressed as Paris-Erdogan law type formulation as:

$$\left(\frac{da}{dN}\right)^t = B(\Delta J^f)^m + \int [A(\Delta J^c)^n] dt \quad (5.7)$$

where the material parameters  $B, m$  are for fatigue and  $A, n$  are for creep,  $\Delta J$  is the updated  $J$ -Integral range. The relation can be re-described for a symmetric, triangular waveform with an optional hold time (dwell period) at maximum load as [29]:

$$\left(\frac{da}{dN}\right)^t = B(\Delta J^f)^m + A(\Delta J^c)^n \left[ \frac{Z}{w(n+1)} + \frac{t_{hold}}{(1-R)^n} \right] \quad (5.8)$$

where  $R$  is the load ratio ( $R$ -ratio) and  $Z$  is defined as:

$$Z = \frac{1-R^{n+1}}{(1-R)^{n+1}} \quad (5.9)$$

In Eq. (8), the first part of the crack growth rate per cycle formulation ( $da/dN$ ) governs the fatigue contribution and the latter part accounts for creep. The crack growth rate description includes the magnitude of the cyclic J-Integral parameter ( $\Delta J$ ) that is analogous to the SIF, the frequency of the waveform, hold time at maximum load, and the load ratio.

Lu et al. [12] showed that the fatigue-creep crack growth can be described by Paris-Erdogan law-type formulation including only the  $C_t$  parameter under the small-scale yielding assumption. The formulation represents the crack growth behaviour of the solid solution strengthened superalloy, Alloy230, including hold-time effects and temperatures in the range of 816 and 927 °C. The crack growth rate is given as

$$\left(\frac{da}{dt}\right) = 0.0447(C_t)^{0.864} \quad (5.10)$$

#### 5.2.4.4 XFEM implementation

Fracture mechanics related problems remain a challenge in the numerical simulations by their complicated nature to serve as a reliable tool in an industrial perspective. In the classical numerical approach, since the nodal shape functions for the finite element approximations represent discontinuities in the pre-constructed mesh, the fracture model restricts the crack growth along the predefined element boundaries. Mesh updating and treating the crack-tip with special purpose elements can overcome the discontinuities and singularities reflected by the modelling part and its features. However, re-projecting the solution on the remeshed field of interest in each crack propagation step and constructing a solution mosaic from the sub-steps can significantly increase the computation cost and influence the accuracy of the results.

A relatively recent approach XFEM, which is a numerical technique based on partition of unity method, enables modelling crack domains in engineering component analysis without explicitly meshing the crack surface [31-37]. The XFEM method creates a new displacement-field approximation by enriching the FEM approximation. The key idea is to extend the conventional formulation by enrichment functions and model a discontinuity inside an element by adding shape functions to the finite element approximation. The initial crack geometry is typically represented implicitly by a so-called level set method that tracks moving interfaces [38-40]. The mesh is independently generated from the crack geometry and the elements of the meshed structure do not necessarily need to conform to the crack surfaces. The convergence rate is improved for the solution by crack-tip enrichment. The displacement approximation for modelling the crack takes the new form,  $\mathbf{u}_{xfem}$  by enriching the classical FE approximation,  $\mathbf{u}_{fem}$ .

$$\mathbf{u}_{fem}(\mathbf{x}) = \sum_{i \in L} N_i(\mathbf{x}) u_i \quad (5.11)$$

$$\mathbf{u}_{xfem}(\mathbf{x}) = \sum_{i \in L} N_i(\mathbf{x}) u_i + \sum_{i \in M} N_i(\mathbf{x}) H(\mathbf{x}) a_i + \sum_{i \in N} [N_i(\mathbf{x}) \sum_{\alpha=1}^4 F_{\alpha}(\mathbf{x}) b_{i\alpha}] \quad (5.12)$$

where  $L$ ,  $M$ , and  $N$  are the set of all nodes, respectively, for the classical finite element, whose support is bisected by the crack, containing all the nodes of the crack-tip elements;  $N_i(\mathbf{x})$  is the shape function associated with node  $i$ ,  $H(\mathbf{x})$ , the Heaviside function and  $F_{\alpha}$ , the crack-tip

functions are the enrichments functions. The function introduces the discontinuity across the crack faces;  $H(x)$  is defined as;  $H(x) = 1$  for  $x > 0$  and  $-1$  for  $x < 0$ . The crack-tip is represented by four enrichment functions ( $F_{\alpha=1-4}$ ) to span the asymptotic near-tip displacement field of the Westergaard solution for an isotropic elastic material [32]:

$$[F_{\alpha}(r, \theta), \alpha = 1 - 4] = \left[ \sqrt{r} \sin \frac{\theta}{2}, \sqrt{r} \cos \frac{\theta}{2}, \sqrt{r} \sin \theta \sin \frac{\theta}{2}, \sqrt{r \sin \theta} \cos \frac{\theta}{2} \right] \quad (5.13)$$

where  $(r, \theta)$  belongs to the polar coordinate system having the origin at the crack-tip and tangent to the crack at its tip at  $\theta=0$  in 2D situation.

### 5.3 Results

In this section, the experimental and the numerical results are presented. Firstly, the test combustor operating points are characterised and the stable and unstable operating conditions are presented in the stability map. The measured surface temperature and pressure profile in the downstream region are shown. Next, the prediction of the stress concentration location on the flame-box specimen by the thermal-structural coupled analysis is presented. Subsequently, the results of the XFEM-based fracture mechanics analysis for the introduced crack are shown. Consequently, the fatigue and creep contributions to the remaining lifing are described.

#### 5.3.1 Combustion characterisation

The stability map was constructed for the test combustor and is presented in Figure 3.9. The diamond markers represent the stable combustion and the square markers are for the unstable combustion with respect to the initial settings such as the air/fuel ratio and the thermal power. There is a clear transition to generate the combustion instability mainly depending on the air/fuel ratio so that the air fed into the system is reduced at a ratio to the fuel of 1.4. The power of 60 kW and the air/fuel ratio of 1.2 were selected as the extreme case within the test points for further investigation in this work and can be seen in the bottom-right corner in the stability map. This operating point will be denoted as Case6012 in the rest of this work.

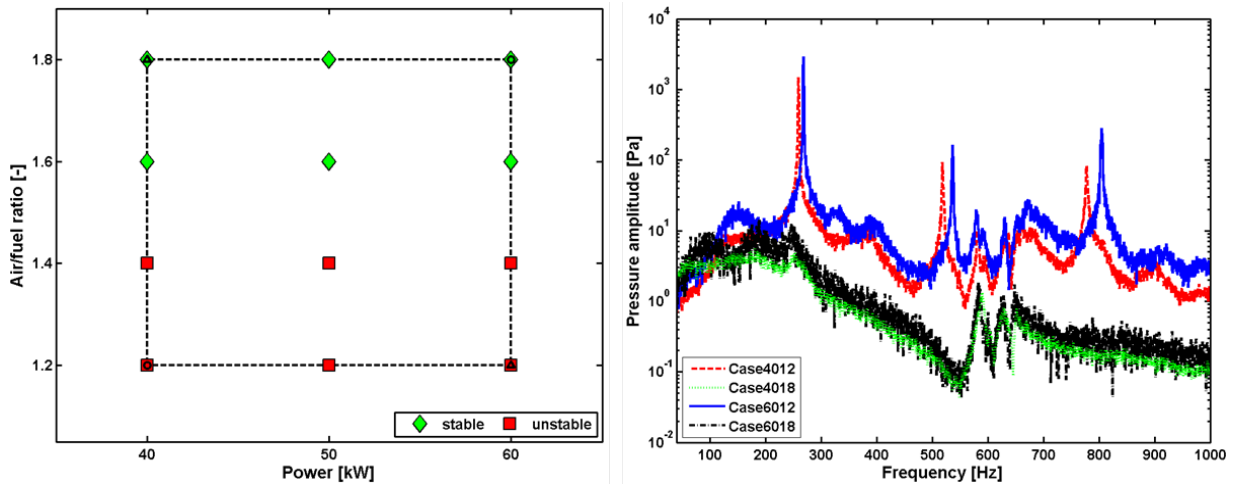


Figure 5.4. Stability map (left) and pressure spectrum at p2 sensor location (right)

In Figure 3.9, the pressure spectrum is shown for the sample operating points including two unstable and two stable cases. The unstable cases show a distinct pressure peak at a characteristic combustion frequency. The higher-harmonics of the characteristic frequency, where the first peak stands, were generated due to the nonlinear effects of the instability.

The pressure amplitudes for the unstable cases are more than 100 times of the amplitudes for the stable cases. In Case6012, the pressure in the combustor ranges from 2130Pa to 3663Pa and the surface temperature of the liner ranges from 601.5°C to 301.5°C. Previous experiments showed that the temperature and pressure loads in the flame-box region were found to be sufficiently close to the measurements at the ‘p2’ location. The loads along the downstream are depicted in Figure 5.5. These data were post-processed to be compatible for importing in the created mesh in the thermal-structural coupled analysis.

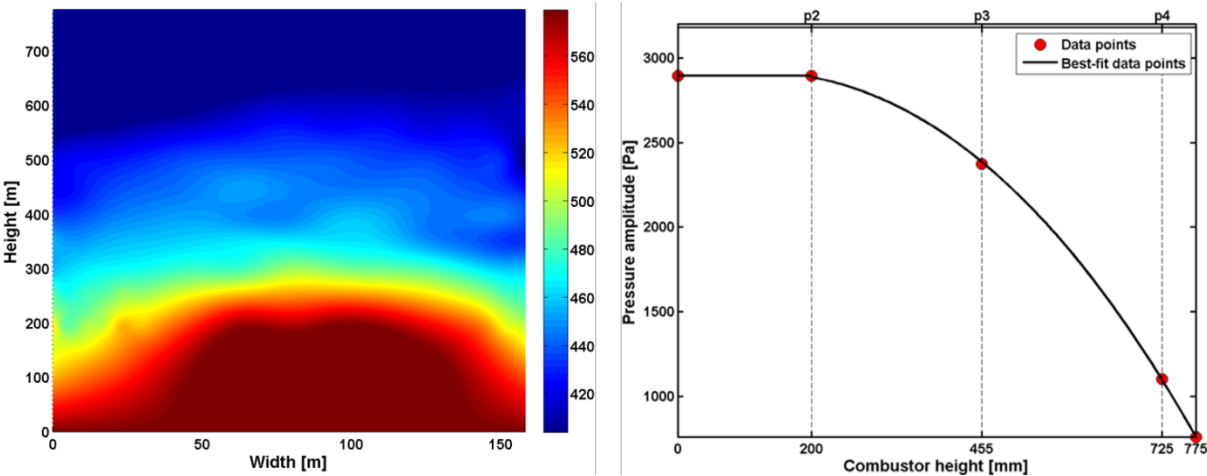


Figure 5.5. Downstream surface temperature and pressure profile

### 5.3.2 Temperature-structural analysis

The temperature and pressure profile in the downstream part of the combustor at Case6012 is presented in Figure 5.6 (a) and (b). In the figure, the highest temperature and pressure amplitudes are present in the flame-box region and the specimen is exposed to nearly-constant load amplitudes. Initially, a numerical test was carried out to compare the full-model and the sub-model results. In the analysis, the stress and strain distribution on the specimen geometry was found to be identical for the two numerical tests, which implies the high stiffness of the flame-box structure. Thus, further investigation was performed in the sub-model in order to reduce the computational cost.

The stress distribution of the sub-model was calculated by the temperature-structural analysis presented in Figure 3.21 (left-background). This shows that the out-of-plane stresses are concentrated near the long edge sections. In Figure 3.21, the maximum principal stress directions were calculated in the FEM mesh (b) and they are indicated by red arrows (a). The calculated stress field was transferred to the fracture mechanics analysis and a new mesh was generated for the XFEM analysis (d). In the XFEM analysis, an initial slot-type crack (yellow-line) was located in the maximum stress region, assuming that the crack propagation direction will be perpendicular to the calculated principal stress directions. Hence, the slot

crack is placed at the mid-height near the longitudinal edge (0.5 mm from the edge) and it is aligned along this edge with 1 mm artificial initial crack length ( $a_0$ ).

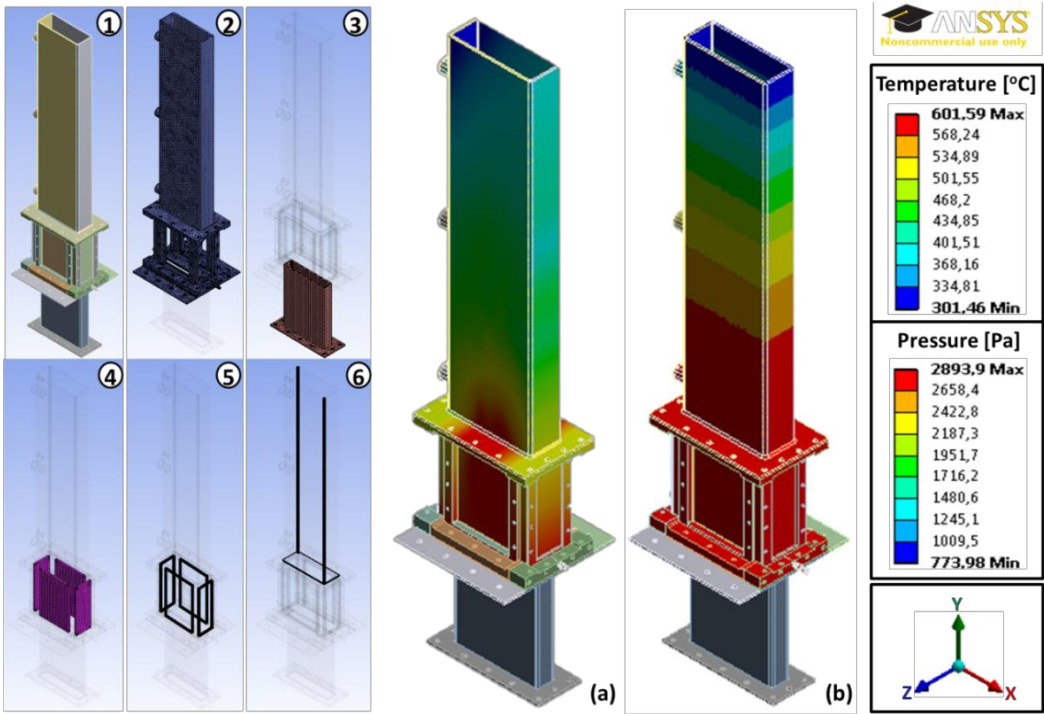


Figure 5.6. FEM modelling: model sections (left), measured (a) temperature and (b) pressure data mapping to the model (right)

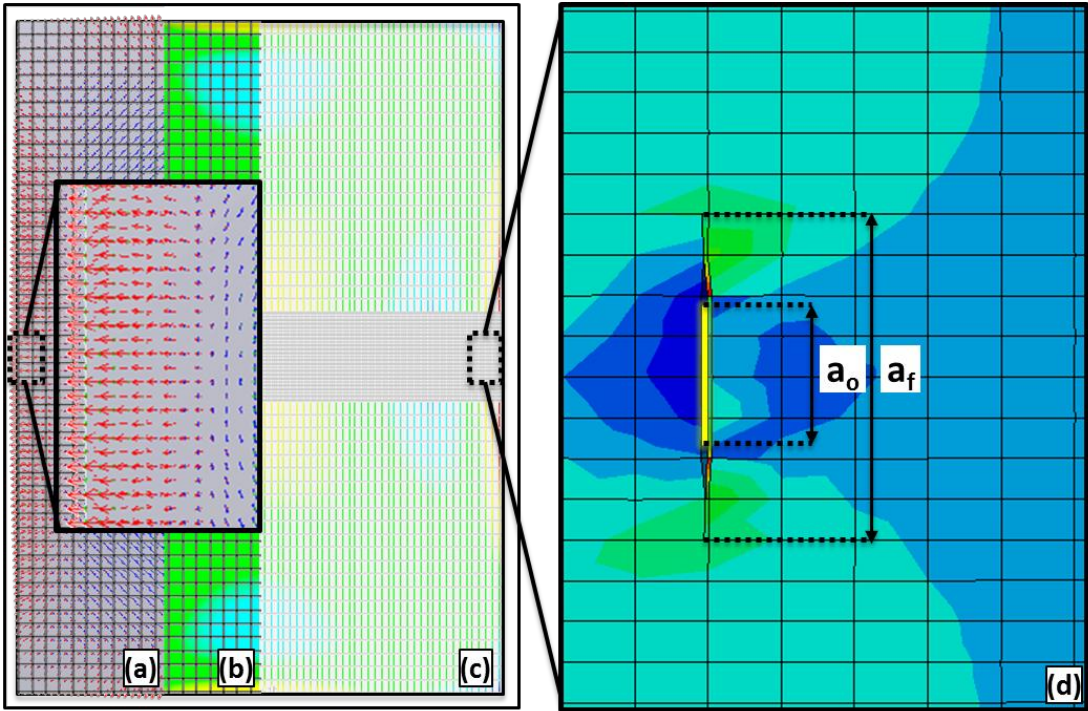


Figure 5.7. Maximum principal stress directions (a), FEM mesh (b), XFEM mesh (c), crack growth from initial crack length ( $a_0$ ) to final crack length ( $a_f$ ) at an instant time (d)

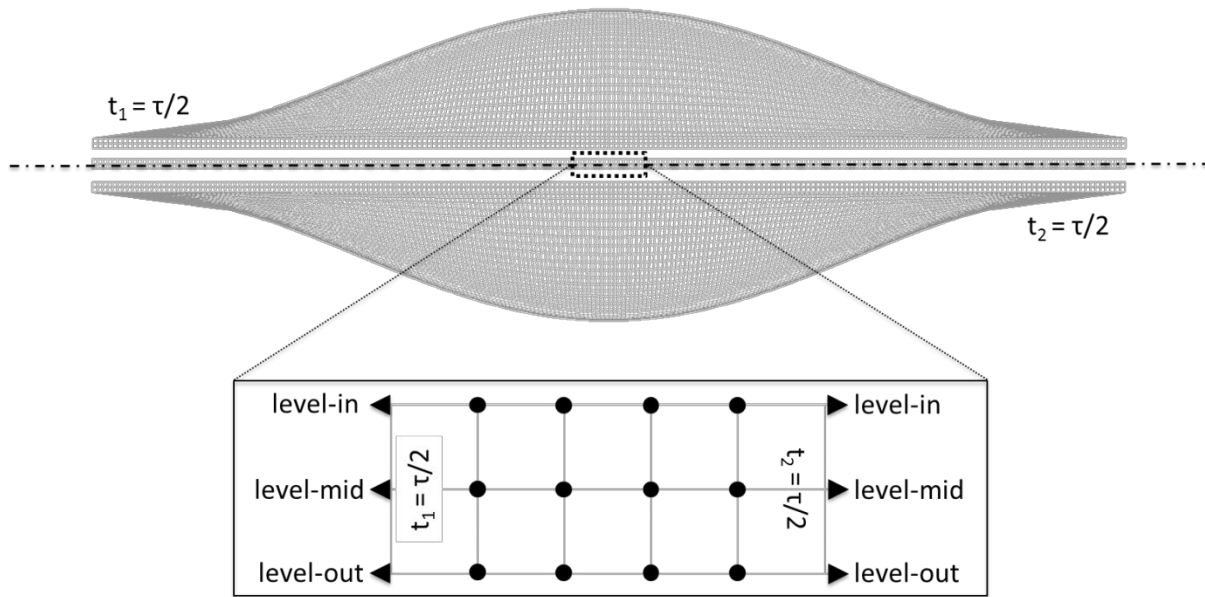


Figure 5.8. Tension and compression state of layers across thickness in one cycle ( $\tau = t_1 + t_2$ )

### 5.3.3 Residual lifing

In this section, the crack-tip parameters relevant to crack growth are presented. As seen from Figure 5.8, three levels (nodes) are designated as the *level-in*, *level-mid* and *level-out*. The level-in and level-out are the outer surface layers of the geometry that experience compression and tension stresses due to the cyclic bending motion of the specimen. Therefore, although the amplitudes belonging to the level-out are higher than the amplitudes of the level-in, they swap each other during one cycle ( $\tau = t_1 + t_2$ ) on the condition that the surface is under tension or compression stresses. At a half cycle, the level, which is under tension stresses, induces higher energy release rates. In a full cycle, the level-out and level-in stress-states alternate. Furthermore, the optimum number of contours was found to be five to capture the stress-field spread around the crack-tip. Therefore, the calculated crack-tip characterising parameters are averaged with respect to the level-layers and five contours for the following calculations. The mesh density was selected by optimising (minimising) two criteria that are the deviation of the average value of the crack-tip characterising parameter, and its fluctuation amplitude around a mean value.

The experimentally measured pressure amplitude,  $P_{EXP}$ , (3663 Pa) was found to be insufficient to cause crack propagation. Therefore, three higher pressure amplitudes were included in the investigation for the comparison. These four pressures will be called the numerical test pressures as follows:  $P_{EXP}$ ,  $P_{EXP} \cdot 10^1$ ,  $P_{EXP} \cdot 10^2$ ,  $P_{EXP} \cdot 10^3$ . Figure 5.9 illustrates the relation between the  $C_I$ -integral and hold time at different pressure levels. In this analysis, the pressure load was kept constant. Increasing the pressure load elevates the stresses, therefore the  $C_I$ -integral increases. On the contrary, the  $C_I$ -integral decreases as the hold time is introduced more, which is due to the stress relaxation around the crack-tip. However, if the hold time is set to infinity, then the  $C_I$ -integral would no longer represent the intensity of the near-tip stresses because creep mechanisms will have sufficient time to develop a larger



creeping zone around the crack-tip. However, small-scale yielding condition will not be violated unless the creep zone development rate is higher than the K-dominant zone development rate.

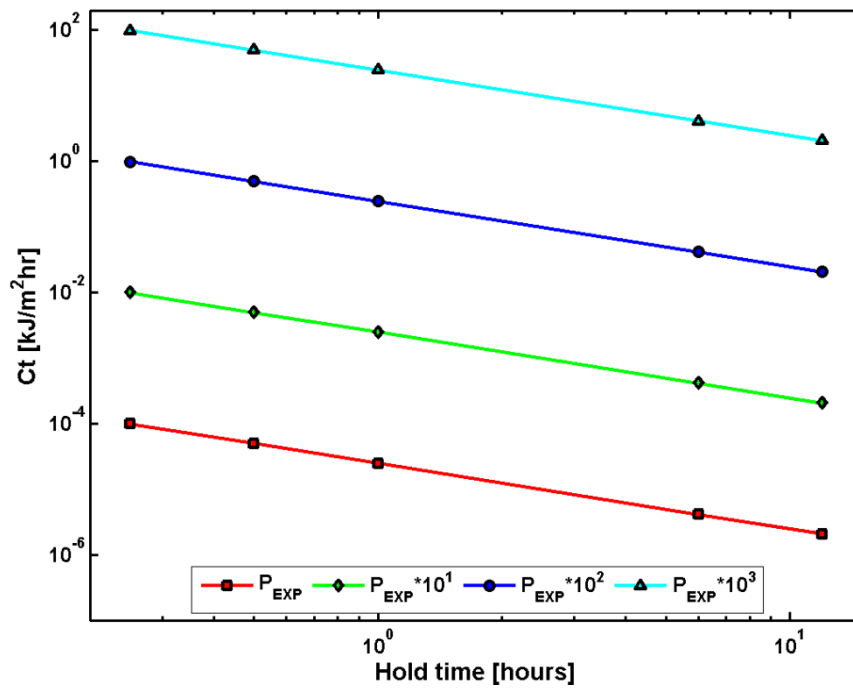


Figure 5.9.  $C_t$  versus hold time

In Figure 5.10, the plot is divided into 4 regions. Each region starts with dash-dot line and ends with a dashed line. The marker-data, delimited by the lines within these regions, belong to the numerical test pressures. Assuming that the crack growth is governed by a modified Paris-Erdogan law-type model (Eq. 10), the crack growth rate is proportional to the J-integral, and hence the  $C_t$ -integral. Because, higher  $C_t$  values, thus higher crack growth rates, consume more lifetime and decrease the remaining lifetime. The results show that the increase in the pressure, thus the increase in  $C_t$ , increases the crack growth rate. Besides, the  $C_t$  values, thus crack propagation rate, decrease with increasing hold time. This is attributed to the stress relaxation process, and promotion of intergranular fracture mode due to material creeping changing from a transgranular one as in pure fatigue fracture mode [12]. This indicates that the time-dependent damage mechanisms related to the creep crack growth are in control as the holding time is introduced instead of the cycle-dependent mechanisms.

Table 5.1. Measured peak pressures and crack growth rates

Operating point	Combustion characteristics	Peak pressure [Pa]	Factor* (Ref. Case4018)	Crack growth rate [mm/h]	Factor* (Ref. Case4018)
Case4018	Stable	5.5	0	3.07E-10	0
Case6018	Stable	14.21	1.6	1.58E-9	4.15
Case4012	Unstable	1471	266.5	4.81E-6	1.56E+7
Case6012	Unstable	2894	525.2	1.55E-5	5.04E+7

\* Factor = (data - Ref. Case4018) / Ref. Case4018



Recalling Figure 3.9, the peak pressure amplitudes of the operating points are listed in Table 2.1. Considering Case4018 as the reference case, the cases, where the combustion instabilities have occurred, induce very high peak amplitude by a factor of 266.5 for Case4012, and by a factor of 525.2 for Case6012. The measured substantial increase in the pressure amplitudes, during the transition from stable to unstable combustion, results in significantly accelerated crack growths, thus accelerated life consumption.

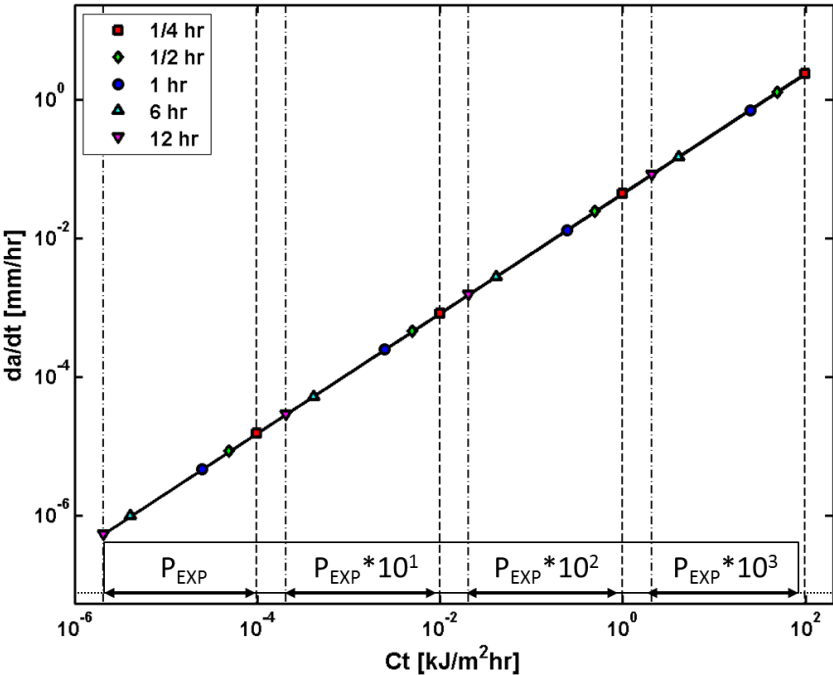


Figure 5.10. Unit time crack growth rates as a function of  $C_t$

### 5.4 Concluding remarks and discussions

A laboratory-scaled generic gas turbine combustor was designed to investigate the structural dynamics due to the combustion instabilities.

The following conclusions are mainly drawn on this work:

- Combustion instabilities are observed to be sensitive to changes in the air-fuel ratio rather than thermal power. Lowering air-fuel ratio from 1.6, reducing the air portion of the mixture, leads to instabilities within the entire test thermal powers. The unstable combustion process induced very high amplitude pressure oscillations compared to stable cases. Furthermore, these high amplitude loads due to combustion instabilities result in accelerated remaining lifetime consumption.

- The measured pressure and surface temperature was successfully linked to temperature-structural FEM analysis to predict the hot-spot (critical cracking) region.

- The fracture characterising parameters was calculated by XFEM-based fracture mechanics analysis including creep and fatigue conditions for a nickel-based super alloy material, Alloy230, that is relevant to typical gas turbine hot section components. The crack growth rates were quantified by only one fracture parameter,  $C_I$ -integral, which is representative for fatigue and creep crack growth.

- In XFEM for crack modelling, the finite element mesh can be generated independently from the geometry, and remeshing, due to the change in topology of the domain as the crack grows, is avoided. Implementation of XFEM into a general purpose finite element program enables accurate results to be obtained from numerically demanding three-dimensional complex geometries. Furthermore, a combined time-dependent creep and cycle-dependent fatigue fracture parameter, satisfying small-scale yielding assumption, is integrated into this framework. Hence, the crack growth rates can be calculated requiring less numerical efforts for crack modelling, and resolving time-dependent creep crack response using linear elastic fracture mechanics concepts significantly reduces computational time.

- Since the pressure generated due to the combustion process is in a cyclic manner, the stresses will vary between tensile and compressive types. This will stimulate the crack to grow on both sides and eventually through thickness. The acoustic volume in the flame-box expands and contracts due to the pressure oscillations that result in the cyclic loadings of the plate and its relative motion. This will enable the crack to open at the outer face at the volume expansion and to close at the volume contraction. Thus, the total remaining lifetime of the through-thickness crack would be half of the calculated lifetime due to this cyclic or sequential crack growth at the two sides of the plate.

- Note that the experimentally measured mechanical and thermal loads driven by the unstable combustion process were used in the numerical analysis to characterise the crack parameters. Hence, the numerical fracture mechanics analysis must be validated by experiments. Therefore, an unconventional test system design is required to cover the fatigue/creep aspects of the combustor structure instead of the standard specimens.

## **Acknowledgement**

The authors would like to acknowledge funding of this research by the EC in the Marie Curie Actions – Networks for Initial Training, under call FP7-PEOPLE-2007-1-1-ITN, Project LIMOUSINE with project number 214905.

## **References**

- [1] Cruse, T. A., Mahadevan, S., and Tryon, R. G., 1997, "Fatigue Reliability of Gas Turbine Engine Structures," No. NASA/CR-97-206215, NASA.
- [2] Tryon, R. G., Cruse, T. A., and Mahadevan, S., 1996, "Development of a reliability-based fatigue life model for gas turbine engine structures," *Engineering Fracture Mechanics*, 53(5), pp. 807-828.
- [3] Yang, J. N., 1994, "Application of Reliability Methods to Fatigue, Quality Assurance and Maintenance," *Structural Safety & Reliability*, Vols 1-3, pp. 3-18.
- [4] Haynes International, 2007, "HAYNES 230 Alloy Product Brochure," No. H-3000.
- [5] ANSYS® Academic Research, "Theory Reference," Release 14.0, ANSYS, Inc.
- [6] Davis, J. R., 1997, *Heat-resistant materials*, ASM International, Materials Park, Ohio.
- [7] Hutchinson, J. W., 1968, "Singular behaviour at the end of a tensile crack in a hardening material," *Journal of the Mechanics and Physics of Solids*, 16(1), pp. 13-31.

- [8] Rice, J. R., and Rosengren, G. F., 1968, "Plane strain deformation near a crack tip in a power-law hardening material," *Journal of the Mechanics and Physics of Solids*, 16(1), pp. 1-12.
- [9] Curbishley, I., Pilkington, R., and Lloyd, G. J., 1986, "Macroscopic creep crack growth in type 316 stainless steel.: III. Application of linear and nonlinear elastic fracture mechanics," *Engineering Fracture Mechanics*, 23(2), pp. 401-422.
- [10] Saxena, A., "For the characterization of creep-crack-growth behavior in 304 stainless steel," *ASTM*, pp. 131-151.
- [11] Fu, L. S., 1980, "Creep crack growth in technical alloys at elevated temperature—A review," *Engineering Fracture Mechanics*, 13(2), pp. 307-330.
- [12] Lu, Y. L., Liaw, P. K., Sun, Y., Wang, G. Y., Thompson, S. A., Blust, J. W., Browning, P. F., Bhattacharya, A. K., Aurrecochea, J. M., and Klarstrom, D. L., 2007, "Hold-time effect on the elevated-temperature crack growth behavior of solid-solution-strengthened superalloys," *Acta Materialia*, 55(3), pp. 767-775.
- [13] Lu, Y. L., Liaw, P. K., Chen, L. J., Wang, G. Y., Benson, M. L., Thompson, S. A., Blust, J. W., Browning, P. F., Bhattacharya, A. K., Aurrecochea, J. M., and Klarstrom, D. L., 2006, "Tensile-hold effects on high-temperature fatigue-crack growth in nickel-based HASTELLOY® X alloy," *Materials Science and Engineering: A*, 433(1–2), pp. 114-120.
- [14] Grover, P. S., and Saxena, A., 1995, "Creep Crack-Growth in Power-Plant Materials," *Sadhana-Acad P Eng S*, 20, pp. 53-85.
- [15] Saxena, A., 1997, "Creep-fatigue crack growth in power-plant materials and components," *Advances in Fracture Research*, Vols 1-6, pp. 51-62.
- [16] Saxena, A., Ernst, H. A., and Landes, J. D., 1983, "Creep crack growth behavior in 316 stainless steel at 594°C (1100°F)," *International Journal of Fracture*, 23(4), pp. 245-257.
- [17] Riedel, H., and Rice, J. R., 1980, "Tensile cracks in creeping solids," *Fracture Mechanics: 12th Conference*, pp. 112-130.
- [18] Riedel, H., 1981, "Creep Deformation at Crack Tips in Elastic-Viscoplastic Solids," *Journal of the Mechanics and Physics of Solids*, 29(1), pp. 35-49.
- [19] Saxena, A., 1984, "Creep Crack-Growth under Non Steady-State Conditions," *J Test Eval*, 12(4), pp. 191-192.
- [20] Saxena, A., 1991, "Creep Crack-Growth in High-Temperature Ductile Materials," *Engineering Fracture Mechanics*, 40(4-5), pp. 721-736.
- [21] Hamilton, B. C., Hall, D.E., Saxena, A., McDowell, D.L. , "Creep crack growth behavior of aluminum alloy 2519: part I - experimental analysis," *Proc. Elevated temperature effects on fatigue and fracture*, ASTM STP 1297, American Society for Testing and Materials, pp. 3-18.
- [22] Hall, D. E., Hamilton B.C., McDowell, D.L., Saxena A., "Creep crack growth behavior of aluminum alloy 2519: part I - numerical analysis," *Proc. Elevated temperature effects on fatigue and fracture*, ASTM STP 1297, American Society for Testing and Materials, pp. 19-36.
- [23] Sadananda, K., and Shahinian, P., 1981, "Review of the Fracture-Mechanics Approach to Creep Crack-Growth in Structural Alloys," *Engineering Fracture Mechanics*, 15(3-4), pp. 327-342.

- [24] Saxena, A., 1991, "Creep crack growth in high temperature ductile materials," *Engineering Fracture Mechanics*, 40(4–5), pp. 721-736.
- [25] Kuo, A.-Y., Chen, K.-L., Saxena, A., and Nagar, A., 1992, "An integral formulation of  $C_t$  for use in creep crack growth evaluation," *International Journal of Fracture*, 57(3), pp. 269-280.
- [26] Bassani, J. L., and McClintock, F. A., 1981, "Creep relaxation of stress around a crack tip," *International Journal of Solids and Structures*, 17(5), pp. 479-492.
- [27] Bassani, J. L., Hawk, D. E., and Saxena, A., 1989, "Evaluation of the  $C_t$  parameter for characterizing creep crack growth rate in the transient regime," *Nonlinear Fracture Mechanics: Time-dependent fracture, Volume I*, (ASTM STP 995), A. Saxena, J. D. Landes, and J. L. Bassani, eds., American Society for Testing and Materials, Philadelphia, PA, pp. 7–26.
- [28] Saxena, A., 1980, "A MODEL FOR PREDICTING THE EFFECT OF FREQUENCY ON FATIGUE CRACK GROWTH BEHAVIOR AT ELEVATED TEMPERATURE," *Fatigue & Fracture of Engineering Materials & Structures*, 3(3), pp. 247-255.
- [29] Gayda, J., Gabb, T. P., and Miner, R. V., 1988, "Low Cycle Fatigue (ASTM STP 942)," *Fatigue Crack Propagation of Nickel-Base Superalloys at 650°C*, H. D. Solomon, G. R. Halford, L. R. Kaisand, and B. N. Leis, eds., American Society for Testing and Materials, Philadelphia, pp. 293-309.
- [30] Zhang, G., Yuan, H., and Li, F., 2012, "Analysis of creep–fatigue life prediction models for nickel-based super alloys," *Computational Materials Science*, 57(0), pp. 80-88.
- [31] Babuška, I., and Melenk, J. M., 1997, "The partition of unity method," *International Journal for Numerical Methods in Engineering*, 40(4), pp. 727-758.
- [32] Belytschko, T., and Black, T., 1999, "Elastic crack growth in finite elements with minimal remeshing," *International Journal for Numerical Methods in Engineering*, 45(5), pp. 601-620.
- [33] Bordas, S., Nguyen, P. V., Dunant, C., Guidoum, A., and Nguyen-Dang, H., 2007, "An extended finite element library," *International Journal for Numerical Methods in Engineering*, 71(6), pp. 703-732.
- [34] Daux, C., Moës, N., Dolbow, J., Sukumar, N., and Belytschko, T., 2000, "Arbitrary branched and intersecting cracks with the extended finite element method," *International Journal for Numerical Methods in Engineering*, 48(12), pp. 1741-1760.
- [35] Fries, T.-P., and Belytschko, T., 2010, "The extended/generalized finite element method: An overview of the method and its applications," *International Journal for Numerical Methods in Engineering*, 84(3), pp. 253-304.
- [36] Melenk, J. M., and Babuška, I., 1996, "The partition of unity finite element method: Basic theory and applications," *Computer Methods in Applied Mechanics and Engineering*, 139(1–4), pp. 289-314.
- [37] Moës, N., Dolbow, J., and Belytschko, T., 1999, "A finite element method for crack growth without remeshing," *International Journal for Numerical Methods in Engineering*, 46(1), pp. 131-150.

- [38] Gravouil, A., Moës, N., and Belytschko, T., 2002, "Non-planar 3D crack growth by the extended finite element and level sets—Part II: Level set update," *International Journal for Numerical Methods in Engineering*, 53(11), pp. 2569-2586.
- [39] Stolarska, M., Chopp, D. L., Moës, N., and Belytschko, T., 2001, "Modelling crack growth by level sets in the extended finite element method," *International Journal for Numerical Methods in Engineering*, 51(8), pp. 943-960.
- [40] Sukumar, N., Chopp, D. L., and Moran, B., 2003, "Extended finite element method and fast marching method for three-dimensional fatigue crack propagation," *Engineering Fracture Mechanics*, 70(1), pp. 29-48.

## 6 Lifetime analysis using integrated fluid-structure approach for combustion dynamics in gas turbines

A. Can Altunlu <sup>a</sup>, Salvatore Matarazzo <sup>b</sup>, Saverio Tufano <sup>c</sup>, Tiedo Tinga <sup>d,a</sup>, Hannes Laget <sup>b</sup>, Phil Stopford <sup>c</sup>, André de Boer <sup>a</sup>, Jim B.W. Kok <sup>e</sup>

<sup>a</sup> University of Twente, Faculty of Engineering Technology, Section of Applied Mechanics, 7500 AE, Enschede, The Netherlands

<sup>b</sup> Department of Combustion and Thermodynamics, Laborelec, 1630 Linkebeek, Belgium

<sup>c</sup> ANSYS UK Ltd., 97 Milton Park, Abingdon, OX14 4RY, UK

<sup>d</sup> Netherlands Defence Academy, PO Box 10000, 1780 CA Den Helder, The Netherlands

<sup>e</sup> University of Twente, Faculty of Engineering Technology, Section of Thermal Engineering, 7500 AE, Enschede, The Netherlands

---

### Abstract

**G**as turbine (GT) combustor liners are subjected to mechanical and thermal loads that damage the structure and reduce their operational lifetime. In-service, the lifetime consumption can be accelerated by high amplitude pressure oscillation due to combustion dynamics, which results in elevated structural vibrations. The structure undergoes repeated reversals of the main deformation mechanisms as a function of the operating load of the engine. Monitoring the condition of the combustor due to operational load histories and evaluating the lifetime consumption rate of the combustor is vital to maintain the mechanical integrity and to perform a reliable risk-based maintenance. A methodology for modelling both the steady-state and dynamic behaviour of a GT cannular combustion chamber by utilising a combined fluid-structure approach is presented in this study. Together with the calculation of the heat fluxes through the liner, the effects of the modifications at the thermal boundary conditions were used to analyse the structural response of the combustion liner at different GT loads. The measured in-service pressure oscillations are investigated by utilising a developed algorithm including statistical distributions and probabilistic analysis, and rainflow cycle counting to calculate the resulting fatigue lifetime. The predicted failure pattern is found to match well with the observations. Furthermore, the contribution of pressure oscillations is characterised by high cyclic crack growth observed in the failure pattern.

**Keywords:** *Combustion dynamics, acoustics, creep, fatigue, lifetime, rainflow counting.*

## 6.1 Introduction

The introduction and the development in the 1970s of the low-NO<sub>x</sub> industrial GT combustors has led to the definition of stringent regulations in the power generation sector. In particular, NO<sub>x</sub> emissions below 25ppm or 50mg/m<sup>3</sup> at 15% oxygen are required in most countries in the world. The need for reducing the pollutant emissions requires the use of modern combustion hardware that allows Gas Turbine (GT) to operate at very low equivalence ratios, between 0.4 and 0.6. In this regard, fuel-air mixing plays a key role to achieve optimum combustion performance, uniform combustion and reduced NO<sub>x</sub> emissions [1]. Various efforts have been devoted in the investigation of the effects of the flow patterns and air/fuel mixing in terms of heat transfer, flame stability, dynamic pressure developments, and blow off [1-3].

A lean, premixed (LP) combustor system, which is designed to operate at low temperatures, is one of the solutions to achieve the emission targets. However, acoustic pressure oscillation phenomenon due to combustion instabilities is a likely LP system problem. This phenomenon is driven by the coupling between the heat release in a thin reaction zone with a characteristic chemical time, the acoustic pressure waves and their specific acoustic time constants such that the acoustic waves are amplified on each passage through the reaction zone till reaching limit-cycle oscillations [4, 5]. These undesired oscillations cause high amplitude vibrations of the hardware that lead to detrimental fatigue damage. Much work has been devoted to enhance understanding and various solutions have been provided for this problem, such as the use of staged combustion, modifications in the flame stabiliser design, introduction of resonators, and modifications of combustor or plenum chamber length [4, 6-11]. However, combustion instabilities are hard to avoid in the entire operating range due to various engine load selections or different ambient conditions. Therefore, the condition of the combustor must be monitored and assessed in-service to prevent excessive deterioration of the materials that leads to failure.

In the power generation industry, the remaining life prediction of the critical components operating under cyclic loadings at elevated temperature levels attracts considerable interest. Safety, durability and reliability, along with the strict engine emission targets and desired efficiency, greatly motivate the investigators to provide solutions for a sustainable economic future. The life assessment of the hot section critical components requires modelling the material inelastic behaviour under high temperature cyclic loadings. As yet several engineering materials have been investigated by means of plastic and creep deformation, under cyclic uniaxial loading conditions, at high temperature levels using standard test specimens. Hence, these data are required to be translated with respect to the non-uniform loading in the structure and the varying operating points, thus varying loading levels. The integrity of the engine is ensured in the design stage; however, the design considerations for the engine in-service can bring about certain conservatism in the pre-estimated low cycle fatigue (LCF) and creep lifetime. Moreover, the combustion dynamics, which generate elevated vibration levels during operation, can violate the pre-estimated structural lifetime. This is due to the fact that the time histories of the local stresses and strains reveal

considerable variations due to high/very high cycle fatigue (HCF/VHCF), which are generally not taken into account in the design stage. Therefore a progressive life assessment must be performed based on the gas turbine in-service measured data covering the engine transients, operation points and sequences. This should be done to optimise the design, but also in the operation phase to improve the maintenance process.

The aim of the work is to generate a mechanical integrity tool for a GT combustor, which can be used in both the design and in-service. The elements of this tool are as follows.

- A combined Computational Fluid Dynamics (CFD) and Finite Element Method (FEM) numerical analysis for predicting the steady-state combustion characteristics and structural behaviour. Using the mechanical and thermal load obtained by this analysis, the critical locations (hot spots) are determined, and LCF and creep lifetimes of these regions are calculated.

- A developed algorithm based on statistical distributions and probabilistic analysis to analyse the measured in-service pressure oscillations due to combustion instabilities, and a rainflow cycle counting to calculate the resulting HCF/VHCF lifetime.

In the following section, the problem and the methodology are described and in section 6.3 the multiphysical modelling, including CFD and FEM, and lifetime prediction method are explained. In section 6.4, the results covering the structural and modal response of the combustor are presented, and the life assessment is shown in section 6.5. In the final section, the conclusions are drawn.

## **6.2 Problem description and methodology**

Present-day gas turbines employ fuel-staging techniques during the load transients. During load ramping only certain stages/fuel lines are fuelled with premixed flames to reach the full premix combustion mode at higher power outputs. The firing curves, by means of the fuel split valves (Figure 6.1), modify locally the equivalence ratio which is retained to be a critical parameter for the development of thermo-acoustic instabilities [12].

The natural gas is fed to the chambers by four fuel lines used for different purposes.

- The primary line brings the fuel at the tip of the nozzle and acts on the pilot flame,
- The quaternary line delivers a percentage of the total feed gas to the air inlet upstream the premix swirler,
- The secondary and tertiary lines bring the fuel to, respectively, the 4<sup>th</sup> and 1<sup>st</sup> burners with premix gas injectors. The opening of the split valve changes according to the power output and the start-up or turn-down procedure.

In practice the combustion liner is exposed to four combustion regimes that are start-up (1), transients from an isothermal temperature to a maximum temperature at so-called steady-state operation (2), and then cooling down back to the isothermal condition (3), and finally, shut-down (4). These four regimes cover a general operating cycle. A typical damaged combustion liner is shown in Figure 6.2, where the inner traces indicate a spiral shape temperature distribution along the liner resulting in thermal barrier coating (TBC) spallation and varying deformation along the radial cross section, which signifies the asymmetric thermal gradients incorporated with the cyclic loading.



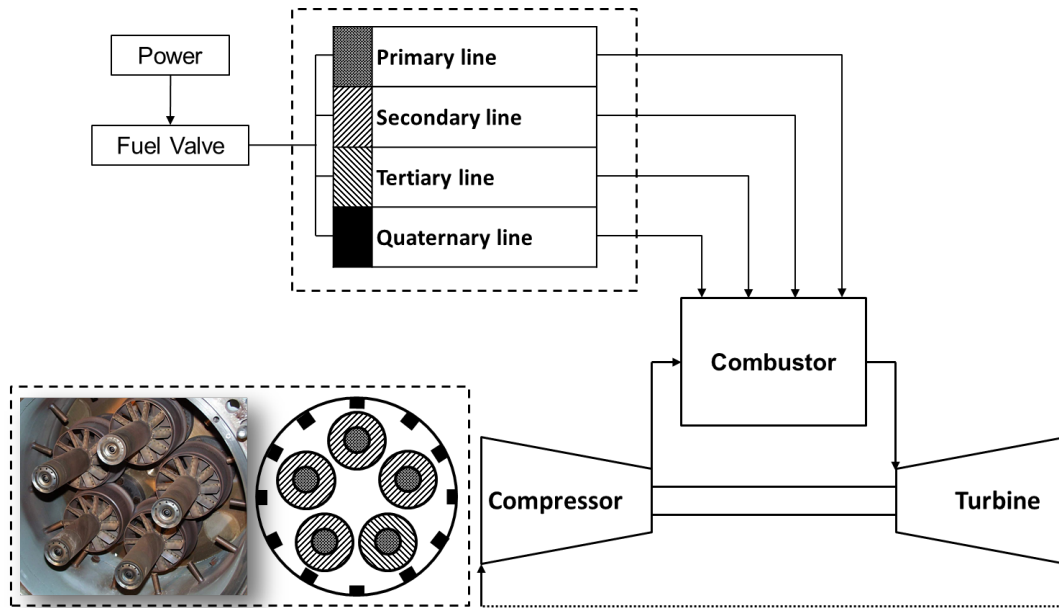


Figure 6.1. Split-cycle of the combustion

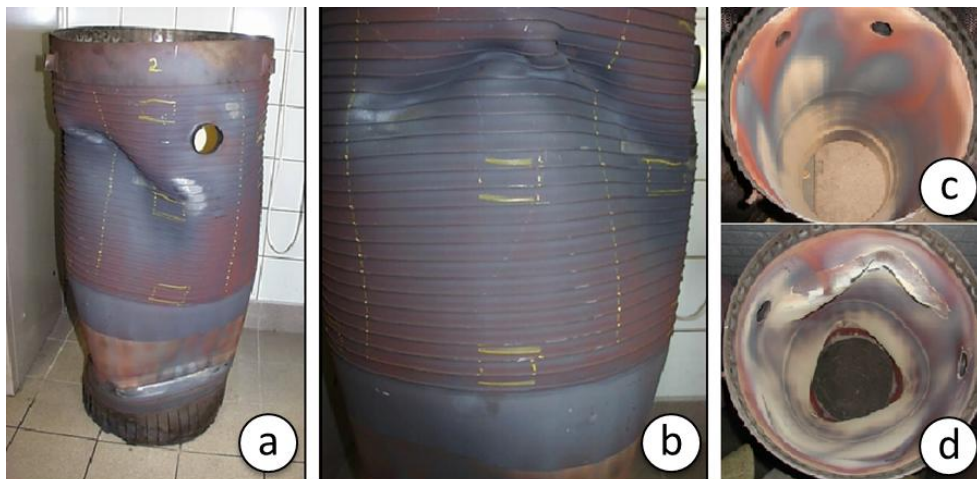


Figure 6.2. Failure pattern of the combustion liner: the deformation (a, b) - outer surface, the spiral-shaped wear (c) - inner surface, and the cracked final failure (d)

Table 6.1. Operating point initial settings

	Base-load	Part-load
Power [MW]	243	177
Air Flow [kg/s]	30.9	21.43
Gas Mass Flow [kg/s]	0.72	0.5
Quaternary Fuel [%]	11	11
Tertiary/Secondary Fuel Split [%]	81.7	82.73
Compressor Air discharge Temperature [°C]	373	337
Compressor Air Discharge Pressure [bar]	14.95	10.3
Equivalence ratio $\Phi$	0.4	0.4

In this work, the following steps are presented: First, CFD analyses are performed for a GT engine with a typical industrial Dry Low NOx fully premixed combustion system based on initial settings of part-load (177 MW) to base-load (243 MW) regime. The operation point initial settings are presented in Table 6.1.

Second, the temperature and pressure loads obtained by CFD analysis are transferred to FEM analysis to investigate the structural behaviour of the combustion liner at these regimes including the nonlinear material, such as creep and plasticity. The time steps are defined for the calculations as: 1e-5, 0.1, 1, 10, 100, 1000, 2000, 5000, 10000, 15000, 20000, 25000, 30000, 40000, 50000 hours. The stress relaxation and creep strain development are calculated over these time periods for the two operating conditions. Note that the loading is considered constant in time for FEM analysis. The structural deformations and stress levels are correlated with the operational experiences.

After that, the stress-strain state of the liner is calculated for the base-load operation, at which the highest temperature and pressure levels are generated. The LCF and creep lifetime are calculated for the critical locations of the liner. And also the HCF lifetime is predicted due to the pressure fluctuations measured in-service at the primary zone of the combustor. With respect to the latter, probability density function (PDF) and cumulative distribution function (CDF) algorithms are executed to obtain the minimum amount of pressure oscillations data (windowed-data) that best represents the overall in-service experience at base load. Thus, the computational cost is reduced.

Next, a rainflow cycle (RFC) counting algorithm is performed on the windowed-data, which represents the complex loading applied to the hardware, and in order to reduce the process to discrete cycles, hence allow the application of Miner’s rule in order to assess the HCF/VHCF lifetime.

Lastly, a modal analysis is performed including structure and acoustic properties in order to understand the reason behind the dynamic behaviour of the combustion process.

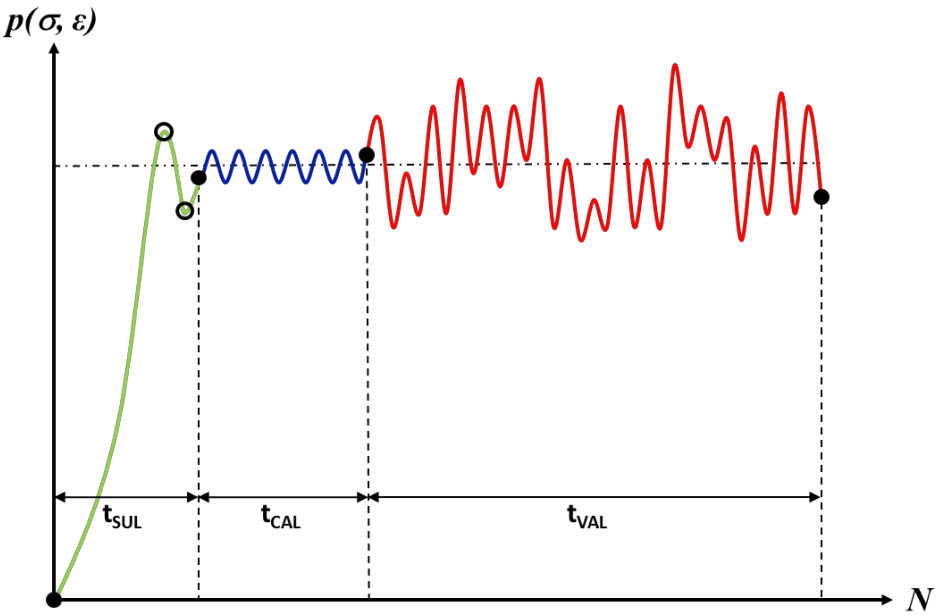


Figure 6.3. Pressure time history generated at half cycle of a typical operation

As seen in Figure 6.3, a half operation cycle can be translated in terms of failure mechanisms as LCF ( $t_{SUL}$ ) due to start-up loads, creep ( $t_{CAL}$  and  $t_{VAL}$ ) during the operation due to sustained load at high temperature HCF/VHCF ( $t_{VAL}$ ) because of the transition from constant to variable elevated amplitude loading generated by the combustion dynamics.

### 6.3 Multiphysical modelling

A CFD analysis was performed to simulate the combustion process of the part and base loads. The thermal and pressure loads are calculated and transferred to the FEM analysis to calculate the stress and strain distributions. The output is used for the life assessment. Furthermore, in-service pressure oscillations due to combustion dynamics are assessed in terms of lifetime consumption using PDF and CDF, RFC algorithms.

The power and equivalence ratio are selected to represent a typical operation. The inlet boundary conditions (IBC) for CFD are defined using the operational parameters acquired from the field, such as airflow, gas mass flow, fuel split, compressor air discharge temperature and pressure. The CFD model is used to predict behaviour of the fluid volume and flow patterns inside the combustion liner, and the FEM model is utilised to calculate the structural response of the liner, which surrounds the fluid volume. Since the combustion dynamics is composed of 3-D flows and complex reaction zones, it is essential to simulate the full fluid domain to include the dynamic thermal and gas behaviour. Furthermore, the compliance of the fluid and structural domain models is crucial such that the models must be coupled at the interface. Therefore, a detailed geometry of a commercial engine is used to model the fluid and structural domain and both models were generated from the same geometry. The fluid domain (a) and the structural model (b) are depicted in Figure 6.4.

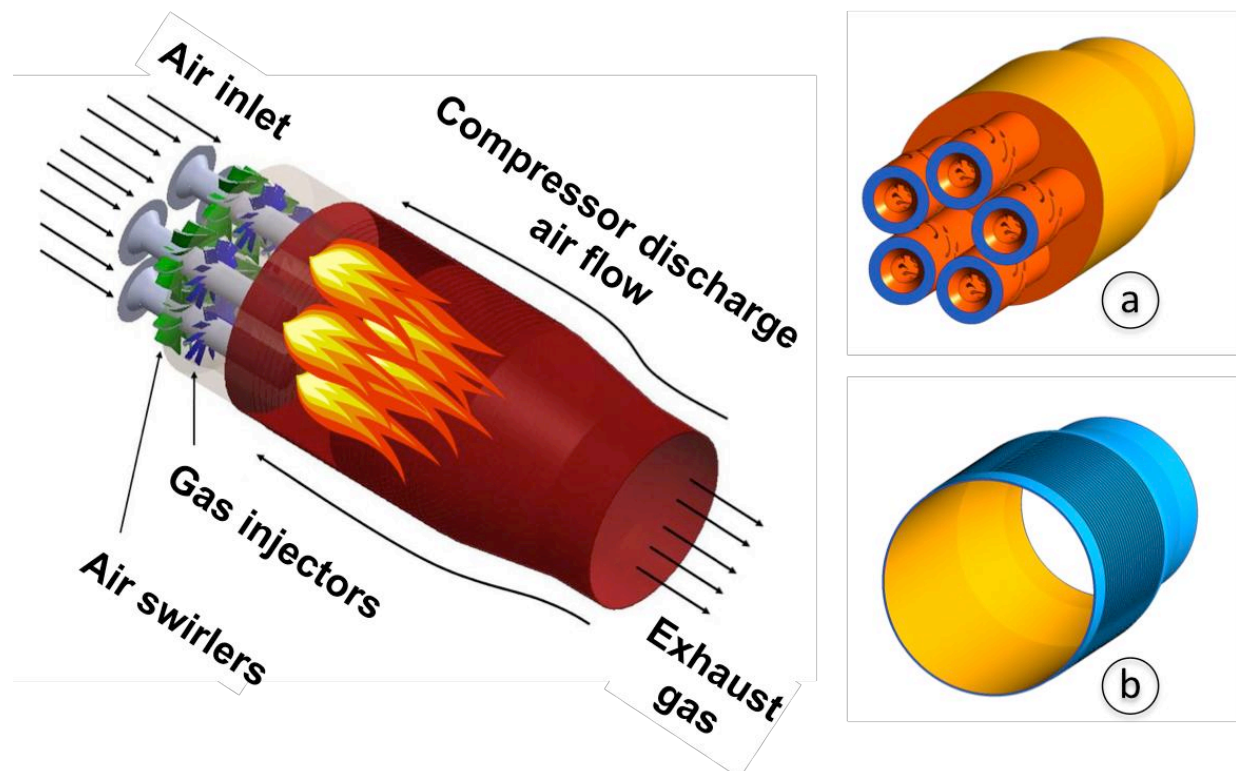


Figure 6.4. Combustor representation, fluid domain (a), structural domain (b)

### 6.3.1 Geometry

The combustion liner, investigated in this work, of a cannular-type combustor system in a heavy-duty gas turbine engine equipped with five premix burners is depicted in Figure 6.4. The high airflow swirlers are used to allow large volumes of air to enter the primary zone of the chamber premixed with the fuel injected downstream of the swirler position and to achieve lean combustion. The liner cooling is provided through the casing cavity by the compressor discharge air. Prior to passing directly to the combustion chamber, the cooling air circulates counter-flow externally with the twofold effect of cooling the liner walls and is pre-heated to increase the combustion efficiency.

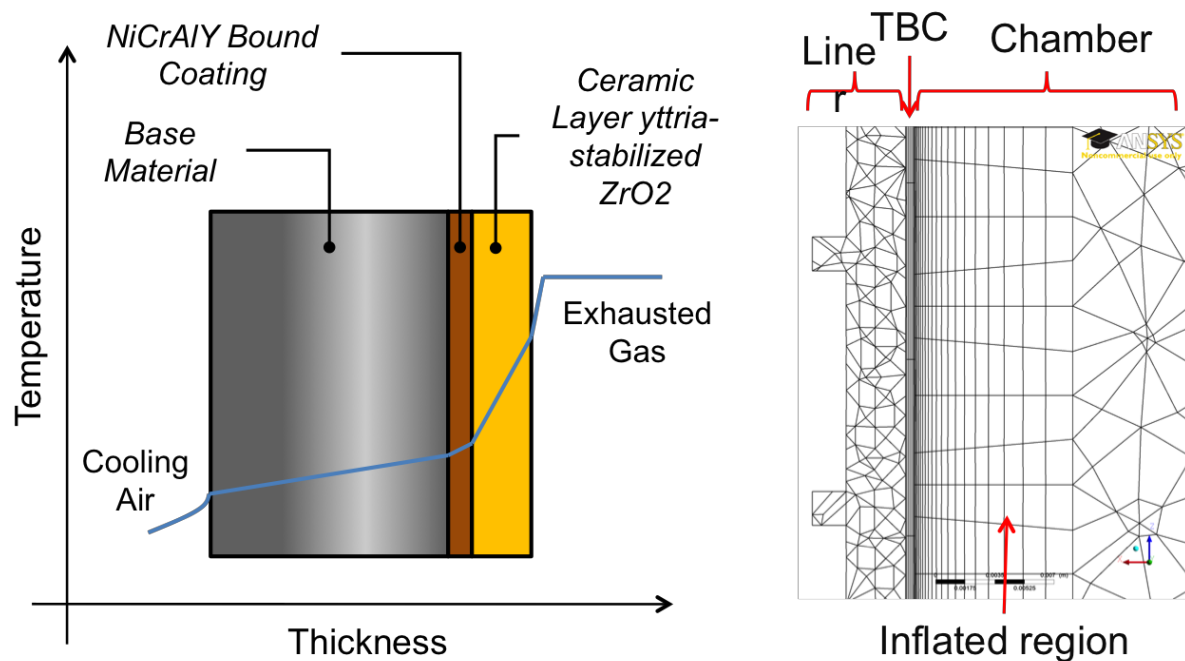


Figure 6.5. Composition of TBC Layers and typical temperature drop through the whole liner

### 6.3.2 Computational fluid dynamics model

The fluid dynamics is analysed using the commercial CFD numerical solver ANSYS-CFX v13. The main model is composed of three sub-domains that are the chamber fluid domain, the liner solid domain and the casing cavity fluid domain. The fluid chamber domain includes the burner swirling vanes and the gas injector and calculates the flow paths. The liner solid domain accounts for heat transfer without flow. The casing cavity fluid domain represents the cooling purposes of the compressor discharge air passing counter-flow on the liner outer surface. The mesh in the model includes an element grid consisting of unstructured tetrahedrons with an average skewness value of 0.28. The number of elements for the chamber, liner and casing cavity is 8.6, 1.6 and 3.8 million, respectively.

The effects of the turbulence on the flow path, heat and combustion process are predicted by using the standard  $k-\epsilon$  turbulence model. The viscous effects are neglected, and thus the thermal energy heat transfer model is utilised, since the Mach number is less than 0.3 in the full domain. The combustion reaction process is simulated by using the combined eddy dissipation-finite rate chemistry model (EDM/FRC). This model used a single-step reaction

model to analyse the evolution of the combustion process including the calculation of the reaction rate for both “turbulent mixing-dominated” and “chemistry-dominated”. The fuel composition alters the combustion reaction zone and stability of the flame behaviour. In general, the natural gas is composed of primarily methane (CH<sub>4</sub>) and between 0 - 20% of higher hydrocarbons. In this analysis, fuel is considered as pure methane and a mixture O<sub>2</sub>-N<sub>2</sub> as oxidizer (0.232-0.768 mass fractions) is used. The P1 thermal radiation model is used to account for radiative effects related to heat transfer. The reader is addressed to see the reference for further information on the CFD model [13].

### 6.3.3 Material behaviour

The combustion liner material is made of a nickel-based superalloy, AlloyX (UNS N06002), which shows significant strain rate sensitivity at elevated temperatures [14, 15]. The strain rate to obtain the temperature dependent average tensile data is referenced as 0.005-inch/inch/minute to 0.2% yield point and 0.5-inch/inch/minute to failure [16].

The implementation of the finite element method for the solution includes the additive decomposition of the strain tensor. The total strain ( $\varepsilon^{tot}$ ) can be described as cumulative addition of the mechanical strain ( $\varepsilon^{mech}$ ) and thermal strain ( $\varepsilon^{th}$ ), which contains the elastic ( $\varepsilon^{el}$ ) and inelastic strain (plastic  $\varepsilon^{pl}$  and creep  $\varepsilon^{cr}$ ) components assuming small deformations.

$$\varepsilon^{tot} = \varepsilon^{mech} + \varepsilon^{th} = \varepsilon^{el} + \varepsilon^{pl} + \varepsilon^{cr} + \varepsilon^{th} \quad (6.1)$$

The material properties have been implemented including the linear elastic and nonlinear plastic behaviour with a bilinear isotropic hardening model that uses the Von-Mises yield criteria coupled with an isotropic work hardening assumption. The mechanical model consists of only the liner structure while the TBC layer has been neglected because its mechanical influence is small. Furthermore, since in Ni-based superalloys the primary creep deformation is typically small compared to the rupture strain, and the tertiary stage, which is described as a rapid increase of strain rate until the creep rupture, is assumed to be beyond in the design for structural integrity, the secondary creep stage was modelled that is characterised by so-called minimal strain rate, in which the existence of an approximate equilibrium between the hardening and the recovery mechanics and the long-time of this equilibrium is assumed. In this regard, the material’s ductile behaviour eliminates the need to resolve the primary and tertiary creep; therefore the viscoplastic behaviour of AlloyX can be represented by the creep Norton law. The creep potential or the equivalent creep rate, dependent on stress and temperature, is often written as a product of two functions

$$\dot{\varepsilon}^{cr} = \frac{\partial W}{\partial \bar{\sigma}} = f_{\sigma}(\bar{\sigma})f_T(T) \quad (6.2)$$

where  $\bar{\sigma}$  is the equivalent stress,  $T$  is the temperature,  $f$  is the function the so-called constitutive or the response function, which allows stress and temperature dependences individually. The stress dependence of the steady-state creep strain rate can be defined by Norton’s power law for dislocation creep as

$$\dot{\varepsilon}^{cr} = C_{\sigma} \bar{\sigma}^n \quad (6.3)$$

and  $C_\sigma$  and  $n$  are material constants. The Arrhenius law describes the dependence on the temperature according to the diffusion control of principal creep deformation mechanisms as

$$f_T(T) = C_T e^{-Q/RT} \quad (6.4)$$

where  $C_T$  is the material constant,  $Q$  is the activation energy and  $R$  is the Boltzmann's constant. Dorn-type relation for the stress ( $f_\sigma$ ) and the temperature ( $f_T$ ) dependency is integrated in the equivalent creep rate equation. The Norton creep model in ANSYS is of the form

$$\dot{\varepsilon}^{cr} = C_1 \bar{\sigma}^{C_2} e^{-C_3/T} \quad (6.5)$$

where  $C_1$ ,  $C_2$  and  $C_3$  are the material coefficients, which model the dependency of the creep strain rate from the stress and the temperature has been derived by a curve fitting procedure from a set of experimental data.

The stress-strain relationship under cyclic loading is considered as strain controlled, thus LCF. The stress-strain hysteresis curve is formed assuming Masing-type material approximation and using the relations ' $\Delta\sigma/2 = \sigma_a$ ' and ' $\Delta\varepsilon/2 = \varepsilon_a$ ' (where the subscript ' $a$ ' refers to alternating). The local stress-strain can be described considering the stabilised cyclic stress-strain curve described by the Ramberg-Osgood equation [17] as

$$\frac{\Delta\varepsilon}{2} = \frac{\Delta\varepsilon_e}{2} + \frac{\Delta\varepsilon_p}{2} = \frac{\Delta\sigma}{2E} + \left(\frac{\Delta\sigma}{2K'}\right)^{1/n'} \quad (6.6)$$

where  $E$  is the elastic modulus,  $K'$  is the cyclic strength coefficient and  $n'$  is the cyclic strain hardening exponent,  $\Delta\varepsilon_e$  and  $\Delta\varepsilon_p$  are the elastic and plastic components of the total strain range  $\Delta\varepsilon$  and  $\Delta\sigma$  is the nominal stress range. The solution of the cyclic behaviour is obtained by simultaneously solving the equation above and the Neuber's equation, expressed by the following equation, to calculate the local stress-strain in which  $K_t$  is Neuber's constant and  $\Delta S$  the gross stress.

$$\Delta\sigma\Delta\varepsilon = \frac{(K_t\Delta S)^2}{E} \quad (6.7)$$

#### 6.3.4 Finite element model: Base material

A finite element analysis was performed using the commercial FEM numerical solver ANSYS-Mechanical v13. A full structural model was built using ANSYS *Solid 186* element (3D) type. The temperature dependence of the linear and nonlinear material models is embedded in the analysis. The temperature and pressure distributions calculated by CFD are used to calculate the stress and strain distribution. The FE model was constrained at the liner aft and fore end to simulate the actual engine installed-configuration as seen in Figure 6.6. At one end the liner is fixed (clamped), and at the other end cylindrical support and elastic foundation is used. In the cylindrical support, the radial and tangential degrees of freedom (DOF) are fixed, and the axial DOF is set free, since the liner at this end has a spring-type connection, which allows axial movement. However, the assembled adjacent component acts as a constraint that prevents continuous axial movement. Therefore, a modified Winkler-type foundation, so-called elastic foundation is used to restrain the free axial motion of the



structure. The elastic foundation stiffness (EFS) is defined as the pressure required to generate a unit normal deflection of the foundation. The contact region is allowed to deform according to basic spring behaviour. The contact between the structure and foundation is never broken, which is the case in the real assembly. The EFS matrix used in the analysis in general form is

$$[K_e^f] = k^f \int_A \{N_z\}\{N_z\}^T dA \tag{6.8}$$

where  $k^f$  is the foundation stiffness,  $\{N_z\}$  is the vector of shape functions representing motions normal to the surface and  $A$  is the area of element.

Normally, material inelastic strain response to either mechanical or thermal loading is described by time independent and time dependent constitutive equations. Plasticity, which is a time independent variable and instantaneous, generally occurs at high stress-strain local regions. And the creep process is dependent on time, and occurs at a stress level sustained for a period of time at elevated temperatures, which is less than the required stress for plastic deformation. In this particular application, the gas turbine experiences transient thermal and pressure loadings as well as dwell periods at elevated temperatures during the operation. Thus, the plasticity and creep interaction takes place. Therefore, even though they are independently solved, the strains are alternated for small sequential increments.

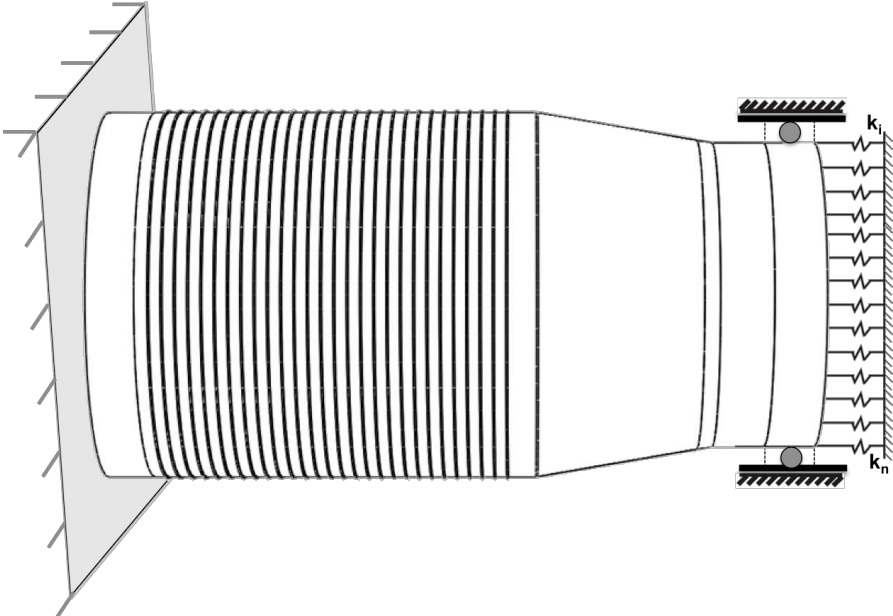


**Figure 6.6. Combustion liner boundary conditions**

**6.4 Combustion dynamics analysis**

The combustion process characteristics are influenced by the operational parameters of the GT, such as flame temperature, equivalence ratio, fuel quality, operational load, and ambient conditions. At certain GT settings, the combustion instabilities can be induced, in which high amplitude pressure oscillations are built up. These dynamic pressures can be measured in-service and used in condition monitoring to detect and prevent catastrophic failure due to fatigue. It is essential not only to understand the reasons of instability, but also to predict the

fatigue lifetime consumption and calculate tolerable limits of the amplitudes that are both beneficial for in-service monitoring and hardware design stage. Since the dynamic pressure levels experienced by the GT liners have a stochastic nature [5, 18-21], in-service pressure data, measured near fore-end, are used for the combustion dynamics related investigation instead of CFD analysis, which is also computationally expensive. However, the measurement of the local stresses/strains at critical locations is difficult. Thus, the pressure oscillations are assumed to be effective near fore-end, which is in compliance with the global pressure field generated in the liner as presented in section 6.6.1, and uniformly applied over the inner surface of the liner in the hoop-direction. Hence, the pressure data are analysed for further analysis.

The physical process of pressure oscillation generation due to combustion instabilities is assumed to be stationary, ergodic, Gaussian, and random. The description of the terms is as follows. The pressure oscillations are considered to be random, which claims an indeterminacy of the future events that cannot be explicitly represented with certainty at any particular time. In addition, this process is assumed to be stationary random, implying that the statistical properties of a data group, cluster, or ensemble will not change over time, for instance the probability distribution measured across the ensemble at two particular data record times remains identical. Furthermore, the process is assumed to be ergodic, which allows the statistics measured along any one cluster to be representative for the statistics measured along the ensemble. Hence, selecting a statistically sufficiently long data cluster enables representation of the process, instead of measuring the full data, ensemble.

The procedure of the analysis on the structural response due to combustion dynamics is as follows. The time history of the measured pressure oscillations due to combustion dynamics is translated to a pressure frequency spectrum. Despite the variations of the amplitudes in time, the presence of a number of peaks in a well-defined range of frequencies is observed. A limit-level of amplitude is defined as 10% of the maximum amplitude. A low-pass filter is applied on the full data with a cut-off frequency of the highest frequency, which satisfies the limit-level condition. Thus, the frequencies higher than the cut-off frequency are attenuated to eliminate low-amplitude data. Nevertheless, analysing this data is numerically costly and time consuming. Therefore, a representative cluster is selected by executing probability density function (PDF) and cumulative distribution function (CDF) algorithms so that the cluster statistically best represents the full data. The measured pressure data within the cluster, variable amplitude loading time history, is reduced into basic cyclic events by applying RFC algorithm. Hence, the pressure amplitude occurrences are represented by the corresponding strain amplitudes and cycles using a rain-flow matrix. Next, the cycles that produce the most severe damage are calculated using a damage matrix and fatigue lifetime is calculated due to the pressure oscillations.

#### **6.4.1 Statistical distribution and probabilistic analysis**

Random parameters are present rather frequently in nature, as in this particular application of gas turbine combustor. The variability of the pressure loads inside the liner is generated due to the stochasticity of combustion dynamics. An infinitely long-time record of data is



theoretically necessary to obtain an explicit description of the irregular motion of the parameter cycles in time. However, practically this is not feasible; therefore, finite-time records of data are rather preferred. Hence, the definition of the length of the finite-time record is very important to statistically represent the overall data history. In general practice, PDF is used to model the statistical behaviour of a random variable.

In this particular investigation, *MATLAB Statistical Toolbox* was used with an accompanying user-defined algorithm to find the best distributions of random data according to the best-fit to the data. The best-fit was obtained by performing goodness-of-fit check, which diagnoses the adequacy of the statistical model. Three criteria were used for the model selection. The first one is the Akaike information criterion (AIC) [22], which compares the models from a perspective of expected Kullback-Leibler (K-L) information (a measure between a conceptual reality and approximating model) [23] and Fisher's maximised log-likelihood estimation (MLE) (a method, which determines the set-of-values of the parameters of an approximating model that maximised the likelihood function) [24]. The second one is the Bayesian information criterion (BIC), which is based on the empirical log-likelihood and related to AIC, whose penalty for additional parameters is more than AIC [25, 26]. The last one is the AIC criterion with a second-order bias correction for finite sample sizes (AICc) [27-31].

Let  $f(x|\theta)$  be the approximating model, for the data  $x$  given the parameters  $\theta$  of the parameter space  $\Theta$ , being measured against the conceptual reality,  $g(x)$ . If the parameters of the approximating model,  $f(x|\theta)$  are estimated using MLE, then it is denoted as  $f(x|\hat{\theta})$  so that the MLE of the unknown true parameter vector  $\theta$  is the  $\hat{\theta}$  that maximises the likelihood function. Then, the approximating models in the candidate set for the representation of the data are denoted as  $\{f_i(x|\hat{\theta}), i = 1, \dots, R\}$ , where  $R$  is the number of models in the candidate set.

The K-L information (distance) between the conceptual reality,  $g$ , and the approximating model  $f$  is defined for continuous functions as the integral

$$I(g, f) = \int g(x) \log \left( \frac{g(x)}{f(x|\theta)} \right) dx \quad (6.9)$$

where  $I(g,f)$  (K-L information) is the 'information' lost when the approximating model  $g$  is used to represent the conceptual reality  $f$ . Therefore, the model with a minimum  $I(g,f)$ , among the models of the candidate set, loses the least information to approximate the reality. The formulas of AIC, BIC and AICc are given, respectively, as follows

$$AIC = -2 \log(\mathcal{L}(\hat{\theta}|x)) + 2k \quad (6.10)$$

$$BIC = -2 \log(\mathcal{L}(\hat{\theta}|x)) + k \log(n) \quad (6.11)$$

$$AICc = AIC + ([2 * kk * (kk + 1)] / (n - kk - 1)) \quad (6.12)$$

where  $\mathcal{L}$  is the vector of optimised log-likelihood objective function (LLF) values associated with parameter estimates of the approximating model,  $k$  is the number of estimated parameters of the approximating model associated with each value in LLF and  $n$  is the total sample size. The natural logarithm of the likelihood function is the log-likelihood function

and it enables easier algebraic manipulation. Note that LFF achieves its maximum value at the same points as MLE, since the logarithm transformation is a monotonically increased function.

The calculated smallest criterion value of these three parameters for each model determines the best-fit model. In the analysis of distributions, the first four models were chosen using the goodness-of-fit check. These four model-types remained the same for the selected time records of data. The following equations of the PDF for the distributions, with two parameters (location parameter (mean)  $\mu$ , scale parameter (standard deviation)  $\sigma$ ), of normal, logistic, extreme value and, with three parameters (location parameter  $\mu$ , scale parameter  $\sigma$ , and shape parameter  $k$ ), the generalised extreme value, respectively, are given as

$$f(x|\mu, \sigma) = \frac{1}{\sigma\sqrt{2\pi}} e^{-\frac{(x-\mu)^2}{2\sigma^2}} \quad (6.13)$$

$$f(x|\mu, \sigma) = \frac{1}{\sigma\left(1+e^{\left(\frac{x-\mu}{\sigma}\right)^2}\right)^2} e^{\left(\frac{x-\mu}{\sigma}\right)} \quad (6.14)$$

$$f(x|\mu, \sigma) = \frac{1}{\sigma} e^{\left(\frac{x-\mu}{\sigma}\right)} e^{\left(-e^{\left(\frac{x-\mu}{\sigma}\right)}\right)} \quad (6.15)$$

$$f(x|k, \mu, \sigma) = \frac{1}{\sigma} e^{\left(-\left(1+k\frac{x-\mu}{\sigma}\right)^{-\frac{1}{k}}\right)} \left(1+k\frac{x-\mu}{\sigma}\right)^{-1-\frac{1}{k}}; 1+k\frac{x-\mu}{\sigma} \geq 0 \quad (6.16)$$

where  $x$  is the random variable, in this case load amplitudes, which is as a function of time as shown  $S(t)$  and the approximating model parameters ( $\mu$ ,  $\sigma$ , and  $k$ ) are described above.

The CDF (or probability distribution function) describes the probability that the instantaneous value  $x(t)$  takes on a value less than or equal to the random variable  $x$ , defined by the CDF. The CDF,  $F(x)$ , of a continuous random variable,  $x$ , can be defined in terms of its probability density function,  $f(x)$ , as

$$F(x) = Prob[x(t) \leq x] = \int_{-\infty}^x f(\xi) d\xi \quad (6.17)$$

The boundaries of the distribution function are zero and one such that the probability of the instantaneous value  $x(t)$  be less than the lower bound ( $-\infty$ ) is zero and more than the upper bound ( $x$ ) is unity. The reader is referred to the references, indicated in this section, for the further theory and detailed information.

#### 6.4.2 Rainflow cycle counting algorithm

The load ranges, the range between the minimum and the subsequent maximum load, are the essential elements for the variable amplitude load fatigue analysis, together with the mean load. Thus, the load-time histories play an important role. Hence, a cycle counting method is essential to determine the equivalent strains, their number of cycles and resulting damage to the variable load ranges of a load-time history. The rainflow cycle (RFC) counting method is one of the widely used approaches [32-35], and also was applied to gas turbines [36, 37]. In this work, the stress/strain reversals are characterised by analysing the variable pressure loading during the complex process of combustion via a RFC counting algorithm [38, 39].

This deterministic counting procedure applied to the time history enables a wide application to any stochastic process.

## 6.5 Lifetime prediction

The service lifetime of the liners is potentially covered by creep, LCF and HCF/VHCF mechanisms. In this section, the lifing approach is described and the interaction between the mechanisms is also discussed.

The endurance of the gas turbine engine against the elevated temperature levels generated by the combustion process is limited to the creeping resistance of the materials. The creep lifetime is calculated using the Larson-Miller parameter (LMP), of which the approach is based on the Arrhenius rate equation. The LMP, which relates the applied stress, temperature and time to failure, was used to extrapolate the experimental data to compare the creep behaviours.

$$P_{LM} = T(C_{LM} + \log t_r) \quad (6.18)$$

where  $P_{LM}$  is the Larson-Miller parameter,  $T$  is the absolute temperature [K],  $C_{LM}$  is the Larson-Miller constant that is generally chosen as 20 for the superalloys as a standard practice,  $t_r$  is the rupture time [h].

The number of start-up and shut-off times in the gas turbine engines are limited; however, high strain levels are generated during these conditions. Therefore, LCF phenomenon is considered for these periods. The LCF behaviour is described by the total strain range, including elastic and plastic strains, experienced by the material. The LCF lifetime predicted by the strain-life approach using the Basquin-Coffin-Manson expression under fully reversed cycling

$$\frac{\Delta \varepsilon}{2} = \frac{\Delta \varepsilon_e}{2} + \frac{\Delta \varepsilon_p}{2} = \left( \frac{\sigma_f'}{E} \right) (2N)^b + \varepsilon_f' (2N)^c \quad (6.19)$$

where  $\sigma_f'$  and  $\varepsilon_f'$  are the fatigue strength and ductility coefficients, respectively, and  $b$  and  $c$  are the fatigue strength and ductility exponents, respectively. However, in situations where the loads are not fully reversed and variable, the mean stress effect must be included. Therefore Smith–Watson–Topper (SWT) mean stress correction model is used.

$$\sigma_{max} \varepsilon_a = \frac{(\sigma_f')^2}{E} (2N)^{2b} + \sigma_f' \varepsilon_f' (2N)^{b+c} \quad (6.20)$$

The cyclic mechanical loads on the structure can induce high stress regions that can lead to fatigue damage. Even though the strain-life approach is generally used to calculate the cycles to crack initiation in LCF regime, it can be extended to describe the HCF behaviour as well [40]. While the fatigue damage forms cracks and subsequently makes the cracks grow and propagate, the elevated temperature under constant pressure stresses enables creep type damage letting material flow. In a GT combustor, potentially the failure mechanism is due to the cyclic loadings leading to fatigue damage superimposed with time-dependent creep damage. ASME Code Case N 47 [41] is used as the first and conservative design method for fatigue-creep interaction life assessment. The basis of the assumption is to linearly accumulate

as the life fractions include the cyclic dependent fatigue so-called Miner's law and time-dependent creep so-called Robinson's rule (Palmgren-Miner cumulative damage rule)

$$D_{tot} = D_f + D_c = \sum_{i=1}^{n_f} \frac{n(i)}{N(i)} + \sum_{j=1}^{n_c} \frac{t(j)}{t_{r(j)}} \quad (6.21)$$

where  $n$  is the number of applied cycles and  $N$  is the number of cycles to fatigue at  $i_{th}$  stress or strain range level,  $t$  is the service time and  $t_r$  is the creep stress level at  $j_{th}$  stress level and  $n_f$  is the number of stress or strain range levels and  $n_c$  is the number of stress levels. In the linear accumulation method the cyclic and time-dependent damage fractions are computed independently and their interaction is only empirically considered in  $D_{tot}$ .

As mentioned earlier, LCF is generally accompanied by macroscopic plastic deformation at every cycle; however, at macro-scale the HCF/VHCF mechanism obeys elasticity. Nevertheless, plasticity phenomenon occurs locally and discontinues in practice at the stress concentration regions [42], even though the stresses are governed by elasticity in the net section. Thus, following the LCF lifetime prediction, the strain-life approach is extended to HCF/VHCF lifetime analysis using the same principals above excluding the creep effects, which is already included prior to HCF/VHCF analysis. Furthermore, the most life-threatening pressure amplitudes obtained by the rainflow algorithm and damage matrix for the test cases (data record times), which are presented in the results section, are compared by means of the crack growth lifetimes. Therefore, the following procedure assume a crack initiation lifetime of LCF lifetime or in other words zero cycles of HCF/VHCF regime [43], and identical initial equivalent flaw sizes in the analysis of the test cases, since the crack initiation lifetime is considered not to be governed by the HCF/VHCF regime, but by the LCF regime.

Consider that the crack propagation lifetime obeys linear elastic fracture mechanics (LEFM) assumption, which is based on the stress intensity factor (SIF) at the crack-tip. The Paris-Erdogan model [44], to calculate the crack propagation rate, reads

$$\frac{da}{dN} = C(\Delta K)^m \quad (6.22)$$

where  $a$  is the crack length,  $N$  is the number of load cycles,  $\Delta K$  is the SIF range,  $C$  and  $m$  are the Paris's coefficient and exponent (slope), respectively. The limitation of this equation is the lack of incorporation with the mean stress, thus the stress ratio ( $R = \sigma_{min} / \sigma_{max}$ ) of the applied cyclic loading [45]. Even though considerable efforts have been devoted to formulate the influence of the stress ratio [46, 47], a universal equation has not been found applicable to nickel-based superalloys. In this work, a widely-used approach Walker model [48] is utilised to account for the  $R$ -effect on crack growth, of which the application to the AlloyX can be found in the literature [49]. In this model, an effective range of stress intensity factor ( $\overline{\Delta K}$ ) is introduced replacing  $\Delta K$  gives

$$\overline{\Delta K} = \frac{\Delta K}{(1-R)^{m'}} \quad (6.23)$$

where  $m'$  is the Walker's exponent (material constant) determined empirically, and the stress ratio  $R$  does not affect the slope (Paris's exponent) of the fatigue crack growth behaviour. The

Walker's model is valid for  $R \geq 0$ , which is satisfied in this case as the pressure oscillations due to combustion dynamics are superimposed on the steady-state pressure equilibrium. The SIF range can be calculated with respect to the maxima and minima of the loading cycles that can be given as

$$\Delta K = \Delta\sigma\beta\sqrt{\pi a} \quad (6.24)$$

where  $\Delta\sigma$  is the range of cyclic stress amplitude and  $\beta$  is the geometry constant. The differential equation can be solved using Fourier method (separation of variables) assuming the material constant  $\beta$  is independent of the crack length  $a$  (relatively short-crack assumption), hence the integral form for the  $\Delta K$  can be formulated as follows

$$C \left( \frac{\Delta\sigma}{(1-R)^{m'}} Y \right)^m \int_0^{N_f} dN = \int_{a_i}^{a_f} a^{-\frac{m}{2}} da \quad (6.25)$$

where  $Y$  is the constant defined as  $Y = \beta\sqrt{\pi}$ ,  $N_f$  is the number of remaining cycles to failure,  $a_i$  and  $a_f$  are the initial and final crack lengths, respectively. Integrating both sides gives

$$N_f = \frac{a_i^{(1-\frac{m}{2})} - a_f^{(1-\frac{m}{2})}}{C \left( \frac{\Delta\sigma}{(1-R)^{m'}} Y \right)^m \left( \frac{m}{2} - 1 \right)}; m \neq 2 \quad (6.26)$$

The equation, above, if  $n > 2$  and  $a_f \gg a_i$ , thus  $a_i^{(1-m/2)} \gg a_f^{(1-m/2)}$ , can be rewritten as

$$N_f = \frac{a_i^{(1-\frac{m}{2})}}{C \left( \frac{\Delta\sigma}{(1-R)^{m'}} \right)^m \left[ Y^m \left( \frac{m}{2} - 1 \right) \right]} \quad (6.27)$$

Logarithm of both sides gives

$$\log N_f = -\log Y^m \left( \frac{m}{2} - 1 \right) - \log C - m \log \left( \frac{\Delta\sigma}{(1-R)^{m'}} \right) + \left( 1 - \frac{m}{2} \right) \log a_i \quad (6.28)$$

This can be written in the form of a linear equation of  $N_f$  in log-space as

$$\log N_f = A_0 + A_1 \log C + A_2 \log \left( \frac{\Delta\sigma}{(1-R)^{m'}} \right) + A_3 \log a_i \quad (6.29)$$

where  $A_i$  can be determined by least squares analysis. This equation shows that fatigue crack growth lifetime is a linear combination of the components derived by the material properties, geometry, stress range and initial crack length. The reader is referred to the given reference for the derivation of the approach and application to a nickel-base superalloy [50].

## 6.6 Results

### 6.6.1 Combustion generated loads

The effects on the heat transfer were addressed in the previous work [13] by means of fluid dynamics and are briefly presented as follows. The fluid and the structure are sequentially-coupled in the CFD analysis. Hence, the temperature field calculated by the fluid solver was interpolated into the solid domain used by the structural solver. Thus, the effects of the thermal gradients generated by the combustion inside the liner can be resolved. Basically, fuel-staging differentiates the maximum temperature exposure inside the chamber and the

temperature field (Figure 6.7). In the figure, the hot-regions ( $T > 0.95 \cdot T_{MAX}$ ) are indicated with black-coloured lines. The zoomed-window is a close-up view to the chamber, liner and casing interface. A significant temperature gradient was generated due to fuel-splits and turbulent flow properties. The compressor discharge air, passing through the cavity walls, cools down the liner and clearly influences the temperature field. The liner temperature remains relatively cool.

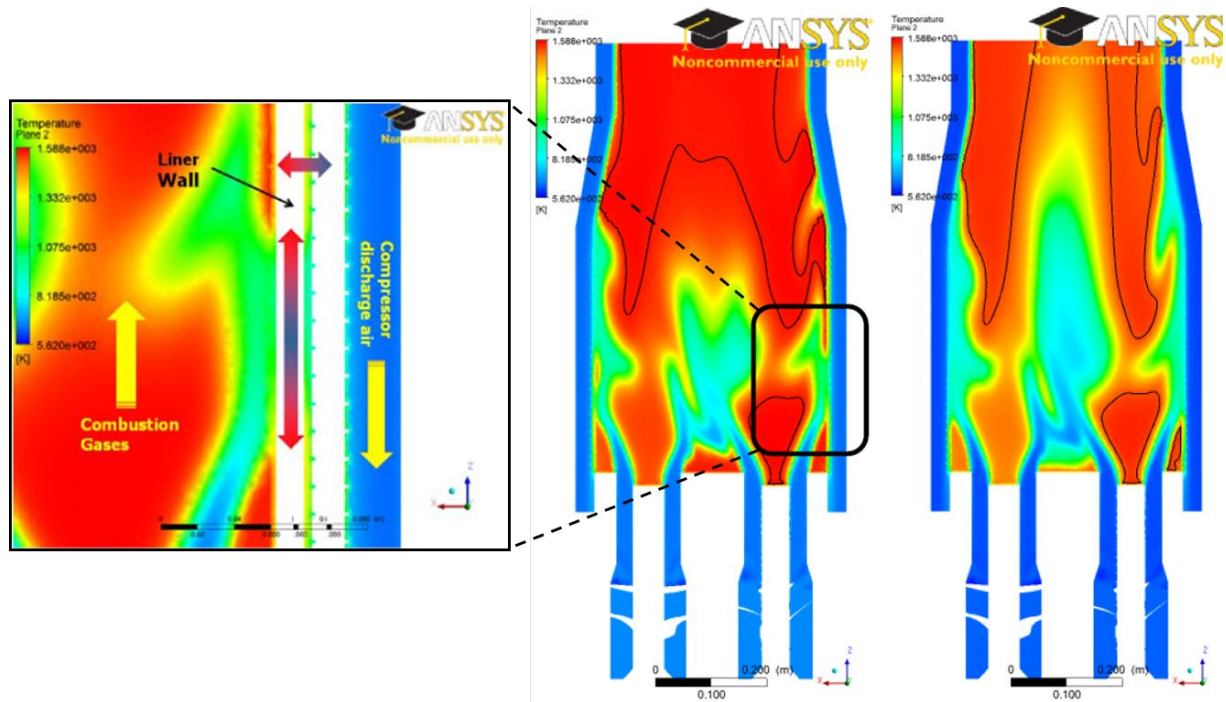


**Figure 6.7. The temperature distribution contour plot at an intermediate plane at base-load (left) and part-load (right) [13]**

Operating the engine at higher temperatures increases the fuel efficiency [51], on the contrary, it increases the material degradation rate [52] resulting in structural failure. In general, the combustion generated heat from the flame is transferred to the liner structure by radiation and convection that is subsequently conducted through the liner. Hence, the structure is exposed to a thermal gradient across the wall. Therefore, the elevated temperature level, together with the thermal asymmetry, result in higher thermally induced stresses in the liner. Moreover, the mechanical properties are strongly dependent on the temperature and the strength reduces rapidly when the temperature exposure level increases. Therefore, protection systems, such as thermal barrier coating (TBC) systems, are applied on the inner surface of the liners in order to provide thermal insulation. Together with cooling systems, the liner temperature can be kept below the maximum allowed amplitude limits. Since the top coat of the TBC has relatively low heat conductivity, a significant temperature difference between the combustion hot gases and the base material (liner) can be achieved, such that a reduction from 1125 to 810 °C (315 °C) at base-load and from 1045 to 746 °C (299 °C) at part-load is obtained at the hot-spot location on the liner (Figure 6.8 and Figure 6.9). The characteristic calculated temperatures for the base-load and part-load are listed in Table 6.2.

**Table 6.2. Calculated temperatures ( $^{\circ}\text{C}$ ) for the base load and part load**

	$T_{\text{avg}}$ (Chamber)	$T_{\text{max}}$ (Chamber)	$T_{\text{avg}}$ (Chamber-liner interface)	$T_{\text{max}}$ (Chamber-liner interface)	$T_{\text{avg}}$ (Liner)	$T_{\text{max}}$ (Liner)	$\Delta T$ at $T_{\text{max}}$ (Liner thickness)
Base-load	1027	1331	843	1125	571	810	126
Part-load	935	1295	682	1045	426	746	107

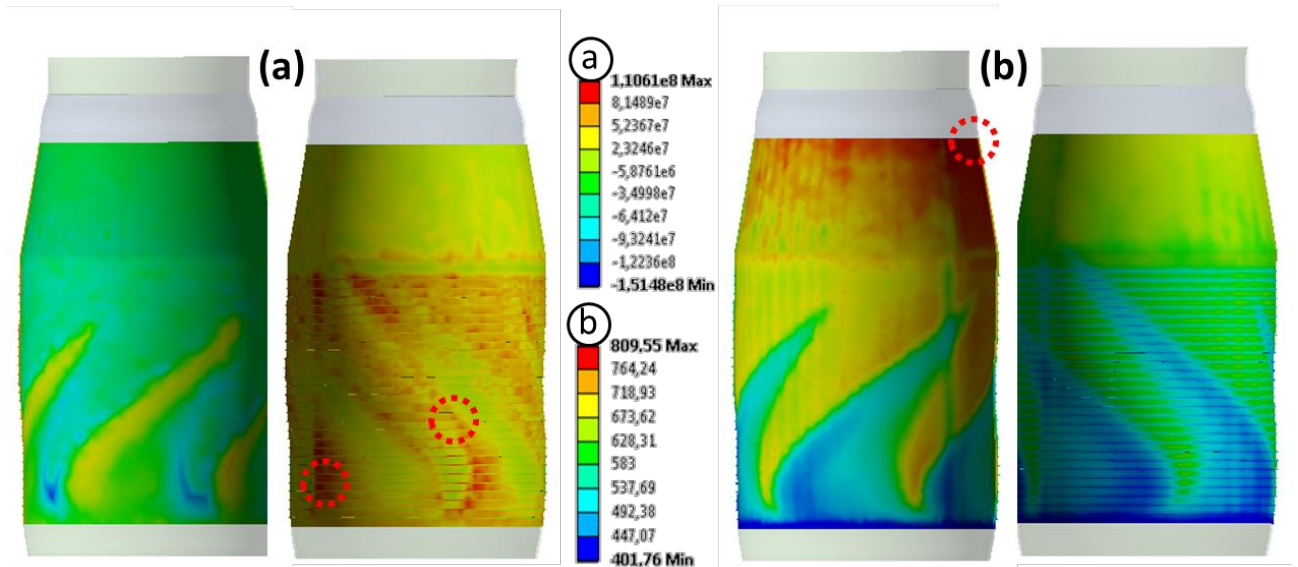


**Figure 6.8. The pressure [Pa] (a) and temperature [ $^{\circ}\text{C}$ ] (b) distributions on the liner inner (left) and outer (right) surface (Base-load)**

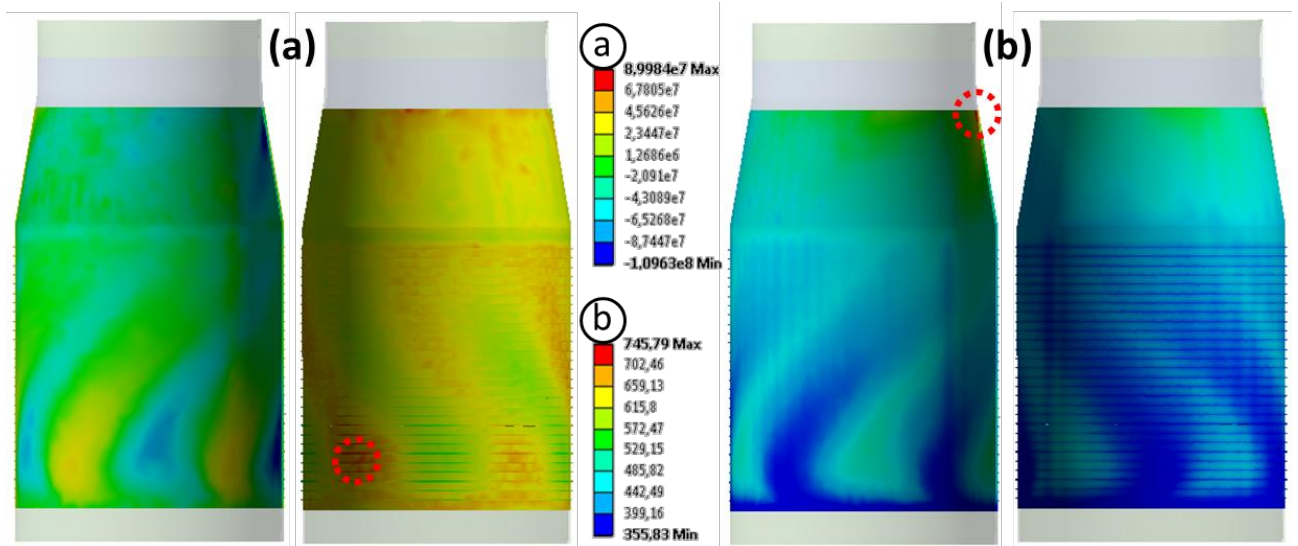


**Figure 6.9. The pressure [Pa] (a) and temperature [ $^{\circ}\text{C}$ ] (b) distributions on the liner inner (left) and outer (right) surface (Part-load)**

The temperature and pressure distributions on the inner and outer surface of the liner are presented in Figure 6.8 (base-load) and Figure 6.9 (part-load). A significant metal temperature gradient was generated on the liner surface in both circumferential and longitudinal directions. The circumferential temperature distribution at three cross sections (fore-end, mid-plane, aft-



end) for the base-load and part-load are depicted in Figure 6.10. As seen in the figure, even though higher temperatures are generated at aft-end of the liner at base-load, the temperature distribution in this region is less uniform at the part-load that induces higher thermal stresses compared to overall geometry. However, the temperature distribution at mid-plane and fore-end is more uniform at part-load. This can be addressed to the combustion generated energy, which is more densely conserved throughout the chamber and transported from the flame region to the combustor exit region by the strong swirled flow pattern at base-load. The hot temperature gradients impart a large  $\Delta T$  rise from the hot to cold sector. These are attributed to the variation in the flame length and shape due to the change from base to part-load. The pressure follows the temperature patterns, which are the traces of the fluid flow paths. Furthermore, the maximum amplitude of the pressure is in near-flame region and reaches a quasi-uniform distribution near aft-end. The red-coloured dotted circle marks designate the hot-spot (critical) locations where the maximum amplitude takes place.

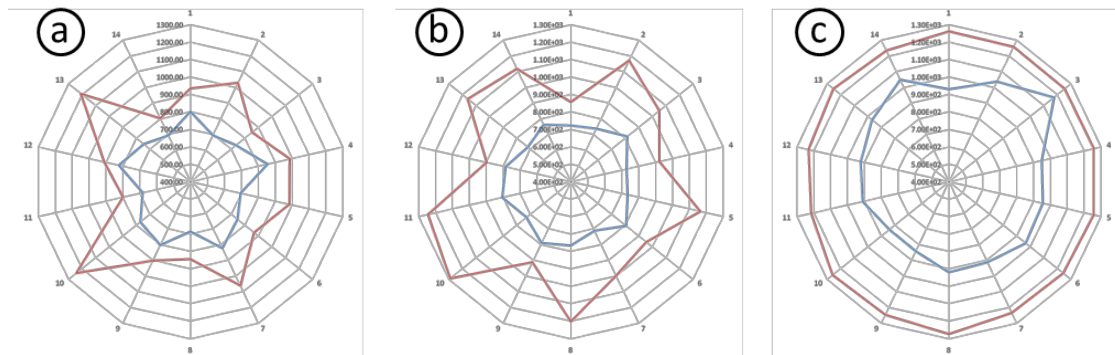


**Figure 6.10. Circumferential temperature [ $^{\circ}\text{C}$ ] distribution at fore-end (a), mid-plane (b), aft-end (c) for base-load (red-line) and part-load (blue-line)**

### 6.6.2 Structural behaviour at part and base load

In Figure 6.11, the equivalent stress distribution due to thermal load is shown. Stress concentration areas are present in the near flame region of the liner where thermal stresses play a dominant role (see radar plot) and at the constrained regions. The maximum values reached (180 MPa) are within the elastic yield limit of the material (237 MPa at 760  $^{\circ}\text{C}$  and 0.2% offset). The hoop stress component is the dominant part, while the radial and axial components are negligible shares.

In Figure 6.12, the stress relaxation effect is shown for the two different operating conditions measured at a point near the flame region. At base load, the higher stresses produce creep and stress relaxation while at part load, the stress generated is not high enough for producing locally visco-plastic effects on the structure. Note that the creep analysis starts at  $t=0$ , and the transient phase is not modelled meaning that at  $t=0$  the full load conditions are applied which give a high initial stress.

At the beginning of the operations, the elastic stresses are within the yield point and the elastic strain is the biggest share of the total strain. Creep strain will manifest over time and the elastic stress slowly will begin to relax. The plasticity produced after 50000 hours is caused by the creep material settlements.



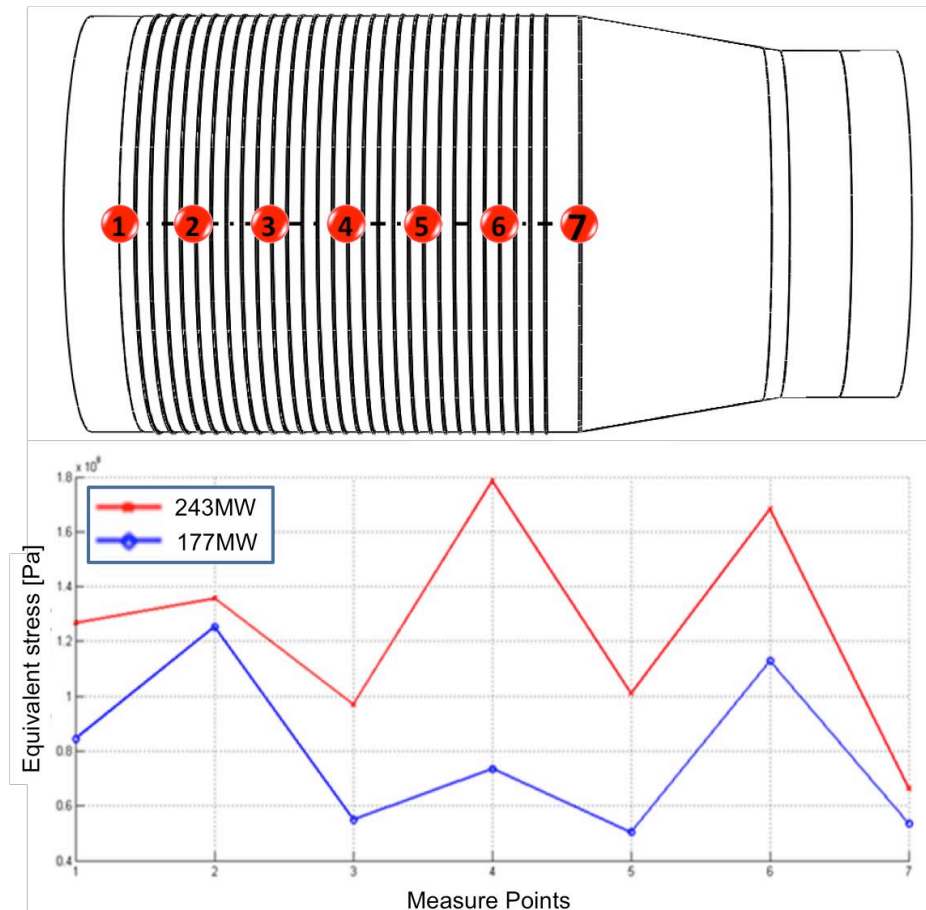


Figure 6.11. Stress plot along the liner inner and outer surface

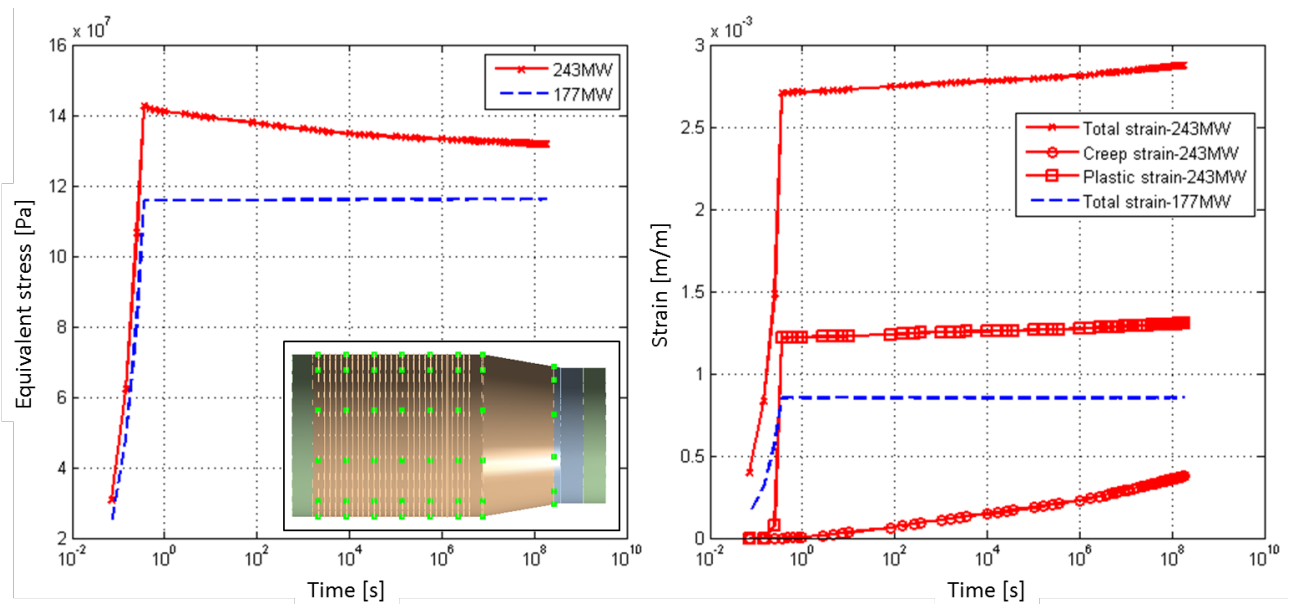


Figure 6.12. Stress relaxation and strain development with time of the green points selected on the liner outer surface

The linear elastic strains associated with these stresses create a strain control environment under a constant strain and temperature in a specified period of time, due to the relief of the thermal stresses when the liners achieve the desired thermal shape. The strain levels have

been calculated at different points of the liner and a comparison has been proposed for the two operating conditions. Again, the creep effect is evident for base load configuration while at part load a constant total strain field is observed. The maximum plastic strain and the maximum creep strain are measured in the near flame region of the liner (as shown in Figure 6.12). The plastic deformation is a consequence of the creep strain and tends to deform the liner toward a desired thermal shape.

An estimation of the deformation of the liner can be done by measuring the directional deformation in the x and y axes. At the central region of the liner, the maximum calculated deformation of the liner is for base load operation equal to 2.3% and for the part load operations (1.5%).

**6.6.3 Structural response at base load**

In Figure 6.13, the developed elastic, plastic, creep and thermal strain distributions are presented. The maximum elastic and plastic strain locations correspond to the pressure load, whereas the temperature field dominates the thermal strain distribution. Besides, the creep strains are generated with respect to the competition between pressure and temperature, of which hot spot is located between the aft-end and fore-end.

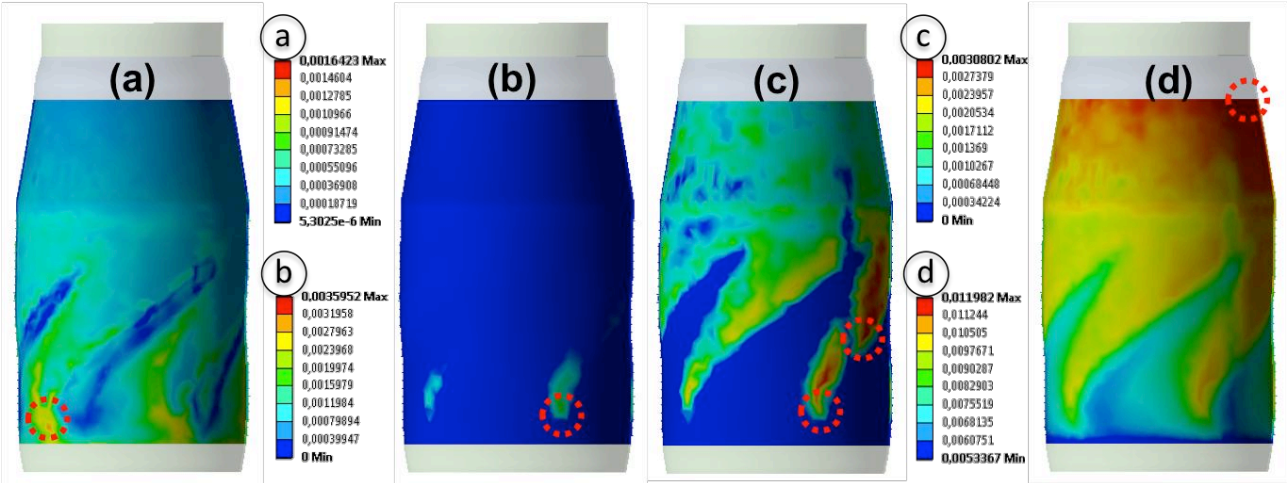


**Figure 6.13. Elastic (a), plastic (b), creep (c) and thermal (d) strain distribution [m/m] on the inner side of the liner**

The loading and stress-strain distribution figures are not sufficient to compare the local response along the liner. Therefore, the liner geometry was sectioned by seven planes, which are presented in Figure 6.14. Each section plane represents the corresponding circumferential path on the liner. The legend colours of sections, which are used in the following figures, are depicted in Figure 6.14.

In Figure 6.15, the temperature, pressure, deformation and stress components in the hoop direction at each section are presented. From the figures, the circumferential asymmetry of the pressures and temperatures, as well as the resulting deformations and stresses can be seen. In the pressure plot, the highest amplitude appears near fore-end; however, the pressure amplitude at the fore-end remains smaller compared to adjacent sections. This is due to the flame shape and location (Figure 6.7). The flame is constructed right after the fore-end and

elongates longitudinally with a wrinkled tip-geometry. Thus, higher-pressure generation takes place right after the fore-end and reaches its maximum near fore-end. Furthermore, the amplitude decreases gradually towards the aft-end and also the circumferential pressure asymmetry tends to vanish near the aft-end, since the momentum generated by the swirl motion reduces and stabilises. On the other hand, the maximum temperature occurs near the aft-end as the hot gases flow from the inlet to the exit with elevated energy levels. Moreover, the cooling flow absorbs the heat starting from the fore-end and is progressively heated towards the aft-end; therefore, the cooling capacity is decreased towards the aft-end. In addition, the thermal asymmetry is more effective at the fore-end, since the jets are introduced in this region and the flame is formed near the fore-end. However, the circumferential temperature field is more symmetric near the aft-end, since the flow pattern is stabilised. The resulting deformation is generated due to the combined effect of pressure and temperature fields. The highest deformation appears at the aft-end, which is dominated by the temperature. Besides, the circumferential asymmetry in deformation is more visible after 'section 4' and it increases towards the fore-end that is more closely linked to temperature distribution. The maximum equivalent stress occurs at fore-end and the highest circumferential asymmetry in stress takes place at 'section 2', which gradually becomes more uniform towards aft-end. The circumferential stress distributions at the sections are more closely related to the pressures. However, high stresses are induced at the fore-end, since this section is adjacent to the location where the boundary condition is defined as fixed at all degrees of freedom. Moreover, the local temperature state plays a crucial role in stress response due to the significant temperature dependency of the material properties.

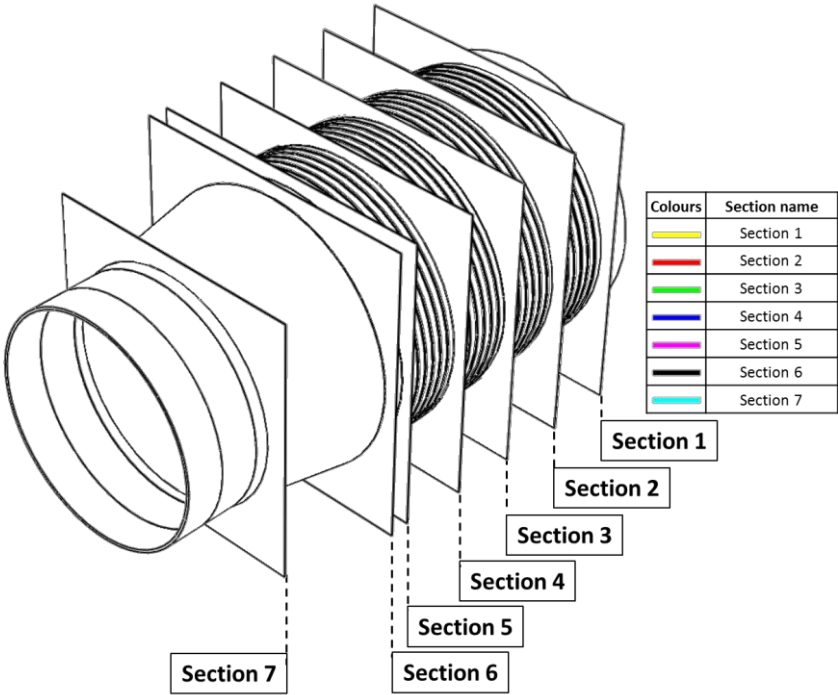


Figure 6.14. Combustion liner cross-section planes and the corresponding legend colours

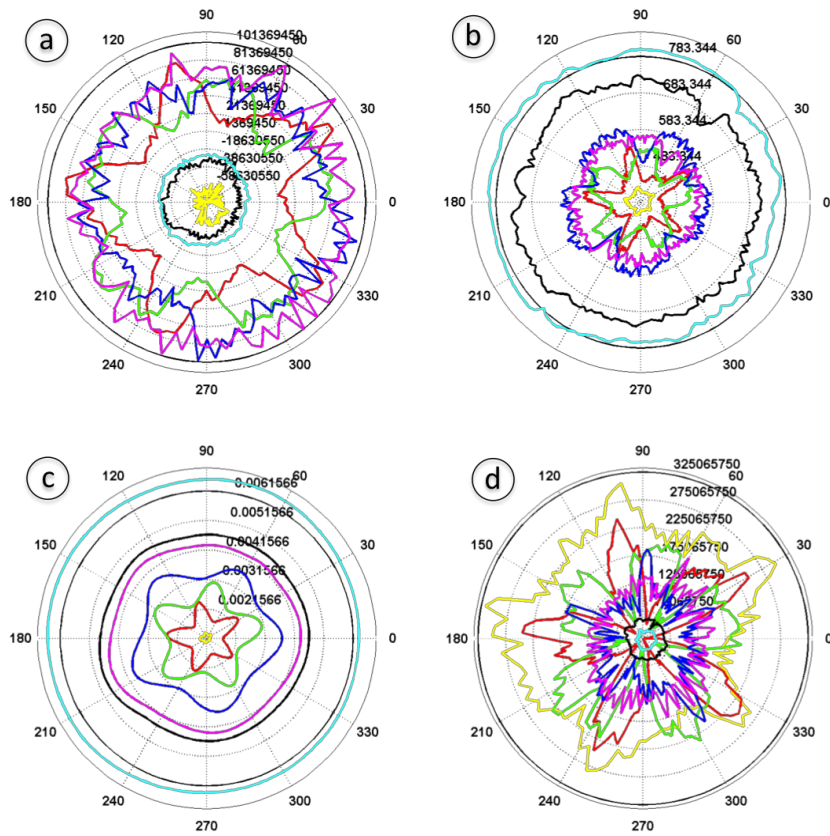


Figure 6.15. Pressure [Pa] (a), temperature [°C] (b), deformation [m] (c) and stress [Pa] (d) at sections

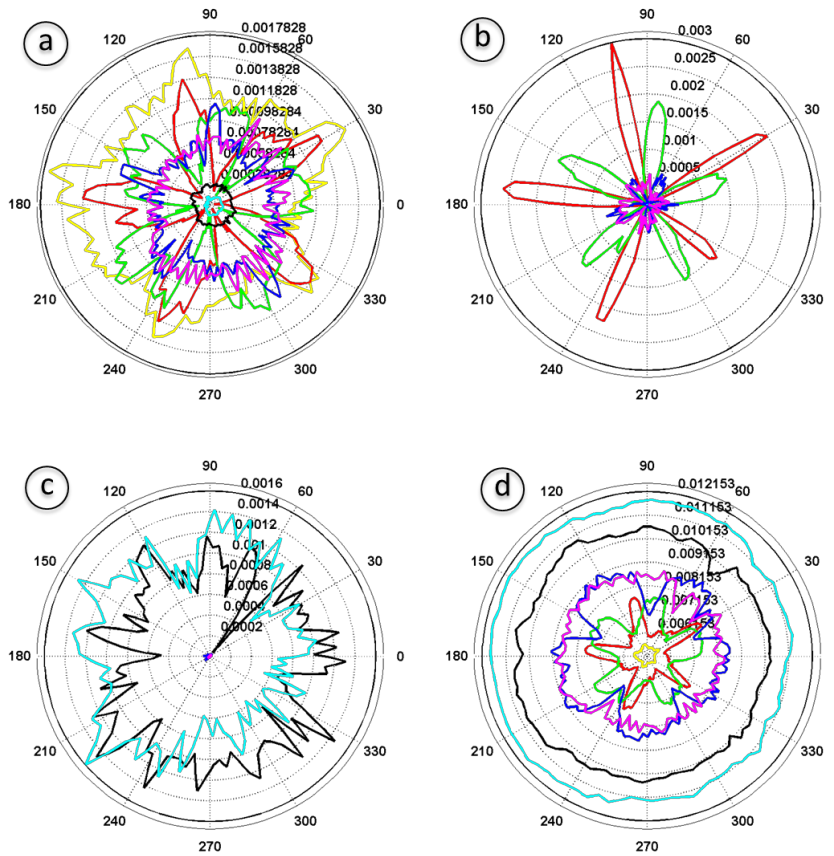
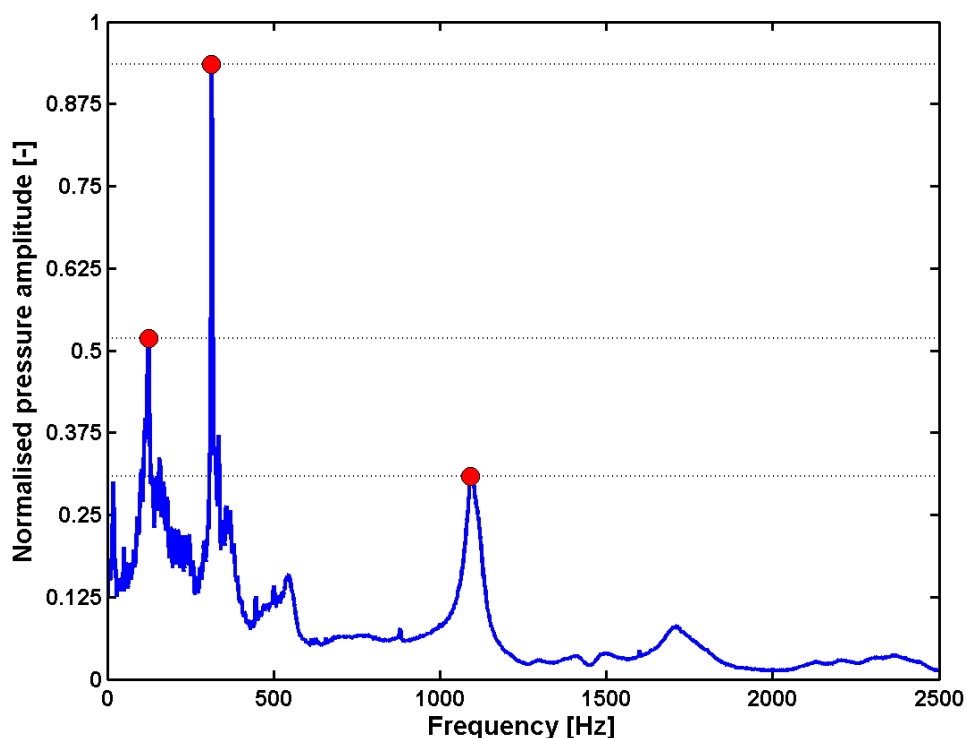


Figure 6.16. Elastic (a), plastic (b), creep (c) and thermal (d) strain [m/m] at sections

In Figure 6.16, the circumferential strain distributions are presented including elastic, plastic, creep and thermal components. The elastic strain distribution is similar to the stress distribution; however, a significant amount of plastic strains are generated at circumferential locations of sections '2' and '3', in which the elastic strain peaks are observed. Together with the elastic strain accumulation, the plastic strain is the main strain-component to consume the local LCF lifetime. The maximum creep strains are induced at the aft-end and adjacent location, 'section 6'; however, the strain amplitudes are limited to relatively negligible amplitudes at the remaining section. The thermal strain distributions at the sections represent the swirled flow pattern, which the hot gasses follow. Sections '7' and '6' experience higher thermal strain compared to the other section locations.

#### 6.6.4 Structural and acoustic modal response

When the GT operates at fully premixed combustion load, the frequency spectrum of the in-service pressure measurement at the primary zone shows the highest peaks at 125, 314 and 1091 Hz as seen in Figure 6.17. Structural and acoustic modal analyses were performed to investigate whether one of the modes matches with the frequency of the pressure oscillations, which leads to combustion instabilities. The results are as follows.



**Figure 6.17. Frequency spectrum of the measured in-service pressure at base-load operation**

The structural eigenfrequencies were calculated using FEM analysis for the base-load and part-load operations. Pre-stress effects were considered, since the stress state of the liner under static pressure and temperature loads affects the eigenfrequencies, and furthermore, the material properties are dependent on the temperature field. The equation of motion of the system can be expressed in the general form as



$$[M]\{\ddot{y}\} + [C]\{\dot{y}\} + [K]\{y\} = \{f(t)\} \quad (6.30)$$

where  $[M]$ ,  $[C]$  and  $[K]$  are the matrices of mass, damping and stiffness, respectively, and  $\{y\}$  is the displacement vector. A solution of free vibration for this equation can be expressed as

$$y = y_0 e^{i\lambda t} \quad (6.31)$$

where  $y_0$  is the vector of amplitude of response for the system. The response of the structure without an excitation can be readily obtained as

$$(-\{\lambda^2\}[M] + i\lambda[C] + [K])\{y_0\} = \{0\} \quad (6.32)$$

where  $\{\lambda\}$  and  $\{y_0\}$  are the eigenvalue and eigenvector, respectively. In the case of a pre-stress condition in an undamped system, the system describing equation can be defined as

$$(-\{\lambda^2\}[M] + [K + S])\{y_0\} = \{0\} \quad (6.33)$$

where  $[S]$  is the stress stiffness matrix, additional stiffness, introduced into the system response equation that is dependent on the pre-stress,  $[\sigma_0]$ . In this case, together with the stiffness matrix  $[K]$  of the system initial condition, the additional stiffness matrix due to pre-stress produces an effective stiffness matrix  $[K_{eff}]$ .

The structural eigenfrequencies change with the square root of the Young's modulus [53]. Moreover, the Young's modulus is significantly influenced by the temperature [16], the operational temperature range in this context. The temperature dependence of the eigenfrequencies by means of the operating condition (base and part load) is estimated as

$$\Delta f = \left| \frac{\Delta f_{base} - \Delta f_{part}}{\Delta f_{base}} \right| \times 100\% \quad (6.34)$$

The reduction of the operating temperature at part load causes an alteration in the eigenfrequencies of the structure of around 3%.

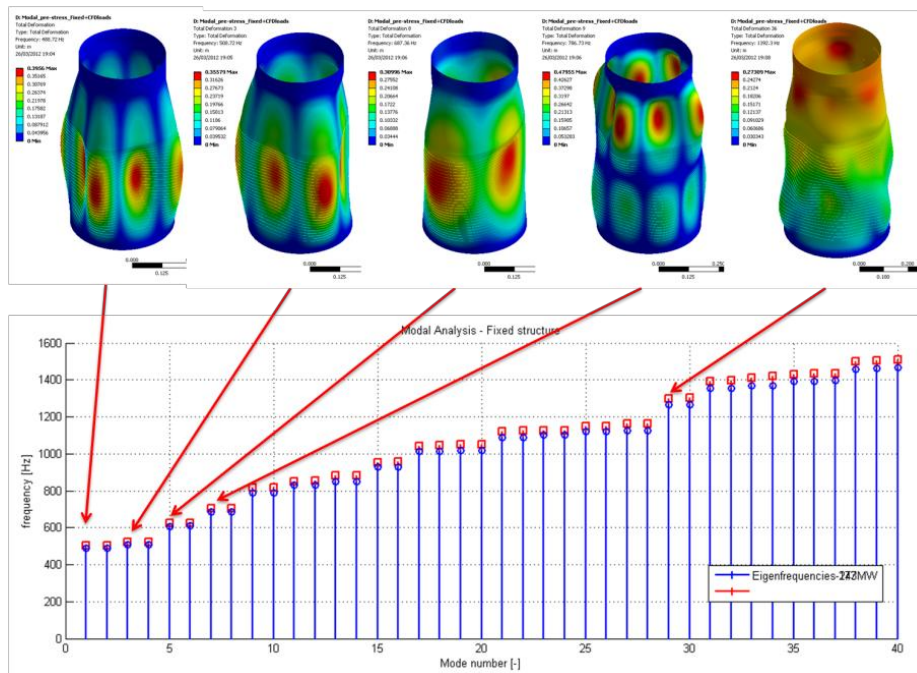


**Figure 6.18. Comparison of the structural eigenfrequencies of the liner for base-load (blue points) and part-load (red points) operations**

A numerical calculation has been performed using the ANSYS structural solver with *FLUID30* elements for the calculation of the acoustic eigenfrequencies of the chamber. A complete domain that includes liner and transition piece has been created in order to define the right reflecting boundary conditions. It is assumed that closed conditions (Reflection coefficient:  $R = 1$ ) are present at the bottom (at the burners) and upper end (at the inlet of turbine blades) of the acoustic domain. The Helmholtz equation was solved and the results for both base-load and part-load operations, and also the measurements, are listed in Table 6.3. Note that the density and the speed of sound are adjusted to the temperature field calculated by CFD and the smallest element size has been chosen according to the smallest acoustic wavelength to be solved.

Both of the analyses were performed in order to understand the impact of combustion dynamics on the structure integrity. The modal structural analysis, in a fixed configuration, shows the first eigenmode at 488 Hz producing an azimuthal - 8 nodes deformation (Figure 6.18 and Figure 6.19). The following modes, at higher frequencies, continue to be azimuthally shaped with different numbers of nodes along the liner circumference and they start to couple with axial mode shapes until the frequency of 1392 Hz where the first pure axial mode is found. As discussed in the previous paragraph, the structural eigenfrequencies change at different loads of the GT because of the different temperature profiles and stiffness. The acoustic analysis performed for base and part-load condition is in good agreement with the measurement performed during operations. The first acoustic axial mode is found at the frequency of 234 Hz. Until the frequency of 699 Hz, the acoustic modes keep a pure axial shape with different wavelength. At higher frequencies, 922 Hz, a first pure azimuthal mode is found. The following modes are a combination of axial and azimuthal modes. At the frequency of 2265 Hz the first radial mode is found. As seen from Table 6.3, the calculated acoustic eigenfrequencies are in good agreement with the measurements.

**Table 6.3. Comparison between calculated acoustic frequencies at base-load and part-load and measured acoustic frequencies during operations.**

Mode#	Acoustic (Base load)	Acoustic (Part load)	Acoustic measurements
1	234 Hz; Axial $l=1/2$	225 Hz; Axial $l=1/2$	225-280 Hz; Axial $l=1/2$
2	474 Hz; Axial $l=1$	456 Hz; Axial $l=1$	470-490 Hz; Axial $l=1$
3	699 Hz; Axial $l=7/4$	672 Hz; Axial $l=7/4$	880-1000 H; Axial $l=2$
4	923 Hz; Azimuthal $m=1$	887 Hz; Azimuthal $m=1$	1050-1100 Hz; Azimuthal $m=1$
...	Combination of axial-azimuthal modes	Combination of axial-azimuthal modes	Combination of axial-azimuthal modes
N	2265 Hz; Radial $n=1$	2176 Hz; Radial $n=1$	2300-2350 Hz; Radial $n=1$

In Figure 6.19, the corresponding mode shapes of the modes listed in Table 6.3 are depicted.

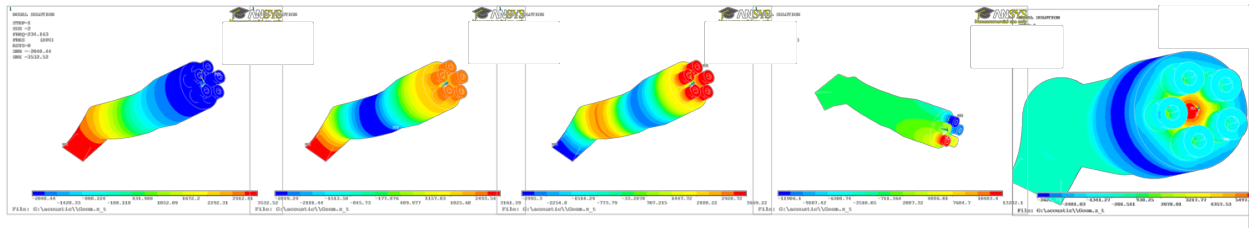


**Figure 6.19. Acoustic mode shapes for 234 Hz, 474 Hz, 699 Hz, 922 Hz and 2264 Hz**

Comparing the characteristic frequency (314 Hz) of the peak pressure (Figure 6.17) with the structural and acoustic modal analyses (Figure 6.18 and Table 6.3), it can be seen that the structural modes are not responsible for the characteristic frequency; however, this frequency is in between the first and second acoustic modes. In conclusion, the combustion instabilities are significantly related to the acoustic properties of the combustor. Moreover, the structural modes contribute to the structural vibrations, since the third peak at the frequency of 1091 Hz in Figure 6.17 is around the structural eigenfrequencies, and probably excites one of the structural modes.

### 6.6.5 Statistical and probabilistic analysis of data record

Four different data record times of pressure oscillations measured in-service are investigated, which are for 1 (a), 10 (b), 60 (c), 600 (d) seconds. In this section, the optimum data record time is determined to best represent the full-data. Therefore, a statistical distribution and probabilistic analysis is performed. The results of PDF, CDF and goodness-of-fit check analysis are presented.

In Figure 6.20, the PDF of the approximating models for 1, 10, 60 and 600 seconds of data record is plotted on the corresponding conceptual data for the given time. Figure 6.21 depicts the CDF of the conceptual reality (empirical) and the approximating models, chosen by the goodness-of-fit check, and the relative error in the CDF of the approximating models with respect to the conceptual reality. As seen from Figure 6.20 and Figure 6.21, the normal distribution describes the empirical data the best. Furthermore, the goodness-of-fit sequence of the approximating models remains the same after 10 seconds of data record.



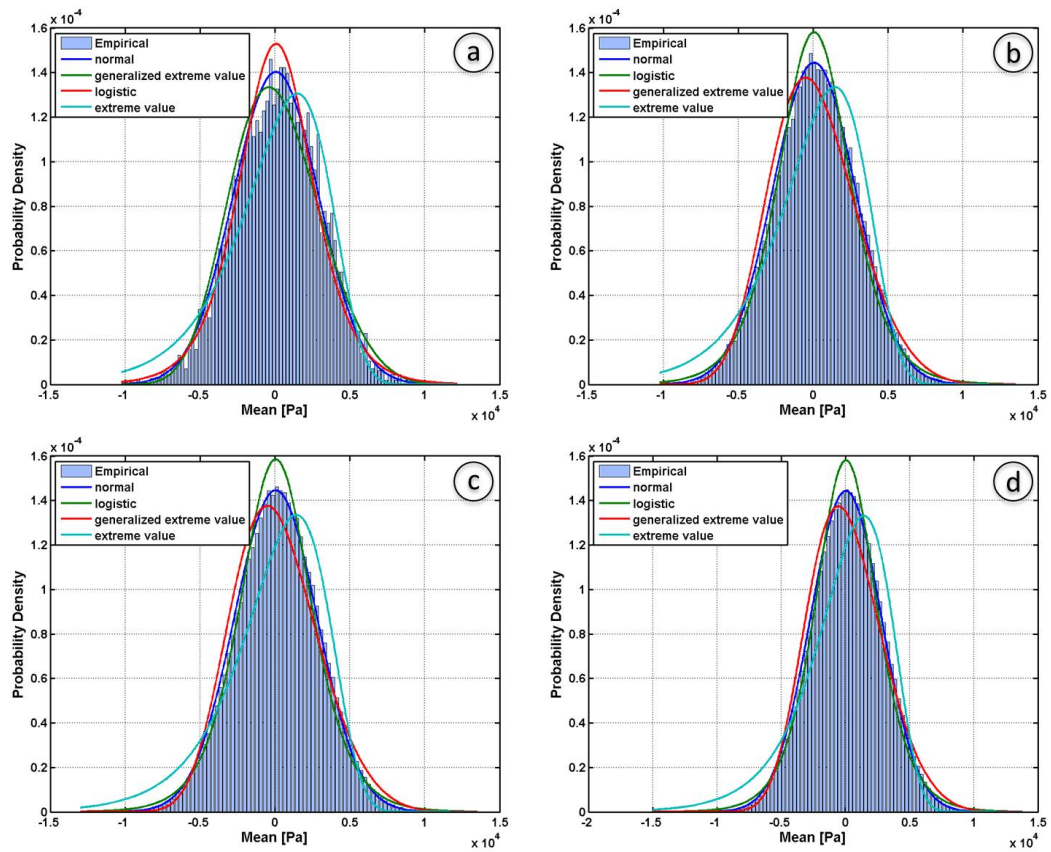


Figure 6.20. Probability density function (PDF) for 1 (a), 10 (b), 60 (c), 600 (d) seconds

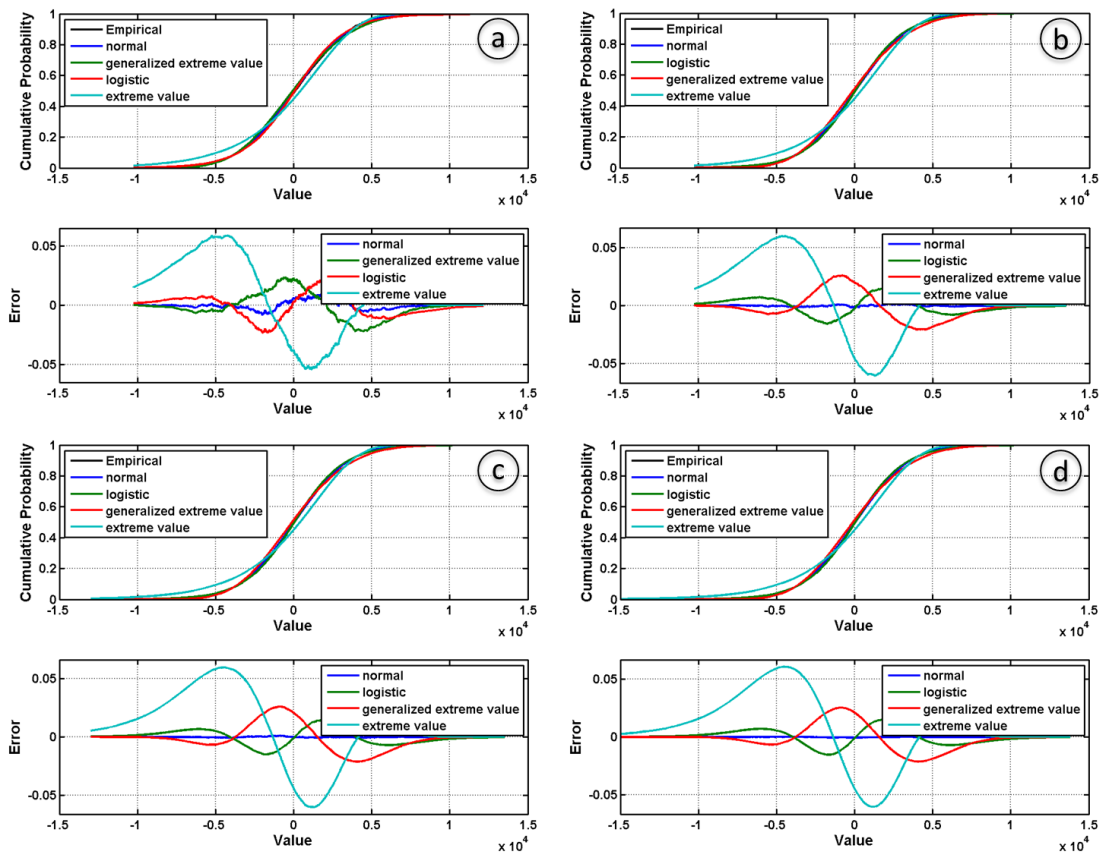


Figure 6.21. Cumulative distribution function (CDF) for 1 (a), 10 (b), 60 (c), 600 (d) seconds

**Table 6.4. Goodness-of-fit check for the approximating models**

<b>Data record time (DRT) [s]</b>	<b>Information Criterion (IC)</b>	<b>Normal</b>	<b>Logistic</b>	<b>Generalised extreme value</b>	<b>Extreme value</b>
1	AIC	86179,43	86302,73	86284,03	86912,53
	BIC	86192,47	86315,76	86303,58	86925,56
	AICc	86179,44	86302,73	86284,03	86912,53
10	AIC	858674,47	859708,54	859892,72	866601,44
	BIC	858692,11	859726,18	859919,18	866619,08
	AICc	858674,47	859708,54	859892,72	866601,44
60	AIC	5151381,21	5156927,45	5158999,2	5199362,84
	BIC	5151402,44	5156948,67	5159031,04	5199384,06
	AICc	5151381,21	5156927,45	5158999,2	5199362,84
600	AIC	51525854,39	51582761,65	51603185,34	52010180,86
	BIC	51525880,22	51582787,48	51603224,08	52010206,69
	AICc	51525854,39	51582761,65	51603185,34	52010180,86

**Table 6.5. Characteristics in goodness-of-fit check**

<b>DRT</b>	<b>Average (w/ IC-normal)</b>	<b>Normalised (w/ DRT)</b>	<b>Deviation [%] (w/ 600 [s])</b>
1	86183,78	86183,78	0,36
10	858680,35	85868,04	0,01
60	5151388,29	85856,47	0,02
600	51525863,00	85876,44	0,00

**Table 6.4 shows goodness-of-fit check results for the approximating models used above. Using the information criterion (AIC, BIC and AICc), the normal distribution model has slightly smaller values at data record times. In**

Table 6.5, the values of the information criteria obtained from the normal distribution model are averaged, normalised with the data record time, and the deviation with respect to the resulting value of the 600 s data record time are presented. Even though the optimum data record time is determined to be 10 s by the goodness-of-fit check for the approximating model sequence, the calculated deviations are significantly small within the data record times. This implies that even 1 s of data record can statistically represent the ensemble within a small deviation. Therefore, HCF/VHCF life assessment was performed using this data record time. Furthermore, a qualitative benchmark testing was performed for data record times by means of crack propagation lifetime. The results are presented in the next section.

## 6.7 Life assessment

In Figure 6.22, the distributions of the LCF lifetime [cycles] and creep strain [m/m] on the liner inner surface due to the base-load, which are calculated by the FEM analysis, are presented. The hot spots are marked with red dotted circles. Note that the creep strain distribution is related to the time-to-rupture.

The total strain range, which is composed of the elastic and plastic components, in the liner at the hot-spot marked in Figure 6.22 (a), reduces the lifetime down to 1317.8 cycles. However, the hot spots marked in Figure 6.22 (b) – upper dotted circle experience a higher temperature, which results in a significant reduction in creep lifetime. The temperature in this region is 700 °C, and the LCF lifetime is calculated as  $2.19 \times 10^4$  cycles and the creep lifetime is calculated as 4.79 hours, as depicted in Figure 6.23. Since the creep process is highly sensitive to the temperature, small changes in temperature can lead to significant lifetime consumption. The creep lifetime is too low, which possibly is a result of overestimation of the temperature from the numerical analysis.

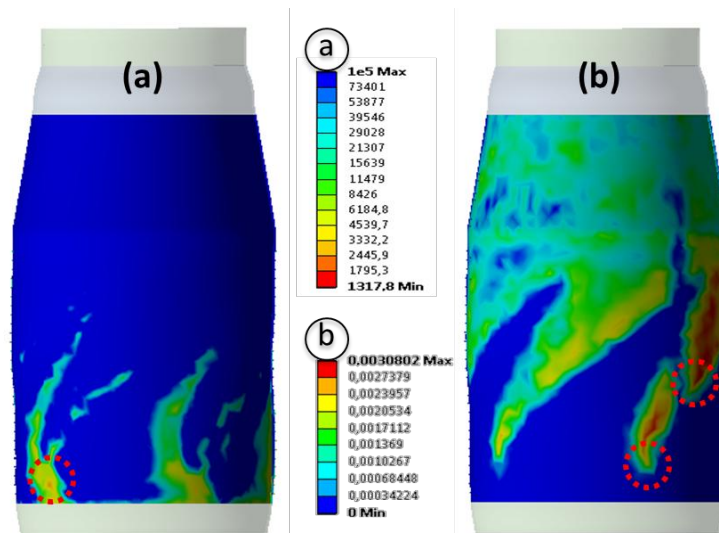


Figure 6.22. The distributions of the LCF lifetime [cycles] and creep strain [m/m] on the liner inner surface due to the base-load (red dotted circles: hot spots)

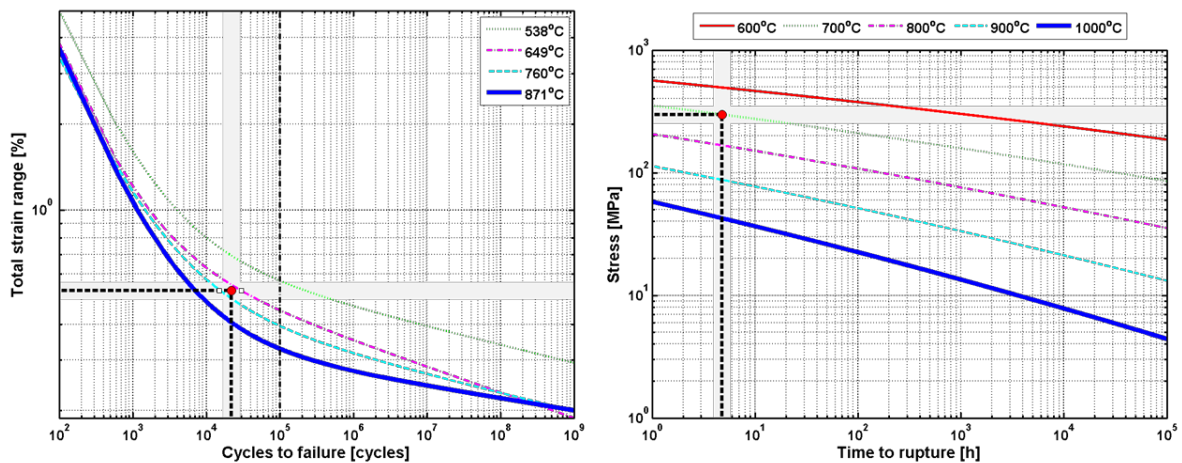


Figure 6.23. LCF lifetime [cycles] and creep lifetime [hours] at the upper hot spot

The observed failure pattern (Figure 6.2) is in very good agreement with the predicted fatigue and creep lifetime distributions (Figure 6.22). The two hot-spot regions marked in Figure 6.22 (b) match with the deformed in-service liner as seen in Figure 6.2 (a and b). Furthermore, as seen in Figure 6.2 (c) the spiral-shaped wear pattern is matching very well with the calculated creep strain distribution as depicted in Figure 6.22 (b). The cracking in the actual component as seen in Figure 6.2 (d) takes place at the two predicted hot-spot locations as shown in Figure 6.22 (b).

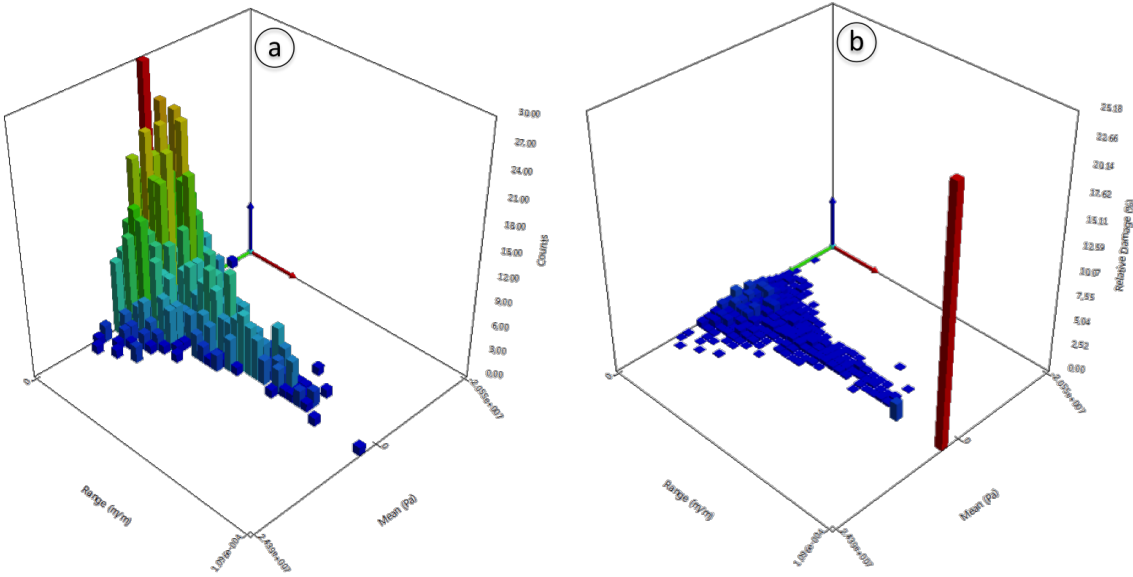


Figure 6.24. Rainflow and damage matrix of the pressure oscillations

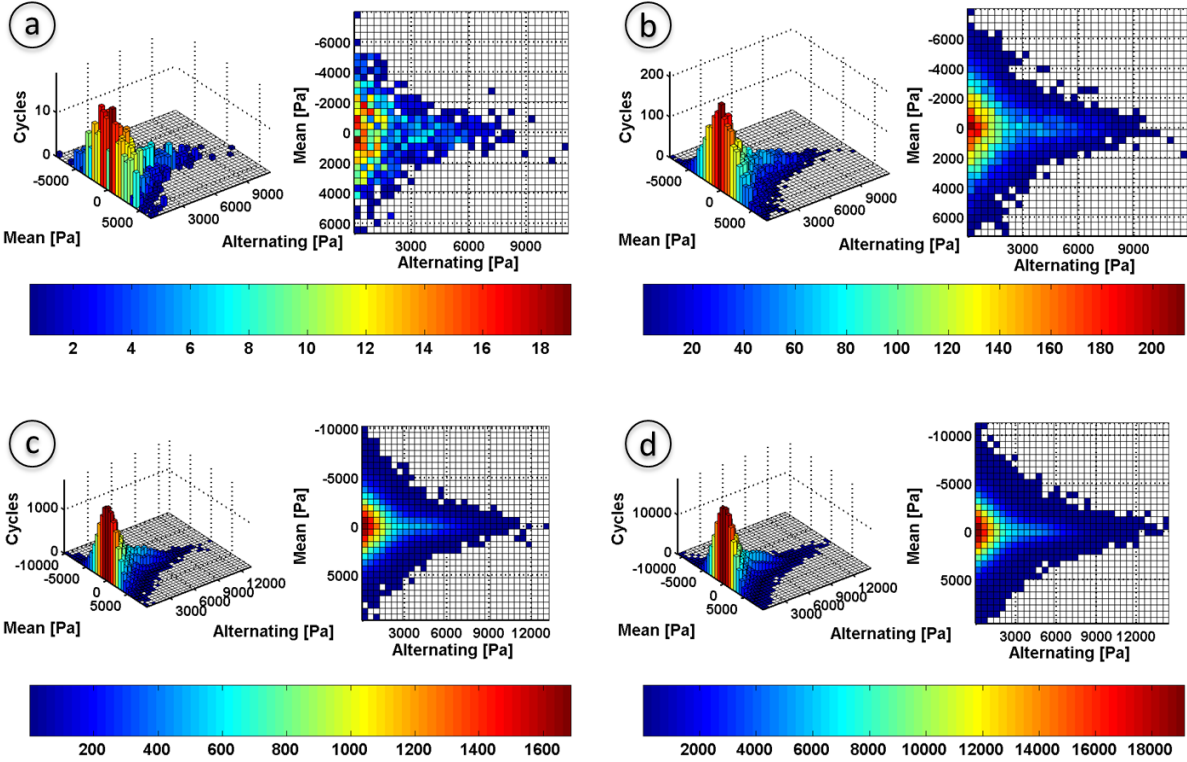


Figure 6.25. Rainflow cycle (RFC) counting for 1 (a), 10 (b), 60 (c), 600 (d) seconds

In Figure 6.24, the rainflow matrix (a) applied to 1 s of data record can be seen. Mainly, the experienced pressure is around the mean, and produces a high number of cycles of small strain amplitudes, whereas a very few number of high strain amplitudes are present. However, as seen in the damage matrix (b) the main life-consuming strain is the high amplitude strain component, even though very few cycles are experienced.

In Figure 6.25, the pressure data within the specified duration is then translated to constant amplitude pressure loading cycles that generate periodic vibration for the corresponding number of cycles. As a result of the analysis, it is evident from PDF and CDF analysis (Figure 6.20 and Figure 6.21) that acquiring data for, starting off at, 10 seconds is statistically sufficient to represent the oscillating pressure due to the combustion dynamics at a particular operating point. However, one must consider the relative damage of the higher pressure amplitudes applied for fewer cycles, which are located at the rear-tail (higher alternating pressures) of the matrix in Figure 6.25 (see Figure 6.24 (b)).

The cycle-dependent crack growth is controlled predominantly by the cyclic amplitudes rather than by maximum amplitude. Therefore the stress components include the load ratio to effectively represent the crack growth. Recalling the crack growth lifetime equation in section 6.5

$$\log N_f = A_0 + A_1 \log C + A_2 \log \left( \frac{\sigma_{max} - \sigma_{min}}{(1 - \frac{\sigma_{min}}{\sigma_{max}})^{m'}} \right) + A_3 \log a_i \quad (6.35)$$

In the equation, rewriting the stress component in terms of the alternating stress  $\sigma_a = (\sigma_{max} - \sigma_{min})/2$  and the mean stress  $\sigma_m = (\sigma_{max} + \sigma_{min})/2$  reads

$$\log N_f = A_0 + A_1 \log C + A_2 \log(2^{(1-m')} \sigma_a \sigma_m^{m'}) + A_3 \log a_i \quad (6.36)$$

The equation above can be simplified assuming that the geometry, initial flaw size and material parameters at operating temperature are identical for the considered data record times. Under the internal pressure  $p$ , the equivalent stress generated in the liner, which has a radius  $r$  and wall thickness  $B$ , considering the material under plane stress state, is formulated in cylindrical coordinates as (see appendix)

$$\sigma_{eq}(t) = \sqrt{\frac{1}{2} \left[ 2 \left( \sigma_{\theta\theta}^2(t) \right) \right]} = \frac{pr}{B} \quad (6.37)$$

Then, the crack growth lifetime reads

$$\log N_f = A + m \log(p_a^{(1-m')} (p_a + p_m + p_{max})^{m'}) \quad (6.38)$$

where  $A$  represents all identical parameters, mentioned above,  $p_a$ ,  $p_m$ ,  $p_{max}$  are the alternating, mean and maximum pressure, respectively. Since the pressure oscillations are superimposed on the steady-state pressure equilibrium, the amplitude of this equilibrium is considered to be the maximum pressure to represent the worst-case scenario. The equation, above, resembles the common form of a linear equation with two variables as  $y = b_1 + b_2 x$ , where the variables are  $y$  and  $x$ , and  $b_1$  and  $b_2$  designate constants, slope of the line and y-intercept, respectively. Hence, it is aimed to perform a qualitative investigation on the relation between

the rear-tail of the matrix of the data time record and crack growth lifetime, rather than an explicit solution of the crack-tip stress state, thus crack growth rate. Therefore, constant parameters are set to the same values for the analysis of data record times. As seen from the deviation calculation ( $\Delta Z_t$ ), the equation constant 'A' becomes an inactive element due to the time normalisation. However, the equation constant 'A<sub>2</sub>' (or the Paris's exponent  $m$ ) and the Walker's exponent are the power of pressure components, so that it must be correctly chosen. For AlloyX, the Paris's exponent  $m$  is taken as 2 and the Walker's exponent  $m'$  is the constant determined empirically, which is taken as 0.2 [49].

The Miner's law is used, which accumulates cycle fractions linearly, and the summation is normalised by the data record time for the comparison. The normalised relative damage parameter and the deviation parameter is given as

$$Z_t = \sum_{i=1}^{n_f} \frac{n_{f(i)}}{N_{f(i)}} / t \quad (6.39)$$

$$\Delta Z_t = \left| \frac{Z_{t=600s} - Z_t}{Z_{t=600s}} \right| \times 100 \quad (6.40)$$

where  $n_{f(i)}$  is the number of applied cycles and  $N_{f(i)}$  is the number of cycles to fatigue at  $i_{th}$  pressure range level,  $t$  is the data record time. The cracking behaviour, as seen in Figure 6.2 (d), is considered to be governed by the pressure oscillations due to the combustion instabilities, which leads to fatigue crack growth. The qualitative benchmark of crack growth lifetime for the data record times is presented in Table 6.6. These results claim that 1 second of data record time can be used to represent the full-data (operation data of pressure amplitudes) with a small error. This result is in compliance with the goodness-of-fit check presented in Table 6.5.

**Table 6.6. Qualitative benchmark of crack growth lifetime**

<b>DRT [s]</b>	<b>1</b>	<b>10</b>	<b>60</b>	<b>600</b>
<b>Deviation [%]</b>	2,8	2,7	1,3	0

## 6.8 Conclusions

- The 3D temperature and pressure output of a CFD analysis is transferred to a FEM model to analyse the structure response due to the complex combustion process at base load.
- Even though the LCF, creep and HCF/VHCF lifetimes are predicted with certain conservatism, the resulting deformation is in agreement with the failure pattern observed in-service. The failure pattern matches with the calculated swirl motion of the hot gas, which generates a non-uniform temperature distribution.
- The origin of the combustion instabilities is governed by the acoustic properties of the combustor. The measured characteristic frequency, at which the peak pressure is located, is found to be between the predicted first and second acoustic eigenfrequencies.
- Statistical distribution and probabilistic analysis in the pressure oscillation amplitudes for various data record times concludes that even though the combustion instabilities, as a physical process, are stochastic, the pressure output, with sufficiently enough data record

time, exhibits statistically deterministic characteristics. Thus, the optimum data record time is used in the rainflow cycle counting algorithm, considering the combined maximum and minimum loads, to predict the HCF/VCHF lifetime due to the variable load-time history and to define the most life-threatening pressure amplitude in the load history. The contribution of the high amplitude of pressure oscillations is characterised as crack growth, which contributes to the lifetime consumption of the liner.

## Appendix: Stress analysis and assumptions

The liner is considered to be a thin-walled cylindrical structure ( $B / r < 0.1$ ) with wall thickness  $B$ , radius  $R_s$ ,  $R_e$ , tapering angle of  $\theta_R$  and a total axial (longitudinal) length of  $L$ . The liner operates under combined internal and external pressures ( $p_i - p_e$ ). In the combustion process, the pressure and temperature loads vary along the longitudinal and hoop directions due to the swirling motion. However, the pressure fluctuations inside the liner, which are superimposed on the main pressure distribution, are assumed to be uniform internal pressure, since the combustion dynamics remain throughout the liner. Assume a section of the geometry, which is cut by two normal planes at  $x$  and  $x + dx$  along the longitudinal axis. And consider the resulting representative element of the cylindrical liner in cylindrical coordinate system ( $x, r, \theta$ ), axial, angular and radial coordinate, respectively. The body is considered as in static equilibrium. The outer surface is stress-free ( $\sigma_{rr} = \tau_{rx} = \tau_{r\theta} = 0$ ) at  $r = R$  and on the inner surface at  $r = R - t$ , only a balancing compressive normal stress counterpart of the applied pressure exists on the inner surface at  $r = R - t$  ( $\sigma_{rr} = -p, \tau_{rx} = \tau_{r\theta} = 0$ ). However, the radial stress is neglected, since it is much smaller than the axial ( $\sigma_{xx}$ ) and hoop stress ( $\sigma_{\theta\theta}$ ), and the corresponding tangential stresses are set to zero due to the thin-wall assumption on the outer and inner surface. The axial and hoop stresses are assumed to be uniform across the wall thickness and along the liner. The corresponding reciprocator shear stresses at inner surface, belonging to the radial components, are set to zero ( $\{\tau_{rx} = \tau_{zr}\} = \{\tau_{r\theta} = \tau_{\theta r}\} = 0$ ). The geometry is axially symmetric and no torsional load is considered, thus  $\{\tau_{x\theta} = \tau_{\theta x}\} = 0$ . In general, thin-walled pressure vessels operate under multiaxial stress state including  $\sigma_{xx}$  and  $\sigma_{\theta\theta}$ . The liner is clamped at one end and the other end has limited sliding degrees of freedom due to the assembly of the adjacent components. Thus, the stresses in the longitudinal direction can be compensated by the elastic foundation-type boundary condition (Section 6.3.4). This implies that the structure is considered to be governed by one principal stress, the hoop stress  $\sigma_{\theta\theta}$ . The stress matrix describing the normal stress state then reads

$$\begin{bmatrix} \sigma_{xx} & 0 & 0 \\ 0 & \sigma_{\theta\theta} & 0 \\ 0 & 0 & \sigma_{rr} \end{bmatrix} = \frac{pR}{2B} \begin{bmatrix} 0 & 0 & 0 \\ 0 & 2 & 0 \\ 0 & 0 & 0 \end{bmatrix} \quad (6.41)$$

The liner material is assumed to be homogeneous, elastic and isotropic. According to the Hooke's law in terms of Young's modulus ( $E$ ) and Poisson's ratio ( $\nu$ ), the strain can be expressed as a function of the stresses in the general form as

$$\varepsilon_{ij} = \frac{1}{E} (\sigma_{ij} - \nu [\sigma_{kk} \delta_{ij} - \sigma_{ij}]) \quad (6.42)$$



where  $\delta_{ij}$  is the Kronecker delta. The equivalent (von-Mises) stress in terms of principal stresses (cylindrical coordinates) is given in the general form as

$$\sigma_{eq}(t) = \sqrt{\frac{1}{2}[(\sigma_{xx}(t) - \sigma_{\theta\theta}(t))^2 + (\sigma_{\theta\theta}(t) - \sigma_{rr}(t))^2 + (\sigma_{rr}(t) - \sigma_{xx}(t))^2]} \quad (6.43)$$

Consider a material under plane stress state (thin-walled assumption) and axial stress is compensated by the boundary conditions described above, and then the equivalent stress reduces to the hoop stress component as

$$\sigma_{eq}(t) = \sqrt{\frac{1}{2}[2(\sigma_{\theta\theta}^2(t))]} = \frac{pr}{B} \quad (6.44)$$

In pressure vessel calculations, the shear stresses are considered as zero. However, the swirler, which is used to set up a local low pressure zone that stimulates the combustion products to recirculate and create turbulence, generates swirled flow inside the combustor that creates an analogous temperature field on the liner, thus non-uniform thermal stresses are induced. At steady-state conditions the thermal stresses are assumed to cause circumferential deformation, and at transient regime these stresses are assumed to induce torsional stresses due to the motion of the flow, thus temperature traces left behind. Even though the temperature field induces some torsional stresses due to this non-uniformity, these stresses are considered to be compensated by the boundary condition at one end with limited amount of rotational degree of freedom. This is due to the rotational flexibility formed by assembling with the adjacent component.

### Acknowledgement

The authors would like to acknowledge funding of this research by the EC in the Marie Curie Actions – Networks for Initial Training, under call FP7-PEOPLE-2007-1-1-ITN, Project LIMOUSINE with project number 214905.

### References

- [1] Leonard, G., and Stegmaier, J., 1994, "Development of an Aeroderivative Gas-Turbine Dry Low Emissions Combustion System," *J Eng Gas Turb Power*, 116(3), pp. 542-546.
- [2] Turek, L. J., Dawson, R. W., Chaos, M., and Chen, R. H., 2005, "An investigation of the effect of swirl vane angle on fuel concentration and velocity fields in gas turbine mixers," *Proceedings of the ASME Turbo Expo 2005*, Vol 2, pp. 87-96.
- [3] Zhang, C., Xu, Q. H., Lin, Y. Z., Zhu, J., Yuan, Y. X., and Sung, C. J., 2012, "Experimental Characterization of Fuel-Air Mixing in a Multihole Tube," *J Eng Gas Turb Power*, 134(3).
- [4] Lieuwen, T., Torres, H., Johnson, C., and Zinn, B. T., 2001, "A mechanism of combustion instability in lean premixed gas turbine combustors," *J Eng Gas Turb Power*, 123(1), pp. 182-189.
- [5] Dowling, A. P., 1997, "Nonlinear self-excited oscillations of a ducted flame," *J Fluid Mech*, 346, pp. 271-290.
- [6] Krebs, W., Bernd Prade, P. F., and Hoffmann, S., 2002, "Thermoacoustic stability chart for high-intensity gas turbine combustion systems," *Combustion Science and Technology*, 174(7), pp. 99-128.
- [7] Nicoud, F., and Poinot, T., 2005, "Thermoacoustic instabilities: Should the Rayleigh criterion be extended to include entropy changes?," *Combustion and Flame*, 142(1-2), pp. 153-159.



- [8] Krediet, H. J., 2012, "Prediction of limit cycle pressure oscillations in gas turbine combustion systems using the flame describing function," PhD Thesis, University of Twente, Enschede, Netherlands.
- [9] Hubbard, S., and Dowling, A. P., 2001, "Acoustic resonances of an industrial gas turbine combustion system," *J Eng Gas Turb Power*, 123(4), pp. 766-773.
- [10] Dowling, A. P., and Morgans, A. S., 2005, "Feedback control of combustion oscillations," *Annu Rev Fluid Mech*, 37, pp. 151-182.
- [11] Mcmanus, K. R., Poinso, T., and Candel, S. M., 1993, "A Review of Active Control of Combustion Instabilities," *Progress in Energy and Combustion Science*, 19(1), pp. 1-29.
- [12] Rizkalla, H., Strohl, P., and Stuttaford, P., 2007, "Prediction and Mitigation of Thermally Induced Creep Distortion in Gas Turbine Combustors," *ASME Conference Proceedings*, 2007(47942), pp. 501-508.
- [13] Matarazzo, S., and Laget, H., "Modelling of the heat transfer in a gas turbine liner combustor," *Proc. Proceedings of the 7th Mediterranean Combustion Symposium (MCS 7)*, Combustion Institute.
- [14] Moreno, V., Meyers, G. J., Kaufman, A., and Halford, G. R., 1983, "Non-Linear Structural and Life Analyses of a Combustor Liner," *Comput Struct*, 16(1-4), pp. 509-515.
- [15] Tsuji, H., and Kondo, T., 1987, "Strain-time effects in low-cycle fatigue of nickel-base heat-resistant alloys at high temperature," *Journal of Nuclear Materials*, 150(3), pp. 259-265.
- [16] Haynes International, 1997, "HASTELLOY® X ALLOY."
- [17] Ramberg, W., and Osgood, W. R., 1943, "Description of stress-strain curves by three parameters," *Technical note No. 902 National Advisory Committee for Aeronautics*.
- [18] Lieuwen, T. C., 2002, "Experimental investigation of limit-cycle oscillations in an unstable gas turbine combustor," *Journal of Propulsion and Power*, 18(1), pp. 61-67.
- [19] Culick, F. E. C., Burnley, V., and Swenson, G., 1995, "Pulsed Instabilities in Solid-Propellant Rockets," *Journal of Propulsion and Power*, 11(4), pp. 657-665.
- [20] Lieuwen, T. C., 2003, "Statistical characteristics of pressure oscillations in a premixed combustor," *J Sound Vib*, 260(1), pp. 3-17.
- [21] Culick, F., Heitor, M. V., Whitelaw, J. H., and North Atlantic Treaty Organization. Scientific Affairs Division., 1996, *Unsteady combustion*, Kluwer Academic, Dordrecht ; Boston.
- [22] Akaike, H., 1981, "Citation Classic - a New Look at the Statistical-Model Identification," *Cc/Eng Tech Appl Sci*(51), pp. 22-22.
- [23] Kullback, S., and Leibler, R. A., 1951, "On Information and Sufficiency," *Ann Math Stat*, 22(1), pp. 79-86.
- [24] Leeuw, J. d., 1992, "Introduction to Akaike (1973) Information theory and an extension of the maximum likelihood principle," *Breakthroughs in Statistics*, S. Kotz, and N. L. Johnson, eds., Springer-Verlag, London, pp. 599-609.
- [25] Schwarz, G., 1978, "Estimating Dimension of a Model," *Ann Stat*, 6(2), pp. 461-464.
- [26] Weakliem, D. L., 1999, "A critique of the Bayesian information criterion for model selection," *Sociol Method Res*, 27(3), pp. 359-397.
- [27] Hurvich, C. M., and Tsai, C. L., 1989, "Regression and Time-Series Model Selection in Small Samples," *Biometrika*, 76(2), pp. 297-307.
- [28] Brockwell, P. J., and Davis, R. A., 1991, *Time series : theory and methods*, Springer-Verlag, New York.
- [29] Cavanaugh, J. E., 1997, "Unifying the derivations for the Akaike and corrected Akaike information criteria," *Statistics & Probability Letters*, 33(2), pp. 201-208.
- [30] Burnham, K. P., and Anderson, D. R., 2002, *Model selection and multimodel inference : a practical information-theoretic approach*, Springer, New York.
- [31] Sugiura, N., 1978, "Further Analysis of Data by Akaike's Information Criterion and Finite Corrections," *Commun Stat a-Theor*, 7(1), pp. 13-26.

- [32] Matsuishi, M., and Endo, T., 1968, "Fatigue of metals subject to varying stress," Japanese Society of Mechanical Engineers.
- [33] Dowling, N. E., 1972, "Fatigue Failure Predictions for Complicated Stress-Strain Histories," *J Mater*, 7(1), pp. 71-&.
- [34] Downing, S. D., and Socie, D. F., 1982, "Simple Rainflow Counting Algorithms," *Int J Fatigue*, 4(1), pp. 31-40.
- [35] ASTM International, 2005, "Standard practices for cycle counting in fatigue analysis," ASTM E 1049-85.
- [36] Naeem, M., 2009, "Implications of Turbine Erosion for an Aero-Engine's High-Pressure-Turbine Blade's Low-Cycle-Fatigue Life-Consumption," *Journal of Engineering for Gas Turbines and Power*, 131(5), pp. 052501-052501.
- [37] Siladic, M. F., and Rasuo, B. P., 2009, "On-Condition Maintenance for Nonmodular Jet Engines: An Experience," *Journal of Engineering for Gas Turbines and Power*, 131(3), pp. 032502-032502.
- [38] Hancq, D. A., Walters, A. J., and Beuth, J. L., 2000, "Development of an Object-Oriented Fatigue Tool," *EWC*, 16(2), pp. 131-144.
- [39] Nieslony, A., 2009, "Determination of fragments of multiaxial service loading strongly influencing the fatigue of machine components," *Mechanical Systems and Signal Processing*, 23(8), pp. 2712-2721.
- [40] Dowling, N. E., 1999, *Mechanical behavior of materials : engineering methods for deformation, fracture, and fatigue*, Prentice Hall, Upper Saddle River, NJ.
- [41] ASME Boiler and Pressure Vessel Code, 1977, Code Case N-47.
- [42] Fuchs, H. O., and Stephens, R. I., 1980, *Metal Fatigue in Engineering*, John Wiley & Sons, Inc.
- [43] Asquith, G., and Pickard, A. C., 1988, "Fatigue Testing of Gas-Turbine Components," *High Temp Technol*, 6(3), pp. 131-143.
- [44] Paris, P., and Erdogan, F., 1963, "A Critical Analysis of Crack Propagation Laws," *Journal of Fluids Engineering*, 85(4), pp. 528-533.
- [45] Iost, A., 1991, "The Effect of Load Ratio on the M-in C Relationship," *Int J Fatigue*, 13(1), pp. 25-33.
- [46] Maddox, S. J., 1975, "Effect of Mean Stress on Fatigue Crack-Propagation - Literature Review," *International Journal of Fracture*, 11(3), pp. 389-408.
- [47] Schijve, J., 1981, "Some Formulas for the Crack Opening Stress Level," *Engineering Fracture Mechanics*, 14(3), pp. 461-465.
- [48] Walker, K., 1970, "The Effect of Stress Ratio During Crack Propagation and Fatigue for 2024-T3 and 7075-T6 Aluminum," ASTM STP 462, American Society for Testing and Materials.
- [49] Jablonski, D. A., Carisella, J. V., and Pelloux, R. M., 1977, "Fatigue crack propagation at elevated temperatures in solid solution strengthened superalloys," *MTA*, 8(12), pp. 1893-1900.
- [50] Tryon, R. G., Cruse, T. A., and Mahadevan, S., 1996, "Development of a reliability-based fatigue life model for gas turbine engine structures," *Engineering Fracture Mechanics*, 53(5), pp. 807-828.
- [51] Maricocchi, A., Bartz, A., and Wortman, D., 1997, "PVD TBC experience on GE aircraft engines," *J Therm Spray Techn*, 6(2), pp. 193-198.
- [52] Schulz, U., Leyens, C., Fritscher, K., Peters, M., Saruhan-Brings, B., Lavigne, O., Dorvaux, J. M., Poulain, M., Mevrel, R., and Caliez, M. L., 2003, "Some recent trends in research and technology of advanced thermal barrier coatings," *Aerosp Sci Technol*, 7(1), pp. 73-80.
- [53] Blevins, R. D., 2001, *Formulas for natural frequency and mode shape*, Robert E. Krieger publishing company, Malabar, Florida.

## 7 Conclusions and recommendations

A. Can Altunlu

*University of Twente, Faculty of Engineering Technology, Section of Applied Mechanics, 7500 AE, Enschede, The Netherlands*

---

### **Abstract**

**T***his section summarises the main results and draws conclusions with regard to the research objectives defined in the introduction. Furthermore, recommendations are indicated for further research.*

## 7.1 Conclusions

The investigation presented in this thesis was initiated by the LIMOUSINE project, which is supported by the European Commission under the Marie Curie Initial Training Network (ITN) program. The main focus of the LIMOUSINE project is the limit cycle behaviour of the unstable pressure oscillations in gas turbines, and the resulting mechanical vibrations at elevated temperatures.

Lean, premix combustor systems are used to meet the emission target for low NO<sub>x</sub> gas turbines; however, these engines are prone to combustion instabilities, which are detrimental to the mechanical integrity. A significant amount of effort in the literature has been devoted to either the design measures on the combustion hardware to avoid instability or passive/active control techniques to control the instability. However, prior to these attempts it is crucial to predict the size and effect of the instability. The thermo-acoustic instability is a multiphysical phenomenon, thus it was investigated in an interdisciplinary framework. In this regard, several collaborations with the project partners (PhD fellows) were achieved, such as the experimental investigation of the limit cycle characteristics such as frequency and amplitude, and the acoustic and vibrational behaviour of a laboratory-scaled combustion system (LCS) with Roman Casano, J.R. [1], the numerical prediction of the liner vibrations due to two-way fluid-structure interaction with hot gas flows in this system with Shahi, M. [2], and the structural response of an industrial combustion system (ICS) under steady-state and dynamic combustion with Matarazzo, S. [3]. These efforts have been linked to the project goal described in this thesis, which is the sensitivity of the structural dynamics, and lifetime of the combustion systems to the instabilities.

The main objective of this thesis is the development and application of experimental and numerical tools to analyse and assess the mechanical integrity of gas turbine engines subjected to combustion instabilities. The main objective in this thesis is composed of sub-objectives as described in Chapter 1. The conclusions are organised according to the sub-objectives, and finally the main objective of the research is highlighted.

### **Development and application of structural health monitoring techniques to analyse the changes in structural dynamics due to the transition from stable to unstable combustion.**

The feedback mechanism of the thermo-acoustic instabilities in a combustion system is considered to be composed of three elements, which are: acoustic oscillations, flow perturbations and unsteady heat release. Nevertheless, this process occurs inside the combustor structure. Hence, a multiphysical investigation is required, including the interaction of combustion, acoustics and structure, to analyse the instability problem.

A laboratory-scaled combustion system (LCS) was designed and built at the University of Twente in order to demonstrate the developed structural health monitoring (SHM) techniques. This test system is representative of a typical industrial combustion system with simplified boundary conditions. The system has well-defined acoustic, structural properties and mixing

(air/fuel), and the limit-cycle behaviour of unstable pressure oscillations due to instabilities can be obtained on demand. Therefore, this robust combustion system enables simplification of this complex instability problem in a controlled way, and to perform an investigation of the SHM techniques in relation to the combustion – acoustics – structural domains under limit-cycle conditions.

Particular attention must be given to damages occurring at the primary zone (the flame-box in LCS), since not only pressure oscillations are activated, but also enhanced heat transfer accelerates the damaging process due to combustion instabilities. Combined vibration and thermal-based measurement systems were integrated to the combustor system to assess the structural dynamics and damage at the instability regime. Non-contact and automated measurement systems were used to deal with the high temperature and harsh environmental conditions.

Three vibration-based (VB) and one thermal-based (TB) SHM method were investigated for the SHM to assess damage due to combustion instabilities.

1. The frequency shift method (VB), in which a shift of one or more of the measured natural frequencies is used as an indication of damage. The method requires a prior numerical analysis to obtain structural modes and to define the contribution of the frequency content from the measured responses.
2. The instability peak method (VB), which is based on the change of the measured dynamics behaviour of the structure at the characteristic frequency and its higher-harmonics generated by the combustion instabilities.
3. The flexibility method (VB), which is based on the change of the flexibility matrix that is composed of the measured mode shapes and the reciprocal of the natural frequencies.
4. The thermographic method (TB), in which an infrared camera is used to obtain the temperature evolution of the specimen during the operation.

In conclusion, only measurements of structural dynamics, followed by a FEM analysis of the structure, are sufficient for the application of the vibration-based SHM techniques mentioned above. The SHM capability can be extended by incorporating a temperature field using a thermographic method. The selection of the SHM method depends on the measurement system and the target. If one point vibration measurement is realised and the target is damage detection, the frequency shift method and the instability peaks method can be used synergistically to detect damage using the information from structural dynamics (eigenfrequencies) and combustion instabilities (the characteristic frequency of limit-cycle pressure oscillations and its higher-order harmonics). If multiple measurement points are used and the target is damage detection, quantification and localisation, the flexibility method is very effective for characterising the damage. There can be situations, in which multiple damages in the structure with different severities are present that are located in close vicinity to each other. If the severity of one of the damages is greater than the others, only the damage with the highest severity will be captured, and the others will vanish. However, if the frequency shift method and the instability peaks are incorporated to assess the data acquired

from the same measurement points, the changes in the vibrations of the individual measurement point will indicate other damage.

Combining the SHM techniques, presented in this thesis, enables an effective assessment of mechanical integrity during in-service operation. Furthermore, these SHM techniques use non-contact measurement methods, which are suitable for high temperature application, such as combustion systems.

### **Prediction of the fatigue and creep lifetime (crack-initiation) reduction due to combustion instabilities using a combined fluid-structural approach.**

The feedback mechanism between acoustic oscillations, flow perturbations and unsteady heat release is responsible for combustion instabilities. In order to predict the key parameters due to the instabilities, a two-way coupled fluid-structure interaction (FSI) analysis, including Computational Fluid Dynamics (CFD) and Finite Element Method (FEM), was performed. The enhanced heat transfer process due to the instabilities observed in the experiments is supported by the numerical analysis. The numerical results showed that the instabilities produce large amplitudes of fluid velocity oscillations at a characteristic frequency in the primary zone; moreover, the flame penetrates the corner recirculation zones and flashes back. The average heat flux was calculated higher in the flame-box region and the heat flux distribution is more intensified due to the compact flame generated by the unstable combustion. However, the fluid temperatures are marginally over-predicted by the numerical analysis compared to the experiment, which yield to a slight over-prediction of the characteristic frequencies. Even though the amplitude of pressure oscillations is considerably under-predicted, the growth rate of pressures can be calculated when a growth function is fitted to the numerical analysis results with a threshold value obtained by a set of experiments. In addition, the temperature fluctuation of the liner stimulated by the instabilities can be resolved in the numerical analysis, whereas the measurement of these fluctuations is difficult due to insufficient capabilities of sensors, thus the measurement of the mean temperature is favourable in the experiments. However, these temperature fluctuations can induce thermal fatigue. The actual magnitude of these fluctuations can be correlated with numerical results by adjusting the mean temperature ratio of the measured temperature and the predicted temperature.

Additionally, it has been found that the lifetime of the liner was significantly reduced by the combustion instabilities due to:

- Elevated oscillatory mechanical loads, thus reducing the fatigue life,
- Enhanced heat transfer, thus higher temperatures, which increase creep damage.

The key parameters due to combustion instabilities can be estimated in the prototype development (design) stage by using FSI analysis supplemented with a set of experiments. Utilising these key parameters in the safe-life design of critical components leads to improved mechanical integrity performance.

## **Development and demonstration of an efficient tool to perform remaining lifetime prediction (crack-growth) by fracture mechanics analysis including fatigue and creep aspects.**

In the gas turbine industry, development and application of mechanical integrity methods are critical to ensure the reliability, safety and efficiency of new and existing equipment. Even though there have been efforts to work on design measures to avoid and control the combustion instabilities, it still remains a challenge to avoid or to control within the entire range of operating settings depending on power transition (idle to nominal), or climate conditions. It is vital to evaluate the impact of the instability on the remaining lifetime so that more strategic and proactive approaches can be carried out to assess the condition of the process equipment. Accordingly, an efficient tool was developed to assess the remaining lifetime of Ni-based superalloys, which are typically used in hot gas path components of an engine. This damage tolerance approach is realised by using the eXtended Finite Element Method (XFEM) based fracture mechanics analysis covering the fatigue and creep conditions that can be used as a supplement to any existing safe-life methodology.

The XFEM extends the displacement approximation of standard FEM by adding a discontinuity function and crack-tip asymptotic function using the partition of unity framework. This concept enables to model cracks without explicitly meshing of cracks, thus removes the re-meshing procedure in crack propagation analysis. The XFEM feature is available in the general-purpose finite element software, Abaqus FEA, in which the cracks can be modelled independently of the mesh of complex geometries related to industrial applications. This offers a unique capability to deal with large models. However, the implemented feature can provide only stress intensity factors for stationary cracks, and is valid for linear elastic fracture mechanics (LEFM). Therefore, a user-defined algorithm was developed incorporating Abaqus FEA to simulate progressive crack growth for arbitrary shaped 3D cracks under creep and fatigue conditions. In this regard, the contour integral evaluation is utilised to calculate the crack-tip parameter for crack growth, which is composed of time-dependent creep and cycle-dependent fatigue.

The creep condition of the crack was determined to be creep-brittle till a transition period. In this period, the near-tip field of the crack can be characterised by the  $C_t$ -integral, where small-scale creep conditions exist. Within this period, the elastic strains are dominant in the small creep zone around the crack-tip. This transition time is the onset of the quasi-steady-state of the crack, where the material behaviour changes from small-scale yield to extensive yielding. As the hold time is increased further than the transition time, the solution of the crack-tip stress and strain fields are realised by calculating the  $C^*$ . These findings conclude that the near-tip fields can be characterised by the parameter  $C^*$  under steady-state conditions; however, for situations, where steady-state distribution of stresses and strains do not have sufficient time, in other words the crack growth rate is faster than the extensive creeping zone development rate around the crack (transition time), the linear elastic parameter  $C_t$ -integral, or analogical stress intensity factor (SIF),  $K$ , can be used to characterise the crack-tip behaviour. This information is essential since the XFEM is valid for LEFM.

For cycle-dependent fatigue crack growth, the predicted SIF values using XFEM at various crack lengths are in good agreement with the results of conventional FEM and ASTM equations. The accuracy of XFEM results are improved when brick elements are used compared to tetrahedral elements. Furthermore, the numerical results showed that higher mesh density provides more accurate results and a higher degree of path independence for the SIF values, which are extracted from the path-independent  $J$ -Integral using the interaction integral method.

The method is demonstrated in the combustion system (LCS) to assess the effect of the instability in the remaining lifetime reduction. The temperature and pressure loads were measured in the experiments and numerically applied in the fracture mechanics analysis. The crack growth path was determined by the maximum principal stress direction and the crack growth rate was quantified by the  $C_t$ -integral. Introducing hold times at a constant load reduces the crack growth rate, which is attributed to relaxation of the stresses around the crack due to the creeping effects. Time-dependent damage mechanisms related to creep crack growth takes more control of the cracking behaviour at longer hold times. Higher-pressure amplitudes increase the  $C_t$  values, thus increase the crack growth rate. The crack growth rates are directly proportional to  $C_t$  values. Higher crack growth rates consume more lifetime, thus decrease the remaining lifetime.

The remaining lifetime prediction tool, described in this thesis, significantly reduces the computational cost, while maintaining accuracy. The reasons can be stated as follows. Cracks can be modelled without confirming the mesh to the discontinuity, and mesh regeneration as the crack advances is avoided in XFEM. Crack growth can be simulated by computing only one crack-tip parameter, which includes a combined time-dependent creep and cycle-dependent fatigue fracture parameter. In the analysis, small-scale yielding assumption is satisfied for of-interest Ni-based superalloys, in which the crack growth rate is higher than the excessive creep zone advancement rate around the crack. Resolving fatigue and creep crack growth within the XFEM framework significantly reduces computational time, while providing accurate results.

### **Development of a probabilistic and statistical analysis algorithm to robustly assess in-service pressure oscillations by means of lifetime.**

A methodology was developed to perform a lifetime assessment of a lean, premixed combustor system (ICS) that experiences combustion instabilities at base-load condition in-service operation. This is realised by a two-step approach:

1. Simulation of stable combustion using an integrated fluid-structure approach (sequentially coupled CFD and FEM analysis),
2. Assessment of measured pressure oscillations due to combustion instabilities.

In the first step, computational fluid dynamics analysis is performed to calculate the temperature and pressure field on the combustion liner. Next, a finite element analysis is performed to calculate the stresses and strains in the liner. After that, a lifetime prediction is performed to calculate the fatigue and creep lifetime for the stable combustion. The main



resulting deformation profile is observed to match with the calculated thermal deformation field on the combustion liner. Even though the prediction of the low-cycle fatigue (LCF) and creep lifetimes reveals a certain conservatism regarding the operational experience, the failure pattern and fracture locations of the combustion liner are in agreement with the numerical calculations.

In the second step, a strategy is implemented to quantify the lifetime reduction due to unstable combustion. Initially, the data of the unstable pressure oscillations is characterised statistically. This is realised by utilising an algorithm based on probabilistic analysis of approximating models for statistical distribution. Even though the combustion instabilities are characterised as a complex process, the oscillations are found to be statistically deterministic. This implies that a sufficiently enough time record of in-service pressure data can be used to represent the pressure spectrum induced in the combustor. In this regard, a very short optimum data record time was found, which significantly reduces calculation time. Subsequently, the prediction of the lifetime reduction due to the combustion instabilities is performed by using a rainflow cycle counting algorithm, which was applied in the optimum data record time. Hence, the variable amplitude loading of pressure was reduced into a series of constant amplitude loadings so that the fatigue lifetime calculation can be performed. It was found that large amplitude, but less frequent, pressure amplitudes caused the highest fatigue damage.

In overall lifetime assessment, the observed failure pattern of the combustion liner is governed by the calculated temperature field due to the combustion process, and the fracture location matches the predicted highest LCF and creep damage zone (hot spot). Furthermore, since very/high cycle fatigue (V/HCF) is considered to be responsible for crack growth emanating from flaws at hot spots, less frequently occurring large amplitude pressures of unstable pressure oscillations are predicted to be the main damage contributors in this regard.

The demonstrated probabilistic and statistical analysis algorithm establishes a powerful approach in the design stage to produce a lifetime reduction map due to combustion instabilities by performing very short-time tests over the entire operation envelope without damaging the combustor. Furthermore, combining conventional pressure measurements with this decisive tool makes condition monitoring of in-service equipment very effective to maintain the mechanical integrity.

### **Main objective: development and application of experimental and numerical tools to analyse and assess the mechanical integrity of gas turbine engines subjected to combustion instabilities**

The gas turbine hot section parts are high value components, and the efficiency of the engine significantly depends on the performance of these parts, which have finite lifetimes. These parts are integrated with each other so that any major damage originating from one part can cause a failure of the subsequent components. Therefore, the development of mechanical integrity analysis tools plays a crucial role in prolonging the total lifetime, improving the engine operational and maintenance practices and minimising the likelihood of failures.

In this thesis, the development and application of mechanical integrity tools for combustors subjected to combustion instabilities are presented. In this regard:

- The safe-life design of the combustor against fatigue and creep damage, including the effects of combustion instabilities, can be improved by FSI analysis supplemented with a set of experiments. Hence, the key parameters, the frequency and amplitude of pressure oscillations and combustion temperature, for this approach can be obtained.

- During the engine operation, damage can be detected and monitored by using combined structural health monitoring methods including vibration-based and thermal-based methods. Furthermore, the remaining lifetime of the detected damage can be predicted by using XFEM-based fracture mechanics analysis proposed in this thesis.

- The elevated fatigue damage due to the high amplitude pressure oscillations generated by the combustion instabilities can be assessed by the condition monitoring method, presented in this thesis. This is realised by performing a probabilistic and statistical analysis algorithm to assess in-service pressure measurements.

## **7.2 Recommendations**

The impact of combustion instabilities was comprehensively linked to the structural domain by means of structural dynamics, structural health monitoring, fatigue, creep and fracture mechanics aspects. The methodologies and tools presented in this thesis are intended to contribute towards mechanical integrity of gas turbine engines under limit-cycle conditions. However, the multiphysical and interdisciplinary nature of this complex problem revealed various challenges during this research. In this section, recommendations are proposed for future work.

The laboratory-scaled combustion system (LCS) is representative of a typical industrial gas turbine combustion system. The main advantages of this system are: scaled-down version, thus cheaper, usability, repeatability and well-studied geometry in the literature. However, some improvements in the design can significantly contribute to validation of the analyses. These aspects are:

- The rectangular combustion liner in this system is assembled by welding two L-shaped profiles. Two corner-welds in the opposite sides along the liner length act as a stiffener thus increase the rigidity. This results in asymmetric structural response and significantly alters the structural dynamics. The welds were attempted to be modelled in the numerical analysis; however, the unknown material properties and the non-uniformity of the weld material used along the liner length hindered efforts for better accuracy. Therefore, it is recommended to either weld two U-shaped profiles along the smaller side of the liner, or to choose more robust assembly techniques with well-defined properties, such as laser beam welding.

- In the design of a combustion system, it should be considered that even though the pressure peaks at higher-order harmonic frequencies had relatively smaller amplitudes, mechanical resonance can be generated when the frequency of the oscillation matches the structural eigenfrequencies. In industrial applications, this can lead to accelerated deterioration of the liner due to introducing resonance peak vibration to the system.

- When operation settings are changed during experiments, the combustion process requires sufficiently enough time to reach its state, stable or unstable, since the temperature plays a significant role in instabilities. However, monitoring the temperature hot gas flow would be misleading, since the reaction rate of the fluid temperature to the variation of the operating settings is faster than the structure temperature. Therefore, a sample point on the structure far away from the primary zone of the combustion system should be monitored and test data can be recorded after the surface temperature reaches a steady-state level.

The accuracy of the results for the fracture mechanics analysis should be investigated. However, validation of the code with the standard test methods is not sufficient to capture the effects of unstable combustion. Therefore, a high-pressure combustion test rig should be used for a realistic experience that is challenging to control the test conditions.

The lifetime prediction analysis can be integrated into two-way coupled fluid-structure interaction (FSI) simulations to improve the accuracy of the results. However, this will significantly increase the computational time due to the solution of time-dependent creep damage, which is already a problem in FSI simulations.

## **References**

- [1] Roman Casado, J. C., 2013, Ph.D. Thesis, University of Twente, Enschede, Netherlands (in progress).
- [2] Shahi, M., 2014, Ph.D. Thesis, University of Twente, Enschede, Netherlands (in progress).
- [3] Matarazzo, S., 2013, Ph.D. Thesis, University of Twente, Enschede, Netherlands (in progress).

## Acknowledgements

Finally I came to the point of writing the acknowledgement part of my thesis, which many of my friends will look at firstly after giving a quick, a very quick-look to the summary and contents. I have been in this PhD journey for a bit more than 3.5 years, and I am delighted and proud to present this work as the scientific output of my journey. Besides, throughout this journey I gained massive experience, which grew me scientifically and personally, and most important I made a lot of *friends*. I will always remember that this journey wouldn't be as amazing without you, all. In case I miss any name to mention below, and in case you are in my party, we will cheer you name together!

Firstly, I heartily acknowledge my promotor and supervisor Prof.dr.ir *André* de Boer. André, the first time we met face to face was the day for the interview on 17th June 2009. You left me a very good first impression, quite frankly, I said what a cool Prof!. I now realise that I have made the right decision. You have been supporting me from the first day till the last day during this journey. We had many and long debates, even starting from the interview day in setting the deadline of your offer. Every time, I kept my eyes and ears fully open and gained valuable learning.

Dr.ir. *Peter* van der Hoogt. Peter, this thesis is dedicated to you; you have been my motivational and inspirational supervisor, and my friend. I would wish that you would be in my defence and hear your absorbing voice again. From you, I learned how to grip the life, to enjoy and get the most out of it, to go around the obstacles, to communicate ... The words would be inadequate to describe. Just stay with me! ... Thank you to invite me for participating as a performer in the 9<sup>th</sup> Lustrum by W.S.G. Isaac Newton (as the first international participant, luckily I didn't have to speak Dutch), where I shared the stage with two nice ladies and good friends *Dorien* and *Marieke*. It was very much fun to practice dancing after work.

André and Peter; you shared my enthusiasm of my achievements, you motivate me when I was despairing, you inspired me when I was blind and deaf to work, you put me in my shoes again when I was tired and rioting against science, you believed me and gave me the full responsibility of my project and make me represent you in the project meetings, you generously supported and gave frank advices to me, which played an important role in my scientific and personal development, you made me understand that leading and management is not about being bossy or hierarchy, but the power of the communication is the key. I am really proud to have such cool supervisors and glad to have you as friends.

I would like to thank Prof.dr.ir *Tiedo* Tinga. You became my promoter and supervisor in the very last period of my thesis and supported me to finalise my thesis. You were highly responsive, very punctual and we had fruitful discussions, what can be more than that. Tiedo, your experience in the gas turbine industry and your scientific competence, together with your critical touches, were of great help and value for my thesis.

The Limousine project involved several partners that I have been working collaboratively. Firstly, I would like to thank Dr.ir *Jim* Kok from the Thermal Engineering Department. Your smart ideas and wise advices in our meetings were of great value. Furthermore, during the project you opened many doors for me with full trust on me, which made me develop personally and scientifically. You were my project leader and a friend. If you haven't told me, I wouldn't have continued horseback riding and wouldn't have bought a bass guitar and get lessons from the same lecturer.

Next, I would like to thank to my project partners, where I spent some time as a secondment or short-time stay. From Siemens, UK, I would like to thank! my manager *Jon* May, you made me feel as a part of the family, and also I really enjoyed the talks about Sunderland AFC; thank! you Dr. *Martin* Hughes, you have a high-level experience that was of great value reflecting to my work; thank! you Dr. *Lingli* Lu, we had many fruitful discussions, your knowledge were of great help to me; furthermore thank you for sharing your Chinese tea with me and taking care of my plan after I left; thank! you to my colleagues over there, I had really great time. From Laborelec, Belgium, thank! you Dr. *Hannes* Laget, I really appreciate your experience and knowledge about gas turbines, and the discussion we had that led to a paper at the end. You were a good company during the ASME Turbo Expo Conference in Vancouver. And also thank you for your frank opinions on my career. From ANSYS, UK, thank! you Dr. *Phil* Stopford, our long and late meeting in Abingdon motivated the Chapter 6. From DLR, Germany, thank! you Dr.ir *Massimiliano* Di Domenico and Dr.ir *Rainer* Lueckerath for the valuable discussions and your comments.

Hey Gents! I would like to acknowledge the Limousine project fellows. This work is truly a result of an intensive collaboration. And also I had great fun during the project meetings. *Mehmet*, Naber Koc? Being another Turkish in the project, you were my PhD-buddy sharing the same journey. Luckily, you haven't answered incorrectly to the question on Mother Tongue that made you to come this far, be successful and meet me. Thank you for your support at all times. ¿qué pasa tío? My crazy experiment-mate *Juan Carlos*, you are a special guy, always be well-remembered, except our failure to start a music-band. *Salvo*, great time in Brussels and thank you for hosting me! Kumpelino *Antonio*! We had a great time in Stuttgart. *Ignacio*, good chap! We hardly cycled back to home after a night out in Toulouse, thank you for hosting me there. *Basti*, my street singing partner: 'Yesterday' in Brno. *Saverio*, it was a good day in Oxford and Bristol! And also the fellows: *Patrick*, *Bela*, *Thomas*, *Lukas*, *Lipari*, *Simone*, *Roel*, *Harmen*, *Santi*, *Mina*, *Oliver* and *Sebatian*; I had a lot of fun with you guys during the project. In addition, I would like to thank Dr. *Reddy* Alemela from the project. Reddy, your scientific knowledge on the multiphysics in gas turbines were of great value for me, and thank you for being in my graduation committee.

*Debbie*, I just can't thank you enough! I can't just say our secretary; you are an amazing person, who I will always remember. You were always ready to help without any hesitation, even at your busiest times. Always smiling and laughing, and come with a solution or find a corresponded person for solution at the times when I was down. Done, done and done!. You even set your vacation plan according to my graduation day. I highly appreciate your time, interest and help that is available for us at anytime! Thank you very much!

Thank you *Bert* and *Axel*. You were both super-tech helpful! There were times that my work would be delayed if you wouldn't be there and bother yourself for me.

I had great officemates during these years. *Emre*, you made me prove that having me as a paranymp means getting a cum-laude. It was great to meet you, I gained a life-long friend. *Marten*, comrade MJJ, together we made our office more competitive than 7-Eleven, our office light never went off during the day. *Anne*, you never got tired of being beaten in Achtung die Kurve; I really enjoyed our brain-breaker discussions in&out of the office, stay smart as you are and always bear in mind: "How do you know that?". *Andrea*, the reason of the perfume smell and flowers in our office, you were kind to tolerate our noise during our gaming sessions between 12-13.00, but don't expect Anne to show the same tolerance to you rest of the day.

In these years, I made a lot of good friends that I would like to thank them. *Can*, for inviting me to your old-house party on my first day in the Netherlands, for being a close friend, long breaks and introducing me to the kiler-drink sniper; *Laura*, a proud Catalan and the only one to take care Can; *Dimitris* (Dimitrois) and *Pavlina* (Pavlinos), cool and trustworthy Greeks made me play 'sirtaki' in every party and join me for 'damat halayi', great time spent in Tarragona. *Cuneyd*, mudurum!, we shared the last year PhD's stress intensity, lots of discussions, thus having longer breaks, my highly-motivated gym buddy, great story teller, future politician, and I hope you can make for the Turkish MIT. *Sa-muele*, I understood that the meaning of the Turkish hand gestures can be slightly different than the Italian ones that piss off your father (thanks to Signore Nicola for cooking tasty pasta), you took care of me (almost breast-fed) when I was badly injured during snowboarding and couldn't move in Chamonix-Mont-Blanc, and many city trips in Europe in the first year of the PhD, and also thank you being shorter than me that didn't make me the shortest in the basketball team. Thank you *Greg* for being my diving buddy and attempt to kill me with your cylinder under the water, for being the super-cyclist in the triathlon competition and call me the legend even after I lost my route in running, and for sharing your cooking products with us, especially the organic apple and side-products that turn you a Michael Jackson style lap-dancer, and our super-unconscious Hamburg trip and The Black Eyed Peas. Thank you *Markus*, *Rene*, *Mili*, *Daniela*, *Shrii*, *Mouez*, *Eduardo*, and many more; having great days and nights together in Calslaan 38, I tried hard to deserve the title you gave me, Dr. Can of the house. *Markus*, *aslanim!*, I have to admit that you are the most possible Turkish version of a Swiss; Good times in Istanbul and Luzern; you are the far best man-oriental dancer and far worst backgammon player (going to Mars frequently), writing 'nasilsin' (= What's up) in many different combination of letters each time, saying perfectly 'ssshishh' in a Turkish way; anyway you became one of my best friends. And *Florian*, Flo, good times in Australia, where you almost see me death, what a nightmare!; you were a great housemate in Lincoln, screaming in the middle of the night on Friday while I was driving on the wrong line in Cornwall.

I would like to thank all the group members of Applied Mechanics; we had good times, in and out of the office; the former and current fellows from my group that I haven't mentioned

before: *Semih, Didem, Ronald, Vikas, Arjan, Pieter, Alex, Erwin, Ted, Mahmoud*, and also Nonlinear Solid Mechanics group. Good times during the coffee break and group social events. I would like to thank to my master students, *Bert* and *Niek*, who performed really successful studies that contributed in this work.

I had a great experience and good time in *TUSAT* (Turkish Student Association at Twente). *Hasan* and *Arzu*, thank you for making me meet TUSAT and convince me to become the chairperson after a tasteful dinner. I cannot forget my friends in the board for the 2010-2011 period, who were with me till the end, gave me a great support and share a great time and drinks with me: *Yakup, Aykan, Haktan*. I made a lot of friends from Turkey that we had fun: *Deniz Ece, Gizem, Janet, Ramazan, Ugur, Merve, Melis, Gozde, Sertan, Ozlem, Fehmi, Kardelen, Muharrem, Cagri, Umut, Hasan, Recep, Erdi*, and many more... I would like to acknowledge the Turkish Consulate in Deventer, especially Consul General *Nihat Erşen*, and also Prof.dr.ir *Mehmet Akşit* for your support and advices, and your generous contributions in the organisation of the Wise Seminar Series of TUSAT. In addition, I would like to thank *Karin* and *Ansfrida* from the *International office, Student Union* and *Apollo* for their support to TUSAT. All the efforts, which have been devoted to TUSAT, reflected as receiving the Henk Zijm International Award in 2011 from the Student Union of the university for taking very active role in the internationalization of the University of Twente, and establishing successful collaborations with the other associations.

I had a great time with my teammates in the basketball club of the university, *Arriba*. Shoulder to shoulder on the basketball field, cool team presentation nights, got destroyed all together after a nargile (water-pipe) session, broke the couch, and of course making me Sinterklaas that the team claimed they have found the real one from Turkey. I also appreciate the friends from the horseback riding club, *Hippocampus*. Especially, *Gea*, you showed a very kind approach from the first day and not being annoyed from my late arrivals to saddle my horse, and helped me to be on time. And *Jannes*, helping me to memorise the riding comments in Dutch, which made me deal with the club competitions. *Jitske*, you for being very patient and accept me in the top-level course as a non-Dutch person that I only knew the riding-comments in Dutch. Amazing outside riding sessions, after course chats in the bar and Easter brunches. I also would like to thank my diving club, *Piranha* for making the course in English the first time in their history on my request and made me get a license. It is highly appreciated, because I had the chance to dive in Brazil and Australia. Thank you *Rene* and *Swenne* from *Tango Entero*, kindly repeat everything in English during the course, and many more people that I have met or danced; Rene unfortunately we couldn't organise a Tango promotion event with Turkish tango music in the university as we planned; thank you for being open and supportive.

Yes, my paranymp babies: *Rene* and *Batuhan*. *Batuhan*, my brother, we met in high school at the age of 12, literally done everything together, always stayed together even though I left home for the PhD, I wish we will share the outstanding experiences of future to the last moment as we have done for the first moments in our lives. *Rene*, partner!, my first and last housemate in Enschede spending 4 years together, truly amazing personality and now more

stronger version with his feeling from your Turkish-side and discipline from your German-side, thank you to take care of me and listen me when I was washing your brain.

Especially I would like to thank to my parents *Bilent* and *Nesrin*, and my sister *İdil* Altunlu for their endless support, love and encouragement at all times. You are the best family on earth that you are always ready to support me and to sacrifice from yourselves for my goodness and happiness. What I have is already yours, because I wouldn't come this far if I wouldn't have you. And I also thank you for calling me with Skype and for showing me the sun and the sea in Istanbul, the dinners that you cooked, when you come with friends and etc... that made me so frustrated. *İdil*, if I would be the only child, I would have more toys in my childhood, yet nothing would be this much meaningful to me; however this doesn't completely imply that I have no shadow of a doubt. Love you all!..

*Can*



## About the author

Abdullah Can Altunlu was born in Istanbul, Turkey on 31 August 1985. He graduated from Huseyin Avni Sozen Anatolian High School in 2003.

Afterwards, he obtained his BSc. degree in 2007 in Manufacturing Engineering, Faculty of Mechanical Engineering, at *Istanbul Technical University*, Istanbul, Turkey. During his studies he received a fellowship from *Istanbul Technical University Project Management Center*, where he worked on the development and realisation of “*ITU Young Entrepreneur Development Program*” (ITU Genç Girişimci Geliştirme Programı - G3P) supported by *Turkish ISBANK* (Türkiye İş Bankası), *Technology Development Foundation of Turkey* (TTGV), *Technobee* and *Istanbul Technical University Project Management Center*. The main purpose of the project is to provide professional support, vitalise and realise the technology-based innovative ideas of young entrepreneurs in the university.

He studied for a master’s degree in the Manufacturing and Automation Research Center, College of Engineering, at *Koc University*, Istanbul Turkey. During his master studies, he worked as a teaching assistant and research fellow, and he received a SAN-TEZ Graduate Fellowship from Republic of Turkey Ministry of Industry and Commerce as well as a Vehbi Koc Full Graduate Scholarship from Koc University. His master thesis was based on the project, named ‘*An Investigation on the Impact Fatigue Characteristics of Compressor Valve Leaves*’, supervised by Assoc. Prof. Dr. Ismail Lazoglu, and supported by *the ARCELIK A.S.* and *Ministry of Industry and Trade of Turkey*. He worked at *ARCELIK A.S.*, Istanbul, Turkey, in 2009 as a visitor research engineer, and he mainly worked with Dr. Emre Oguz (Thermodynamics Technologies Department) and Serkan Kara (Product Development Department).

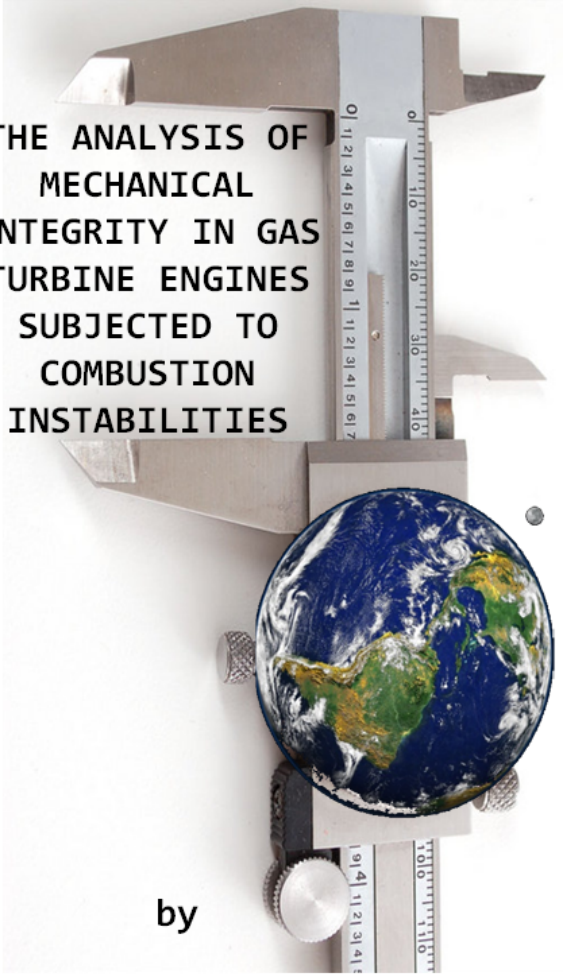
After obtaining his MSc degree in 2009, he started his PhD in the Structural Dynamics and Acoustics research group in Applied Mechanics section, Faculty of Engineering Technology, at *University of Twente*, Enschede, The Netherlands, under supervision of Prof. Dr. Ir. André de Boer and Dr. Ir. Peter van der Hoogt. He worked as a research fellow, and he received a European Union/Marie Curie Initial Training Network Fellowship. During his PhD, as part of his project he worked at *SIEMENS Industrial Turbomachinery*, Lincoln, UK, in 2011, and he mainly worked with Dr. Lingli Yu (Combustion Department) and Dr. Martin Hughes (Mechanical Integrity Department), and at *LABORELEC*, Linkebeek, Belgium, in 2012, with Dr. Hannes Laget (Combustion, Thermodynamics and Biomass Department).

Following his PhD, he continues his career at *SHELL*, Rijswijk, The Netherlands as Research Engineer Wells in the Research & Development Department.



# INVITATION

TO ATTEND THE PUBLIC  
DEFENCE OF THE  
DOCTORAL THESIS



THE ANALYSIS OF  
MECHANICAL  
INTEGRITY IN GAS  
TURBINE ENGINES  
SUBJECTED TO  
COMBUSTION  
INSTABILITIES

by

**A. Can Altunlu**

*altunlua2@asme.org*

---

**Paranymphs:**

*Batuhan Gultakan*

*René Heimbuch*

---

**Friday, July 12<sup>th</sup>, 2013**

**at 14.30 hrs,**

**in the Prof. dr. G. Berkhoff**

**Hall, De Waaier building,**

**University of Twente,**

**Enschede, The Netherlands**

---

